INTERNATIONAL DOCTORAL
SCHOOL OF THE USC

Enrica
Soprano

PhD Thesis

Smart biomimetic nanosystems for stimuli-responsive drug delivery carriers

Santiago de Compostela, 2022

Doctoral Programme in Materials Science

DOCTORAL THESIS

SMART BIOMIMETIC NANOSYSTEMS FOR STIMULI-RESPONSIVE DRUG DELIVERY CARRIERS

Enrica Soprano

INTERNATIONAL PHD SCHOOL OF THE UNIVERSITY OF SANTIAGO DE COMPOSTELA

PHD PROGRAMME IN MATERIAL SCIENCE

SANTIAGO DE COMPOSTELA, 2022

DECLARACIÓN DEL AUTOR/A DE LA TESIS

D./Dña. **Enrica Soprano**

Título de la tesis: **Smart biomimetic nanosystems for stimuli-responsive drug delivery carriers**

Presento mi tesis, siguiendo el procedimiento adecuado al Reglamento y declaro que:

1) La tesis abarca los resultados de la elaboración de mi trabajo.
2) De ser el caso, en la tesis se hace referencia a las colaboraciones que tuvo este trabajo.
3) Confirmo que la tesis no incurre en ningún tipo de plagio de otros autores ni de trabajos presentados por mí para la obtención de otros títulos.
4) La tesis es la versión definitiva presentada para su defensa y coincide la versión impresa con la presentada en formato electrónico.

Y me comprometo a presentar el Compromiso Documental de Supervisión en el caso que el original no esté depositado en la Escuela.

En **Santiago de Compostela**, **22 de febrero de 2022**.

Firma electrónica

AUTORIZACIÓN DEL DIRECTOR DE LA TESIS

Smart Biomimetic nanosystems for stimuli-responsive drug delivery carriers

Dª. Beatriz Pelaz
Dª. Ester Polo

INFORMAN:

Que la presente tesis, se corresponde con el trabajo realizado por Dª. Enrica Soprano, bajo mi dirección, y autorizo su presentación, considerando que reúne los requisitos exigidos en el Reglamento de Estudios de Doctorado de la USC, y que como director de esta no incurre en las causas de abstención establecidas en la Ley 40/2015.

De acuerdo con lo indicado en el Reglamento de Estudios de Doctorado, declara también que la presente tesis doctoral es idónea para ser defendida en base a la modalidad de Monográfica con reproducción de publicaciones, en los que la participación de la doctoranda fue decisiva para su elaboración y las publicaciones se ajustan al Plan de Investigación.

En Santiago de Compostela, 22 de Febrero de 2022.

AUTORIZACIÓN DEL TUTOR DE LA TESIS

Smart Biomimetic nanosystems for stimuli-responsive drug delivery carriers

D. Pablo Taboada Antela

INFORMA:

Que la presente tesis, se corresponde con el trabajo realizado por Dª. Enrica Soprano, bajo mi tutorización. y autorizo su presentación, considerando que reúne los requisitos exigidos en el Reglamento de Estudios de Doctorado de la USC, y que como director de esta no incurre en las causas de abstención establecidas en la Ley 40/2015.

De acuerdo con lo indicado en el Reglamento de Estudios de Doctorado, declara también que la presente tesis doctoral es idónea para ser defendida en base a la modalidad de Monográfica con reproducción de publicaciones, en los que la participación del doctoranda fue decisiva para su elaboración y las publicaciones se ajustan al Plan de Investigación.

En Santiago de Compostela, 22 de Febrero de 2022.

Contents

List of Abbreviations

AFM	Atomic Force Microscope
Alexa Fluor 555 BT7R	Beta Tubulin Monoclonal Antibody
aPD-1	Programmed Death-1 antibody
APS	Ammonium persulfate
AuNS	Gold Nanoshell
BODIPY ™ FL DHPE	*N*-(4,4-Difluoro-5,7-Dimethyl-4-Bora-3a,4a-Diaza-*s*-Indacene-3-Propionyl)-1,2-Dihexadecanoyl-*sn*-Glycero-3-Phosphoethanolamine
BP	Black phosphorus
BPQD-RMNVs	RBCM-derived black phosphorus QDs nanovesicles
BSA	Bovine serum albumin
CCNP	Cancer membrane coated PLGA NP
cDMEM	Complete DMEM
CIE	Clathrin-independent endocytosis
CME	Clathrin-mediated endocytosis
CP	Chlorpromazine
CPP	Cell-penetrating peptides
CPPN	Cancer cell membrane-coated paclitaxel-loaded polymeric core nanoparticle
CQ	Chloroquine
CSM	Cellsome
CTAB	Hexadecyltrimethylammonium bromide
CTCF	Corrected total cell fluorescence
CTCs	Circulating tumor cells
CTL	The cytotoxic T lymphocyte
DC	Dendritic cells
DDS	Drug delivery systems
DS	Seminaphtorhodafluor labeled Dextran (Dextran-SNARF)
DLS	Dynamic Light Scattering
DMEM	Dulbecco´s Modified Eagle Medium
DOPE	1,2-Dioleoyl-*sn*-glycero-3-phosphoethanolamine
DOTAP	1,2-dioleoyl-3-trimethylammonium-propane
DOX	Doxorubicin
DTT	Dithiothreitol
DYN	Dynasore
ECM	extracellular matrix
EGFP	Enhanced Green Fluorescent protein
EM	Electron microscopy
EPR	Enhanced Permeability and Retention effect
EV	Extracellular vesicles
FBS	Fetal bovine serum
FC	Flow cytometry
FCSM	Fusogenic cellsome
FDA	Food and Drug Administration
FEME	Fast Endophilin-Mediated

	Endocytosis
FITC	Fluorescein isothiocyanate
FL	Fusogenic liposome
FSC	Forward scatter
GNP	Gold nanoparticle
GPI-AP	Glycosylphosphatidyl inositol-anchored proteins
HA	Hemagglutinin
HEPES	2-(4-(2-hydroxyethyl)-1-piperazinyl)-ethanesulfonic acid
HIV-1	Human immunodeficiency virus type 1
HOE	Hoechst
HSV-1	Herpes simplex virus type I
ICAM-1	Endothelial intracellular adhesion molecule 1
ICP-MS	Inductively coupled plasma mass spectroscopy
IR	Infrared
LDA	Laser Doppler anemometry
LFA-1	Lymphocyte function-associated antigen 1
LFN	Lipofectamine
LLV	Leukolike vector
LPPN	Liposome vesicle coated paclitaxel-loaded polymeric core NP
LSPR	Localized surface plasmon resonance
MBCD	Methyl-ß-cyclodextrin
MFI	Mean fluorescence intensity
miRNA	MicroRNA
MPCM	Macrophages membrane coated nanoparticle
MPS	Mononuclear phagocytic system
MRI	Magnetic resonance imaging
MS	Mass Spectrometry
MSC	Mesenchymal cell
N_A	Avogadro number
NC_A	Tumor necrosis factor α loaded nanovesicles
NC_B	Platelet membrane-coated acid-responsive dextran nanostructure
NG	Nanoghosts carriers
NIR	Near infrared window
NNI	National Nanotechnology Initiative
NP	Nanoparticle
NTA	Nanoparticle tracking analysis
NYS	Nystatin
PBS	Phosphate-buffered saline
PDI	Polydispersity index
PEG	Poly(ethylene glycol)
PET	Positron Emission Tomography
PHA	Phalloidin-FITC
PI	Propidium Iodide
PIC	Protease inhibitor cocktail
PLGA	Poly(lactic-co-glycolic acid)
PM	Platelet membrane
PM-NV	Platelet membrane-coated core-shell nanovesicles
PSNP	Polystyrene nanoparticle
PTT	Photothermal therapy

PTX	Paclitaxel
QDs	Quantum dots
RBC	Red blood cell
RBCM	Red blood cell membrane
RBCNP	Red blood cell coating PLGA
RES	Reticuloendothelial system
RGD	Arg-Gly-Asp peptide
ROI	Region of interest
RPPN	Red blood cell-coated paclitaxel-loaded polymeric core nanoparticle
RT	Room temperature
SDS-PAGE	Sodium Dodecyl Sulphate-PolyAcrylamide gel electrophoresis
SEM	Scanning electron microscopy
siRNA	Short interfering RNA
SMC	Smooth muscle cells
SpA	Staphylococcus aureus protein A
SPION	Superparamagnetic iron-oxide nanoparticles
SPR	Surface plasmon resonance
SSC	Side scatter
STM	Scanning Tunneling Microscope
TEMED	*N*,*N*,*N'*,*N'*-Tetramethylethylenediamine
TNF	Tumor necrosis factor
TNF-α	Tumor necrosis factor α
TRAIL	Tumor necrosis factor-related apoptosis factor
VLP	Virus-like particles
WBC	White blood cell

Acknowledgments

Me gustaría agradecer a mis directoras de esta Tesis doctoral, Dra. B. Pelaz y Dra. E. Polo, y al Dr. P. del Pino. Gracias por todas las enseñanzas y por darme la oportunidad, el apoyo y el tiempo que necesitaba para entender que quería emprender este camino. Sabed que no fue mi gran amor por Santiago lo que me animó, sino vuestro ejemplo de pasión y entusiasmo por este trabajo. Espero seguir buscando este tipo de ilusión para el resto de mi carrera profesional.

También quería agradecer al Dr. P. Taboada, a la Dra. S. Barbosa y al Grupo de física de coloides y polímeros (GFCP) por su colaboración y apoyo. Así como al Instituto de investigación sanitaria de Santiago de Compostela (IDIS), y a la colaboración con el Dr. M. Collado.

Agradecer a la Agencia Estatal de investigación, (CTQ2017-89588-R), y comisión europea (0624_2IQBIONEURO_6_E-1, y ERC-St SPACING 95041) por la financiación que hizo posible mi Tesis doctoral.

Quiero también agradecer a todo el personal de RIAIDT por el análisis de microscopia electrónica que aparecen a lo largo de este trabajo. De igual manera, gracias a la Universidad de Santiago de Compostela, al CiQUS y a todos sus técnicos por poner a mi disposición sus medios de apoyo para el correcto desarrollo de esta Tesis doctoral.

Abstract

The research conducted in this thesis finds its purpose in the development of cell-derived biomimetic nanosystems, aiming to further broaden nanomedicine´s tools towards advanced therapeutics in the drug delivery field.

Nanotechnology offers a plethora of opportunities to design nanodelivery platfoms capable of crossing biological barriers and achieving specific targeting. Nowadays, nanoparticles (NPs) have gained widespread attention as drug delivery vehicles. Thanks to their physical and chemical properties, NPs can be tuned with multiple features, which makes them promising candidates for personalized nanomedicines. Despite the remarkable progress of the last decades in the field, multi-ligand strategies for targeted NPs delivery still suffer from poor *in vivo* efficacy caused by inadequate interfacing of synthetic NPs with biological environments. The main drawbacks are low specificity *in vivo*, fast renal clearance, short permanence time in blood torrent and the activation of the immune response.

An innovative approach that exploits the natural biological membrane of living cells has been proven to be a successful strategy to improve the *in vivo* behavior of synthetic nanocarriers. Designing nanostructures by replicating the natural (bio)-physical properties and highly complex functionalities of the cell surface provides delivery nanosystems with effective biointerfacing, preserving the key functionalities of the origin cells. Depending on the type of the cell source, specific functionalities can be exploited for the development of tailored systems with different therapeutic outcomes, which regulate signaling, transport process and immune responses. Specific targeting of cancer cells represents an important challenge for nanomedicine to promote tumor regression while reducing the side effects of anti-cancer drugs. Potentially, cancer cell-derived NPs can exploit their homotypic affinity towards cancer cells from which they are extracted. It is known that cancer cells shown altered expressions of adhesion molecules on their surface that promote changes in their adhesive properties.

In this thesis, cancer cells were used to obtain biomimetic membrane based nanosystems, with the aim of exploiting natural cell membrane features to enhanced biocompatibility, obtain high specific targeting efficacy and improve immune evading capability.

The first part of this work was aimed to design and develop bio-synthetic cell-derived NPs (named cellsomes, CSMs) using plasmatic membranes of cancer cells. An easily scalable bottom-up process was optimized to obtain CSMs from different cell lines. Their physicochemical and biological properties were comprehensively characterized. To this end, a large variety of techniques were used to study the physiochemical properties of CSMs such as their morphology, hydrodynamic size, colloidal stability in different media, and concentration, among others. The presence of cell membrane components and specific surface biomarkers inherited from the cell source was assessed. The interaction between CSMs and different cell lines was investigated *in vitro.* Selective targeting capabilities of CSMs for the homotypic tumor cells were demonstrated across several tumoral and non-tumoral cell lines. Hybrid CSMs composed of tumoral and non-tumoral cell membranes fragments proved the possibility of translating the targeting capabilities of the tumoral derived CSMs into other non-cancer cell-derived CSMs, thereby expanding their versatility and potential applications.

To study the possibility of applying biomimetic coatings to synthetic materials, solid NPs (*i.e.,* polystyrene NPs) were coated with CSMs membranes. The biomimetic effect on the biointerfacing behaviour of core-shell NPs was studied in 2D and 3D cell culture models. Specifically, it was observed that the CSMs-coated NPs inherently mimic the surface properties of the source cells and thus: (i) acquire homotypic targeting ability; (ii) decreased uptake by macrophage cells and; (iii) present a more efficient penetration into 3D tumor model. Remarkably, the possibility to escape from the immune system by avoiding the rapid recognition by the RES, confers an enhanced therapeutic efficacy to synthetic NPs.

Based on the studies on their biomimetic properties and their exciting capability to interact with cells, the CSM carrier proved to be a promising candidate for the development of an effective drug delivery nanosystem. Two kinds of smart CSMs-based nanocarriers were set up in this study, focusing on the development of innovative strategies to achieve the intracellular delivery of different cargoes that otherwise would not overcome the cell membrane barrier or would be trapped in endo/lysosome vesicles.

The first nanocarrier design was based on a hybrid stimuli-responsive drug delivery nanostructure. The CSMs were combined with photo-responsive NPs (gold nanorods, GNRs), which upon near infrared (NIR) activation, rapidly convert the absorbed energy into thermal energy,

mediating the heating of the local environment. The GNRs-tagged CSMs presented several advantages inherited from the cell-membrane nature, such as the ability to target specific cell populations (homotypic targeting) and preventing cargo´s degradation. On the other hand, due to the thermoplasmonic properties of plasmonic GNRs, a spatiotemporal-controlled intracellular release of cargoes into the cytosol of living cells was obtained under NIR stimulation. NIR-triggered cargo release was demonstrated either at the level of single cells (micrometer NIR spot) and at the level of thousands of cells (energy-homogeneous collimated NIR excitation area of ~0.33 cm^2; circular spot with a diameter of ~0.65 cm). Through these procedures, photo-controlled intracellular delivery of non-permeant antibodies (anti-Tubulin antibody as a proof of concept) was achieved without compromising cell viability nor the antibody´s function. These results set the stage for the development of photoactive cell-derived nanocarriers, which in addition to cell specific functions, promise straightforward access to spatiotemporal-controlled intracellular delivery of antibodies for application in different immunotherapies.

A second alternative strategy to achieve intracellular cargo delivery, escaping the lysosomal entrapping, was successfully developed by surface-engineering the cell-derived nanocarrier to obtain fusogenic CSMs (FCSMs). The direct fusion of the nanocarrier with the plasma membrane of the cells is a straightforward strategy to achieve the intracellular release of the carried cargos into the cytosol. To this aim, the lipidic composition of CSMs was modified by integrating an optimal combination of cationic and dye-labeled neutral lipids (DOTAP and DOPE-Atto) without compromising the cell-derived membrane features. FCSMs were efficiently loaded with manifold types of cargo, from small hydrophobic molecules such the bisbenzimide compound Hoechst H 33258 (HOE) to large molecular mass macromolecules such dye-labeled phalloidin, dextran polymers or polystyrene beads. Upon entering in contact with living cells, in contrast to non-fusogenic CSMs, FCSMs were proved to be able to fuse with the cell membrane of living cells, thereby leading to the release of the encapsulated compounds into the cytosol of cells, avoiding the endocytosis pathway and lysosomal entrapping of the cargo. This technology could represent a powerful tool for fast cytoplasmatic delivery of sensitive drugs, especially proteins and nucleic acids, enabling of designing a new generation of carriers for nanovaccines.

The results of the research conducted in this thesis underline the importance of the biomimetic cell-derived coating technology, which offers a versatile tool for developing improved drug delivery nanovectors by easily recreating natural scenarios at the bionano-interface. These biomimetic interfaces have emerged to overcome some of the main drawbacks inherent to synthetic nanomaterials by translating specific complex functionalities from the cell surfaces that remain complex to replicate synthetically.

Resumo

A investigación realizada nesta tese ten como obxectivo o desenvolvemento de nanosistemas biomiméticos derivados de células para ampliar aínda máis as ferramentas de nanomedicina cara a terapias avanzadas no campo da administración de fármacos.

Nas últimas décadas, a nanotecnoloxía experimentou un crecemento exponencial que continúa na actualidade, introducindo un novo enfoque científico-tecnolóxico que fai uso da materia á nanoescala, dotándoa de propiedades e características especiais, relativas ás propiedades ópticas, eléctricas e magnéticas, á reactividade química e á fluorescencia. Grazas a ditas propiedades, as nanopartículas (NP) adquiriron unha ampla atención como vehículos de administración de fármacos. O uso de nanotecnoloxías farmacéuticas permite superar as propiedades críticas (liberación, penetración, estabilidade) e unha farmacocinética desfavorable das moléculas activas. As vantaxes de utilizar NPs como vehículos para a administración de fármacos están relacionadas co seu pequeno tamaño, permitíndolles atravesar barreiras biolóxicas e pequenos capilares, alcanzando así destinos de interese como tecidos, tumores ou células individuais. Ademais, a súa estrutura ofrece a posibilidade de encapsular o fármaco ou conxugalo na superficie, mediante adsorción ou enlace químico, protexendolo deste xeito da prematura degradación e/ou eliminación *in vivo* e, ao mesmo tempo, garantindo a súa solubilidade no medio biolóxico. As dimensións dos nanosistemas presentan unha ampla superficie en comparación cos materiais de maiores dimensións, o que mellora a capacidade de unión de moléculas na superficie que atribúen unha funcionalidade específica ás NPs. Esta característica ofrece a capacidade de alcanzar dianas biolóxicas grazas á conxugación cun ligando específico (anticorpo, péptido, etc.). Ademais, o emprego de NP como vectores favorece a acumulación do fármaco no lugar de interese terapéutico, reducindo a súa dispersión no organismo. En consecuencia, permite non só diminuír a frecuencia de dosificación, senón tamén os efectos secundarios, resultando nun sistema máis beneficioso para o paciente.

A pesar do notable progreso deste campo nas últimas décadas, as estratexias multiligandos para a administración dirixida de NPs sofren dunha escasa eficacia *in vivo* causada pola interacción inadecuada das NP sintéticas con ambientes biolóxicos. Tras a administración, as NP enfróntanse a un ambiente complexo que presenta numerosas barreiras físicas e biolóxicas

para a súa acción. A primeira delas é ofrecida polo torrente circulatorio, xa que o sangue é rico en proteínas que se adsorben na superficie das NPs formando unha coroa biomolecular. Esta coroa confire ás NPs unha nova identidade biolóxica, desempeñando un papel importante na súa distribución e posiblemente comprometendo a súa acción. A adsorción de proteínas plasmáticas (como apolipoproteínas, compoñentes do complemento e inmunoglobulinas) na superficie da NP facilita o seu recoñecemento e a súa eliminación do sangue (opsonización), accións levadas a cabo polos fagocitos circulantes, así como polos macrófagos dos tecidos (principalmente as células de Kupffer hepáticas e os macrófagos do bazo), tamén coñecido como sistema fagocítico mononuclear (MPS). Este rápido recoñecemento e secuestro representan o principal desafío para o desenvolvemento de función eficaces *in vivo* das nanoformulacións. Ademais, a exposición de certos dominios proteicos pode desencadear de xeito potencial vías específicas de recoñecemento celular, dando como resultado a activación de determinados procesos biolóxicos como a activación do sistema inmunitario.

Un enfoque innovador que explota a utilización da membrana biolóxica natural das células vivas demostrou ser unha estratexia exitosa para mellorar o comportamento *in vivo* dos nanoportadores sintéticos. Deseñar as nanoestruturas replicando as propiedades (bio)-físicas naturais e as funcionalidades altamente complexas da superficie celular proporciona aos nanosistemas de entrega unha biointerfaz eficaz, preservando as funcionalidades clave das células de orixe.

Dependendo do tipo celular utilizado, pódense transferir funcionalidades específicas para o desenvolvemento de sistemas personalizados con diferentes resultados terapéuticos. Deste xeito, é posible regular a sinalización, os procesos de transporte e as respostas inmunitarias. Por exemplo, as NPs recubertas de membranas de glóbulos vermellos (RBC, tamén coñecidas como eritrocitos) asócianse cun maior tempo de circulación sanguínea, reducindo a súa eliminación polo sistema inmunitario. As NPs derivadas de células nai presentan boas propiedades de orientación y emerxen como posibles terapias contra o cancro debido á predisposición destas células a migrar cara o tecido afectado e inflamado. Normalmente, estas rexión caracterízanse por condicións ambientais como a hipoxia ou á interacción con receptores ou citocinas tipo Toll.

A decoración da membrana celular dos macrófagos promove a captación das NPs polas células do cancro de mama metastático mediante a interacción entre a integrina α4 e a molécula de adhesión celular vascular-1 (VCAM-1), o cal se viu que produce un notable efecto inhibitorio sobre a metástase pulmonar. Os leucocitos están implicados na protección do organismo contra enfermidades contaxiosas e invasores foráneos. Polo tanto, as membranas dos leucocitos teñen a propiedade de evadir o sistema inmunitario e de localizar os tecidos ou diana, mostrando así a súa capacidade de orientación mediante interaccións célula-célula. As NPs recubertas de membranas de células cancerosas presentan unha excelente internalización por parte das liñas celulares orixinais (afinidade homotípica). En particular, a interacción específica coas células tumorais representa un reto importante na nanomedicina, co obxectivo de promover a regresión do tumor ao mesmo tempo que se reducen os efectos secundarios de fármacos anticanceríxenos. As células tumorais agloméranse facilmente o que desencadea a formación de tumores sólidos debido aos mecanismos de adhesión celular mediados por proteínas específicas (proteínas de adhesión focal, integrinas, etc.) da superficie celular. Desta maneira, ditas interaccións homotípicas entre as células tumorais pódense aplicar como estratexia de especificidade de cara ao tumor mediante revestimentos biomiméticos que permiten o auto-recoñecemento.

Nesta tese, as células cancerosas utilízanse para obter nanosistemas baseados en membranas biomiméticas co obxectivo de aproveitar as características naturais das membranas celulares para mellorar a biocompatibilidade, obter unha alta especificidade, e promover a capacidade de evasión inmunolóxica.

A primeira parte do traballo realizado ao longo desta tese, tivo como obxectivo deseñar e producir NPs bio-sintéticas derivadas de células denominadas cellsomas (CSMs) utilizando membranas plasmáticas de células cancerosas. Optimizouse un proceso ascendente facilmente escalable para obter CSMs de diferentes liñas celulares. Os CSMs producíronse mediante a combinación de dous métodos de perturbación física capaces de romper as membranas usando diferentes forzas externas como a calor e a presión. A lise celular completa levouse a cabo mediante (i) un choque osmótico producido mediante unha solución tampón hipotónica e, (ii) lise térmica realizada mediante ciclos repetidos de conxelación-desconxelación.

A solución hipotónica proporciona a presión osmótica necesaria para expansión celular. A concentración de sal que rodea a célula diminúe rapidamente, polo que a membrana celular faise permeable á auga debido ao efecto osmótico. A combinación da presión osmótica e o efecto de choque térmico provocado polos ciclos de conxelación-desconxelación induce aberturas transitorias na membrana celular para baleirar a célula dos seus compoñentes. Para minimizar a posible desnaturalización das proteínas de membrana, a extracción da membrana plasmática foi o máis suave posible, co obxectivo de manter a súa bioactividade. As proteínas solubles, as biomacromoléculas intracelulares e o núcleo foron eliminados mediante centrifugación. Posteriormente, os fragmentos de membrana purificados son presionados contra pasar a través de membranas de policarbonato con poros nanométricos para obter CSMs autoensamblados cun tamaño que oscila entre 100 e 400 nm.

As nanoestruturas caracterizáronse completamente mediante unha gran variedade de técnicas coa finalidade de avaliar as características fisicoquímicas dos CSM: Scanning Electron Microscopy (SEM) para a determinación da morfoloxía, Dynamic Light Scattering (DLS) para o tamaño hidrodinámico e a estabilidade coloidal, anemometría láser Doppler para o potencial ζ, Nanoparticle Tracking Analysis (NTA) para a análise de concentración e distribución de tamaño e fluorescencia espectroscopia para cuantificar a eficiencia de carga de moléculas fluorescentes, entre outras. Realizouse un estudo das propiedades biolóxicas e avaliouse a presenza de compoñentes da membrana celular, como biomarcadores específicos de superficie transferidos da liña celular orixinal. A interacción entre CSMs e diferentes liñas celulares investigouse mediante estudos *in vitro*. A capacidade dos CSMs de levar a cabo un mecanismo de interacción homotípica coas células tumorais móstrase en varias liñas de células tumorais e non tumorais. Por outra banda, CSMs híbridos compostos por fragmentos de membranas celulares tumorais e non tumorais demostraron a posibilidade de trasladar as capacidades interacción específica dos CSMs derivados do tumor a outros CSMs, ampliando así a súa versatilidade e aplicacións potenciais.

Para estudar a posibilidade de aplicar revestimentos biomiméticos a materiais sintéticos, recubríronse NPs sólidas (neste caso, NPs de poliestireno) con membrana CSMs. O comportamento e efecto biomimético das NPs formadas por núcleo e cuberta foi estudado en modelos de cultivo celular 2D e 3D. En concreto, observouse que as NP revestidas de CSMs

reproducen as propiedades inherentes da superficie das células de orixe e, polo tanto: (i) adquiren capacidade de interacción homotípica; (ii) diminúen a captación polos macrófagos e; (iii) presentan unha penetración máis eficiente no modelo de tumor 3D. Sorprendentemente, a posibilidade de escapar do sistema inmunitario evitando o rápido recoñecemento por parte do RES, confire unha eficacia terapéutica mellorada en comparación coas NPs sintéticas.

Baseándose nos estudos sobre as propiedades biomiméticas e a emocionante capacidade para interactuar coas células, o uso de os CSMs como vehículos demostraron ser candidatos prometedores para o desenvolvemento dun nanosistema eficaz de administración de fármacos. Cómpre ter en conta as vías de internalización das NPs, xa que a liberación citosólica do fármaco é un requisito previo fundamental para obter sistemas exitosos de administración de fármacos. A vía de transporte implicada na internalización celular dos CSMs foi investigada en diferentes liñas celulares. Os resultados suxiren que (i) os CSMs seguen a vía da endocitose, (ii) poden utilizar diferentes mecanismos de captación para entrar en diferentes tipos celulares e (iii) os CSMs acumúlanse nos endosomas tardíos e nos lisosomas. Cando as NPs e as súas cargas quedan atrapadas no interior dos endosomas son expostas a mecanismos de degradación e exocitose mediados por proteasas, resultando nunha fracción limitada de moléculas liberadas con éxito no citosol. Nesta fase, necesítanse métodos específicos de administración intracelular de fármacos, representando un dos retos máis relevantes para as terapias baseadas en proteínas. Para este fin, establecéronse dous tipos de nanoportadores de nova xeración baseados en CSMs, centrándose no desenvolvemento de estratexias innovadoras para lograr a entrega intracelular de diferentes cargas as cales doutro xeito non superarían a barreira da membrana celular ou quedarían atrapadas en endosomas ou lisosomas.

O primeiro deseño de vectores baseouse nunha nanoestrutura híbrida de transporte de fármacos de resposta a estímulos. Os CSMs combináronse con NPs plasmónicas foto-sensibles. A luz foi un dos estímulos externos máis empregados para promover a liberación controlada de fármacos e mellorar a sua (súa) distribución. As NP plasmónicas son particularmente interesantes neste caso, xa que poden absorber e difundir a luz incidente a través da oscilación colectiva dos electróns de condución confinados na superficie da NP, un fenómeno coñecido como resonancia plasmónica de superficie localizada (LSPR). Aplicando unha radiación luminosa cunha frecuencia

superposta á banda de absorción SPR das NPs, a enerxía absorbida disípase rapidamente e convértese en enerxía térmica, producindo o quecemento do ambiente local. A gran vantaxe das NPs de ouro é que o seu LSPR pódese estender á rexión próxima ao infravermello (NIR) axustando o seu tamaño, forma e funcionalización. O rango de lonxitudes de onda NIR (650-900 nm) é a chamada "xanela biolóxica", xa que a absorción da radiación luminosa pola auga, a hemoglobina e, polo tanto, os tecidos do corpo humano é mínima, acadando altos niveis de penetración nos tecidos brandos. Ditas propiedades abren así grandes posibilidades para o uso de NPs de ouro no campo biomédico, que poden usarse non só para o transporte de fármacos e a liberación localizada da carga, senón tamén na terapia do cancro por hipertermia. Neste estudo, seleccionáronse nanorods de ouro (GNRs) como fontes de nanoquecemento sensibles á luz debido as súas características ópticas, dando lugar ao efecto fototérmico inducido pola iluminación NIR de 800 nm. Os CSMs marcados por GNR como sistema de administración de fármacos presentaron varias vantaxes herdadas da natureza da membrana celular, por exemplo, a capacidade de dirixirse a poboacións celulares específicas (interacción homotípica) e previr a degradación da carga. Por outra banda, debido ás propiedades termoplasmónicas dos GNR, obtívose unha liberación intracelular das moléculas transportadas controlada espazo-temporalmente no citosol das células vivas tras a estimulación NIR. A liberación controlada de moléculas activada por NIR demostrouse con dúas configuracións ópticas: i) irradiación NIR altamente enfocados (densidades de potencia elevadas dun "punteiro" láser NIR cun diámetro de ~ 5 µm, semellante ás pinzas ópticas clásicas) en experimentos de células individuais, e ii) iluminación de conxuntos de células cun laser NIR colimado de gran diámetro (~ 0,65 cm; baixa densidade de potencia). A través destes procedementos, conseguiuse a liberación intracelular fotocontrolada de anticorpos non permeantes contra compoñentes celulares (anticorpo antitubulina como proba de concepto) sen comprometer a viabilidade celular nin a función do anticorpo. Estes resultados establecen o marco para o desenvolvemento de nanovehículos fotoactivos derivados de células, que ademais das funcións específicas das células das que proveñen, amosan unha capacidade de entrega intracelular controlada espazo-temporalmente. Este mecanismo podería empregarse por exemplo, para a administración de anticorpos para a súa aplicación en diferentes inmunoterapias. Ademais, a versatilidade do sistema fai que se poida traducir a calquera diana intracelular mediante a liberación da macromolécula correspondente, como Abs inhibidores activos (ou

minicorpos ou nanocorpos), así como outros factores de transcrición estimuladores, siRNA, miARN, *etc*., no citosol das células.

Unha estratexia alternativa para lograr a liberación das cargas intracelulares, escapando do atrapamento lisosomal foi desenvolvida con éxito mediante a enxeñaría das superficies dos nanovehículos con derivados de células para a obtención de CSMs fusogénicos (FCSMs). Entre as múltiples estratexias de escape endosómicos, a fusión directa do nanovehículo coa membrana plasmática das células amósase como alternativa para conseguir a liberación intracelular dos cargamentos transportados. Ao entrar en contacto, dúas rexións de bicapa lipídica fusiónanse, unindo os dominios fosfolipídicos e mesturando compoñentes internos. Este mecanismo de entrega directa de fármacos no citoplasma celular é unha alternativa moi prometedora, xa que reduce o impacto da endocitose, protexendo así a carga de moléculas do medio ácido, así como o secuestro de carga polos lisosomas. Os descubrimentos recentes de Csiszar e os seus compañeiros de traballo levaron ao desenvolvemento dun enfoque innovador para mellorar a entrega de fármacos no citosol celular, aplicando unha combinación de diferentes lípidos directamente relacionados coa eficacia fusoxénica dos vehículos baseados en lípidos (liposomas). Se ben é certo que o mecanismo de fusión aínda non foi profundamente dilucidado, sábese que a carga positiva de (Dioleoyl-3-trimethylammonium propane) DOTAP permite aumentar a interacción electrostática entre os liposomas e o glicocálix cargado negativamente da membrana celular, promovendo así a fusión. A presenza de lípidos neutros con estrutura de cono como (1,2-Dioleoyl-sn-glycero-3-phosphoethanolamine) DOPE e lípidos asociados a cromóforos poderían xogar un papel importante na formación de estados de fusión intermedios, grazas á tendencia a inducir inestabilidades locais na membrana lipídica. Inspirándose nestes estudos, a composición lipídica dos CSMs foi modificada integrando unha combinación óptima de lípidos neutros catiónicos e marcados con colorante (DOTAP e DOPE-Atto). A capacidade fusoxénica foi avaliada mediante microscopía confocal e a eficacia de liberación específica dos FCSMs foi investigada mediante estudos de FC. Confirmouse que as propiedades homotípicas se mantiveron na nova formulación modificada con lípidos. Seguidamente, os FCSMs cargáronse de forma eficiente con múltiples tipos de carga, dende pequenas moléculas hidrófobas (como o composto de bisbencimida Hoechst H 33258, HOE) ata macromoléculas de gran masa molecular (como faloidina marcada con fluoroforos, polímeros de dextrano ou partículas de poliestireno). Ao entrar en contacto coas células vivas, á diferenza dos CSMs non fusóxenos,

os FCSMs son capaces de fusionarse coa membrana de células vivas, provocando así a liberación dos compostos encapsulados no citosol das células e evitando a endocitose e o atrapamento lisosomal das moléculas. Esta tecnoloxía podería representar unha poderosa ferramenta para a rápida liberación citoplasmática de fármacos sensibles, especialmente proteínas ou ácidos nucleicos, o que permite deseñar unha nova xeración de portadores para nanovacinas.

En xeral, os resultados obtidos, así como as capacidades técnicas adquiridas nesta tese, contribuirán a unha ampla gama de posibles innovacións no campo da nanomedicina. Máis concretamente, constitúen un paso máis no deseño dunha nova xeración de vehículos transportadores para a administración de medicamentos. A súa aplicación potencial para o tratamento de diferentes enfermidades pódese conseguir seleccionando a carga específica e un revestimento biomimético capaz de traducir e implementar certas funcións celulares específicas. Deste xeito, permite o desenvolvemento de novos fármacos cunha cinética mellorada e unha maior direccionalidade cara a tecidos específicos. A entrega intracelular eficiente de compostos esóxenos e carga macromolecular facilitará o avance en múltiples aplicacións, incluíndo terapias baseadas en células, edición de xenes, reprogramación celular, nanovacinas e detección de biomarcadores intracelulares, entre outras.

Introduction

1. Introduction

1.1. Nanotechnology

Nanotechnology is a multidisciplinary branch of applied science and technology that deals with the control of matter on a nanometric dimensional scale, typically between 1 and 100 nm (10^{-9} -10^{-7} m), and involves the design and construction of devices on this scale (Figure 1.1.1).[1]

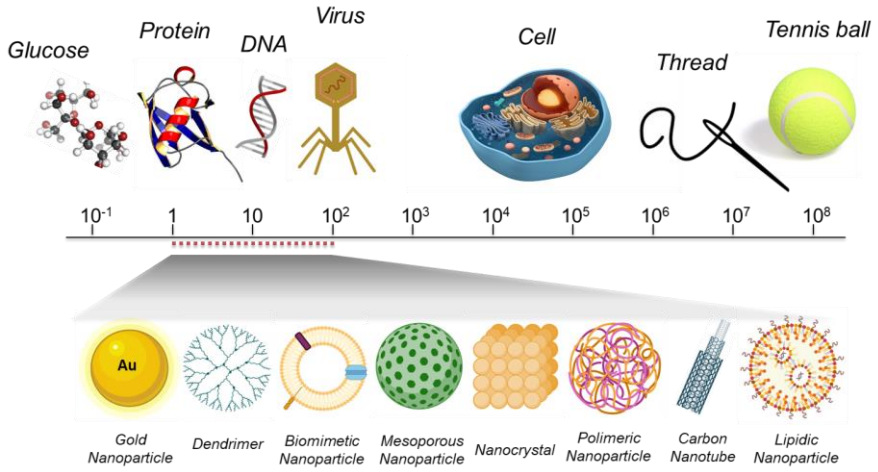

Figure 1.1.1. Scale of interest of nanotechnology (red line).

The concept of nanotechnology was introduced in 1959 by the US physicist Richard Feynman in a lecture entitled "*There's plenty of room at the bottom*", in which he considered the possibility of manipulating matter on a small scale in order to interfere with the biological system at the atomic level.[2] In 1968 a technique was introduced to deposit single atomic layers (Molecular Beam Epitaxy);in 1989 the first example of manipulation at the atomic scale was shown by writing the letters of the company IBM on a copper surface with individual Xenon atoms. As for the technical development concerning the visualization of matter at the nanoscale, the Scanning Tunneling Microscope (STM) was invented in 1981 and the Atomic Force Microscope (AFM) in 1986. These instruments opened the doors of the nanoworld to scientists and revolutionized the imaging and manipulation of surfaces at the nanoscale.

The term "nanotechnology" was actually coined only in 1974 by the researcher Norio Taniguchi, of the University of Tokyo, in relation to the ability to accurately manipulate materials on a nanometric scale, the nanomaterials.[3] The term was introduced in the scientific and social field in 2000, on the occasion of the National Nanotechnology Initiative (NNI).[4] Subsequently (2004), the Royal Society & Royal Academy of Engineering (UK) defined nanoscience as the study of phenomena and manipulation of materials on the atomic, molecular and macromolecular scales, at which materials acquire chemical-physical properties that differ significantly from those of materials on a larger scale. Nanotechnologies were defined as a discipline for the design, characterization, production and application of structures, devices and systems at the nanoscale.[5]

Nanotechnologies have undergone an exponential growth that continues today, introducing a new scientific-technological approach that exploits matter at the nanoscale. At the nanoscale, manifold materials present optical, electrical and magnetic properties, chemical reactivity and fluorescence that diverge from these at the macroscopic scale.[6] Along with the development of strategies to synthesize nanomaterials, an effort has been made to characterize the unique size-dependent properties of nanoparticles (NPs). Indeed, the radical change in material dimensions affects various physico-chemical properties to a large extent, which needs to be understood to exploit them. An important peculiarity of NPs is their high surface to volume ratio. Cutting a 1 cm^3 cube into 10^{21} cubes, each of 1 nm side, will result in the same overall volume and mass, but with an increase of the surface area by a 10 million factor.[7] This aspect is fundamental if we consider the NPs in a biological system,[8] since it allows to have a greater surface of interaction with the molecular targets, as well as a wider functionalization surface, with an exponential increase in the molecules' reactivity. In addition, the high surface to volume ratio implies great differences in their electronic, optical, and chemical properties as well as in their mechanical characteristics. For instance, the force of gravity at nanoscale range becomes less influential, being directly proportional to the body weight, while weak interaction forces, such as Van der Waals forces and surface tension, become more relevant. The classical physics laws are no longer appropriate to describe the behavior of nanoscale matter and are replaced by those of quantum physics. The high confinement of electrons causes an increase in the bandgap of semiconductors, optical absorption, and photo-luminescence. Furthermore, mechanical properties such as elasticity, hardness and ductility also change. The distinctive properties of NPs open the way to a wide range of

applications in multiple fields, from industry to medicine, from information technology to cosmetics (Figure 1.1.2).[9]

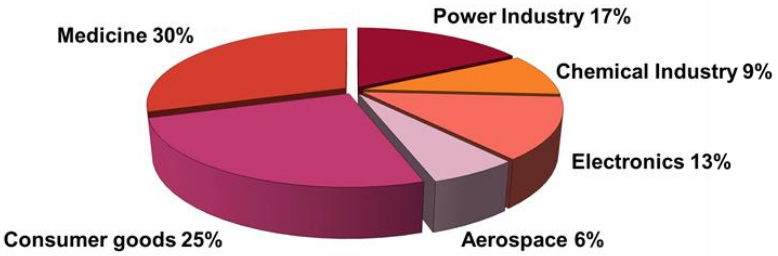

Figure 1.1.2. The major fields of use of nanotechnology and percentage of incidence.

Among the various sectors of interest in which nanotechnology is involved, in the field of nanomedicine, it can offer unique powerful solutions to fight manifold diseases such as cancer, immunological diseases and to develop new vaccines or novel personalized nanomedicines.[10-12] Nanomaterials are similar in scale to biologic molecules as nanoscale systems and colloidal syntheses have enabled the engineering of NPs with innumerable designs (*i.e.*, composition, structure, surface chemistry and functionalities), making the nanotechnology potentially useful in several biomedical applications.[13] The field of nanomedicine aims to use the properties and physico-chemical characteristics of nanomaterials for the diagnosis and treatment of diseases at the molecular level.

1.1.1. Nanomaterial classification

A wide range of NPs have been designed and described for different applications in nanomedicine. They can be classified based on different parameters, namely, their origin (natural or anthropogenic), chemical composition (organic and inorganic), formation (biogenic, geogenic, anthropogenic, and atmospheric), their size, shape and characteristics, their applications in research and industry, *etc*.

As for chemical composition, the first category is represented by inorganic NPs, consisting mainly of metals and their oxides, such as gold NPs, iron oxide, quantum dots (QDs) and silica NPs (Figure 1.1.3). Their

nature defines different properties such as high electron density and strong optical absorption (in particular Au),[14] photoluminescence in terms of fluorescence (semiconductor QDs, *e.g.*, CdSe or CdTe)[15] or phosphorescence (doped oxide materials, *e.g.*, Y_2O_3), or magnetic moment (*e.g.*, iron oxide or cobalt NPs).[16] These properties are widely used for diagnostic and therapeutic purposes.[17]

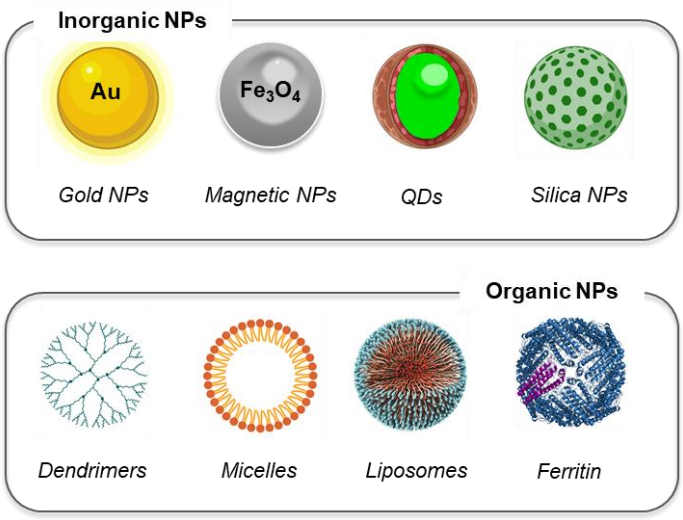

Figure 1.1.3. Some examples of inorganic and organic NPs.

Organic NPs are made from totally biodegradable materials. For this aspect they are very useful for applications in the medical field, given their compatibility with biological materials. This class of NPs includes liposomes, dendrimers, micelles, and protein-based NPs (*e.g.*, ferritin), mostly having spherical three-dimensional morphology. They not only have a surface that can be exploited for anchoring molecules to increase specificity and selectivity of action, but also have an internal cavity that is mainly used to encapsulate organic material such as drugs, nucleic acids or other molecules that may be insoluble in water. These characteristics determine their main use as vehicles for the transport of molecules to the target of interest (drug delivery systems).[11,18,19]

The third category is represented by hybrid (core-shell) NPs, so named for their composition combining organic and inorganic material (Figure 1.1.4). They can have an internal core, usually of an inorganic nature, which

constitutes the origin of the magnetic or fluorescence signal, and an external shell, *i.e.*, the shell of organic nature, which covers the internal portion and makes the NP biocompatible.[9,17] The outer shell can be functionalized so that the surface exposes recognition molecules, such as antibodies or ligands for specific receptors.[20,21] The functionalization of these elements leads to the formation of nanocompounds which, thanks to their magnetic and electronic properties, can be exploited as nanodevices. Furthermore, hybrid NPs offer a tool for the study of biological interactions,[22] an innovative drug delivery system and the possibility of new theranostic techniques.[23,24]

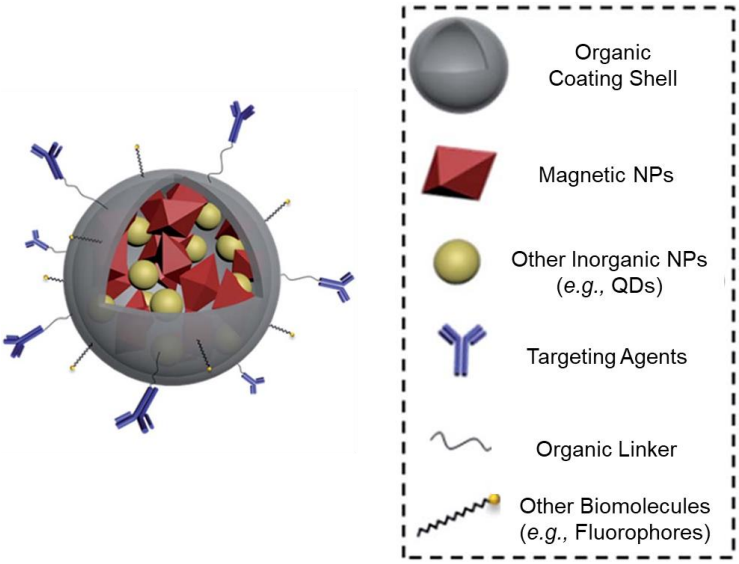

Figure 1.1.4. Illustration of multifunctional nanocompounds consisting of multiple inorganic NP cores, functionalized organic coating shells and different surface conjugated biomolecules (adapted with permission from ref.[24] Copyright 2013, Royal Society of Chemistry).

In the last decade, there has been considerable interest to develop bioinspired nanomaterials derived from biological entities already present in nature. Thanks to their biointerfacing capabilities, cellular structures (*i.e.*, erythrocytes, leukocytes, platelets, and exosomes) or invasive pathogens (*i.e.*, bacteria and viruses) can be exploited to design a new class of nanomaterials in order to overcome the limitations of synthetic NPs.[25] Biomimetic membrane-derived NPs will be described in the next sections.

1.1.2. Nanobiotechnology in medicine

In the context of biomedical application, nanobiotechnology is an extended term that can be defined as the manipulation of materials at molecular levels, which aims to produce non-toxic bioactive devices that have specificity toward the desired tissue type and location. Nanobiotechnology can find its niche in a multitude of applications, wherein nanomaterials provide great advantages in developing small detection and theranostic systems given their small size, thereby allowing the targeting and detection at the single cell or even at molecular level.[26,27]

1.1.3. Nanodiagnostic

To date, the creation of multifunctional tools that allow simultaneous diagnosis and therapy falls within the scope of theranostics, for which nanomaterials are proving excellent candidates. Nanotechnology-based sensors (*e.g.*, nanowires, nanotubes, NPs, cantilevers and micro /nanoarrays) can enable fast and high throughput detection of disease biomarkers under non-invasive conditions, allowing the early identification of the disease and, ideally, the detection of the predisposition to it. Thanks to their small size and high functional versatility, NPs prove to be excellent candidates as contrast agents to obtain sharper and easier-to-analyze images.[28] In fact, they are used as diagnostic devices for *in vivo* applications as contrast agents for medical imaging such as Positron Emission Tomography (PET) and Magnetic Resonance Imaging (MRI)) of various pathologies.[29] Nanotechnology also offers innovative solutions for early detection of viruses, bacteria and circulating tumor cells, as well as for single cell analysis. [30,31] Subsequent to diagnosis, the same NPs can be conjugated with a pharmacologically active agent and used for therapy, as detailed in the next section. Certain nanomaterials have unique therapeutic properties that differ from conventional drugs and therefore, can be directly used to treat diseases. For instance, hafnium oxide- and gold-based NPs can greatly enhance X-ray therapy;[32] gold nanoshells/nanorods, carbon nanotubes, magnetic NPs can induce hyperthermia to kill cancer cells;[33] and nanocrystalline silver is used as antimicrobial agent. Some other possible opportunities include reporting *in vivo* efficacy of therapeutics and tracking nanocarrier biodistribution in the body.

1.2. Drug delivery system

Drug delivery systems (DDS) represent alternative systems to today's drug delivery methods that allow for the spatial and temporal control of drug release within the body.[34] The use of pharmaceutical nanotechnologies allows to overcome the critical biopharmaceutical properties (release, permeation, stability) and an unfavorable pharmacokinetics of the active molecules. Thus, substances that show low bioavailability can be conveyed by particles in such a way as to be directed to the specific site of action, modulating their release, and increasing their absorption. Many of these systems can use polymers with particular chemical and physical characteristics, such as biodegradability, bioabsorbability and sensitivity to changes in temperature and pH.

The advantages of using NPs as DDS are related to their small size, which allows them to cross biological barriers and small capillaries thus reaching targets of interests such as tissues, tumor or individual cells.[35] Furthermore, their structure offers the possibility of encapsulating the drug or conjugating it on the surface, by adsorption or chemical bond, thus protecting it from premature degradation and / or elimination *in vivo* and, at the same time, guaranteeing its solubility in the biological environment.[36] The dimensions of the nanosystems allow for a high surface area compared to bulk materials, which improves the ability to bind to the surface molecules that attribute specific functionality to NPs. This feature offers the great advantage to reach biological targets thanks to the conjugation with a specific ligand (antibody, peptide, *etc.*). In addition, the use of NPs as drug delivery vectors favors the accumulation of the drug in the site of therapeutic interest and reduces its dispersion in the body. Consequently, it allows not only to decrease dosage frequency, but also to reduce side effects, favoring patient compliance.[34]

Based on the mechanisms through which the diseased tissue is reached, the DDS are broadly classified into passive and active targeting (Figure 1.2.1).

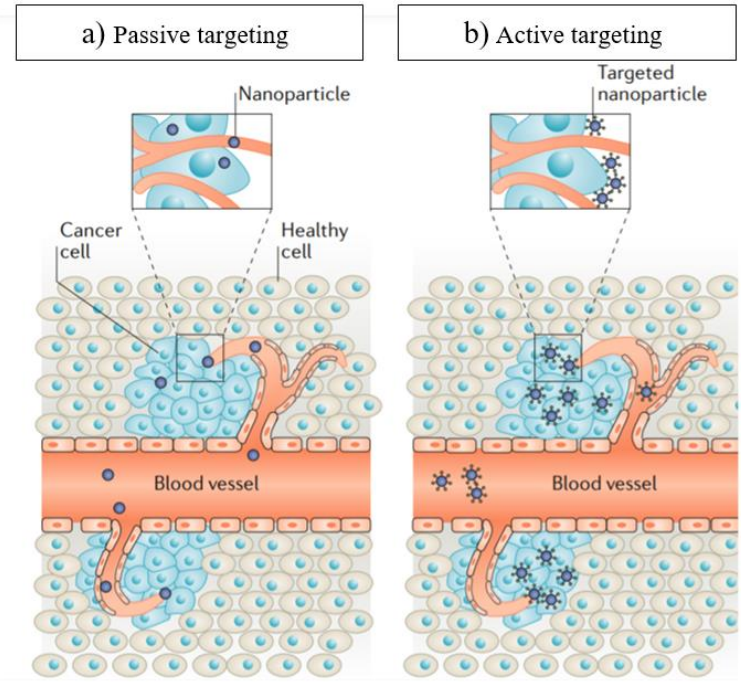

Figure 1.2.1. Representation of passive and active targeting. a) By enhanced permeability and retention effect, NPs passively diffuse through the blood vessels and accumulate in tumor tissue. b) In active targeting, NPs are functionalized with targeting ligands, triggering the receptor-based endocytosis and the enhanced accumulation in tumor tissues (adapted with permission from ref.[37] Copyright 2019, Springer Nature Limited).

Passive targeting is driven simply by the size and shape of the NPs, which determine their biodistribution and accumulation at the tissue level.[38] For this reason, passive targeting is mainly used to treat pathologies that alter the characteristics of the body's tissues, as in the case of tumors. The physiology of solid tumors has been shown to differ from that of normal tissues in several aspects, including abnormal blood vessels, with slow-flowing dilated capillaries.[39] The endothelium of the afferents that are formed present large fenestrations with a diameter of 600-800 nm, which allows the extravasation of NPs up to 600 nm in size from the bloodstream to the tumor tissue.[40] Furthermore, the low efficacy of lymphatic drainage in these tissues allows prolonged retention times of NPs at the tumor level. Passive permeation at the tumor tissue level is defined as the Enhanced Permeability and Retention effect (EPR) (Figure 1.2.2).[41]

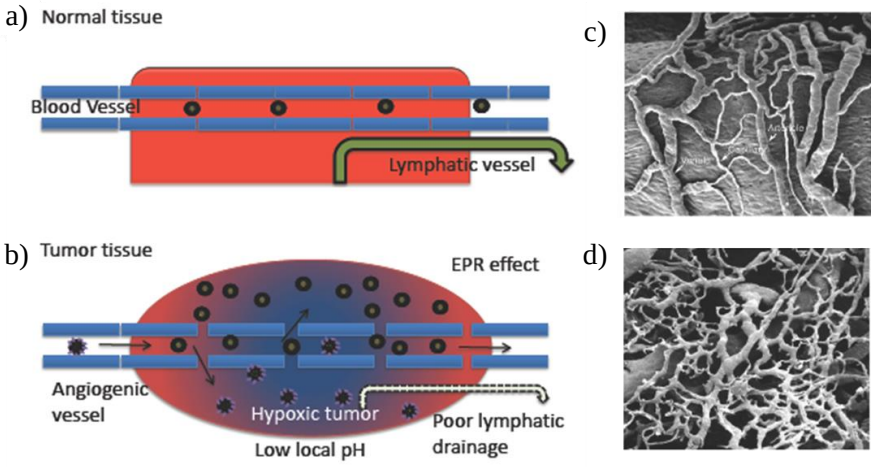

Figure 1.2.2. Representation of the EPR and vascular pathophysiology. a) and c) microcirculation of a healthy tissue, b) and d) microcirculation of a tumor tissue with numerous blood vessel afferents (adapted with permission from ref.[42] Copyright 2013, Royal Society of Chemistry).

Although the EPR effect is pronounced in preclinical models of solid tumor and in humans too, the potential to harness it therapeutically in patients remains unclear, and most nanotherapeutics investigated in clinical trials showed no improvement in relation to it, compared to conventional chemotherapy.[43,44]

Because passive targeting does not rely on biochemical identification, it has the disadvantage of low target specificity. In fact, it can affect normal cells or inflamed areas that, in hypoxic conditions or in a pathological state, may be characterized by vessels with the same characteristics as in tumor tissue, reducing the possibility of a selective transport system.[40]

The disadvantages of passive targeting can be overcome by functionalizing the surface of the NPs with specific molecules such as peptides, proteins or antibodies. This approach is called active targeting and is based on the capability to identify and bind to cell-specific ligands that are expressed on the plasma membrane.[45,46] Trafficking processes, access to barriers and into specific cellular locations are regulated by active biological recognitions. To be successful, active targeting requires that the receptor of interest be exclusive of, or overexpressed by, the cells of the target tissues,[47]

in order to achieve a preferential drug accumulation in the diseased tissue and, thus, a selective therapeutic system. Targeting moieties such as antibodies,[48] aptamers,[49] transferrin,[50] biotin[51] and folic acid,[52] among others, are employed as ligands to promote the specific recognition of the cellular plasma membrane components. Targets can also be part of the intracellular or extracellular matrix (ECM), such as mitochondria,[53] nuclei[54] or lysosomes,[55] with specific ligands (nuclear localization signal (NLS) peptide, ceramide chain, *etc*.) being selected for their recognition.

1.2.1. Cargo release

The release of the drug carried by the NPs (cargo) is a key step in nanotheranostic applications. Among other advantages, nanocarriers can be designed to respond to the microenvironment changes that trigger the drug release in the target site. A number of infection and inflammation-derived conditions, associated to different pathologies, can be exploited as stimuli to promote the disassemble of the nanocarrier, such as variations in pH,[56,57] oxygen,[58] specific enzymes[59] or biomolecules.[60,61] In this way the drug is released specifically inside the target cells or in the target tissue where it has to play its role. For example, in acid-responsive DNase I nanocapsules the polymeric shell are shed at low pH, resulting in self-degradation and promoting the release of Doxorubicin (DOX) for enhanced therapeutic efficacy.[62]

The drug release can also be triggered by external physical stimuli such as ultrasounds,[63,64] light[65,66] or magnetic field[67,68] in a spatiotemporal controlled way. Several strategies are developed in the NP formulation in order to combine the biocompatible properties of organic nanomaterial with the physicochemical properties of inorganic nanomaterials.

Magnetic NPs such as superparamagnetic iron-oxide NPs (SPION) under an external alternating magnetic field can increase the surrounding temperature, a property that can be exploited to improve tumor penetration combined with hyperthermia or anti-cancer drug delivery. Furthermore, magnetic nanocarriers can reach deep into the tumor and exhibit a switchable drug release through an external alternating magnetic field.[69]

Ultrasound-responsive NPs can progress from unstable large-sized particles (100 to 300 μm) to smaller particles of 1-8 μm, which can cross the tumor barrier for image-guided drug delivery. This kind of particles include

gas-generated NPs, which at the tumor can form large numbers of CO_2 bubbles that efficiently absorb ultrasound at the specific site and timing for ultrasound-actuated drug delivery.[70] Moreover, Correa-Paz *et al.* recently encapsulated a protein drug (the serine protease tissue plasminogen activator, typically used in the treatment of ischemic stroke) and demonstrated ultrasound-activated *in vivo* delivery of such protein drug from the cavity of polymer nanocapsules.[71]

Many researchers applied light as external stimuli to promote the triggered release and to enhance drug distribution. Plasmonic NPs such as gold NPs (GNPs) are particularly interesting in this contest because they can absorb and diffuse incident light through the collective oscillation of conduction electrons confined to the surface of the NP, a phenomenon called localized surface plasmon resonance (LSPR).[14] Using a light radiation with a frequency strongly superimposed on the SPR absorption band of the NPs, the absorbed energy is rapid dissipated and converted into thermal energy, mediating the heating of the local environment. The great advantage of GNPs is that their LSPR can be extended to the near infrared window (NIR) region by tuning their size, shape and functionalization. The NIR wavelength range (650-900 nm) is the so-called "biological window" since the absorption of light radiation by water, hemoglobin and, therefore, the tissues of the human body is minimal and the light is able to penetrate deeply into the soft tissues.[72] These properties thus open up great possibilities for the use of GNPs in the biomedical field which can be used not only for the drug delivery and the cargo release,[73] but also in cancer therapy by hyperthermia.[74,75]

In pioneer studies conducted by Parak and co-workers in this field, plasmonic NPs were embedded in a multilayer polymer microcapsule (≈3–5 μm). Upon photoactivation (by focused NIR micrometric beam) such microcarriers internalized by cells allowed for cytosolic delivery of manifold macromolecules, including small drugs,[76] proteins,[77] fluorescence reporters,[78] and nucleic acids.[79] It is worth nothing that in these experiments cargo delivery was demonstrated at individual cell level, 'opening' the microcapsules one by one with a NIR focused pointer (*i.e.*, optical setup equivalent to optical tweezers), thus leading, for instance, to fluorescence labeling of different intracellular compartments.[80]

1.3. Biointerfacing dilemma

Although the expectations for translational medical solutions based on nanotechnology are high and the proof-of-concept reports are increasing in the literature, only a few nanomedicines (first generation) are currently commercialized. Nanoformulations such as Doxil® (pegylated, DOX-loaded liposomes, Janssen Biotech, Inc., Horsham, PA), Abraxane® (paclitaxel-containing albumin NPs, Celgene, Summit, NJ), AmBisome (liposomal amphotericin B, Gilead, Foster City, CA), Onivyde®, Marqibo®, and Nanotherm® were approved by the Food and Drug Administration (FDA) and are applied in clinics.[81]

The gap between high theoretical progress and quite limited application of nanotechnologies is caused by issues related to the biointerfacing between the synthetic material with the human body environment. The main drawbacks are the low specificity *in vivo*, fast renal clearance, time-short permanence in circulation torrent and activation of immune response. It has been demonstrated that over 99% of all administered cancer-targeting NPs are sequestered by the organs of the reticuloendothelial system (RES) and largely by the macrophage-rich liver. Only 0.7% (median) will accumulate in or interact with solid tumors,[82] and many of the administered NPs will be taken up by macrophages, which are cells of the innate immune system.

By many reported nanoformulation designs, when nanosystems are applied into the *in vivo* field, the liver and the spleen are the major organ where the NPs deposit into. After administration, the NPs face a highly complex environment that presents numerous physical and biological barriers to their action. The first barrier is offered by the circulatory torrent, as the blood is rich in protein that are adsorbed onto the NPe surfaces forming a biomolecular corona. This biomolecular corona gives the NPs a new biological identity, paying an important role in the NP distribution and possibly compromising NPs action.[83,84] The adsorption of plasma proteins, such as apolipoproteins, complement components and immunoglobulins on the NP surface facilitates the recognition and clearance from the blood (opsonization) by circulating phagocytes, as well as the tissue macrophages (mainly the hepatic Kupffer cells and macrophages in the spleen), also known as mononuclear phagocytic system (MPS). This rapid recognition and sequestration represent the major challenge for effective *in vivo* targeting of nanoformulations.[85] In addition, the exposure of certain protein domains can potentially trigger specific cellular recognition pathways,

resulting the activation of determined biological processes such as the activation of the immune system.[86]

To reduce the MPS recognition, strategies minimizing nonspecific interaction in complex media have been developed by using stealth polymers, such as poly(ethylene glycol) (PEG) to modify the NP surface. Despite its good performance, recently several publications have reported immune responses against the synthetic polymer at different degrees and the presence of antibodies against PEG.[87,88]

Among the nanomaterials, liposomes have shown to be an effective DDS with less side effect thanks to their biodegradability, biocompatibility and easy-to-manipulate size and surface.[89] In fact, liposomes are the DDS that have been more widely approved and commercialized.[89,90] Their stability in the blood environment can be increased by entrapped hydrophilic and/or hydrophobic agent, while a high compatibility with the biological environment is allowed by their chemical compositions (phospholipids) and the lipid bilayer structures (Figure 1.3.1).

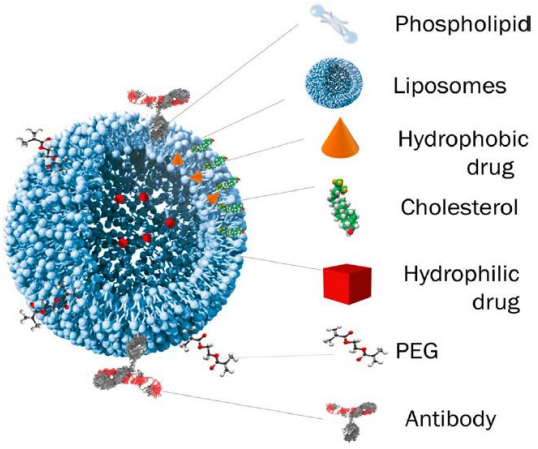

Figure 1.3.1. Schematic structure of functionalized liposome encapsulating drugs. Hydrophilic drugs can be encapsulated in the inner aqueous compartment. Hydrophobic drugs can be encapsulated in the phospholipidic non-polar bilayer. Different kind of moieties can be used to functionalize liposome structure (reused with permission from ref.[91] Copyright 2019, Esteban Beltrán-Gracia *et al.*).

However, several drawbacks such as their stability and their relatively simple structure, hardly close to the complexity of cell membranes, have limited the application of liposomes which require further improvements as DDS.[92,93]

Hence, delivery and control release of nanotherapeutic payloads inside living entities (intracellular delivery) still represents a key challenge in materials science. Most of NPs end up in endocytic vesicles, when they interact with cells that undergo lysosomal fusion, resulting in the degradation of the active cargo.

1.4. Biomimetic cell-derived nanocarries

Recent progress in cell-derived nanosystems has further broadened the nanomedicine tools for advanced therapeutic approaches in drug delivery, imaging, phototherapy, detoxification, and immune modulation, among others.[94] In particular, translating cell membrane features to nanocarriers, such as NPs, liposomes, or other common DDS, offers exciting opportunities to fabricate next-generation of biomimetic nanomaterials for various biomedical applications.[95-97]

The complexity and dynamism of the cell membrane go beyond just being a passive lipid bilayer envelope. Cell membrane proteins and carbohydrates (*e.g.,* glycoproteins and glycolipids) are active components of the cellular machinery, and they are the first responders to what surrounds the cell. In fact, the cell membrane regulates signaling, transport, and immune response, which has stimulated the idea of taking advantage of their intrinsic properties as an integral part of therapies and biomimetic nanoformulations, still exploiting the physical properties related to the synthetic nanomaterial.

Biomimetic nanosystems based on the use of cellular structures have shown numerous advantages compared to the synthetic nanomaterials. The use of entities that the body does not recognize as foreign agents, avoids rapid recognition by the RES, leading to a slower clearance and avoiding immune response. Furthermore, there are countless receptor-ligand, binding, and adhesion interactions that can be taken advantage of to achieve high targeting efficiency without applying elaborate functionalization methods. Cell membrane receptor profiles and characteristics are vital in performing

therapeutic functions that can be translated onto the membrane coating with no loss in their native functionalities.

On this note, recent studies have been focusing on the possibility to develop DDS using whole cells, cell-derived membranes or extracellular vesicles (EVs) as drug carriers (Figure 1.4.1).[98]

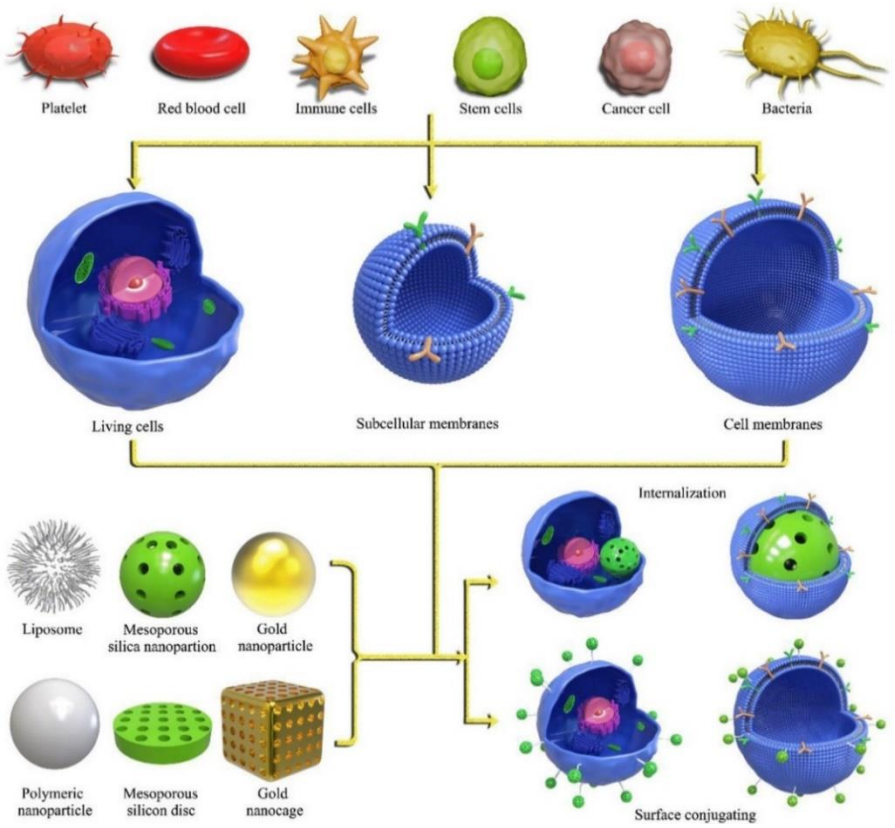

Figure 1.4.1. Schematic illustration of the recent types and sources of cell-derived biomimetic nano-drug delivery systems (reused with permission from ref.[98] Copyright 2018 WILEY-VCH Verlag GmbH & Co. KGaA, Weinheim).

Whole cell-based nanocarriers have been developed using different kind of cells such as red blood cells,[99] platelets,[100] stem cells,[101] macrophages,[102] or microorganisms[103] to encapsulate drugs, proteins or NPs. Depending on the type of the cell source used, specific functionalities can be exploited for

the development of tailored systems with different therapeutic functions. Generally, organisms such as bacteria and viruses can be exploited for their infection ability; white cells for the activation of immune pathways; red blood cells for their ability to stay in the bloodstream; and tumor cells for homotypic targeting.

However, a limitation in the use of whole cells as nanocarriers is the possibility that drugs loaded on their surface or inside them may be cytotoxic and damage the cell membrane or the whole cell,[104] which poses restrictions to the drug dosage to be internalized. To date, cell therapies are very expensive and can also cause clinical syndromes of immunotoxicity and autoimmunity,[105] which lead to explore safer, and more affordable immunoregulatory alternative approaches for cell-based personalized medicines. In this direction, the immune system is a highly suitable objective for nanotechnology-based formulations, that have recently attracted the interest of the scientific community and pharmaceutical companies.

In addition to cells, extracellular vesicles have been recently reported as promising active targeted nanocarriers. These are a heterogeneous group of cell-derived membranous structures comprising exosomes and microvesicles. In particular, exosomes originating from the endosomal system are capable of delivery of various cargos, including proteins, lipids, and nucleic acids acting as communicators that mediate signaling between cells,[106] which attributes them an innate therapeutic potential. Thanks to their biocompatibility, cargo protection, long circulation time and targetability to specific tissue or cells, exosomes have been largely studied as potential DDS of protein and different RNA species such as siRNA[107] and microRNA,[108] drugs[109] and NPs.[110] However, their use has been limited by the lack of standardized methods to rapidly produce, isolate and purify exosomes in sufficient amounts.[111]

1.4.1. Cell membrane sources and their main applications

Most of the targeting and biointerfacing abilities of a cell can be attributed to its plasma membrane. Hence, current efforts focus on the development of core-shell structures by using plasma membrane of different cell sources as biomimetic coating for synthetic NPs. Cellular membranes used for NP camouflaging are generally isolated from blood cells, immune cells, cancer cells, and stem cells. The presence of specific moieties involved in

recognition, adhesion and interaction mechanisms makes these different cell types suitable for several applications in the field of tumor theranostics (Figure 1.4.2).

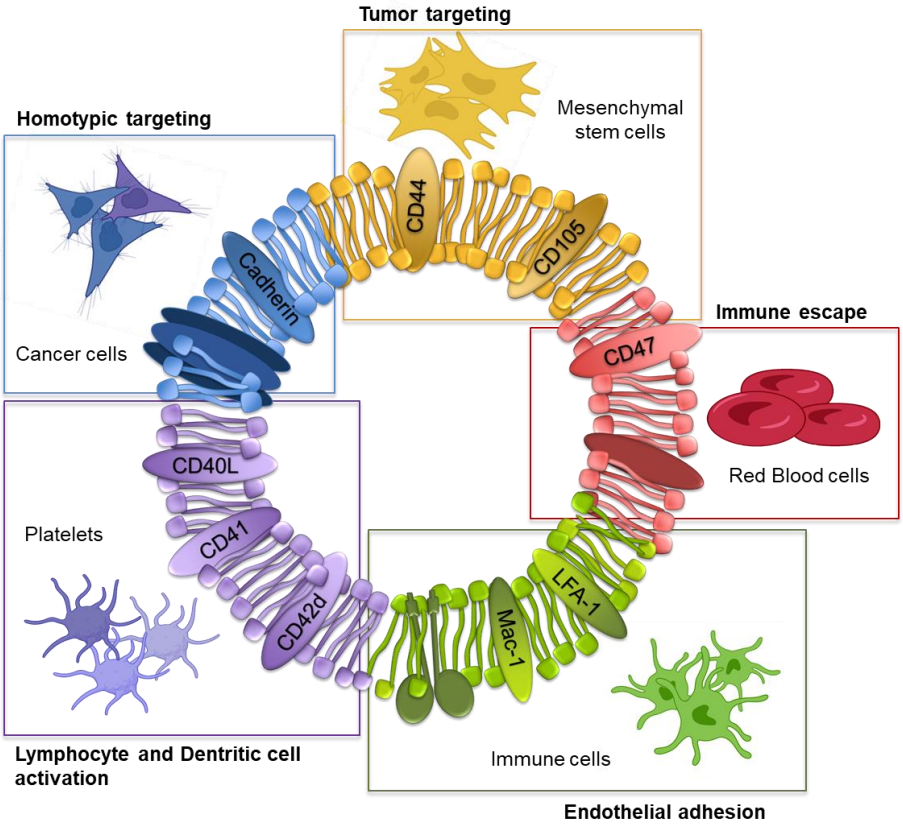

Figure 1.4.2. Schematic illustration of cell membrane-based NPs. Depending on the cell type used as membrane coating source, specific features can be exploited for different applications.

1.4.1.1. Red Blood Cells

Thanks to their interesting properties, such as prolonged blood circulation time, absence of nuclei and abundance in the body, red blood cells (RBC) represent the more exploited source of cell membrane coatings. Zang and co-workers were pioneers to explore RBC membrane (RBCM) camouflaged NPs for cancer therapy. In their first study, biomimetic NPs composed by

poly(lactic-*co*-glycolic acid) **(**PLGA) NPs combined with RBCM purified from fresh RBCs showed a half-life significantly longer than PEGylated NPs (39.6 *vs.* 15.8 h) with an in-blood retainment even 72 h long after injection.[112] Improved pharmacokinetic behavior of RBCM-camouflaged NPs is mainly due to the expression of specific membrane proteins, such as CD47 that inhibit the phagocytosis by macrophages residing in the RES system (liver, spleen and lungs). In fact, CD47 is also known as a *do not eat me* signal and is responsible of the RBCM ability to escape the recognition by the immune system and minimize the premature blood clearance, phenomena observed in PEG functionalized NPs.[113] Besides the biological advantages, the RBCM coated-NPs have shown to improve structural rigidity and particle stability, also leading to a more reliable cargo/dye encapsulation.[114,115]

RBCMs have recently been used for cancer immunotherapy, leveraging host anti-cancer immune reaction.[116] Liang *et al.* developed biomimetic-based photothermal cancer immunotherapy using a nanoformulation of RBCM-derived black phosphorus (BP) QDs nanovesicles (BPQD-RMNVs) combined with Programmed Death-1 antibody (aPD-1); they induced apoptosis in triple-negative breast cancer cells, *in situ* by NIR laser irradiation and neoantigen release-mediated immune system activation to eliminate residual and metastatic cancer cells. The NIR mediated apoptosis promoted the recruitment of dendritic cells (DC) and the neoantigens release. Subsequently, an intensive tumor-specific CD8+ T cells response was activated against primary and secondary tumor growth (Figure 1.4.3). BP-mediated photothermal therapy (PTT) combined with checkpoint antibody treatment has promise as a potential clinical treatment for breast cancer.[117]

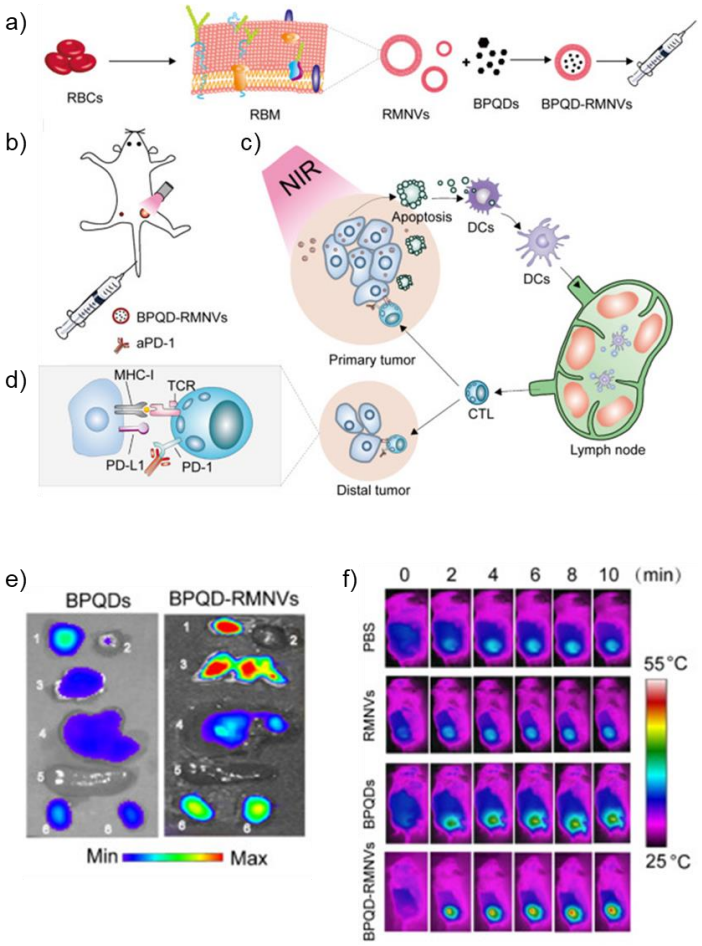

Figure 1.4.3. Photothermal cancer immunotherapy via BPQD-RMNVs and aPD-1. a) Schematic representation of preparation of BPQD-RMNVs by the extraction of RBCM. b) administration of BPQD-RMNV-mediated PTT and aPD-1 to a mouse with a 4T1 tumor. c) *In situ* induction of NIR-mediated apoptosis in tumoral cells and DC recruitment for the cytotoxic T lymphocyte (CTLs) activation d) against the distal tumor. e) Preferentially accumulation of BPQD-RMNVs into the tumor tissue compared to bare BPQD resulted by *in vivo* images (1) Tumor, (2) heart, (3) lungs, (4) liver, (5) spleen, and (6) kidney). f) Infrared (IR) thermographic maps of temperature increase in the 4T1 tumor-bearing mice upon NIR irradiation. Mice were treated with PBS, RMNVs, bare BPQDs and BPQD-RMNVs (adapted with permission from ref.[117] Copyright 2019, published by Elsevier B.V.).

1.4.1.2. Platelets

Another type of cell membrane that can be extremely useful in biomimetic nanotechnology development are the platelets-derived ones. The platelets originate in the bone marrow and are involved in numerous vital process as homeostasis, tissue repair and thrombosis as well as inflammation and adaptive and innate immune responses.[118,119] Platelets have a crucial role in cardiovascular disease and carcinogenesis too.[120,121] In fact, platelets membrane (PM) expresses proteins such as D-selectin that recognizes and interacts with CD44-overespressing circulating tumor cells (CTCs), which are strictly involved with tumor metastasis and angiogenesis.[122] Hu *et al.* developed PM-coated core-shell nanovesicles (PM-NVs) loaded with (i) tumor necrosis factor (TNF)-related apoptosis factor (TRAIL) and (ii) DOX. In this formulation the TRAIL was efficiently delivered toward cancer cell membrane where it activated the extrinsic apoptosis signaling pathway. Simultaneously, equipped with an acid-responsive encapsulation matrix, the PM-NV can be digested after endocytosis and enhanced the DOX accumulation at the nuclei for activation of the intrinsic apoptosis pathway (Figure 1.4.4).[123]

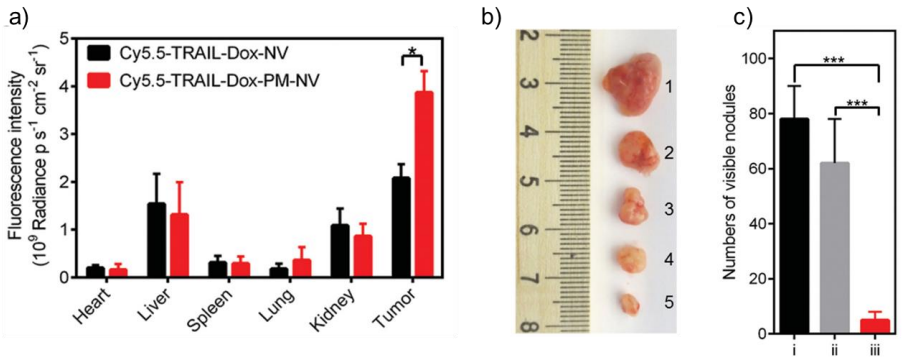

Figure 1.4.4. *In vivo* targeting and antitumor efficacy of PM-NVs. a) Enhanced accumulation in tumor of PMNVs resulted by region-of-interest (ROI) analysis of fluorescent intensities taken out form *ex vivo* images of tumors and normal tissues._b) Growth inhibition of MDA-MB-231 tumors after treatment with different TRAIL/Dox formulations at day 16 (image of tumors treated with saline (1), TRAIL-Dox-NV (2), TRAIL-PM-NV (3), Dox-loaded PM-NV (4), TRAIL-Dox-PM-NV (5). c) Inhibition of metastatic nodules after i) saline, ii) TRAIL-Dox-NV and iii) TRAIL-Dox-PM-NV treatments. Adapted with permission from ref.[123] Copyright 2015, John Wiley and Sons.

The same group, to improve the drug accumulation in tumor, developed a new strategy combining two nanocarriers. For the first one, they used Arg-Gly-Asp (RGD) peptide to decorate tumor necrosis factor α (TNF-α) loaded nanovesicles (NC_A). The RGD peptide selectively bind the integrins such as $\alpha v\beta 3$, overexpressed in tumor blood vessels, while TNF-α, inflammation-induced cytokine, is applied to trigger tumor vascular damage. The second nanocarrier is a PM-coated acid-responsive dextran nanostructure (NC_B) loaded with the chemotherapeutic agent Paclitaxel (PTX). The study showed that PM proteins as CD36, CD42d, P-Selectin and CD40L were efficiently transferred with their origin membranes and enriched the NP coating. Thanks to the specific interaction between the L-Selectin and the CD44 receptor of the tumoral cells, the authors demonstrated that the presence of the PM give to the NPs the ability to target the myeloma cells with high internalization, high intracellular drug localization and decreased side effect.[124]

1.4.1.3. White blood cells

Biomimetic coating for NPs has recently also been obtained from membranes extracted from white blood cells (WBCs), which are recruited into the tumor site in relation to chronic inflammation. First studies showed that this approach can enhance immune evasion and inflammation targeting.[125] 'Leukolike vectors' (LLVs) retain many critical leukocyte transmembrane proteins from the cell donor,[126] which by clustering reduce MPS uptake; others are involved in the adhesion to inflamed endothelium and tumor targeting, or in immune tolerance and interaction with platelets.[127,128]

Thanks to the presence of lymphocyte function-associated antigen 1 (LFA1 or CD11a), coated NPs bind actively the TNFα-activated endothelium as evidenced by clustering of endothelial intracellular adhesion molecule 1 (ICAM-1). Furthermore, a transwell chamber assay showed the high suitability of LLVs to cross the layer of inflamed endothelium.[125]

Leukocyte membrane coating was also used for designing nanoformulations for imaging and photothermal therapies. Xhuan *et al.*[129] successfully developed macrophages membrane coated (MPCMs) Au Nanoshells (AuNSs) for PTT cancer therapy (Figure 1.4.5). In mice, the macrophagic coating demonstrated significant biocompatibility increase, opsonization reduction, circulating time prolongation and tumor-tropic

accumulation of MPCM-AuNSs enhancement. Moreover, *in vivo* PTT showed the inhibition of tumor growth upon NIR irradiation and even its disappearance after 25 days.

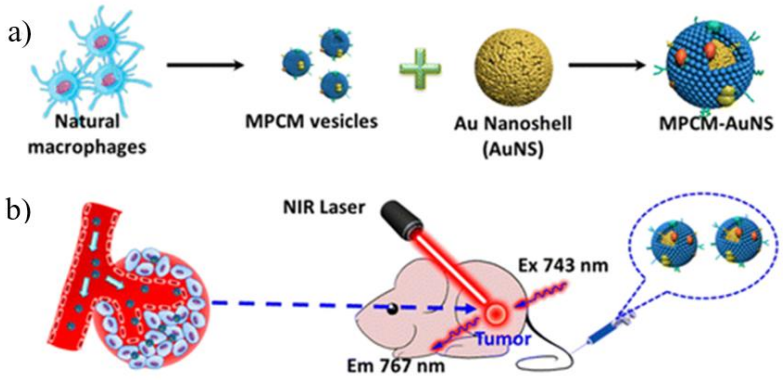

Figure 1.4.5. a) Schematic illustration of the preparation of MPCM-AuNSs and b) *in vivo* PTT (reused with permission from ref.[129] Copyright 2016, American Chemical Society).

1.4.1.4. Mesenchymal cells

Mesenchymal cells (MSCs) are multipotent stem cells with the ability to differentiate in other types of cells such as adipocytes, fibroblast, osteoblasts, chondroblasts, and pericytes. Furthermore, the MSCs migrate to the injured and inflamed tissue under environmental conditions such as hypoxia, and interaction with Toll-like receptors or cytokines. Since tumor is considered to be a chronical inflammation disease, MSCs membrane coated NPs strategy has been harnessed as a biomimetic approach for targeted delivery of cancer drugs to tumors.[130,131] Toledano Furman *et al.*[132] developed MSCs-derived nanoghosts carriers (NGs) as model platform entrapping therapeutics and achieving specific tumor targeting and tumor growth inhibition. On the other hand, synthetic liposomes as negative control did not show analogous results. It was suggested that the NGs ability to bind and fuse to the tumor cell surface was due to the presence of specific MSC integrins, retained on the membrane coating that can mediate NGs interaction with the tumor-infiltrating immune cells, blood vessel endothelium, and tumor-associated fibroblasts.[132] Similarly, Changyong and co-workers used MSCs membrane to coat a gelatin nanogel loaded with DOX. Their studies demonstrated high tumor-targeting capability both *in vitro* and *in vivo* of their NGs. The MSCs

membrane coating significantly improved the cellular uptake, intratumoral accumulation and penetration comparing with gelatin-DOX and free-DOX administration.[133]

1.4.1.5. Cancer cells

Besides RBCs, platelets, WBCs, and MSCs, cancer cells present exciting advantages to be exploited as membrane coating against tumors. Camouflaging strategies based on their use take advantage of innate homotypic aggregation properties and the immune escape ability.

Homotypic targeting is the intrinsic ability of cancer cell coating nanoformulation to interact preferentially and strongly with the same cells from which they are originated. This feature provides unique asset for any specific targeted drug delivery strategies against cancer. The homotypic affinity between cancer cells can be attributed to the interaction between galectin-3 and carcinoembryonic antigen expressed on cancer cells.[134] Fang *et al*.[135] first studied the homotypic targeting of MDA-MB-435 cancer membrane-coated PLGA NPs (CCNPs) as DDS. CCNPs showed a 20-fold increase accumulation in MDA-MB-435 cells compared with the bare PLGA NPs, while no difference was observed in human foreskin fibroblasts. Therefore, analogous formulation was performed using a non-specific RBC coating PLGA NPs (RBCNPs) and it showed reduced particle binding to the cancer cells, suggesting that the cancer cell coating enhanced particle-cell adhesion.[135]

A similar approach was applied by Sun and colleagues developing a 4T1 cell membrane-coated paclitaxel-loaded polymeric core as biomimetic (CPPNs) drug delivery system against breast cancer and its metastasis in lungs.[136] 4T1 coated CPPNs preferentially targeted its tumoral cells but not lung fibroblast WML2 cells or macrophage RAW264.7 cells. The accumulation of that nanoformulation in primary tumor and metastasized site in lungs increased by 3.3- and 2.5-fold when delivered with CPPNs instead of bare NPs (Figure 1.4.6). Furthermore, RBC-coated PPNs (RPPNs) and synthetic liposome vesicle coated PPNs (LPPNs) were used as negative control, and they exhibited a rather lower uptake than the CPPNs, suggesting that the enhanced internalization of the CPPNs was probably caused by the 4T1-tumor-cell-membrane proteins obtained from the source cells. The membrane proteins including TF-antigen and E-cadherin associated with the adherence capabilities during the colonization of metastasis lesion also have

effects on the homotypic interactions among the tumor cells.[137-140] CD44 and CD326, the surface adhesion molecules on the 4T1 cells, have been recognized as surface markers which also played main roles in the adherence of the metastatic cells to the distant sites.[141-142]

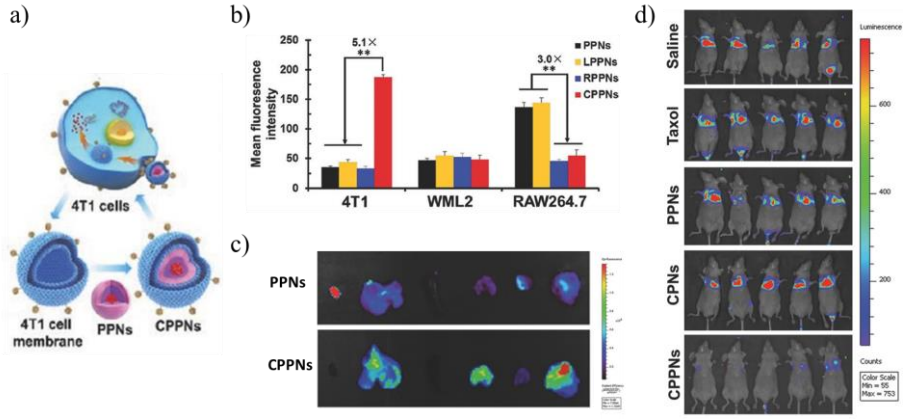

Figure 1.4.6. a) Schematic illustration of CPPNs synthesis procedure. b) Targeting effect of CPPNs resulted from quantitative analysis by flow cytometry after 1 h incubation in different cell lines. c) *Ex vivo* tissue distribution in the main organs of PPNs and CPPNs (from the left: heart, liver, spleen, lung, kidney, and tumor). d) *In vivo* bioluminescence imaging of the mice bearing lung metastasis of the 4T1 bloodstream metastasis model with different treatments (adapted with permission from ref.[136] Copyright 2016, WILEY-VCH Verlag GmbH & Co. KGaA, Weinheim).

Many other results regarding the exciting specific interaction capabilities leverage by cancer cell coating have recently been reported in the literature.[143-145] Besides cancer targeted drug delivery, cell membrane coated NPs could also be exploited for developing novel bio-synthetic nanocarriers for vaccines. Because many tumor antigens are surface markers, tumoral cell membrane can activate immune system to recognize and kill malignant tumor cells based on variant antigen expression.[146,147] Approaches based on a single tumor-associated antigen can be inadequate when facing the high heterogeneity and mutation rate of cancer cells.[148] On the other hand, when cell lysates are used in multiantigen-based strategies to prime the immune system, the large presence of intracellular, housekeeping proteins may divert focus away from the relevant antigens, which compose a small percentage of the total protein, thus compromising the treatment efficacy.[149] Therefore, cancer cell coated NPs represent a good approach to combine the homotypic capability to recognize the tumoral cells and the active delivery tumor-

associated antigens to dendritic cells for immune processing, which allowed for the subsequent stimulation of tumor antigen-specific T-cells (Figure 1.4.7).[135]

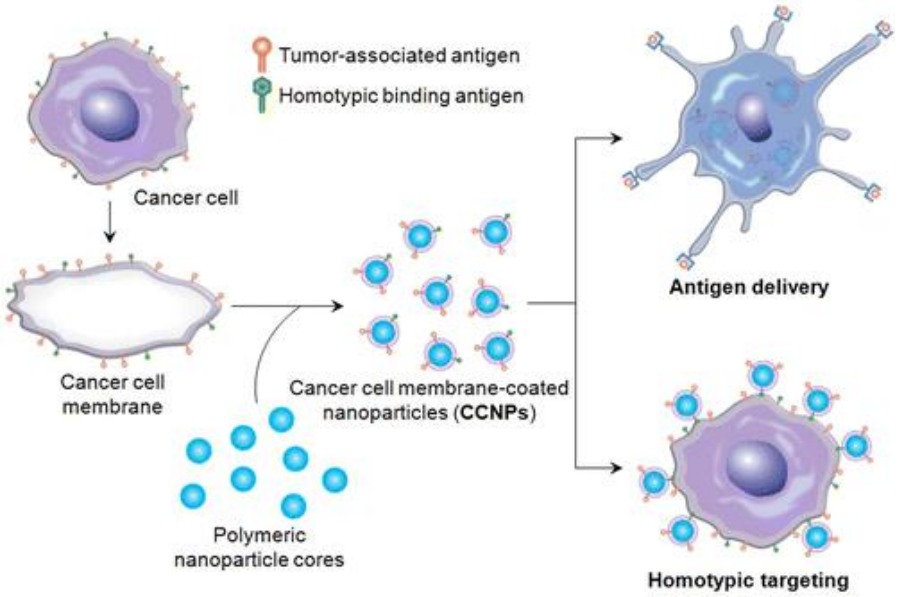

Figure 1.4.7. Schematic representation of the synthesis of CCNPs. The presence of tumor-associated antigens can be exploited to deliver the antigen to APCs and mediate the activation of immune response against cancer. In the other hand, the selective tumor affinity of the nanoformulation allows to homotypically target the source cancer cells (reused with permission from ref.[135] Copyright 2014, American Chemical Society).

Despite the growing number of research aimed at developing these new biomimetic systems, the mechanisms involved in biointerfacing with the biological environment, *i.e.*, how these membrane coatings interact with cells at molecular level, still require in-depth studies. In addition, because in most cases the cargo consists of drugs that need to reach the cytosolic target, it is crucial to investigate the intracellular delivery mechanisms.

1.5. Intracellular delivery

In addition to the general *in vivo* improvements in terms of avoided sequestration by MPS, prolonged circulation time and specific cell or tissue targeting allowed by the use of cell membrane coated technology, NPs

internalization pathways must be taken into account, as cytosolic delivery is a fundamental prerequisite for obtaining successful drug delivery systems. In most cases, NPs are taken up through the processes of endocytosis, by which cells internalize them in vesicles, the endosomes. Depending on the entry pathway, endosomes can be recycled, exocytized or transported to organelles such as lysosomes, Golgi and mitochondria (Figure 1.5.1).[150]

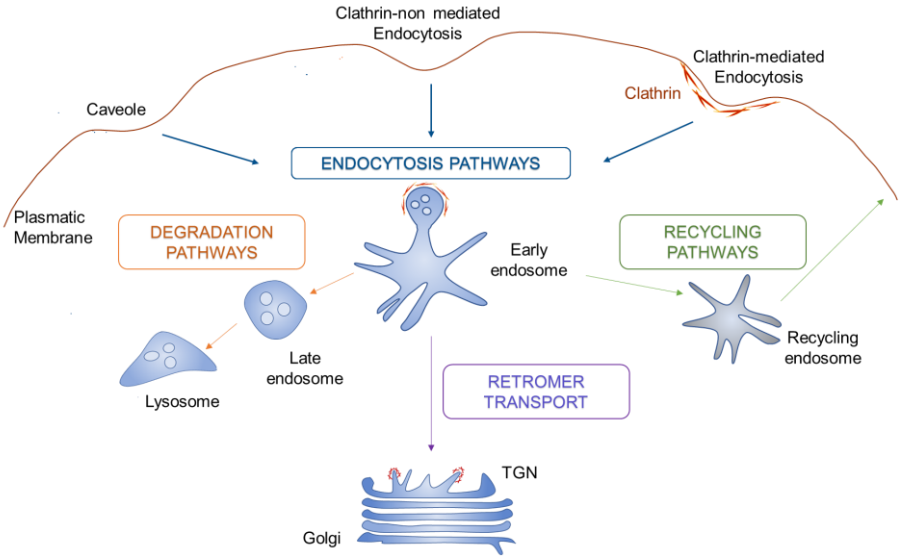

Figure 1.5.1. Illustration of the main fates of the endosome.

In some cases, the NPs, and their cargos, get trapped inside the endosomes and undergo protease-mediated degradation and exocytosis, resulting in a very limited fraction of successfully delivered molecules achieving their cytosolic target. At this stage, specific methods of drug intracellular delivery are required, which represents one of the most relevant challenges for the protein-based therapies.

Intracellular delivery can be achieved by a range of carrier-based or membrane-disruption-based techniques (Figure 1.5.2).

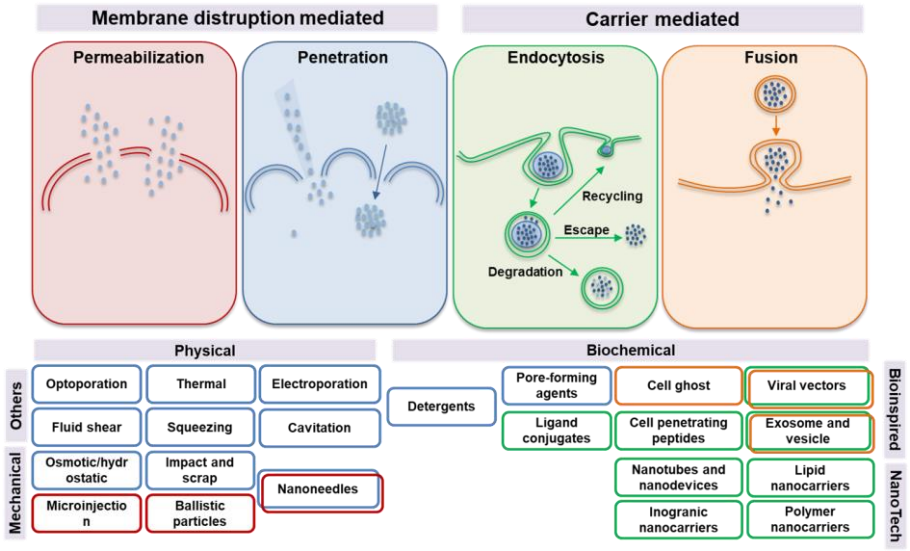

Figure 1.5.2. Schematic representation of substance transportation into the cells, four involving molecular cargo (grey), membrane (double lines), and carrier material (purple). physical-induced membrane disruption mechanisms (via permeabilization or direct penetration), and cargo transportation through endocytosis allowed by biochemical assemblies and viral vectors. If a Fusogenic potential of the carrier allows it to enter through membrane fusion. Membrane permeabilization is facilitated by detergents and pore-forming proteins. Schematics at the top show the four subcategories with molecular cargo (grey), membrane (double lines), and carrier material (purple).

Physical and mechanical methods are considered the conventional approach to permeabilize the cell membrane. Microinjection, sonoporation, electroporation and other techniques have been developed as membrane-disruption modalities to induce transient discontinuities in the plasma membrane using mechanical, electrical, thermal, optical or chemical forces. These approaches found success in several *in vitro* proposes.[151-153] However, the use of these methods in large scale treatments and pharmaceutical applications is severely limited by their low-throughput and disruptive techniques that require sophisticated and expensive instrumentations.

As an alternative to mechanical methods, carrier-based delivery nanosystems have inherent advantages making them attractive but, as explained above, when the nanocarriers are taken up by cells via endocytosis the cargo release from the endosome vesicles is required.

Several endosomal escape strategies have been developed based on the endosome rupture promoted by membrane destabilizing agents such as pH-sensitive membrane-perturbing peptides and polymers.[154,155] These molecules are designed to switch their structures and lyse endosomal membranes, in accordance with the pH decrease in endosomal compartments during their maturation. The vesicle rupture allows to the protein cargo liberation into the cytosol.[156]

Others natural peptide sequences (for example, cell-penetrating peptides, CPPs) have been used to facilitate passage through the membrane to specific organelles within the cell. Using a mix of peptides that contain cell permeation or nuclear localization sequences, a wide range of synthetic and biological molecules have been transported into the cytosol.[157] Among the many types of CPPs designed, the arginine-rich CPPs are the most exploited ones. One of them was obtained from the human immunodeficiency virus type 1 (HIV-1) Tat protein,[158] whose cell-penetrating ability is conferred by a specific cation-rich peptide sequence, $Tat_{49–57}$. The efficiency of CPP-cargo conjugated is still hard to predict due to the numerous features that could influenced it (such as physicochemical properties, local concentration, membrane potential, cell-entry mechanism, *etc*.).[159]

An alternative solution to achieve the intracellular delivery is represented by the direct fusion of specific nanocarrier with the plasma membrane of the cells. This approach is inspired by the natural mechanism the viruses use to deliver their genetic material into the cytosol while transfecting their hosts. The mechanisms behind the viral genome release vary among the several family types of viruses. Some envelope viruses, as herpes simplex virus type I (HSV-I), entry into host cells either by fusion at the plasma membrane or intracellularly after internalization by endocytosis.[160,161] Among the twelve glycoprotein species that compose the membrane envelop, five of them (gB, gC, gD, and the complex of gH and gL) are entry-associated viral glycoprotein and mediate the fusion process between viral and host's membranes.[162] On the other hand, Hemagglutinin (HA), a coating peptide of the influenza virus, acts as a membrane fusion agent by exploiting the structural modification induced by the acid pH typical of the lysosomal environment from a hydrophilic and anionic random coil conformation to a hydrophobic helix conformation.[163] This conversion, which typically promotes the fusion of the viral membrane with the cell membrane, can be exploited for endosomal escape strategies.

On this note, virus-inspired systems used for drug delivery have been developed, namely, (i) viral gene vectors, (ii) virus-like particles (VLPs), and (iii) virosomes (Figure 1.5.3).

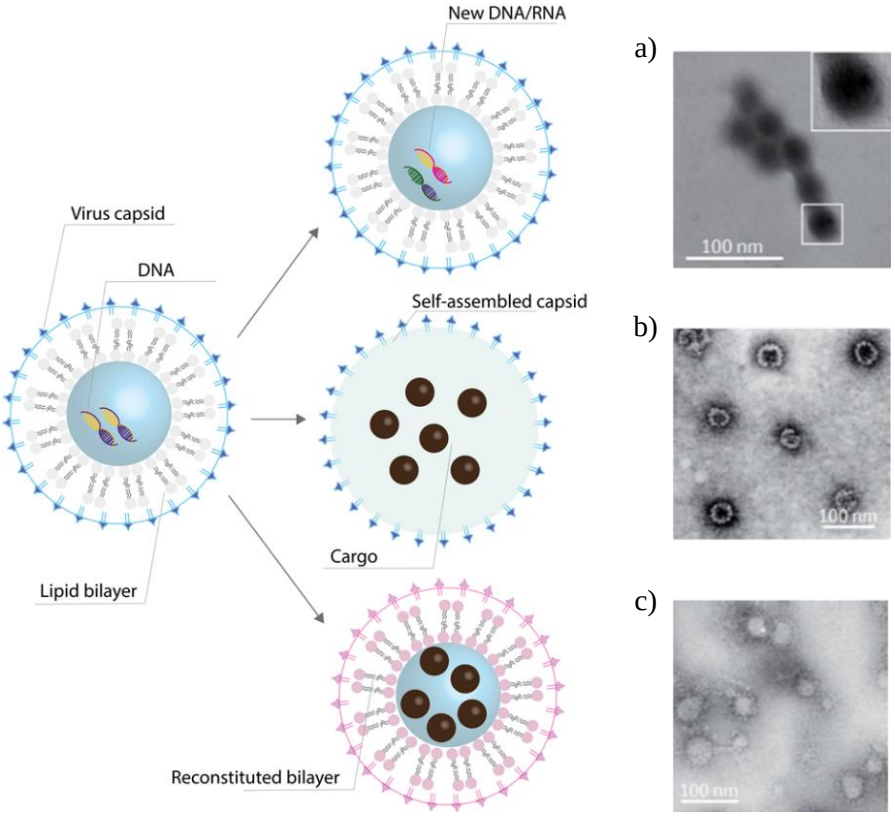

Figure 1.5.3. Schematic representation of virus-inspired drug and gene delivery systems a) Electron microscopy (EM) image of viral gene vectors originated from adenovirus and coated with GNPs (adapted with permission from ref.[164] Copyright 2006, American Chemical Society). b) EM image of VLPs originated from polyomavirus (adapted with permission from ref.[165] Copyright 2001, John Wiley and Sons). c) EM image of virosome originated from native influenza virus (adapted with permission from ref.[166] Copyright 2005, Nature Publishing Group).

Generally, viral vectors are used to deliver therapeutic genes and are mainly applied as engineered vaccines. Retroviruses, adenovirus, adeno-associated virus, herpesvirus and poxvirus have been selected as gene delivery vehicles thanks to their capability to carry and deliver foreign genes.[167] The viral vectors derived from them are employed in more than

70% of clinical gene therapy trials worldwide. Besides the drawbacks linked to the safety of the use of a viral component, these vectors cannot be used as drug carriers due to their limited loading capacity.

VLPs and Virosomes are an interesting alternative and more applicable protein delivery. VLPs are self-assembled capsules that mimic the capsid structure, while virosomes are liposome-like vesicles made of a phospholipid bilayer that is modified to incorporate the surface glycoproteins of viruses.[168] Since these systems are not endowed with viral genome, they are not able to replicate in human cells, which allows to overcome all the safety-related concerns.[169] Recent reports show that VLPs can be used to mediate efficient delivery of guest proteins to the cytosol.[170-172] In addition, these particles also mimicked virus ability to overcome biological barriers, including avoidance of opsonization and tumor homing properties.[173] Chatterjee and co-workers demonstrated effective cytosolic delivery of proteins, such as, Caspase 8, GFP and Cre recombinase, using VLPs with Gag fusion proteins on their surface.[174] On the other hand, Savithri and colleagues developed VLPs using *Sesbania mosaic virus* coat protein engineered with Staphylococcus aureus protein A (SpA) to deliver multiple antibodies.[175]

1.5.1. Fusogenic Nanocarriers

Fusogenic liposomes (FLs) are a newly developed class of liposomes which, thanks to their lipid composition, have the ability to fuse their phospholipid bilayer with the plasma membrane. There are numerous examples of drug delivery that use classical liposomes for molecule's carriage across membranes, thanks to their capacity of encapsulation that protects and stabilizes the cargo, preserving its structure and functionality. Classical liposomes used for DNA delivery are based on a composition of neutral and positively charged lipid molecules. Liposomes generally are taken up by cells via endocytosis, thus requiring further mechanical or chemical manipulations to access the cytosol (see above). In alternative, the use of Lipofectamine (LFN) reagents in largely used in order to enhance the transfection and the delivery of DNA and short interfering RNA (siRNA)/microRNA (miRNA) across cell membrane. However, a satisfactory mechanism-based explanation of the superior efficacy of LFN reagents has remained mostly elusive thus far.

Recently, it has been shown that by adjusting the lipid composition of these carriers it is possible to obtain FLs that interact with the membrane and

release the cargo directly into the cytosol, avoiding the endosomal trapping (Figure 1.5.4).

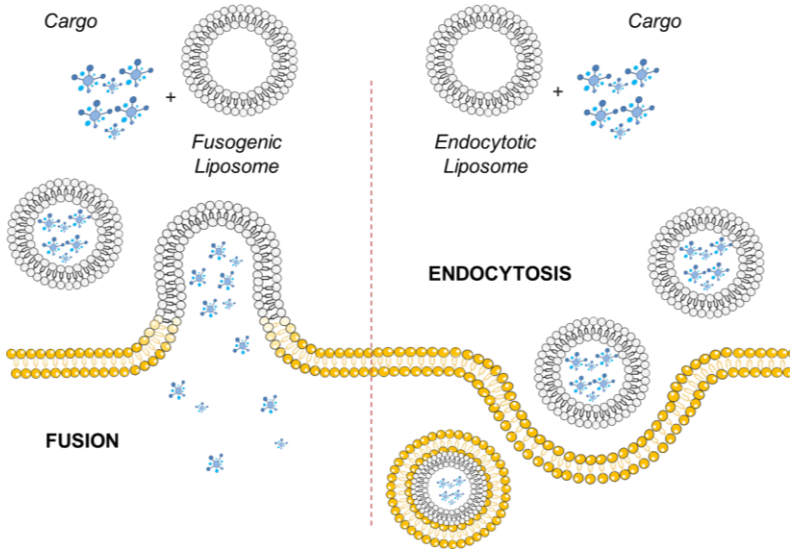

Figure 1.5.4. Comparison of fusogenic and endocytotic liposomes for the cargo delivery inside the cell. Putative cargos that are carried by FLs are directly delivered into the cytoplasm due to the interaction, and the subsequential fusion, between the FLs phospholipidic membrane and the plasmatic membrane of the cell. Otherwise, when the cargo is carried by commercial phospholipid vesicles, it is typically taken up via endocytosis leading to the degradation of most loaded biomolecules.

The synergistic combination of three lipidic compounds, the neutral lipid 1,2-Dioleoyl-sn-glycero-3-phosphoethanolamine (DOPE), the positively charged lipid 1,2-dioleoyl-3-trimethylammonium-propane (DOTAP), and lipids with an aromatic group as N-(4,4-Difluoro-5,7-Dimethyl-4-Bora-3a,4a-Diaza-s-Indacene-3-Propionyl)-1,2-Dihexadecanoyl-sn-Glycero-3-phosphoethanolamine (BODIBY-FL-DHPE) resulted in an effective fusogenic mixture.[176] Although the mechanism of fusion has not been deeply elucidated yet, it is known that the positive charge of DOTAP allows to increase the electrostatic interaction between the liposomes and the negatively charged glycocalyx of the cell membrane, thus promoting the fusion.[177,178] The presence of neutral lipid with cone-like structure as DOPE and chromophore associated lipid could play an important role in the formation of intermediate fusion states, thanks to the tendency to induce local instabilities in the lipid membrane.[178,179] Liposome fusion events were

observed in different kinds of cells (such as HEK293 cells, human macrophages, rat embryonic cortical neurons, smooth muscle cells, and rat myofibroblasts) (Figure 1.5.5);[176] they were demonstrated to be an efficient intracellular delivery system for proteins, including Enhanced Green Fluorescent protein (EGFP), Dendra2, R-phycoerythrin (R-PE); peptides like LifeAct-FITC and NTF2-AlexaFluor488;[180] NPs,[181] nucleic acid,[182] pholyfenoles,[183] and coding plasmids.[184]

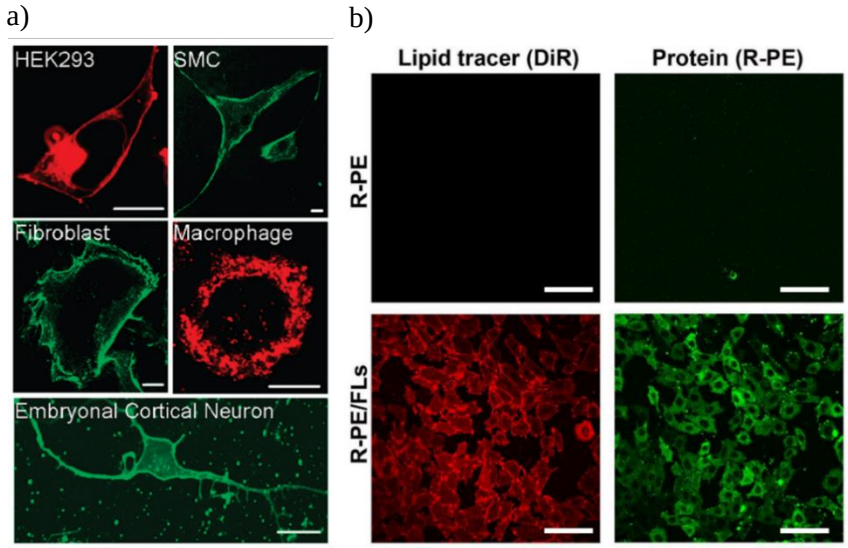

Figure 1.5.5. Labeled cells upon the fusion of FLs and cell membranes. a) Confocal microscope images of cell membranes of HEK293, smooth muscle cells (SMC), rat myofibroblasts, human macrophages, and embryonal cortical neurons that were fluorescently labeled by liposome fusion. As aromatic lipids, either LR-DOPE (red) or BODIPY FL-DHPE (green) were used to synthesize FLs. Scale bars: 10 µm (adapted with permission from ref.[176] Copyright 2010, American Chemical Society). b) R-PE delivery by FLs. CHO cells were incubated with a solution of R-PE (top row) and R-PE encapsulated in FLs (R-PE/FLs) (bottom row) at the same concentration. Optical microscopy was used to record the lipid tracer DiR (left column), the protein fluorescence (middle column). Scale bars: 100 µm (adapted with permission from ref. [180] Copyright 2017, American Chemical Society).

However, fusogenic liposomes showed to be unsuitable for the delivery of positively charged proteins due to the electrostatic repulsion that prevents the complex formation. Moreover, the exact mechanism should be elucidated in the future. This new type of fusogenic liposomes paves the way to manifold applications in different biotechnological fields.

1.6. Objectives

The research conducted in this thesis finds its motivation in the recent increased attention raised by biomimetic systems as novel drug delivery nanosystems with effective biointerfacing. These bioactive nanostructures preserve the natural (bio)-physical properties and mimic functional features, which regulates signaling, transport processes and immune responses.

The overall objective of this thesis work is to provide versatile smart biomimetic nanocarriers with tissue-specific targeting capabilities. The aim is to design biomimetic coatings by self-assembly of natural components derived from cancer cell lines, thereby replicating highly complex functionalities of the cell surface and implementing specific cell functions on nanocarriers.

The work described in chapter 3.1 aims to design, develop and characterize bio-synthetic nanostructures derived from cancer cell membranes, hereinafter named cellsomes (CSMs). The objective here is to obtain an easily scalable bottom-up process to fabricate CSMs derived from different cancer cell lines, which can be programmed to perform specific biological tasks such immune escape and homotypic targeting. The specific objectives are:

- to characterize the physicochemical properties of a library of CSMs, including morphology, hydrodynamic size, colloidal stability in different media, and concentration, among others;
- to evaluate the presence of surface biomarkers (lipids, proteins, *etc*.) inherited from the cell source that are retained in the purified CSMs;
- to investigate the bioactivity of the CSMs *in vitro*, namely i) their intrinsic capability to preferentially recognize the cell source from which they originated (homotypic targeting), ii) the transport pathway involved in the cellular internalization, iii) the CSMs camouflaging ability to avoid the recognition from immune cells and iv) the biomimetic coating effect on solid NPs in 2D and 3D cell cultures.

The results obtained in the studies described in the first chapter stablish the fundamental basis of the development of CSMs as drug delivery carriers for effective intracellular delivery of specific cargos that otherwise would not overcome the cell membrane barrier or would be trapped in endo/lysosome vesicles.

In particular, the work described in chapter 3.2 aims to provide a photoresponsive drug delivery biomimetic nanocomposite, aiming to achieve intracellular spatiotemporally controlled cargo release. The specific objectives here can be summarized as:

- to functionalize CSMs with gold nanorods (GNRs) thereby leading to plasmonic CSMs having thermoplasmonic properties;
- to characterize the thermoplasmonic properties of GNRs-tagged CSMs;
- to use plasmonic CSMs as photo-responsive biomimetic nanocarriers for intracellular delivery of macromolecules (*e.g.*, from small to large molecules and macromolecules);
- to perform *in vitro* studies of NIR light-controlled release of non-permeant Abs with spatiotemporal resolution, either at the level of single cells and at the level of thousands of cells, without impairing cell viability.

As an alternative drug delivery strategy, the work described in chapter 3.3 aims to achieve intracellular cargo delivery by direct fusion mechanism between the plasma membrane and the phospholipidic structure of CSMs. The specific objectives are:

- to derive fusogenic CSMs (FCSMs) by modifying the biomimetic coating composition with different combinations of cationic and neutral lipids;
- to verify the biomimetic properties of FCSMs;
- to investigate the intracellular delivery of manifold types of cargo, from small hydrophobic molecules to large molecular mass macromolecules or solid NPs from tunable FCSMs.

Materials and Methods

2. Materials and Methods

2.1. Synthesis and characterization of CSMs

2.1.1. Synthesis Method

The synthesis of cellsomes (CSMs) was carried out following the protocol described in the literature,[185,186] with a procedure to obtain monodispersed vesicles of variable size ranging between 100 and 400 nm. Synthesized CSMs are derived from different cell lines (tumoral cell lines such as cervix epithelial carcinoma cells, HeLa cell, and adenocarcinomic human alveolar basal epithelial cells, A549 cells; healthy embryonic adrenal cell line, HEK cells; and macrophages, RAW cells), which were purchased from ATCC®. To prepare the CSMs, cells were incubated in 75 cm^2 or 175 cm^2 cell culture flasks in Dulbecco´s Modified Eagle Medium (DMEM, high glucose (4.5 $g \cdot L^{-1}$) and pyruvate, GIBCO™ #41966052), supplemented with 10% fetal bovine serum (FBS, GIBCO™ #10270106) and Penicillin-Streptomycin (50 $U \cdot mL^{-1}$ - 50 $\mu g \cdot mL^{-1}$) (GIBCO™ #15140122) (complete DMEM, cDMEM) in a humidified chamber at 37 °C under 5% CO_2. Cells were grown in their preferred environment as they approached 70 – 80% surface coverage. Then, the cells were harvested after trypsinization for 2 min with 2 mL of 0.25% Trypsin–EDTA (GIBCO™ #24200056). 10 mL of cDMEM was added to recover the cells and transferred to a 50 mL sterile tube. The cells were collected after centrifugation at 500 g for 5 min. The collected cells (10-20 · 10^6 cells) were washed with precooled phosphate-buffered saline (PBS, pH 7.4 Thermo Fisher # 14190169) and centrifuged at 600 g for 5 min. The cell pellet was re-suspended in 10 mL of hypotonic buffer (0.25X PBS) containing 1X Protease inhibitor cocktail (PIC, Sigma-Aldrich™ #P2714-BTL) and incubated in an ice bath for 10 min (Figure 2.1.1, 1). Then the cell lysis was carried out using a freeze-thaw method consisting of 4 cycles of freezing in liquid nitrogen for 1 min followed by thawing at 37 °C for 10 min. Finally, the solution was placed in a bath sonicator for 5 min (Figure 2.1.1, 2). To purify the cell membrane fragments, the solution was subjected to several centrifugation steps. First the solution was centrifuged at 700 g for 10 min at 4 °C to discard the nuclei or whole cells. Then the cell membrane fragments remaing in the supernatant were precipitated by centrifugation at 15,000 g for 30 min at 4 °C. To allow for self-assemblage of the membrane

fragments into CSMs, a mechanical extrusion process was applied. The pellet was dispersed in 1 mL of PBS buffer (or 1 mL of 20 mM of 2-(4-(2-hydroxyethyl)-1-piperazinyl)-ethanesulfonic acid (HEPES) buffer) and subject to 10 cycles of extrusion by using an Avanti® Mini extruder with 800 nm polycarbonate membrane (Figure 2.1.1, 3). Selecting a specific pore size of the membrane used during the extrusion process can modulate the size distribution of the final CSM product.

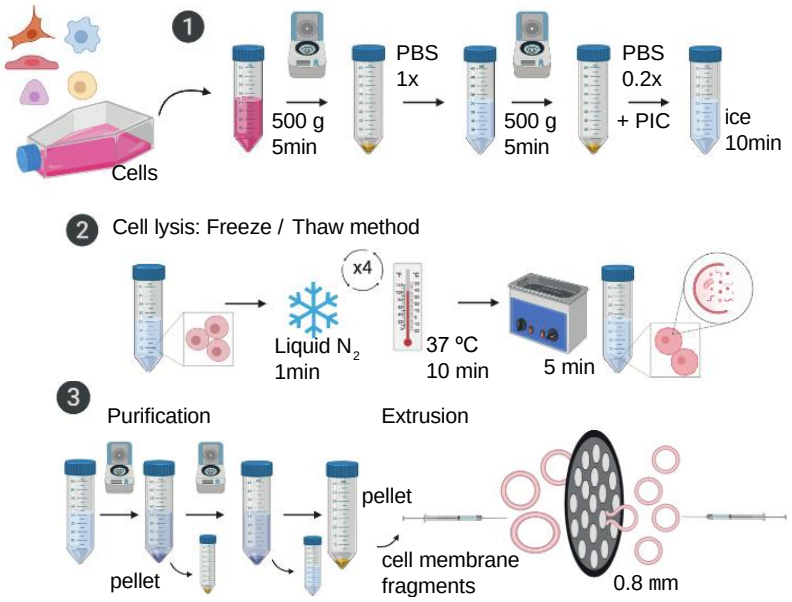

Figure 2.1.1. Schematic representation of the synthesis procedure for CSMs preparation.

2.1.2. Physical Chemical Characterization

Dynamic Light Scattering (DLS). DLS was used to characterize the colloidal properties of the CSMs by measuring their hydrodynamic size and polydispersity index (PDI). All the samples were analysed in PBS or HEPES buffer by using a DLS Malvern Zetasizer Nano ZSP (Malvern Instrument Ktd.) equipped with a 10 mW He-Ne laser operating at a wavelength of 633 nm laser and fixed scattering angle at of 173º. Disposable cells for DLS were used. All measurements were carried out in PBS buffer at 37 ºC.

ζ potential. ζ potential of the MilliQ water dispersed CSMs was measured with laser Doppler anemometry (LDA) by using the same Malvern Zetasizer Nano ZSP instrument. Disposable capillary zeta cell for ζ potential were used.

Nanoparticle tracking analysis (NTA). NP tracking analysis was used to characterize the colloidal properties of the CSMs and determine the CSMs concentration in solution. All the samples were analysed by using a NanoSight NS300 (Malvern Instruments, UK) equipped with a 488 nm laser module, a sCMOS camera and a syringe pump was used for all NTA measurements. All measurements were carried out at 24 ºC. A CSMs were diluted in filtered MilliQ water to a final volume of 1mL and loaded in the measurement chamber with a flow rate of 50 µL/min. Flow mode measurements were obtained recording 3 videos of 60 s for each measurement. The NanoSight NS300 software was used to analyze the sample (10-100 particles/frame).

Scanning Electron Microscopy of CSMs. Scanning electron microscopy (SEM) analysis allowed characterizing the morphology of the CSMs. The sample solution was stained by using a 2% Uranyl acetate solution. All SEM images in this section were obtained using a scanning electron microscope ZEISS FESEM ULTRA Plus. The CSMs were deposited from a diluted solution onto a 3-4 nm thick film of amorphous carbon supported by a 400 µm mesh copper grid (Ted Pella Inc., #01822-F). One drop (2 µL) of CSMs suspension was deposited onto the grid, and the solvent was evaporated at RT.

2.1.3. Biological Characterization

Bradford Coomassie Assay. The Bradford assay (PierceTM Coomassie Plus Assay Kit; ThermoFisher #23236) was used to determine the protein concentrations. Following the manufacturer's instructions, 150 µL of diluted standard protein samples (standard bovine serum albumin, BSA stock 2 $mg \cdot mL^{-1}$) in a working range of 1-25 $\mu g \cdot mL^{-1}$ and samples to be analyzed were mixed with 150 µL of Coomassie reagent in a 96 well microplate. The absorbance at 570 nm was read using a microplate reader (TECAN, Infinite® 200 PRO) and the protein content was calculated by the standard curve in Figure 2.1.2.

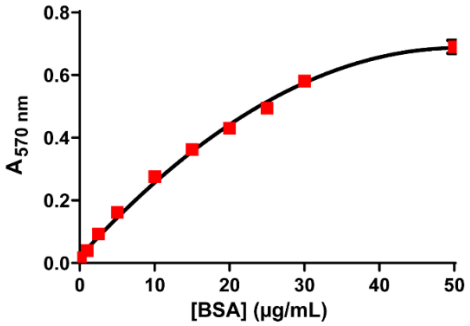

Figure 2.1.2. Bradford assay standard curve of BSA concentration versus absorbance (A) (a.u.) at 570 nm.

SDS-PAGE electrophoresis and Mass Spectrometry (MS) analysis. The protein content on the CSMs samples was analysed by Sodium Dodecyl Sulphate-PolyAcrylamide gel electrophoresis (SDS-PAGE) electrophoresis and electrospray liquid chromatography (nLC-MS/MS). SDS-PAGE was used to separate the proteins contained in the CSMs. The protein content was analysed by 10% SDS-PAGE using an ENDURO™ VE10 vertical gel electrophoresis system from Labnet. The CSMs sample was treated with a solution of Triton 0.1% for 10 minutes and then denatured by incubating the samples for 5 min at 100 ºC in 4 X loading buffer (5 mL of 0.5 M Tris-HCl pH 6.8, 1.2 g of SDS, 4 mL of glycerol, 0.03 g of bromophenol blue and 40 mM dithiothreitol, DTT).

A 10% Tris-Glycine SDS-PAGE running gel was precast before each experiment by mixing 3.6 mL of MilliQ water, 3.7 mL of 1.5 M Tris – HCl buffer pH 8.9 and 0.1 mL of 10% SDS with 2.5 mL of acrylamide and 5 µL of *N*,*N*,*N*′,*N*′-Tetramethylethylenediamine (TEMED). As initiator, 50 µL of ammonium persulfate (APS) 10% was added. Stacking gel (5%) was made up with 0.5 mL acrylamide, 1.6 mL 0.4 M Tris-HCL buffer pH 6.8, 50 µL 10% SDS, 2.8 mL MilliQ water, 50 µL APS 10% and 5 µL TEMED.

The electrophoresis was run under constant voltage of 150 V for 45 min and the gel was stained with Coomassie blue visible staining. Afterwards, MS analysis was performed to identify the proteins recovered from the CSMs samples. The gel section containing the protein band was removed using a sterile scalpel and transferred to a clean 0.5 mL sample tube. The gel sections were trypsin-digested in gel. The samples were analysed by electrospray liquid chromatography (nLC-MS/MS, Bruker Amazon ETD).

Flow cytometry (FC). FC measurements were performed to detect the lipid presence of CSMs and to characterize the fluorescence signal from the cargo encapsulation and any specific surface markers at the CSMs surface composition.[83] The lower size-detection limit for light scattering of conventional flow cytometers is typically in the order of 200-500 nm. We can distinguish the signal of the CSMs from the background by fluorescence, forward and the side light scattering detector. The forward and side scattering and fluorescence intensity of the CSMs samples were measured with a Guava® easyCyte BG HT flow cytometer (Millipore®), using a blue laser emitting at 488 nm and a green laser emitting at 532 nm as excitation sources. Background measurements in PBS buffer were performed before each measurement series and the corresponding threshold applied to remove the PBS signal. Forward (FSC) and side scattering (SSC) signals were recorded to gather information of the CSMs concentration and dispersion. Concentrations between $1{\cdot}10^5$ and $1{\cdot}10^8$ CSMs·μL^{-1} for CSMs and functionalized CSMs (CSMs@GNR, CSMs@Cargo and CSMs@GNRs@Cargo) were analyzed by using a flow rate of 0.12 $\mu L{\cdot}s^{-1}$. Fluorescence and SSC signals were recorded to gather information of the fluorescently labeled encapsulated cargo and to evaluate the presence of membrane components (proteins and lipids) on the CSMs by using different fluorescence reporters: a lipid staining dye, CellMask™ Deep Red Lipid staining, and the E-Cadherin/ECAD/Cadherin-1/CD324 Protein human (Sigma-Aldrich™ #SRP6426), an Alexa-488 labeled monoclonal anti-cadherin antibody that recognizes human CD324. 20 µL of CellMask™ 1X and 2 µL of antibody ($1g{\cdot}L^{-1}$) were independently added to the CSMs solution and stirred for 15 min at RT. The fluorescence signal was measured from the corresponding channel of the CellMask™ (620/50 nm channel) and the Alexa-488- anti-cadherin antibody (525/30 nm channel).

2.2. Functionalization and modification of CSMs

2.2.1. Functionalization with fluorescent phospholipid.

Fluorescently labeled CSMs were produced using fluorescent phospholipids that can be intercalated within the bilayer. In particular, 1,2-Dioleoyl-*sn*-glycero-3-phosphoethanolamine labeled with Atto488 (DOPE-Atto488, Sigma-Aldrich™ #67335) or Atto647N (DOPE-Atto647N, Sigma-Aldrich™ #42247) were added to the lipid bilayer of the CSM. 1mL of obtained CSMs dispersed in PBS 1X were mixed with the 2µL of 1 $mg{\cdot}mL^{-1}$ of DOPE-Atto488 (dissolved in Methanol/Dichloromethane) or DOPE-Atto647N

(dissolved in Dichloromethane) and sonicated for 5 min. The resulting CSMs were extruded 10 cycles using an Avanti® Mini extruder (with a 800 nm polycarbonate membrane) (Figure 2.2.1) and purified by dialysis, size exclusion chromatography or ultrafiltration (see section 2.3). After the CSMs modification, size distribution of DOPE-functionalized CSMs was analyzed by DLS and NTA, and the fluorescence signal was determined by a microplate reader (TECAN, Infinite® 200 PRO).

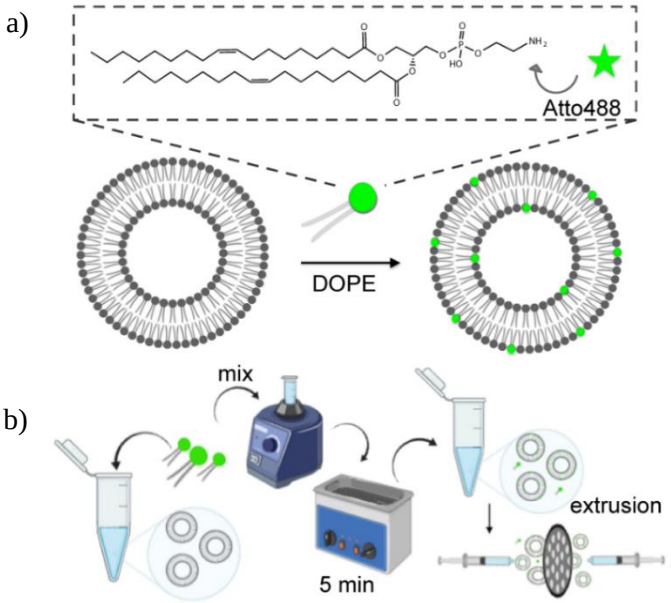

Figure 2.2.1. a) Scheme showing the Labeling of CSMs with fluorescent phospholipids (DOPE-Atto488) and b) the experimental process to obtain the CSMs@DOPE-Atto488.

2.2.2. Functionalization with other lipids (Fusogenic CSMs)

The fusogenic CSMs (FCSMs) were prepared using a lipids mixture of neutral lipid as 18:1 (Δ9-Cis) PE (DOPE) (Avanti #850725P), positively charged lipid as 18:1 TAP (1,2-dioleoyl-3-trimethylammonium-propane, DOTAP) (Avanti® Polar Lipids #890890) and aromatic/fluorescent lipid as BODIPY™ FL DHPE (N-(4,4-Difluoro-5,7-Dimethyl-4-Bora-3a,4a-Diaza-s-Indacene-3-Propionyl)-1,2-Dihexadecanoyl-sn-Glycero-3-Phosphoethanolamine, Triethylammonium Salt) (Invitrogen™ #D3800).

According to Rejhana Kolašinac *et al.*,[187] the mixture of DOPE/DOTAP/BODIPY-FL-DHPE was used at a ratio of 1/1/0.01–0.1 mol/mol (Table 2.2.1). Precisely, 1mL of obtained CSMs dispersed in 20 mM of HEPES buffer was mixed with 20 µL of DOPE (1 mg·mL^{-1}), 9 µL DOTAP (1 mg·mL^{-1}) and 1.43 µL DHPE (BODIPY-FL-DHPE) (1 mg·mL^{-1}). The solution was sonicated for 10 min and extruded 10 cycles using an Avanti® Mini extruder with a 800 nm polycarbonate membrane and purified by ultrafiltration using Amicon® Ultra-0.5 Centrifugal Filter Devices (cut-off of 100 kDa, Millipore Sigma-Aldrich™ #UFC510096) and washing the solution with 20 mM HEPES at least 3 times (see section 2.3) (Figure 2.2.2). The solution of FCSMs was concentrated/resuspended in 100 µL 20 mM HEPES volume.

To encapsulate small or large molecules inside the FCSMs, the corresponding volume of the selected cargo (Table 2.2.1) was added to the FCSMs solution before the sonication step. The samples were purified from the excess of free molecule, by size exclusion chromatography (see section 2.3)

Table 2.2.1. The different lipids used to prepare the FCSMs. For 1 mL of CSMs (corresponding to 10^{11} NCs·mL^{-1}) the lipid ratio indicated in the table was used.

Sample	C. (solvent)	Mass	Vol	Ratio*
DOPE-Atto488	1 mg·mL^{-1} ($MeOH/CH_2Cl_2$)	2-20 µg	20 µL	1
DOPE-Atto647N	1 mg·mL^{-1} (CH_2Cl_2)	2-20 µg	20 µL	1
BODIPY-FL-DHPE	1 mg·mL^{-1} (EtOH)	1.43 µg	1.43 µL	0.1
DOTAP	10 mg·mL^{-1} ($CHCl_3$)	9 µg	0.9 µL	1

*** Molar ratio lipids:DOTAP.**

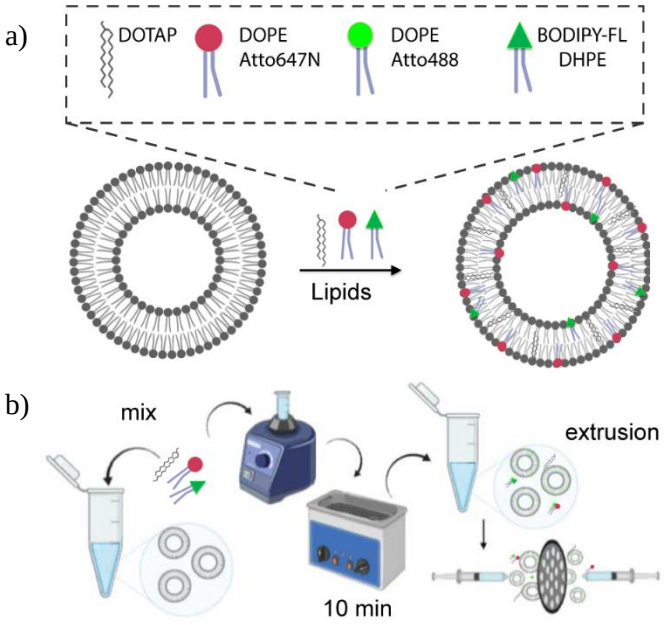

Figure 2.2.2. a) Scheme showing CSMs functionalization with lipids and b) the experimental process to obtain the FCSMs.

2.2.3. Functionalization with cargo.

To functionalize the CSMs and the FCSMs with different cargo, such as Alexa545-$PEG_{(4)}$, seminaphtorhodafluor labeled Dextran-70 kDa (DS), fluorescein isothiocyanate labeled Phalloidin (PHA) and HOECHST-33258 (HOE), or biomolecules, such as β Tubulin monoclonal Ab labeled with Alexa Fluor 555 BT7R (Alexa555 BT7R Ab), the same procedure described above was followed. 1 mL of CSMs dispersed in PBS 1X or FCSMs dispersed in HEPES were mixed with the corresponding volume of the selected cargo (see Table 2.2.).

Table 2.2.2. The different kind of cargo molecules used to functionalize the (F)CSMs.

Cargo	Reference	Stock Conc.	Volume	Reaction
DS	Sigma-Aldrich™ #D3304	70 µM (H_2O)	10 µL	77 nM
HOE	Thermo Fisher Scientific™ #H3569	1 mg·mL^{-1} (H_2O)	50 µL	80 µM
Alexa555 BT7R Ab	Thermo Fisher Scientific™ #MA5-16308-A555	1 mg·mL^{-1} (H_2O)	2 µL	10 nM
Alexa545-$PEG_{(4)}$	Sigma-Aldrich™ #760773	1 mg·mL^{-1} (EtOH)	50 µL	53.4 µM
PHA	Sigma-Aldrich™ #P5282	1 mg·mL^{-1} (H_2O)	10 µL	8 µM

The cargo/CSMs solution was stirred for 30 min and sonicated for 5 min at RT. The resulting CSMs were extruded 10 cycles using an Avanti® Mini extruder with a 800 nm polycarbonate membrane (Figure 2.2.3).

The samples were purified from the excess of free molecules by dialysis, size exclusion chromatography or by ultrafiltration (see section 2.3). The cargo-loaded CSMs were characterized by DLS, NTA and fluorescence spectroscopy.

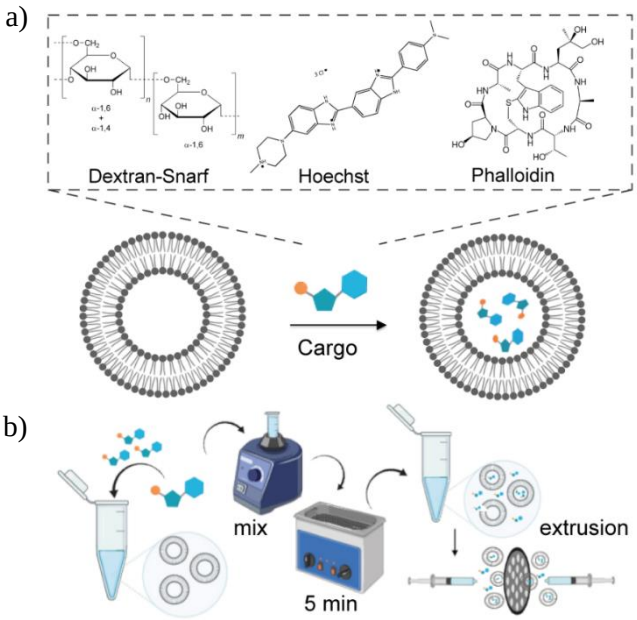

Figure 2.2.3. a) Scheme showing the encapsulation of different cargo molecules into CSMs and b) the experimental process to obtain the CSMs@Cargo sample.

2.2.4. Polystyrene NPs encapsulation

To prepare CSM-coated NPs, 1mL of obtained CSMs dispersed in PBS were mixed to Polystyrene NPs of 200 nm diameter (PSNPs, FluoSpheres™ Carboxylate-Modified Microspheres, 0.2 µm, red fluorescent (580/605), Thermo Fisher Scientific™ #F8810) or PSNPs of 100 nm diameter (Malvern Panalytical #NTA4093) at 2:1 molar CSMs/PSNPs ratio. The solution was left under stirring for 1 h at RT. An excess of CSMs helps avoiding uncoated PSNPs. After 10 min sonication, the mixture was extruded using an Avanti® Mini extruder with a 800 nm polycarbonate membrane (Figure 2.2.4) where the CSMs and PSNP fused under the mechanical force forming the CSMs-coated NPs. The resulting product was purified by centrifugation (see section 2.3) at 12,000 g for 30 min and the collected CSMs@PSNPs were re-suspended in PBS 1X.

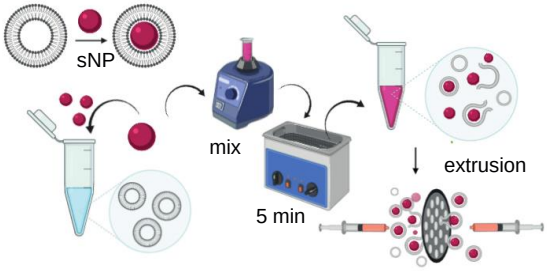

Figure 2.2.4. Scheme showing the experimental process to coat solid NPs with CSMs.

2.2.5. Functionalization with other CSMs (hybrid CSMs).

To obtain the mixture of CSMs extracted from different cell sources, firstly the HeLa-derived and the HEK-derived CSMs were labeled with Atto488 and/or Atto647N, as described above. Then, the samples were mixed at different ratios (1:9, 1:3, 1:1, 3:1 and 9:1) and sonicated for 10 min. Each sample obtained was extruded using an Avanti® Mini extruder with a 800 nm polycarbonate membrane (Figure 2.2.5) and characterized by DLS, NTA and fluorescence spectroscopy.

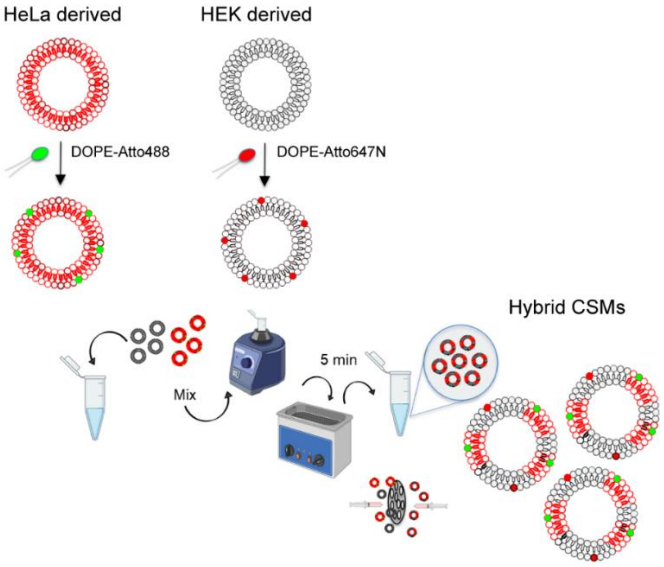

Figure 2.2.5. Scheme showing the experimental process to synthesize hybrid CSMs.

2.2.6. Functionalization with GNRs

2.2.6.1. Synthesis and characterization of GNRs

Seed mediated CTAB-stabilized rod-shaped gold NPs were synthesized following the method described by Sau *et al*.[188] Small gold seeds of nominal diameter around 3 - 4 nm were synthesized. A solution of Gold (III) chloride hydrate ($HAuCl_4$, #SLBR1101V, 0.25 mL, 0.01 M) was added to 7.5 mL of Hexadecyltrimethylammonium bromide (CTAB, #MKBX6159V, 0.2 M) solution at 26 ºC. Then 0.6 mL of freshly prepared 0.01M $NaBH_4$ (#213462) was added rapidly to the stirring solution (350 rpm) and let 2 min. The solution color changed immediately from yellow to brown. The seed solution remained under stirring for 1 h. The temperature was kept at 26 ºC over all the reaction steps. For GNR formation, 4.25 mL of 0.01M $HAuCl_4$ solution was added to 100 mL of 0.2 M solution of CTAB stirring at 26 ºC. Then 1.23 mL of 0.01 M $AgNO_3$ (#209139) solution was added, and after 2 min stirring, freshly prepared ascorbic acid solution (0.68 mL 0.1 M) was added. After 10 min of stirring, 1.1 mL of the seed solution synthesized as described above was added and stirred for other 2 min. The final solution was left overnight at 26 ºC in a water bath. The synthesized GNRs were purified twice by centrifugation at 10,000 g for 30 min, and finally the pellets were dispersed in 0.16 $mg \cdot mL^{-1}$ CTAB solution to ensure the stability of GNRs during their storage. Then, a ligand exchange of CTAB-coated GNRs with thiolated PEG was carried out. Positive (HS-PEG5K-NH_2, #JKA5145) thiol-PEG of 5 kDa weight was used. An excess of 40,000 PEG chains per GNR was added to ensure a complete coverage of the nanorod surface.[189] The PEG addition was done in two steps. In the first step, a calculated amount of a stock PEG solution (HS-PEG is dissolved in MilliQ water at final concentration of 10 $mg \cdot mL^{-1}$) was added to a final concentration of 10 nM GNRs and the solution was stirred at 350 rpm overnight. The GNR solution was centrifuged for 30 min at 13,000 g. In the second step, the same amount of PEG diluted in 5 mL of methanol 90% was added to the pellet recovered from centrifugation (GNRs) and stirred for 5 h at 350 rpm. Finally, the GNR solutions were stored at 4 ºC for further characterization.

2.2.6.2. Characterization of GNRs

UV-visible spectroscopy of GNRs. All UV-Vis spectroscopy measurements were performed on a A Biochrom Libra S60 UV–visible spectrophotometer using a 1 cm path length Hellma quartz cells, measuring in the 300-1000 nm

range. UV-Vis absorption spectra was measured of the GNRs dispersed in water.

Electron microscopy. SEM was used to analyse GNR morphology and size distribution. All SEM micrographs were obtained using a ZEISS FESEM ULTRA Plus. Using ImageJ software, the length and width of at least 300 NPs were extracted from SEM images and used to build size-frequency histograms for both length (d_l) and width (d_w).

ζ potential. ζ potential of the CTAB-coated GNRs and PEG-coated GNRs dispersed in MilliQ water was measured with laser Doppler anemometry by Malvern Zetasizer Nano ZSP (Malvern Instrument Ktd.). ζ potential measurements reported are an average of three independent measurements.

Inductively coupled plasma mass spectrometry (ICP-MS). ICP-MS was used to determine the GNR mass concentration (m) following the protocol described in the literature.[189] The ICP data shown a gold concentration of 0.7077 g/L in the GNR solution analysed. The GNR molar concentration (C_{NP}) was calculated as follows (please note that the organic contribution is not considered). The mass of a single GNR m_{GNR} was determined as the product of the core material density (ρ Au = 19.3 $g \cdot cm^{-3}$) and the core volume ($V_{NP,}$ obtained by the TEM micrograph analysis showing GNR as cylinder with mean length (d_l) of 41.7 ± 5.2 nm and mean width (d_w) of 11.1 ± 1.8 nm). The molar mass of the GNR M_{GNR} was calculated by multiplying the m_{GN} by the Avogadro number N_A. The V_{GNR} is equal to $4 \cdot 10^{-18}$ cm^3. The M_{GNR} was $4.7 \cdot 10^7$ $g \cdot mol^{-1}$. Then, the resulting molar GNR concentration C_{GNR} was $1.5 \cdot 10^{-8}$ M (15 nM). The ICP-MS data and the UV-Vis measurements provides the value of the extinction coefficient of the GNRs. According to the Beer-Lambert law, a sample absorbance is directly proportional to its concentration (C), light passing distance (l) and the sample extinction coefficient (molar absorptivity) (ε). Different dilutions of the concentrated GNR sample were prepared and the absorbance of each sample was measured at 450 nm. The extinction coefficient is obtained from the slope of the curve ($\varepsilon = 6 \cdot 10^8 M^{-1}$).

2.2.6.3. Synthesis of GNRs functionalized CSMs

To prepare plasmonic CSMs, 1mL of obtained CSMs dispersed in PBS 1X was mixed with 0.05 mL of 10 nM positively charged PEGylated-GNRs and sonicated for 5 min. Then the sample was left under stirring for 1 h at

RT (or 24 h at 4 ºC). The resulting CSMs were extruded using an Avanti® Mini extruder (with a 800 nm polycarbonate membrane 10 times) and purified by centrifugation at 10,000 g for 10 min (see section 2.3), and the collected CSMs@GNPs were re-suspended in PBS 1X (Figure 2.2.6Figure 2.2.6). The CSMs@GNPs were characterized by UV-Vis, DLS, NTA and fluorescence spectroscopy.

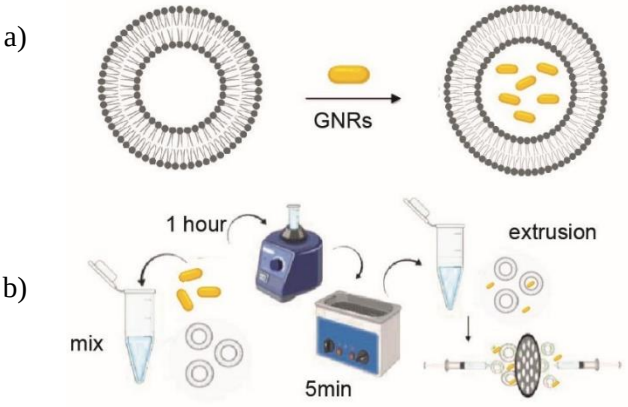

Figure 2.2.6. a) Scheme showing the functionalization of CSMs with GNRs and b) the experimental process to obtain the CSMs@GNRs.

2.3. Purification of functionalized CSMs

Engineered functionalized CSMs should be purified from the excess of free macromolecules, either large (Abs, DS, *etc*.) or small molecules (Alexa545-$PEG_{(4)}$, HOE, *etc*.), as well as separated from free solid NPs (PSNPs, GNRs). The purification strategy selected depends on several factors such as: the size of the molecules and the density of the products to be removed from, the colloidal stability of CSMs and the efficiency achieved in the separation process. The purification step selected after CSM functionalization should be specific for each reaction.

Size Exclusion Chromatography. Free small molecules such as HOE, DOPE-Atto or DOTAP were separated from the functionalized CSMs by size exclusion chromatography. The PD-10 Desalting Column and contains Sephadex G-25 Medium (gel filtration) were used, which allows rapid group separation of high molecular weight from low molecular weight substances.

Dialysis. The reaction excess of Alexa545-$PEG_{(4)}$ or Alexa555 BT7R Ab was separated from the functionalized CSMs using the dialysis purification method. Float-A-Lyzer G2 with the cut-off of 1,000 kDa was used for overnight purification.

Ultrafiltration. Molecules with molecular weight below than 100 KDa such as DS, PHA, DOTAP and DOPE, can be easily separated from the functionalized CSMs with Amicon® Ultra-0.5 Centrifugal Filter Devices with the appropriate cut-off (3-5-100 kDa) washing the solution with PBS 1X at least 3 times. The limitation of using a filter centrifugation step arises from the unspecific interactions between some molecules and the filter materials. To reduce this effect and the sample loss, the Amicon® filters were washed with 0.2% of BSA in PBS two times before to use them.

Purification of Solid NPs by centrifugation. Due to differences in density, the empty CSMs can be separated from the CSMs-coated PSNPs or CSMs-coated GNRs by normal centrifugation. In the PSNPs case, the excess of empty CSMs was removed by centrifugation at 12,000 g for 30 min and the collected CSMs@PSNPs were re-suspended in PBS 1X. Regarding the purification of GNRs-tagged CSMs, the excess of GNRs not incorporated into the nanosystem was washed off by centrifugation at 10,000 g for 10 min. At these conditions, the CSMs@GNRs were collected thanks to their increased weight while the free GNRs remained in the supernatant and were easily removed with it.

2.4. Characterization of functionalized CSMs

Quantification by Fluorescence Measurements. The amount of cargo molecules loaded into the CSMs was quantified measuring the fluorescence signal by using a Microplate reader (TECAN, Infinite® 200 PRO) equipped with monochromator-based optics and wavelength selection between 280 and 850 nm. In the Table 2.4.1, the $\lambda_{exc}/\lambda_{em}$ ranges used for the different fluorescent molecule are reported. The cargo concentrations in the solution ware determined by interpolation of the measured fluorescence intensity from a previously constructed analytical calibration curve (see Table 2.4.1 and Figure 2.4.1).

Table 2.4.1. The concentration of encapsulated cargo calculated by measuring the fluorescence intensity of CSMs@Cargo samples.

Cargo	$\lambda_{exc}/\lambda_{em}$ (nm)	Equation	R Squared	C.Cargo ($\mu g \cdot ml^{-1}$)	C. ($CSMs \cdot ml^{-1}$)	Cargo/CSM
DS	500/594	Y = 173.2·X + 2712	0.9928	2.58 ± 0.3	$2 \cdot 10^{11}$	110 ± 14
HOE	361/497	Y = 1133·X + 5490	0.9358	2.18 ± 0.4	$2 \cdot 10^{11}$	12310 ± 1462
Alexa555 BT7R Ab	560/610	Y = 11222·X + 630.6	0.9997	0.15 ± 0.1	$1 \cdot 10^{11}$	60 ± 22
Alexa545 -$PEG_{(4)}$	560/610	Y = 201637·X + 1450	0.9937	0.28 ± 0.1	$7 \cdot 10^{9}$	24353 ± 8777
PHA	488/520	Y = 4290·X + 974.1	0.9945	1.79 ± 0.9	$2 \cdot 10^{11}$	4311 ± 1183

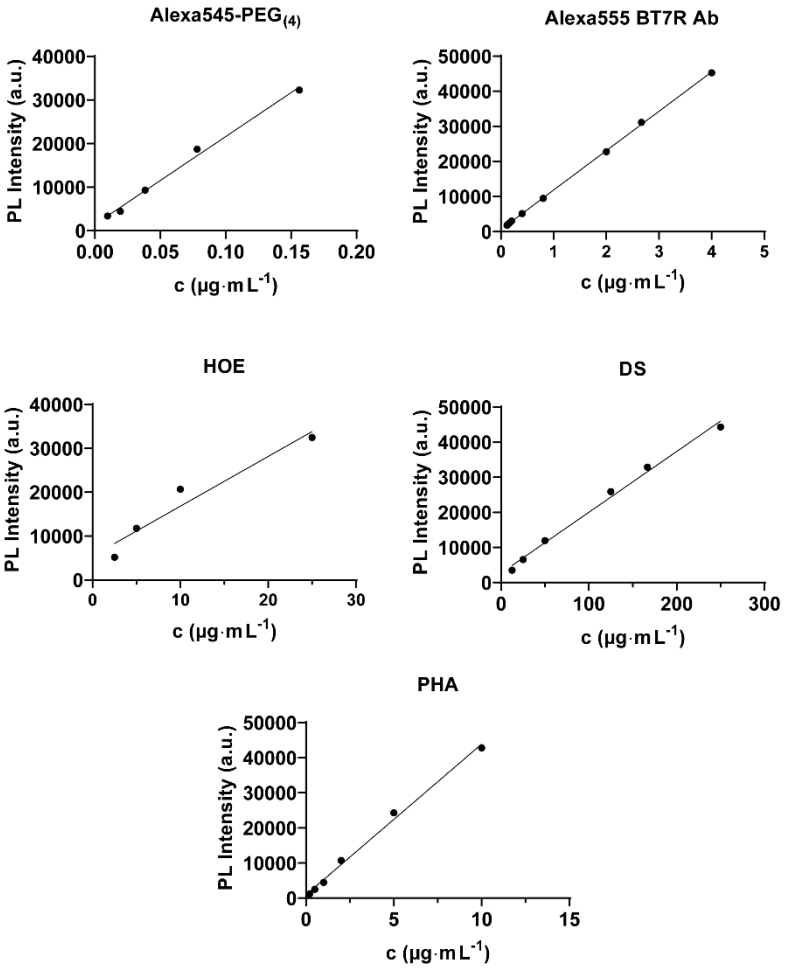

Figure 2.4.1. Calibration curves of different cargos in PBS 1X or HEPES. These calibrations curves were used to quantify the concentration or number of the cargo encapsulated into CSMs.

Colloidal stability. The functionalized CSMs were characterized with DLS and NTA analysis (see section 2.4) in order to study the colloidal properties of the CSMs after the functionalization reaction and the purification step.

Quantification of encapsulated GNRs by ICP-MS. Once the CSMs@GNRs were obtained and purified following the protocol above, $2.40 \cdot 10^9$ CSMs were used to quantify the GNRs and, thus, the number of incorporated

particles for each nanostructure (Table 2.4.2). Concurrently, also 0.05 mL of 10 nM positively charged PEGylated-GNRs was analyzed in order to obtain a more precise quantification. Both samples were digested overnight in aqua regia (200 µL). Then, they were diluited with 2 mL of HCl 2% v/v for ICP-MS analysis. The ICP-MS analysis was performed in an Agilent 7700x inductively coupled plasma mass spectrometer.

Table 2.4.2. ICP-MS analysis of total GNRs added to the CSMs and purified CSMs@GNRs sample.

CSMs@GNRs	g Au·L^{-1}	mol·L^{-1}	GNRs·L^{-1}	GNR	CSMs	GNRs·CSM^{-1}
AV	0.0036	$1.48 \cdot 10^{10}$	$8.89 \cdot 10^{13}$	$8.89 \cdot 10^{10}$	$2.40 \cdot 10^{9}$	37.06
SD	0.0013	$5.28 \cdot 10^{11}$	$3.18 \cdot 10^{13}$	$3.18 \cdot 10^{10}$		13.25
GNRs	**g Au·L^{-1}**	**Mol·L^{-1}**	**GNRs·L^{-1}**	**GNR**		
AV	0.0180	$7.32 \cdot 10^{-10}$	$4.41 \cdot 10^{14}$	$4.41 \cdot 10^{11}$		
SD	0.0040	$1.63 \cdot 10^{-10}$	$9.82 \cdot 10^{13}$	$9.82 \cdot 10^{10}$		

2.5. *In vitro* studies

2.5.1. Cell culture

HeLa, A549, RAW and HEK cell lines were cultured in cDMEM. Cells were maintained under humid conditions at 37 °C and 5% of CO_2. Cells were passaged after cleaning DPBS 1X with 0.25% Trypsin-EDTA 1X when the culture reached confluency.

2.5.2. 3D Cell Culture

The HeLa and A549 cell lines were used to obtain the 3D spheroids. 100 µL of suspension of 50,000 cells·mL^{-1} were transferred to a 96 multi-well plate previously treated with agarose as follows: a 1-1.5% agarose solution was prepared in filtered PBS 1X and heated up to 100 °C; 50 µL of agarose solution were used to cover the bottom of the wells. The plate was let to cool at RT in sterile conditions without the lid for at least 30 min before seeding the cells. The 3D spheroids were grown at 37 °C in a humidified 5% CO_2

atmosphere, with 100 µL of fresh complete media gently added every day, for 3 days in order to obtain spheroids with a ~ 0.5 µm diameter.

On the fourth day, the spheroids were washed with PBS 1X twice, carefully avoiding displacing them from the wells. The spheroids were incubated with a 200-300 µL solution of CSMs. After 3, 6 and 24 h, the CSMs solution was removed, and the spheroids were washed twice with PBS 1X.

LIVE/DEAD Assay. Each spheroid was individually transferred into the 96 multi well plate without agarose. Then, they were harvested after trypsinization for 2 min with 0.05 mL of 0.25% Trypsin–EDTA. 0.2 mL of cDMEM was added to recover the cells, which were transferred to 1.5 mL sterile tubes. The cells were collected after centrifugation at 500 g for 5 min. The cell pellets were resuspended in 0.2 mL of PBS 1X at 0.1 µM calceinAM (Invitrogen, C1430, C3099, C3100) and 3 µM Propidium Iodide (Sigma-Aldrich™ #25535-16-4). The cells were incubated for 15-20 min at room temperature in the dark. To have a negative control, some of the spheroids were treated with 0.2% Triton solution for 15-20 min. A suspension of 100,000 cells·mL^{-1} was used as alive cell control. After the incubation period, the stained cells were analyzed by flow cytometry using a 488 nm excitation and measuring green fluorescence emission of calcein (*i.e.*, 530/30 bandpass) and red fluorescence emission of the propidium iodide (*i.e.*, 610/20 bandpass).

Confocal Microscopy Assay. Each spheroid was individually transferred in a µ-Slide Angiogenesis plate (81506, IBIDI) and added 40 µL of cDMEM without phenol red.

To obtain a more accurate view of the spheroids, CellMask™ Orange, Deep Red, and Green plasma membrane stains (ThermoFisher™) were used. The CellMask™ plasma membrane stain (1,000X concentration) was used at 1X in cDMEM, following the Thermofisher's protocol. The spheroids were incubated with the CellMask™ 1X for 1-2 min at 37 °C. Thus, the staining solution was removed and the spheroids were washed 3 times with PBS 1X. Fresh cDMEM without phenol red was added. The spheroids were observed in transmitted light and fluorescence microscopy using an Andor Dragonfly spinning disk confocal system with the 20X objective (MRH07241, Nikon). Z-scans consisted of ~ 300 different stack images in the Z-axis. 3D reconstructions were done with ~300 stack images (total thickness ~150 µm,

step thickness ~0.5 µm). ImageJ was used to analyze the 2D images. The deconvolution of the Z-scans was done with the Fusion software. Imaris software (Oxford Instruments) was used for the 3D reconstruction.

2.5.3. Flow Cytometric Studies

2.5.3.1. CSMs Uptake

To expose the cells to CSMs, the HeLa and A549 cells were seeded in 24-well plate at a density of 50,000 cells per well while the MRC-5, RAW and HEK cells were seeded at a density of 60,000 cells per well in 0.5 mL of cDMEM. After 24 h, cells were washed with PBS 1X and the medium was replaced with the freshly prepared CSMs dispersions of interest in cDMEM. Experiments were performed by exposing the cells to CSM dispersions at $2 \cdot 10^5$ CSMs per cell at 37 °C and 5% CO_2 for 10 min, 1, 3 or 6 hours. After CSMs exposure, cells were washed with 1 mL PBS per well. Then, cells were harvested after trypsinization for 2 min with 0.075 mL 0.25% Trypsin–EDTA. 0.15 mL of PBS or cDMEM was added to each well to recover the cells. Cells were pelleted by centrifugation at 1,500 rpm for 3 min, then resuspended in 200 µL of cell media or PBS. Cell fluorescence intensity was measured using a Guava Millipore flow cytometer equipped with a 488 nm blue laser and a 532 nm green laser coupled with 525/30 nm, 583/26 nm, 620/50 and 695/50 filters, depending on the CSMs fluorescence. Results are reported as the median of cell fluorescence intensity.

2.5.3.2. Endocytosis inhibition

For inhibition studies, cells were seeded in 48-well plates in 0.3 mL of cDMEM at a density of 25,000 cells per well for the HeLa and A549 cells and of 30,000 cells per well for the MRC-5, RAW and HEK cells. After 24 h, the medium was replaced with the freshly prepared inhibitor solutions of interest in cDMEM at the concentrations reported in Table 2.5.1.

Table 2.5.1. Inhibitors used to block the cell endocytosis.

Inhibitor	C.		Pre-treatment (min)
	(mM)	(μg·mL^{-1})	
Nystatin (NYS)	0.01	10	30
Dynasore (DYN)	0.08	25.78	30
Chloroquine (CQ)	0.1	32	30
Chlorpromazine (CP)	0.03	10	30
Methyl-β-cyclodextrin (MBCD)	5	6250	20

After 30 min of treatment, the inhibitor solutions were removed and replaced with the same solutions enriched with fluorescent CSMs at a concentration of $2 \cdot 10^{11}$ CSMs·mL^{-1} at 37 °C and 5% CO_2 for 10 min, 1, 3 or 6 h. Then the cells were washed with 1 mL PBS per well and harvested after trypsinization for 2 min with 0.075 mL 0.25% Trypsin–EDTA. 0.15 mL of PBS or cDMEM was added to each well to recover the cells. Cells were pelleted by centrifugation at 1,500 rpm for 3 min then redispersed in 200 μL of cell media or PBS. The CSMs uptake under the different inhibitor conditions was evaluated by cell fluorescence intensity that was measured using a Guava Millipore flow cytometer equipped with a 488 nm blue laser and a 532 nm green laser coupled with 525/30 nm, 583/26 nm, 620/50 and 695/50 filters, depending on the CSMs fluorescence.

2.5.3.3. Homotypic targeting

The homotypic targeting experiments were performed using CSMs obtained from different cell lines (HeLa, A549, HEK, see section 2.1) equivalently labeled with DOPE-Atto488 or DOPE-Atto647N. HeLa and A549 cells were seeded in a 48-well plate at a density of 25,000 cells per well and the MRC-5, RAW and HEK cells were seeded at a density of 30,000 cells per well in 0.3 mL of cDMEM. After 24 h, cells were washed with PBS and the medium was replaced with the freshly prepared CSMs dispersions of interest (HeLa derived CSMs@DOPE, A549 derived CSMs@DOPE and HEK derived CSMs@DOPE) in cDMEM. Experiments were performed by exposing the cells to CSMs dispersions at $2 \cdot 10^{11}$ CSMs·mL^{-1} at 37 °C and

5% CO_2 for 10 min, 1, 3 or 6 h. After CSMs exposure cells then were washed with 1 mL PBS per well. Then the cells were harvested after trypsinization for 2 min with 0.075 mL 0.25% Trypsin–EDTA. 0.15 mL of PBS or cDMEM was added to each well to recover the cells. Cells were pelleted by centrifugation at 1,500 rpm for 3 min and then redispersed in 200 µL of cell media or PBS. Cell fluorescence intensity was measured using a Guava Millipore flow cytometer equipped with a 488 nm blue laser and a 532 nm green laser coupled with 525/30 nm, 583/26 nm, 620/50 and 695/50 filters, depending on the CSMs fluorescence. Results are reported as the median of cell fluorescence intensity.

2.5.4. Confocal Microscopy

In order to perform all the confocal imaging experiments with living cells, the HeLa and A549 cell lines were seeded in IBIDI dishes at the concentrations reported in Table 2.5.2. Regardless of the cell line and the plate type, the cells were let to grow in cDMEM at 37 °C and 5% CO_2 for 24 hours to reach 70% of confluence.

Table 2.5.2. Different seeding condition in confocal microscopy experiments of HeLa, A549 and MRC-5 cells depending on the IBIDI dishes.

IBIDI dish		HeLa	A549
µ-Slide 8 Well (#80826)	Cells	25,000	25,000
	Vol. (mL)	0.3	0.3
µ-Slide VI 0.4 (#80606)	Cells	15,000	15,000
	Vol. (mL)	0.03	0.03
µ-Dish 35 mm (#80136)	Cells	50,000	50,000
	Vol. (mL)	0.5	0.5
µ-Slide 18 Well (#81816)	Cells	10,000	10,000
	Vol. (mL)	0.1	0.1

The CSMs samples were exposed to the cells at different time treatments (10 min in PBS 1X, 1, 3 or 6 h in cDMEM) at a concentration of $2 \cdot 10^{11}$ CSMs·mL^{-1} at 37 °C and 5% CO_2 condition. Then the cells were washed 3

times with fresh PBS 1X in order to remove non-associated CSMs with cells and added with HEPES supplemented media (DMEM without phenol red, 4.5 $g \cdot L^{-1}$ D-glucose and L-glutamine, 25 mM HEPES and without pyruvate, Gibco, #21063-029).

To reach a more accurate view of the cells, different intracellular compartments were stained. CellMask™ Orange, Deep Red, Green plasma membrane stains and others ThermoFisher™ products provide excellent and rapid compartment staining in live cells for 30–90 minutes depending on the cell type and experimental conditions (Table 2.5.3). For the lysosome staining, a LysoTracker™ Blue DND-22 (ThermoFisher, #L7525) dilution of 50 nM was prepared in cDMEM. 0.1 mL of this staining solution was gently added to the cells and incubated 30 min at 37 °C in dark conditions. For cell membrane staining, a CellMask™ Deep Red (ThermoFisher, #C10046) solution (1 µL in 1 mL of cDMEM) was added to the cells 3 min at 37 °C in dark conditions. Subsequently, the cells were washed three times with PBS and HEPES supplemented media.

To perform the confocal imaging experiments with fixed cells, after the specific cell treatment (CSMs incubations and/or intracellular compartment staining) the cells were washed three times with PBS and incubated with 3.6% Formaldehyde solution (Sigma-Aldrich™ #F8775) in PBS solution for 20-25 min at RT. Then, the formaldehyde solution was removed, and the cells were washed with PBS before adding few drops of IBIDI Mounting Medium (#50001 IBIDI).

Table 2.5.3. Thermo Fisher products used for the intracellular compartment staining and the experimental conditions used.

	Staining	Stock solution	Working solution	Incubation conditions	Em/exc (nm)
CellMask™ Green plasma Membrane stain	Plasma membrane	5 mg·mL^{-1} (1,000X)	1X in cDMEM	1 min 37 °C	490/525
CellMask™ Orange plasma Membrane stain	Plasma membrane	5 mg·mL^{-1} (1,000X)	1X in cDMEM	1 min 37 °C	556/572
CellMask™ Deep red Plasma Membrane stain	Plasma membrane	5 mg·mL^{-1} (1,000X)	1X in cDMEM	1 min 37 °C	660/680
LysoTracker® Blue DND-22	Lysosomes	1 mM (DMSO)	0.1 µM in cDMEM	30-45 min 37 °C	373/422
MitoTracker® Green FM	Mitochondria	1 mM (DMSO)	0.1 µM in cDMEM	15-20 min 37 °C	410/516

Confocal images of living cells were captured on an Andor Dragonfly spinning disk confocal system mounted on a Nikon TiE microscope equipped with a Zyla 4.2 PLUS camera (Andor, Oxford Instruments) and an OKO-lab incubator to keep cells at 37 °C during the whole experiment. The samples were excited with four different lasers (405, 488, 561 and 637 nm lasers) and the emitted fluorescence was collected by the filter wheel (450 (50) nm, 525 (50) nm, 620 (50) nm and 725 (40) nm) with appropriate combinations of them (Table 2.5.4). Images were taken with different magnification objectives (20X, 60X, 100X). All the images were processed with ImageJ®.

Table 2.5.4. Laser and filter combination based on the $\lambda_{exc}/\lambda_{em}$ of each dye used for the confocal microscopy studies.

Dye/Staining	$\lambda_{exc}/\lambda_{em}$ (nm)	Laser (nm)	Filter (nm)
DS	500/594	561	620 (50)
HOE	361/497	405	450 (50)
Alexa555 BT7R Ab	560/610	561	620 (50)
Alexa545-$PEG_{(4)}$	560/610	561	620 (50)
PHA	488/520	488	525 (50)
DOPE-Atto647N	635/670	637	725 (40)
DOPE-Atto488	485/535	488	525 (50)
CellMask™ Green plasma Membrane stain	490/525	488	525 (50)
CellMask™ Orange plasma Membrane stain	556/572	561	620 (50)
CellMask™ Deep red Plasma Membrane stain	660/680	637	725 (40)
LysoTracker® Blue DND-22	373/422	405	450 (50)
MitoTracker® Green FM	410/516	488	525 (50)

2.5.5. Corrected total cell fluorescence

Fluorescence intensity from confocal microscopy images was quantified by calculating the corrected total cell fluorescence (CTCF) with ImageJ® software. Areas of cells were selected for each experimental condition (cell treated with CSMs@Cargo, FCSMs@Cargo and Cargo alone) and the integrated density was measured. Then, the CTCF was calculated as follow:

$$CTCF = Total\ cell\ fluorescence - (Cell\ Area \times Mean\ of\ the\ background)$$

where, total cell fluorescence corresponds to the mean integrated density measured from each cell section and the background is the mean gray value of an image section with no cells.

2.6. NIR laser excitation experiments

In lasers experiments, in order to control the spot size as well as irradiate cells homogeneously, an 808 nm laser (Lasing, #FC-W-808A) with a zoom fiber collimator (Thorlabs, #ZC618SMA-B) was used. To calculate the intensity received by the cell ($W \cdot cm^{-2}$), a power energy meter (Thorlabs, #PM100D) was used with a thermal power head (10 W, 25 mm, Thorlabs, #S425C) to measure the output power. The diameter of the spot size corresponds to 0.65 cm. As the beam is collimated, a homogeneous spot was assumed, and thus the intensity could be calculated dividing the power by the surface (in cm^2) of the spot. The experiments were performed at different times (0.5, 1, 2 and 4 min) and power conditions (16-32 $W \cdot cm^{-2}$) and 2 min of exposure time was chosen as the maximum irradiation time for the final experiments with cells.

2.6.1. Cargo Release in test tube

In the test tube assay, the amount of cargo encapsulated in the CSMs was measured before and after laser irradiation. Samples were placed in a 96-well plates and were irradiated for 0.5, 1, 2 and 4 min at 30 $W \cdot cm^{-2}$. The irradiated samples were centrifuged individually at 10,000 g for 10 min, and the fluorescence intensity signal of the pellet and supernatant was measured by using a Microplate reader (TECAN, Infinite® 200 PRO).

2.6.2. Cell viability

In order to assess the number of viable cells after CSMs exposure and laser irradiation, the resazurin assays was performed. To this aim, HeLa cells were seeded in 96-well plates, 7,500 cells per well in 100 µL of cell growth medium 24 h before the CSMs exposition. Then media was removed and 100 µL of cell culture growth medium with the desired concentration of CSMs was added. The cells were incubated with the CSMs solutions for 3 h at 37 °C and 5% CO_2. Then the samples were irradiated at different times (0.5, 1, 2 and 4 min) using 30 $W \cdot cm^{-2}$.

12 h after irradiation, each well was rinsed three times with PBS and added with 100 µL of freshly prepared solution with 90% of medium and 10% of resazurin (resazurin sodium salt in water, 0.2 $mg \cdot mL^{-1}$, filtered; Resazurin Sodium Salt, Sigma-Aldrich™ #199303-1G). Cells were incubated for 4 hours at 37 °C and 5% CO_2 under dark conditions. Non-fluorescent resazurin (Almar blue) is oxidized by living cells into its fluorescent product resorufin (excitation at 579 nm and emission at 584 nm). Hence, the fluorescence intensity of each well is proportional to the number of living cells there. After the incubation, plates were analyzed with a plate reader (TECAN, Infinite® 200 PRO) under 560 ± 20 nm excitation, collecting fluorescence with a 610 ± 20 nm filter. The fluorescence value of each well is an average of nine consecutive measures in the same well. Final intensity value for control the non-treated cells (Ic) is an average of at least nine independent values. Final intensity values for samples (Is) are the mean of three independent well fluorescence values. So, the cell viability value is calculated as followed:

$$\text{cell viability (\%)} = \frac{I_S}{I_C} \cdot 100$$

2.6.3. Cargo Release *in vitro*

The cargo release inside living cells was studied by fluorescence confocal microscopy imaging. To this aim, HeLa cells were seeded as reported in Table 2.5.3 and let grow to reach 70% of confluence. Cells were exposed to CSMs@GNRs@Cargo samples for 3 h in cDMEM at a concentration of $2 \cdot 10^{11}$ $CSMs \cdot mL^{-1}$ at 37 °C and 5% CO_2 condition. Then, the cells were washed three times with fresh PBS 1X in order to remove non-associated CSMs and added with HEPES supplemented media. Once validated that CSMs preloaded cells were morphologically and fluorescently coherent with previous confocal microscopy studies, two different irradiation protocols were followed using two different irradiation set-ups:

I. *Single-cell irradiation*. Highly focused NIR spot (high power densities of a 785 nm laser "pointer" with a spot diameter of ~5 µm, *i.e.*, optical setup equivalent to optical tweezers.[80] This irradiation setup was achieved by coupling a NIR laser through the optical path of the microscope. Selected cells were irradiated for ~5 seconds, leading to staining of the whole cell.

II. *Multi-cell irradiation.* Illumination of thousands of cells with a large diameter (~0.65 cm; low power density) collimated NIR beam (808 nm laser) in order to irradiate a higher area of the cell culture (0.33 cm^2 corresponding to he area capable to host ~10^4 cells). The cell plate was irradiated for 1 minute at 30 $W \cdot cm^{-2}$. Subsequently, the cells were washed twice with PBS 1X and HEPES supplemented media was added.

Confocal images of living cells were captured on an Andor Dragonfly spinning disk confocal system mounted on a Nikon TiE microscope equipped with a Zyla 4.2 PLUS camera (Andor, Oxford Instruments) and an OKO-lab incubator to keep cells at 37 °C during the whole experiment. Images were taken with different magnification objectives (20X, 60X, 100X). All the images were processed with ImageJ®.

Results and Discussion

3. Results and Discussion

3.1. CSMs: biomimetic nanoplatforms for interaction with cells

Although multi-ligand strategies for targeted NPs delivery have received considerable attention, they still suffer of poor *in vivo* efficacy caused by biointerfacing issues between the synthetic material and the human body environment. The main drawbacks are low specificity *in vivo*, fast renal clearance, short-time permanence in the circulation torrent and the activation of immune responses.

A biointerfacing approach that exploit the biological natural membrane is proven to be a successful strategy to improve the performance of synthetic nanocarriers *in vivo*. Designing the nanostructures by replicating the natural (bio)-physical properties and highly complex functionalities of the cell surface provides delivery nanosystems with effective biointerfacing, preserving the key functionalities of the origin cells.

In this first part, it has been designed and developed off-the-shelf bio-synthetic ghost cell-derived NPe (CSMs) capable of controlling and modulating a specific cellular response. CSMs were prepared in an easily scalable bottom-up process that can be used to produce and functionalize cell membrane vesicles. The nanostructures were fully characterized using a large variety of techniques to assess the physicochemical features of CSMs: SEM for morphology determination, DLS for hydrodynamic size and colloidal stability, laser Doppler anemometry for ζ-potential, NTA for concentration and size distribution analysis, and fluorescence spectroscopy for quantification of loading of fluorescence probes or labels, among others. The information extracted from the physicochemical characterization will be used to optimize the design of the CSMs. Biomimetic capacities of the CSMs were determined by the *in vitro* cells experiments and the biointeraction with 2D and 3D cell cultures models was investigated in the following sections (Figure 3.1.1).

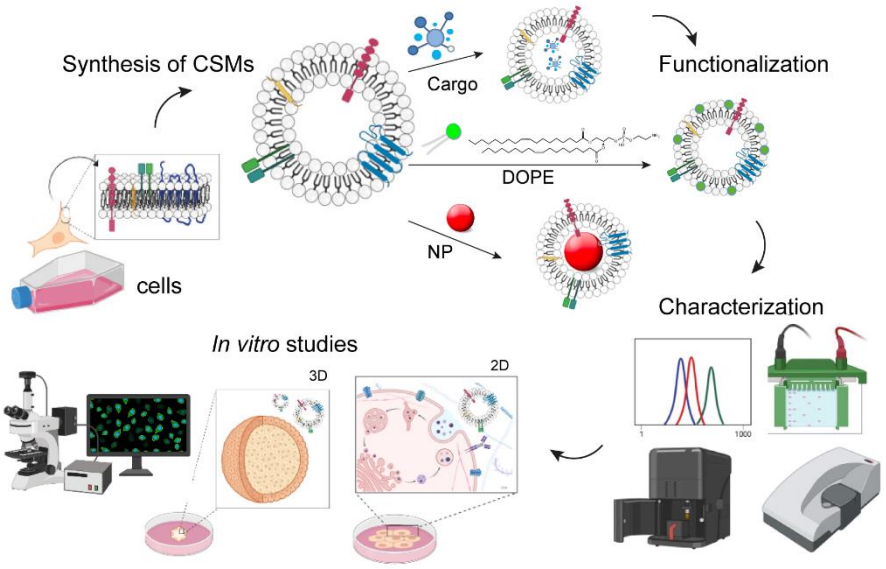

Figure 3.1.1. Schematic representation of the workflow for CSM preparation and evaluation of the interaction with 2D and 3D cell culture models.

3.1.1. Design and characterization of CSMs

The cell membranes, like derived bio-vesicles, are asymmetric phospholipid-based membranes embedded with active surface compounds that are essential for their bio-functions.[190]

Human cell cultures derived from cervix epithelial carcinoma (HeLa cells) were first selected as a model cancer cells and the cell membrane fragments synthesis was carried out following the method previously reported in the literature by Zhu *et al.*[185] and described in the Materials & Methods, section 2.1. First, a number of cells ranging between 10^6 and 10^7 were harvested from culture dishes and collected by centrifugation. CSMs were produced by combination of two physical disruption methods capable of breaking down cell membranes using different external forces such as heat and pressure. The complete cell lysis was carried out by (i) an osmotic shock produced with a hypotonic buffer and, (ii) thermal lysis conducted by repeated freezing-thawing cycles. The hypotonic solution provides the osmotic pressure required for cell swelling. The concentration of salt surrounding the cell is rapidly decreased, so that the cell membrane becomes

permeable to water due to the osmotic effect. The combination of the osmotic pressure and the thermal shock effect caused by the freezing-thawing cycles induce transient openings in the cell membrane to empty the cell from its components. To minimize the possible denaturation of the membrane-oriented proteins, plasma membrane extraction was as gentle as possible, while protease inhibitors were added to the solution to maintain the bio-activity of membrane.[185,191] Soluble proteins, intracellular biomacromolecules, and nucleus were removed via centrifugation, and the purified membrane fragments were subsequently extruded through polycarbonate membranes with nanosized pores to obtain self-assembled CSMs with size ranging between 100 and 400 nm.

By selecting specific pore size of the membrane used during the extrusion process, it is possible modulate the size distribution of the final CSMs. This step was found to be a critical point to obtain highly monodisperse CSMs. The number of extrusion cycles required to obtained monodispersed CSMs was optimized by DLS analysis. As reported in Table 3.1.1 and showed in Figure 3.1.2, increasing the number of extrusion steps narrowed the size distribution of the CSMs synthesized (Figure 3.1.2a) leading to a decrease of the Polydispersity Index (PDI) (Figure 3.1.2b). A minimum of 7 cycles of extrusion was required to obtain a monodisperse CSMs sample (Figure 3.1.2b and Table 3.1.1). Therefore, 10 cycles of extrusion were applied for the preparation of the samples. EM was used to confirm the morphology of the CSMs that show similar sizes as the DLS measurements (Figure 3.1.2c).

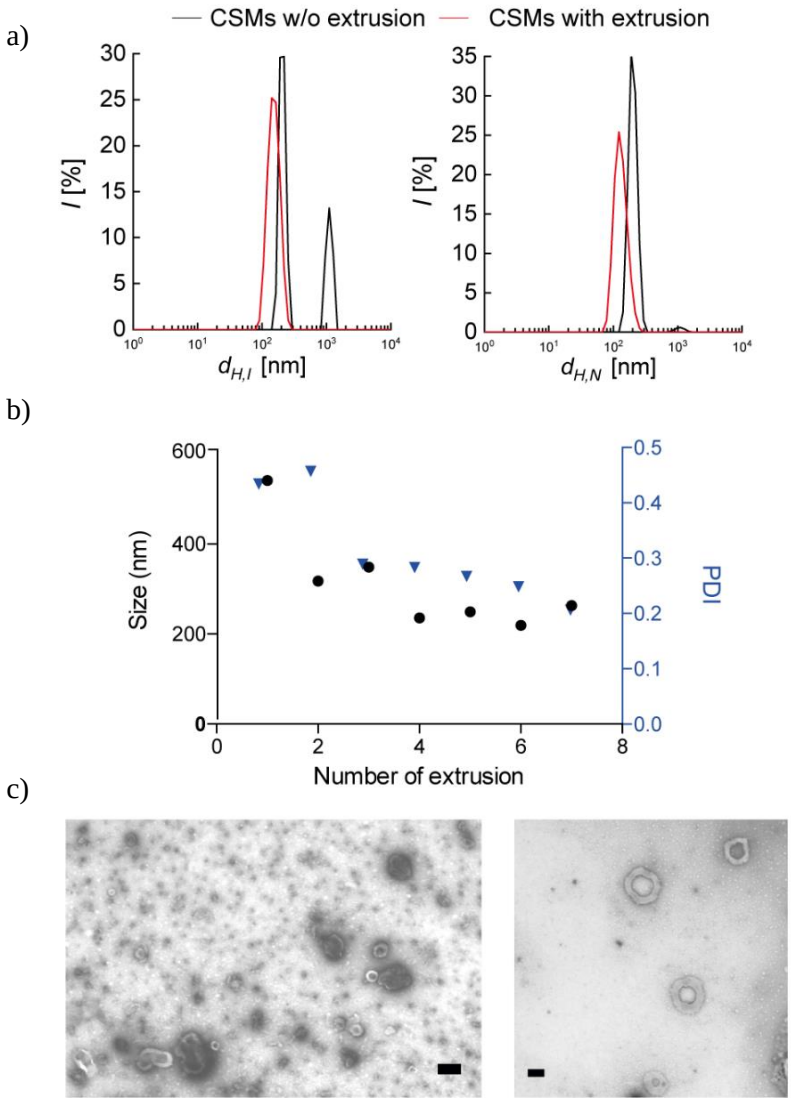

Figure 3.1.2. DLS characterization of CSMs: a) mean hydrodynamic diameter for the DLS distributions in intensity ($d_{H,I}$), and number ($d_{H,N}$) of CSMs before (black line) and after (red line) the extrusion steps; b) variation of the CSM hydrodynamic diameter and the PDI after different number of extrusion steps; c) SEM micrographs of CSMs derived from HeLa cells after their staining with uranyl acetate; scale bars: 200 nm.

Table 3.1.1. DLS measurements of CSMs after 1 to 7 extrusion steps. [1] Mean hydrodynamic diameter derived from the DLS distributions. $d_{H,I}$ and $d_{H,N}$ refer to the mean average hydrodynamic diameter from the intensity and number DLS distributions. Standard deviation values were calculated from five measurements.

N° extrusion step	PDI[1]	$d_{H,I}$ (nm)[1]	$d_{H,N}$ (nm)[1]	Pk 1 $d_{H,I}$ (nm)[1]	Pk 2 $d_{H,I}$ (nm)[1]
0	0.67 ± 0.04	1767.3 ± 71.7	117.7 ± 27.5	2731.2 ± 200.3	118.5 ± 26.7
1	0.45 ± 0.02	371.9 ± 149.8	218.2 ± 21.1	233.8 ± 21.1	5399 ± 227.7
2	0.40 ± 0.02	226.2 ± 27.5	188.2 ± 23.2	198.7 ± 26.6	5452.7 ± 186
3	0.38 ± 0.01	231.7 ± 53.0	218.7 ± 50.6	231.7 ± 53.0	5452.7 ± 182.5
4	0.33 ± 0.01	284.1 ± 50.4	247.7 ± 50.0	267.2 ± 54.5	
5	0.28 ± 0.01	234.3 ± 18.5	216.0 ± 9.5	234.4 ± 18.5	
6	0.29 ± 0.01	328.2 ± 68.2	220.5 ± 8.2	328.2 ± 68.2	
7	0.17 ± 0.02	200.5 ± 5	168.5 ± 6.0	200.5 ± 5.0	

Following the same protocol, three more cell lines were used as source of bioactive membranes: the adenocarcinomic human alveolar basal epithelial cells (A549 cells), the healthy embryonic adrenal cell line (HEK cells) and macrophages from Abelson murine leukemia virus-induced tumor (RAW cells). DLS analysis were used to investigate the hydrodynamic size and the colloidal stability of the CSMs obtained from different cell lines. The results revealed highly monodisperse size distribution (PDI values below 0.2) and nearly constant hydrodynamic diameters for all CSM samples obtained from different cell types (around 200 nm in diameter) for both intensity ($d_{H,I}$) and number distributions ($d_{H,N}$) (Table 3.1.2 and Figure 3.1.3). These results shown that only one size distribution is present in the CSM sample solution and there were no agglomerates or aggregates.

Table 3.1.2. DLS measurements of CSMs obtained from different cell lines: HeLa cells, A549 cells, HEK cells and RAW cells. [1] Mean hydrodynamic diameter derived from the DLS distributions: $d_{H,I}$ and $d_{H,N}$ refer to the mean average hydrodynamic diameter from the intensity and number DLS distributions. PDI refers to polydispersity index. Standard deviation values were calculated from five measurements.

Sample	$d_{H,I}$ (nm)[1]	$d_{H,N}$ (nm)[1]	PDI[1]
CSMs@HeLa	200.5 ± 5.0	168.5 ± 6.0	0.16 ± 0.008
CSMs@A549	279.0 ± 25.0	161.1 ± 21.2	0.17 ± 0.011
CSMs@HEK	345.3 ± 41.1	211.3 ± 16.1	0.20 ± 0.019
CSMs@RAW	245.7 ± 19.6	221.4 ± 15.5	0.20 ± 0.015

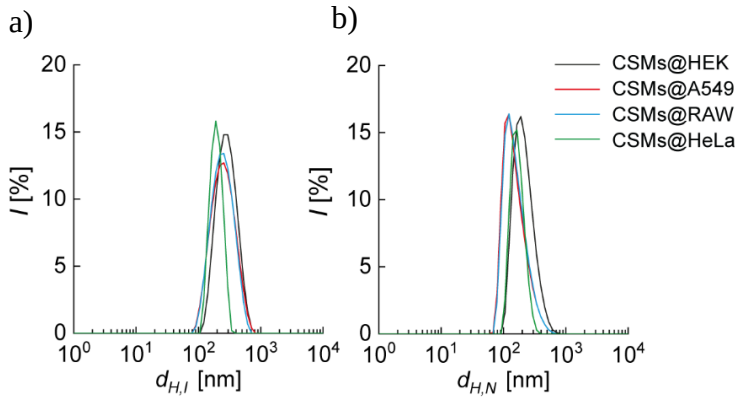

Figure 3.1.3. DLS characterization of the size distribution of CSMs: a) mean hydrodynamic diameter for the DLS distributions in intensity ($d_{H,I}$), and b) number ($d_{H,N}$) of CSMs from different cell-type origin (HEK cells, A549 cells, HeLa cells and RAW cells).

NTA was used to further characterize the colloidal properties of the CSMs and determine their concentration in solution. The results NTA showed similar CSMs size distribution as the data obtained from the DLS analysis (Figure 3.1.4) and allowed determining the CSMs concentration that are reported in Table 3.1.3. This parameter is crucial to establish and modulate the doses of administered CSMs to the cells in subsequent *in vitro* studies, and the cargo loading of the different probes used.

Table 3.1.3. Mean diameter derived from the NTA distributions. Standard deviation values were calculated from three measurements of CSM stock samples.

Sample	C. (CSMs·mL^{-1} ·10^{11})	Size (nm)
CSMs@HeLa	7.57 ± 0.4	155.33 ± 7.1
CSMs@A549	3.93 ± 0.25	167.1 ± 10
CSMs@HEK	4.07 ± 0.11	152.67 ± 11
CSMs@RAW	2.57 ± 0.64	193.1 ± 3

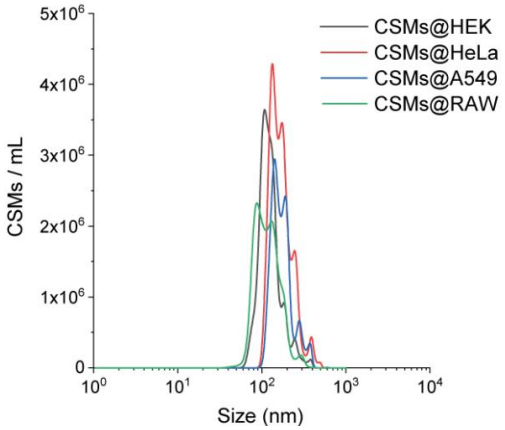

Figure 3.1.4. NTA size distribution of diluted CSMs in water. Representation of the number distribution of the hydrodynamic diameter of individual CSMs. CSMs derived from HeLa (black line), A549 (red line), HEK (blue line) and RAW cells (green line).

Nanomaterials for biological applications are not expected to sedimentate or aggregate. However, aggregation after changes in pH or ionic force of the experiment media can frequently occur.[192] Thus, it is crucial to analyze the nanocomposite behavior under different conditions. Here, PBS, 2-(*N*-morpholino)ethanesulfonic acid (MES) and phagolysosomal simulant fluid (PSF) buffers were used to investigate the CSMs stability at different pH conditions (PBS pH 7.4, MES pH 6.0 and 5.5, PSF pH 4.5). Moreover, cDMEM buffer (pH 7.6) was used as complex media to simulate the protein-enriched bioenvironment of cells. The hydrodynamic diameter of the CSMs after dispersion in the corresponding buffer was measured over time (from 0 to 48 h) because the aggregation or stability loss can be a time-dependent process (see Figure 3.1.5 and Table 3.1.4). The results showed that the CSM size from the four different cell lines and therefore their colloidal stability

was maintained in physiological conditions (PBS buffer at pH 7.4) as well as in complex media such as cDMEM. As expected, the media proteins of biological media help to stabilize the CSMs dispersion by forming the protein corona and preventing the aggregation and sedimentation.[193,194] On the other hand, when the pH decreases bellow 6, the colloidal stability of the CSMs was compromised causing the increase in the hydrodynamic diameter.

Table 3.1.4. DLS measurements of the colloidal stability of CSMs under different pH values and time points. [1] Mean hydrodynamic diameter derived from the DLS distribution: Z-Average, and $d_{H,I}$ refers to the mean average hydrodynamic diameter from the intensity distribution. PDI refers to polydispersity index. Standard deviation values were calculated from three measurements.

Buffer	Z-Average	$d_{H,I}$ (nm)[1]	PDI
CSMs@HeLa			
PBS pH 7.4 (0 h)	209.2 ± 16.6	185.79 ± 14.8	0.21 ± 0.09
PBS pH 7.4 (24 h)	253.1 ± 25.6	255 ± 9.6	0.2 ± 0.1
PBS pH 7.4 (48 h)	277.5 ± 8.7	296.3 ± 3.8	0.27 ± 0.06
MES pH 6 (0 h)	337.7 ± 139.4	195.7 ± 23	0.42 ± 0.04
MES pH 6 (24 h)	343.3 ± 73.9	320 ± 46.8	0.36 ± 0.18
MES pH 6 (48 h)	363.5 ± 65.4	339.3 ± 102.7	0.33 ± 0.20
MES pH 5.5 (0 h)	610.5 ± 149,4	2832.7 ± 20.4	0.48 ± 0.15
MES pH 5.5 (24 h)	668.2 ± 24.5	2542.3 ± 636	0.62 ± 0.25
MES pH 5.5 (48 h)	924.7 ± 276.4	956 ± 407.4	0.61 ± 0.34
PSF pH 4.5 (0 h)	751.6 ± 69.1	1973.7 ± 1350.6	0.61 ± 0.21
PSF pH 4.5 (24 h)	971.5 ± 246	1007.3 ± 717.7	0.67 ± 0.13
PSF pH 4.5 (48 h)	1074.2 ± 159.4	1110 ± 379.4	0.7 ± 0.07
cDMEM pH 7.4 (h)	194.7 ± 2.5	227.7 ± 22.7	0.31 ± 0.04
cDMEM pH 7.4 (24 h)	157.7± 7.8	182.33 ± 17.5	0.36 ± 0.07
cDMEM pH 7.4 (48 h)	208.5 ± 16.9	324.7 ± 33.2	0.50 ± 0.09
CSMs@A549			

PBS pH 7.4 (0 h)	196.7 ± 0.6	224 ± 6.1	0.12 ± 0.03
PBS pH 7.4 (24 h)	205.7 ± 2.1	212.7 ± 10	0.21 ± 0.04
PBS pH 7.4 (48 h)	207 ± 2.7	229.5 ± 2.1	0.24 ± 0.02
MES pH 6 (0 h)	405.33 ± 87.9	303.7 ± 32	0.44 ± 0.06
MES pH 6 (24 h)	354.3 ± 72.9	246 ± 29.7	0.56 ± 0.1
MES pH 6 (48 h)	326.3 ± 36.2	259 ± 2.8	0.58 ± 0.06
MES pH 5.5 (0 h)	1704.7 ± 182.4	616 ± 394.6	0.86 ± 0.19
MES pH 5.5 (24 h)	1115 ± 100.5	1299 ± 17	0.73 ± 0.01
MES pH 5.5 (48 h)	945.7 ± 37.8	1176.3 ± 363.5	0.8 ± 0.06
PSF pH 4.5 (0 h)	1674.7 ± 225.9	1137.7 ± 903.3	0.84 ± 0.11
PSF pH 4.5 (24 h)	1123 ± 193.8	1992.3 ± 1246.1	0.63 ± 0.2
PSF pH 4.5 (48 h)	829.7 ± 120	3001.7 ± 116.8	0.9 ± 0.05
cDMEM pH 7.4 (0 h)	202 ± 1	348.3 ± 9.3	0.28 ± 0.01
cDMEM pH 7.4 (24 h)	219.5 ± 2.2	255 ± 23.8	0.27 ± 0.01
cDMEM pH 7.4 (48 h)	179.8 ± 8.36	234 ± 122.2	0.36 ± 0.12
CSMs@HEK			
PBS pH 7.4 (0 h)	255 ± 29.5	231.6 ± 3.1	0.32 ± 0.01
PBS pH 7.4 (24 h)	303.3 ± 12.1	243 ± 17.7	0.31 ± 0.05
PBS pH 7.4 (48 h)	311.3 ± 50	229 ± 26.5	0.31 ± 0.25
MES pH 6 (0 h)	244 ± 7.9	273.7 ± 40.45	0.29 ± 0.02
MES pH 6 (24 h)	273.7 ± 40.4	158.7 ± 21.55	1
MES pH 6 (48 h)	158.7 ± 21.6	244 ± 7.9	1
MES pH 5.5 (0 h)	681.3 ± 30.7	1601.3 ± 150	0.79 ± 0.02
MES pH 5.5 (24 h)	1343.7 ± 208.7	592 ± 176-5	0.9 ± 0.09
MES pH 5.5 (48 h)	1582.7 ± 100.3	272 ± 55	0.85 ± 0.08

PSF pH 4.5 (0 h)	981.73 ± 84.2	658.7 ± 70.8	0.65 ± 0.2
PSF pH 4.5 (24 h)	999.3 ± 234.7	1244 ± 438.2	0.71 ± 0.06
PSF pH 4.5 (48 h)	1532.3 ± 336.2	248 ± 144.2	0.97 ± 0.06
cDMEM pH 7.4 (0 h)	189 ± 24.25	382.2 ± 90.4	0.57 ± 0.12
cDMEM pH 7.4 (24 h)	208.7 ± 24.01	153.3 ± 20	0.22 ± 0.17
cDMEM pH 7.4 (48 h)	382.3 ± 90.4	189 ± 24.25	1
CSMs@RAW			
PBS pH 7.4 (0 h)	211 ± 6.6	224.7 ± 3.51	0.16 ± 0.02
PBS pH 7.4 (24 h)	229 ± 5.6	258.3 ± 66.4	0.36 ± 0.03
PBS pH 7.4 (48 h)	216.7 ± 0.6	255 ± 9.54	0.31 ± 0.04
MES pH 6 (0 h)	275 ± 8.2	321 ± 41.5	0.22 ± 0.04
MES pH 6 (24 h)	580 ± 17.7	557.5 ± 0.7	0.3 ± 0.05
MES pH 6 (48 h)	914 ± 73	740 ± 140	0.39 ± 0.1
MES pH 5.5 (0 h)	1965.3 ± 295.5	648.5 ± 63	0.32 ± 0.1
MES pH 5.5 (24 h)	1995 ± 35.5	848.9 ± 440	0.93 ± 0.06
MES pH 5.5 (48 h)	3405.7 ± 324.3	1542.3 ± 122.8	0.93 ± 0.1
PSF pH 4.5 (0 h)	1044.7 ± 88.9	1572.7 ± 246.4	0.42 ± 0.04
PSF pH 4.5 (24 h)	2113 ± 114.6	2747 ± 256	0.82 ± 0.02
PSF pH 4.5 (48 h)	2133.7 ± 1083.8	689.3 ± 268	0.71 ± 0.04
cDMEM pH 7.4 (0 h)	214.3 ± 41.2	214.3 ± 268.1	1
cDMEM pH 7.4 (24 h)	363 ± 55	363 ± 55	1
cDMEM pH 7.4 (48 h)	328 ± 51.5	328 ± 51.5	1

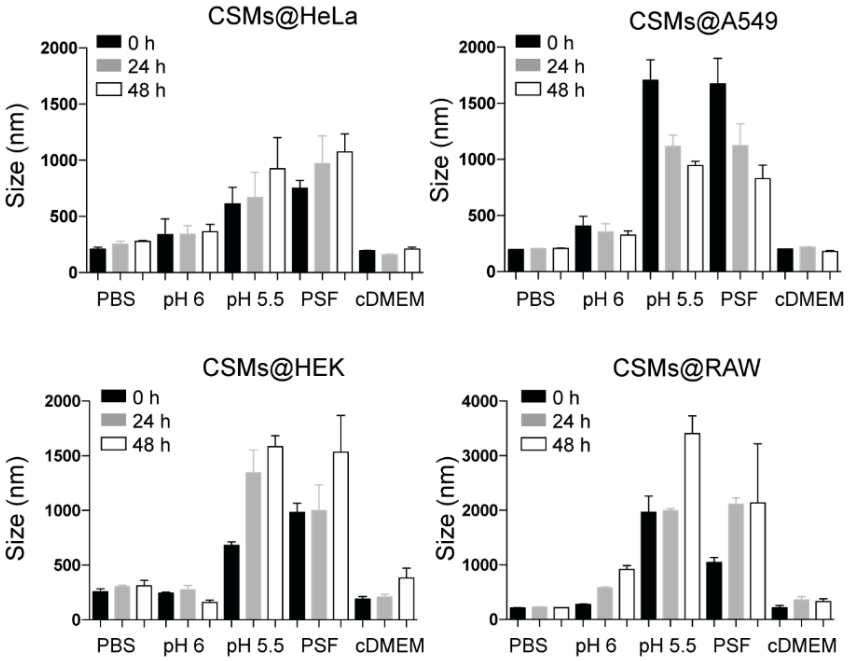

Figure 3.1.5. Hydrodynamic diameter of CSMs@HeLa, CSMs@A549, CSMs@HEK and CSMs@RAW under different conditions (0.1 M of PBS pH 7.4, 0.1 M of MES pH 6, 0.1 M of MES pH 5.5, PSF pH 4.7 and cDMEM pH 7.4). Mean average values from three independent measurements.

Once the colloidal stability was determined, the surface components (lipids, proteins, *etc*.), the right orientation of surface markers (such as specific transmembrane proteins), and the biological activity inherited from the cell source of CSMs were studied. First, the protein content in the sample was quantified by a colorimetric assay. The Bradford assay which is based on the Coomassie dye-binding reaction showed that the total protein content determined in the final CSM sample is directly correlated to the total number of cells used for the CSM preparation (Figure 3.1.7).

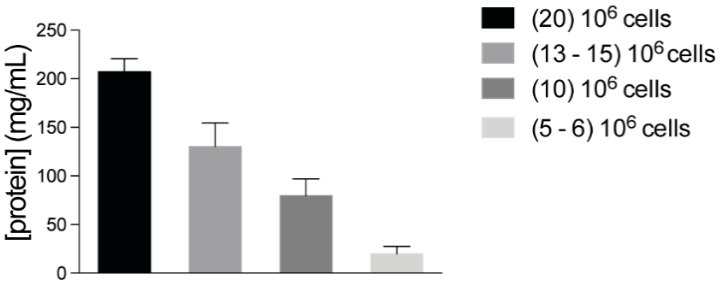

Figure 3.1.6. Protein determination of CSM samples derived from different cell numbers.

The presence of some compounds of the CSM bio-structure such as lipids and proteins, was examined by FC analysis (Figure 3.1.7). CellMask™, a dye commonly used for cell membrane staining, was used to label the lipids on the CSMs and evaluate the lipidic presence by the fluorescence signal. The presence of specific markers such as CD327 (E Cadherin), a transmembrane protein involved in cell adhesion, was studied using a fluorescently labeled antibody, the anti-Cadherin Ab. In both cases, CM and Ab staining, the increase of fluorescence signals demonstrated the presence of lipids and E Cadherin, respectively (Figure 3.1.7a). FSC and SSC signals were recorded to gather information of the CSMs dispersion. The SSC values are similar for all the samples (Figure 3.1.7a and b). However, the mean fluorescence intensity (MFI) increases after the immunostaining (Figure 3.1.7a and b). Since the anti-Cadherin Ab specifically recognizes the extracellular domain of the transmembrane protein, the right-side-out membrane orientation of the bilayer was further verified.

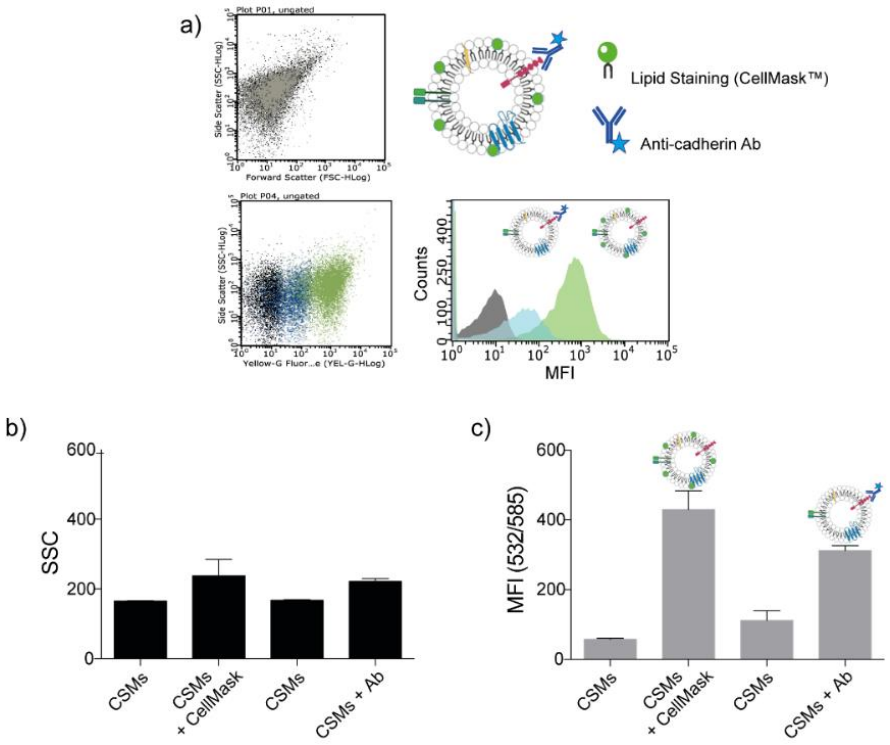

Figure 3.1.7. Bio-characterization of CSMs@HeLa. a) CSM dispersion analysis by FC. The variation of the SSC and the fluorescence signal as a function of the fluorescently labeled CSMs are shown. Scatter density plots of SSC signal versus FSC signal for different CSMs (panel above). Scatter density plots of SSC signal versus fluorescence signal (channel, 512/18 nm) for the CSMs without and with labels (lipid staining in green and immunolabeling in blue) (panel below). Representative histograms of MFI distribution of different CSM samples (CSMs in grey, CSMs + CellMask in green, CSMs + Anti-cadherin in blue). b) SSC signal of the different CSM samples. c) MFI signal of the different CSM samples.

Finally, proteomic analysis was carried out. As first, SDS-PAGE was performed to monitor the protein profiles of HeLa cell lysate and CSMs@HeLa (Figure 3.1.8a). In comparison, electrophoresis bands from protein extracts were similar to the ones observed for CSMs@HeLa, indicating that the protein content of the cell source was maintained in the CSMs over their isolation. MS analysis allowed to identify and quantify the relative abundance of the proteins recovered from the CSMs@HeLa samples, showing that membrane components such as protein receptors (Folate receptor or Transferrin receptor), transporters (amino acid

transporters, Voltage-dependent anion-selective channel protein), or cell surface antigens (CD44, 4F2 cell surface antigen) were retained in the purified CSMs (Table 3.1.5)

The results indicated that the fraction of membrane proteins was enriched from a 12% to a 32% during the preparation of the CSM samples (see Figure 3.1.8b) as we expected.

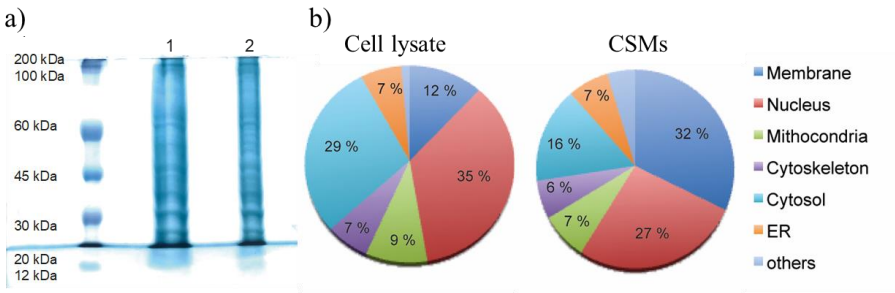

Figure 3.1.8. Proteomics analysis of CSMs. a) 10% SDS-PAGE analysis of the whole cell lysate from HeLa cells and the final CSMs obtained from HeLa cells (lanes 1 and 2, respectively). b) Percentage composition of the CSMs' proteins identified by MS.

Table 3.1.5. Summary of the membrane proteins identified by MS analysis in the sample of CSMs@HeLa.

Name	Name
4F2 cell surface antigen heavy chain	Heat shock protein HSP 90-beta
Alkaline phosphatase tissue nonspecific isozyme	HLA class I histocompatibility antigen, A-68
Alpha-actinin-1	HLA class I hictocompatibility antigen, A-69
Alpha-enolase	HLA class I histocompatibility antigen, B-15
Annexin	HLA class I histocompatibility antigen, Cw-6
Basigin	Integrin beta-1
Brain acid soluble protein 1 (BASP)	Moesin
Catenin beta-1	Neutral amino acid transporter B (0)
CD44 antigen	Ras GTPase-activating-like protein IQGAP1
CD97 antigen	Ras-related protein Rab-11B
Cytoskeleton associated protein 4	Ras-related protein Rap-1b
Desmoplakin	Sodium/potassium-transporting ATPase subunit alpha-1
Elongation factor 1-alpha	Stomatin-like protein 2
Ezrin	Talin-1
Folate receptor alpha	Transferrin receptor protein 1
Glutamate NMDA receptor subunit 3A	Vinculin
Heat shock cognate 71 kDa protein	Voltage-dependent anion-selective channel protein 1
Heat shock protein HSP 90-alpha	

Functionalization with fluorescent phospholipid

All types of CSMs were functionalized with fluorescent phospholipids in order to track them inside the cells for the *in vitro* experiments performed in this study. In particular, DOPE labeled with Atto 488 (DOPE-Atto488) or Atto47N (DOPE-Atto647N) was added to CSMs and it was intercalated inside the bilayer structure by extrusion cycles following the protocol described in section 2.2.1, thus obtaining fluorescently labeled CSMs (CSMs@DOPE).

DLS and NTA analyses of the functionalized CSMs@DOPE showed that the presence of the fluorescent phospholipid did not significantly change the size distribution of the nanostructures (hydrodynamic diameter around 200-300 nm (Table 3.1.6 and Figure 3.1.9), nor their monodispersity (PDI<0.3).

Table 3.1.6. DLS results of measurements of CSMs@HeLa obtained from no labeled CSMs, DOPE-Atto488 labeled CSMs, DOPE-Atto647N labeled CSMs. [1] Mean hydrodynamic diameter derived from the DLS distributions: $d_{H,I}$ and $d_{H,N}$ refer to the mean average hydrodynamic diameter from the intensity and number DLS distributions. PDI refers to polydispersity index. Standard deviation values were calculated from 3 independent measurements.

	Sample	$d_{H,I}$ (nm)[1]	$d_{H,N}$ (nm)[1]	PDI[1]	ζ-potential (mV)
CSMs	No labeled	288 ± 33	234 ± 13	0.26	-24.1 ± 1.0
	DOPE-Atto488	327 ± 7	295 ± 7	0.14	
	DOPE-Atto647N	287 ± 7	219 ± 10	0.25	

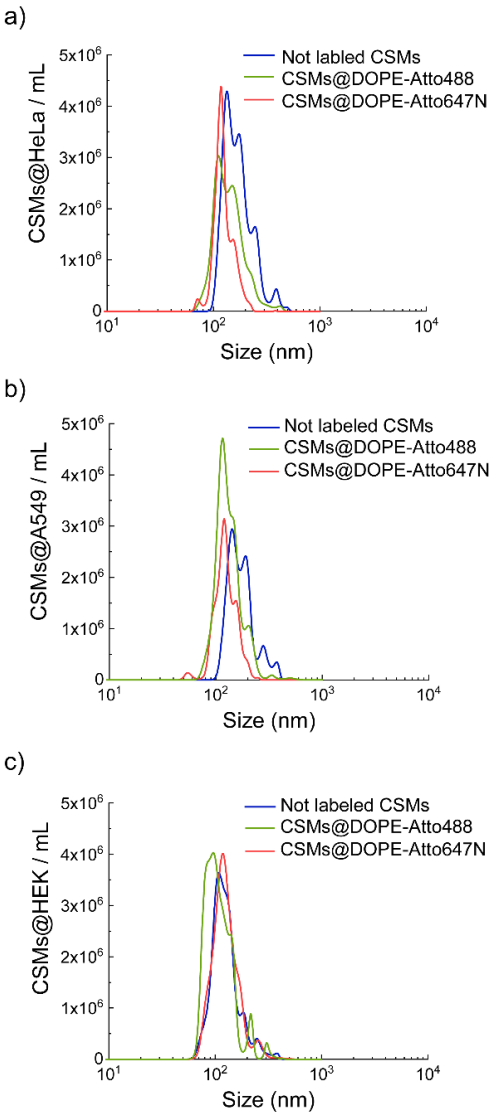

Figure 3.1.9. NTA size distribution of a) CSMs@HeLa, b) CSMs@A549 and c) CSMs@HEK. Representation of the number distribution of the hydrodynamic diameter of individual CSMs.

The intercalation/functionalization was proved by fluorescence measurements and FC analysis, which showed a significant variation of the fluorescence signal of the CSMs@DOPE samples after purification compared to the non-functionalized CSMs (Figure 3.1.10). Because of the high labeling efficiency, the functionalization with the DOPE phospholipid showed to be an excellent staining strategy to label and analyze the CSM behavior in *in vitro* studies and follow their interaction with the cells.

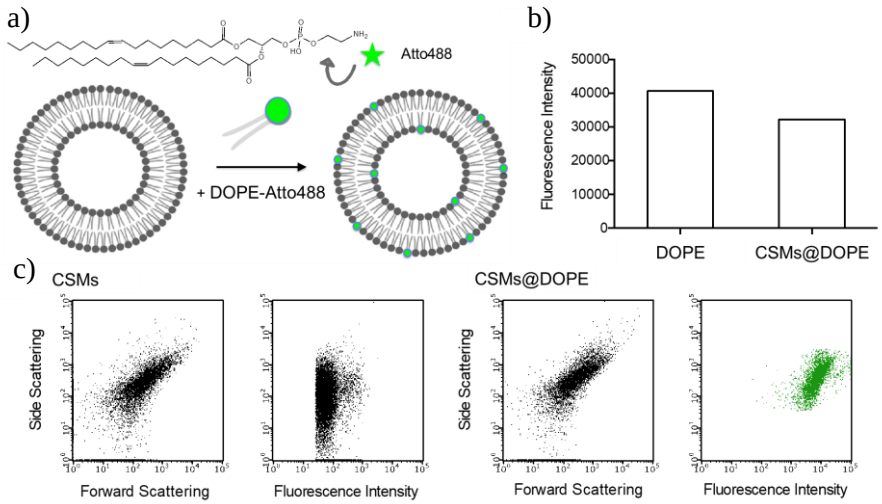

Figure 3.1.10. Characterization of DOPE-Atto488 labeled CSMs@HeLa. a) Scheme representation of CSM labelling by intercalating DOPE-Atto488. b) Fluorescence intensity of the maximum DOPE-Atto488 added and DOPE-Atto488 intercalated in the CSMs@DOPE-Atto48 after dialysis purification. c) FC characterization of CSMs@DOPE-Atto488.

3.1.2. Preferential cancer cell recognition by CSMs

3.1.2.1. CSMs interactions with cells.

The interaction of fluorescently labeled CSMs@HeLa with cells at different doses and different time points were studied by FC and confocal microscopy. FC results of CSMs@DOPE incubation in HeLa cells for different times (1, 3, 6 h and overnight) indicated that the highest internalization levels of CSMs@DOPE occurred after 12 h incubation, when cells showed the maximum level of fluorescence (Figure 3.1.11). However, even shorter time incubations were sufficient to achieve an efficient level of

CSMs@DOPE incorporation. The intracellular signal from labeled CSMs increased with longer incubation times and higher CSMs concentrations. In conclusion, the internalization of the CSMs is time and concentration dependent.

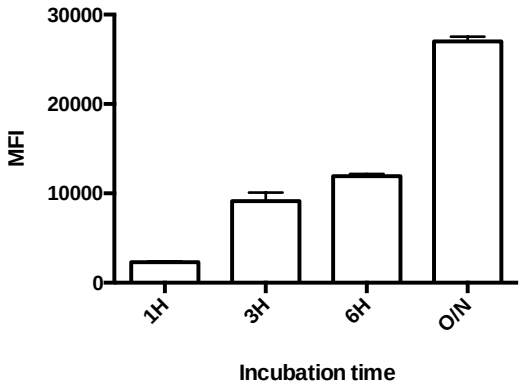

Figure 3.1.11. Preliminary studies of cellular internalization of CSMs@HeLa. Green fluorescence intensity of CSMs@DOPE-Atto48 internalized in HeLa cells and determined by FC. Quantification of the MFI of the cellular uptake of CSMs@DOPE-Atto488 in HeLa cells after 1, 3, 6 h and overnight (O/N) incubations. Data expressed as mean ± s, n=3. Data expressed as mean ± s, n=3.

Confocal microscopy images of internalized CSMs@DOPE in HeLa cells after 3 h and overnight were analyzed. The images confirmed that the intracellular signal from labeled CSMs increases with longer incubation times as the FC results. HeLa cells were also stained with CellMask (Figure 3.1.12). There was no significant colocalization of the cell membrane staining (red channel) with that of the CSMs (green channel). The images confirmed that after 3 h and O/N the CSMs were internalized via endocytosis and the CSMs remained intact inside the cells and accumulated preferentially in endosomes as happened for the majority of nanomaterials. Since the CSMs internalization after 3 h of incubation was efficiently revealed by fluorescence signal, this time point was selected for carrying out the next *in vitro* experiments.

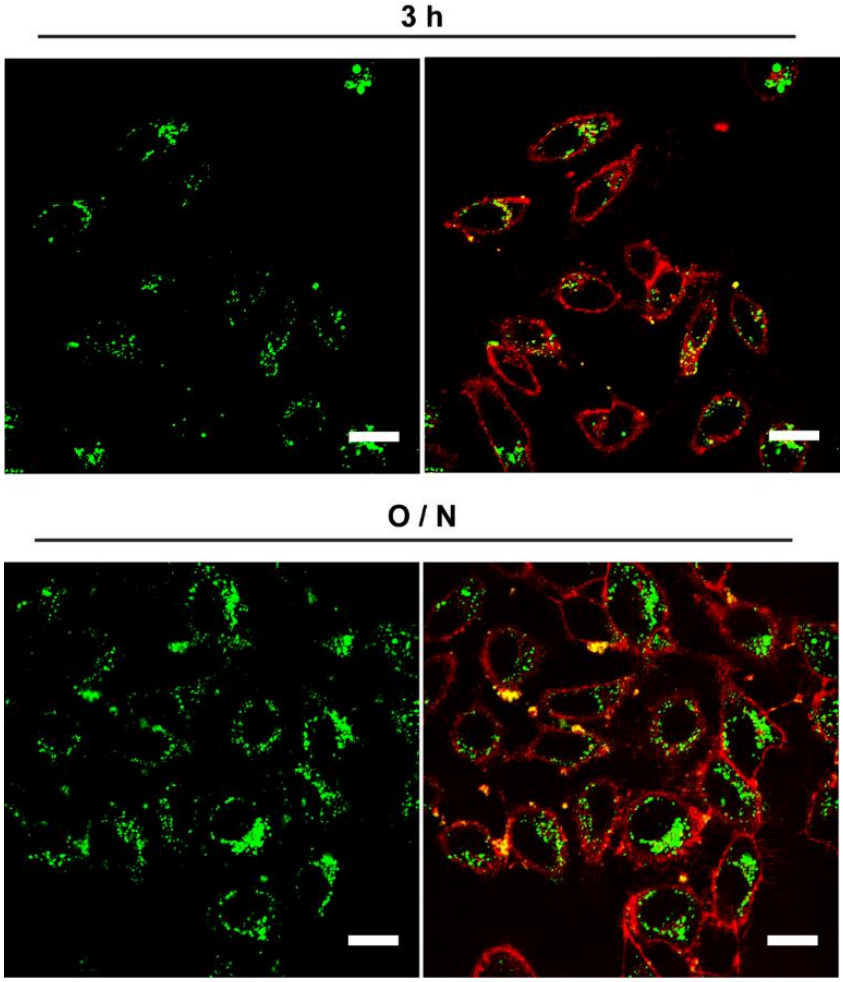

Figure 3.1.12. Confocal images of HeLa cells incubated with CSMs@DOPE-Atto488 (green labeled) for 3 h and overnight incubations. Cell membranes were stained with CellMask Deep Red. Scale bars: 25 μm.

3.1.2.2. Homotypic targeting

Specific targeting of cancer cells represents an important challenge for nanomedicine to promote tumor regression at the same time reducing the side effects of anti-cancer drugs. In this context, homotypic recognition is a new promising targeting strategy that exploits the self-recognition properties of cancer cells. Potentially, biomimetic CSMs system can exploit the

homotypic affinity between cancer cells from which they are extracted, mediated by specific membrane proteins, and it relies on the natural properties of cancer cells to develop strong contacts and adhesive interactions.[135,185,195]

In this section, the self-recognition capability between the CSMs and their source cell line was investigated. Three different cell sources were selected to produce the CSMs: A549 and HeLa cells as tumoral cell lines and HEK cells as model of healthy cell line. The CSMs obtained were equally fluorescently labeled with DOPE-Atto488 in order to assess the uptake in their original cell source by FC analysis. In Figure 3.1.13, internalization profiles of the three different CSMs after 1, 3 and 6 h incubations are reported in HeLa, A549, HEK cell lines and RAW264.7 macrophage-like cell line (RAW). As expected, in all the combinations the HeLa and the A549 cells exhibited higher internalization rates compared with HEK and RAW cells. This difference is justified by the altered cell metabolism provoked by cancer.[196] The CSMs@HeLa were more efficiently internalized by HeLa cells than by the other cell lines at all incubation times, probably due to the homotypic adhesive interactions mediated by the adhesion molecules on the cell membrane.[128] Likewise, this preferential recognition was also found in the case of CSMs@A549, confirming the homotypic affinity between the CSMs and their respectively cell source. Regarding the HEK cell line, as was said above, they showed a reduced internalization rate for all type of CSMs, CSMs@HEK included. Nevertheless, it should be noticed that the CSMs@HEK did not showed a preferential internalization either by the HeLa or A549 cells, exhibiting similar uptake rate in both cell lines. RAW cells showed a low internalization rate for all the CSMs tested, regardless the cell source from which they derived. This fact might be an indicative of the camouflaging ability of CSMs to escape from macrophages uptake.

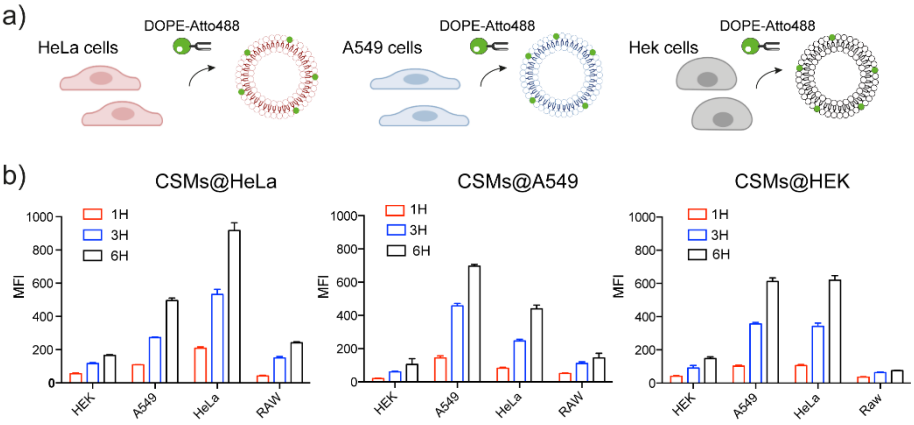

Figure 3.1.13. a) Schematic representation of the CSMs@DOPE-Atto488 derived from HeLa, A549 and HEK cells. b) Internalization profiles of DOPE-Atto488-modified CSMs@HeLa, CSMs@A549 and CSMs@HEK. FC quantification of the cellular uptake of CSMs in HEK, A549, HeLa and RAW cells after 1 h, 3 h and 6 h incubations. MF values (Green fluorescence intensity) of DOPE-Atto488-modified CSMs internalized by cells expressed as mean ± s, n=3.

3.1.2.3. Hybrid CSMs

To further investigate the homotypic affinity of the CSMs, a hybrid nanostructure was prepared by combining cell membrane fragments from two different cell lines. The capacity to introduce additional functionality, in particular the homotypic targeting capabilities described for cancer cell and cancer cell-derived NPs, was studied. The strategy involves transferring the surface properties of cancer cell-derived CSMs to non-tumoral cell-derived NPs. Hybrid CSMs were engineered by mixing cancer cell derived CSMs (CSMs@HeLa) with non-tumoral cell-derived CSMs (CSMs@HEK), previously labeled with two different dyes: CSMs@HeLa with DOPE-Atto488 (green fluorescence) and CSMs@HEK with DOPE-Atto647N (red fluorescence). Then, the samples were mixed at different ratios (1:9, 1:3, 1:1, 3:1 and 9:1) and homogenated together by several extrusion steps, obtaining the hybrid CSMs composed of a green labeled fraction of HeLa membrane and a red labeled fraction of HEK membrane. The size distribution of the hybrid CSMs was studied by NTA analysis (Figure 3.1.14). It showed that the hydrodynamic diameter in maintained around 200-300 nm in all type of hybrid CSMs.

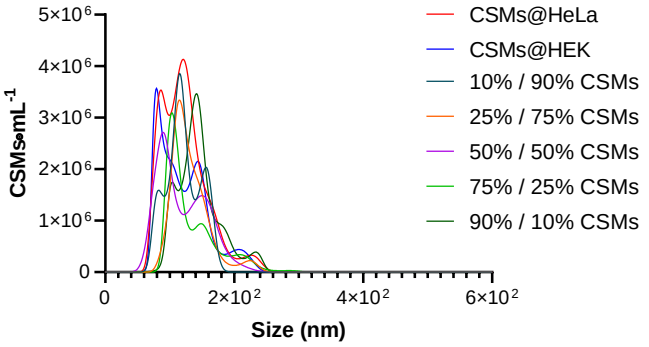

Figure 3.1.14. NTA hydrodynamic size distribution of hybrid CSMs obtained mixing CSMs@HeLa and CSMs@HEK at different percentage composition. Representation of the number distribution of the hydrodynamic diameter of individual hybrid CSMs.

Initially, to determine the stability of hybrid CSMs synthesized (Figure 3.1.15a), confocal microscopy analysis of HeLa cells after CSM internalization were carried out. To define the experiment conditions, the 1:1 hybrid CSMs were used to incubate with HeLa cells. The images in Figure 3.1.15b show the complete colocalization of green and red fluorescence signal after 3 h of CSM incubation with cells. It suggested that at least the majority of the sample was composed by the hybrid CSMs (which are labeled with both green and red fluorescence reporters). Almost any spot of single fluorescence (green or red) is shown in the merged image (last panel, Figure 3.1.15b).

Then, the cancer targeting properties of hybrid CSMs was evaluated by FC analysis. HeLa and HEK cells were incubated with the hybrid CSMs (1:1 ratio) for 3 h and the internalization rate was evaluated by the MFI signal (Figure 3.1.15c). The results from the FC analysis showed similar amount of binding to HeLa cells for the hybrid CSMs than CSMs@HeLa. This indicates that the incorporated surface markers derived from CSMs@HeLa to the hybrid CSMs can enhance their targeting capabilities. In addition, hybrid CSMs show a slightly high amount of binding to HEK cells than CSMs@HeLa. These results confirm that it is possible to fuse CSMs derived from different cells, and they suggest that the hybrid CSMs retain both functionalities derived from the fusion of the two different cell-derived CSMs.

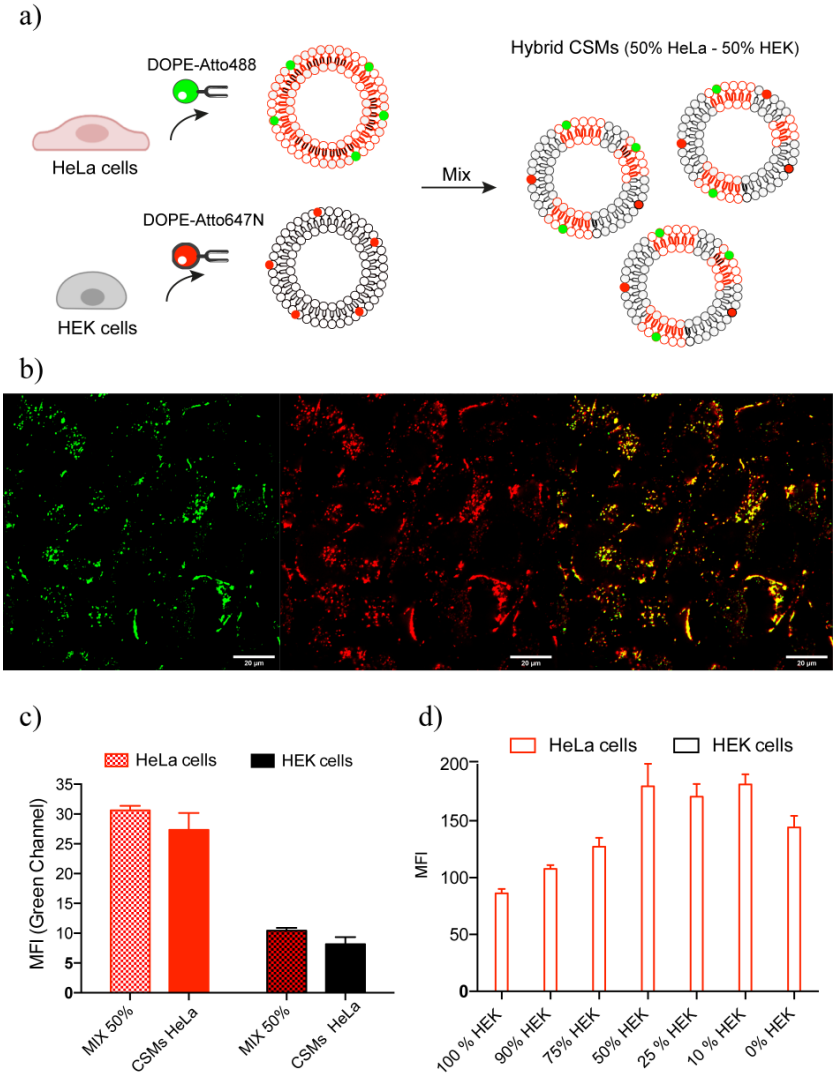

Figure 3.1.15. Synthesis and cellular uptake studies of hybrid CSMs. a) Scheme of hybrid CSMs preparation by mixing the DOPE-Atto488 labeled CSMs@HeLa and DOPE-Atto647 labeled CSMs@HEK. b) Confocal images of HeLa cells incubated with hybrid CSMs for 3 h in green channel (left), red channel (middle) and both channels merged (right). Scale bars: 25 μm. c) Fluorescence signal (by FC, as MFI) from the HeLa and HEK cellular uptake (3 h incubation) of hybrid CSMs and CSMs@HeLa in the green channel. d) Cellular uptake studies of hybrid CSMs mixed at different ratios. Fluorescence signal (by FC, as MFI) from the HeLa cellular uptake (3 h incubation) in the green channel. Data expressed as mean ± s, n=3.

Finally, a comprehensive study by FC was performed. The uptake of hybrid CSMs with different percentages of CSMs@HeLa and CSMs@HEK (1:9, 1:3, 1:1, 3:1 and 9:1 CSMs@HeLa and CSMs@HEK ratio, respectively) was studied. FC analysis was performed with all the types of hybrid CSMs that were incubated in HeLa cells for 3 h (Figure 3.1.15d). The uptake trend showed that the presence of HEK membrane fractions affects the CSMs´ affinity to the cells. In HeLa cells the lowest internalization value corresponded to the higher percentages of HEK membrane fraction (100, 90 and 75 % of HEK). On the other hand, the uptake increased with the prevalence of HeLa membrane fraction (0, 10 and 25 % of HEK), which confirms the higher homotypic affinity of the latter to HeLa cells. The results suggest that a certain amount of HeLa derived membrane fragments is required to introduce the cancer targeting capabilities to CSMs@HEK samples. A ratio of 1:1 (50 %/50 %) is enough to design hybrid CSMs with the maximum affinity for HeLa cells.

Although the mechanisms involved in homotypic recognition are not completely elucidated, their understanding could be an opportunity to develop a new generation of nanovectors, functionalized with a combination of most efficient molecules, in order to improve the targeting efficacy of the nanotherapeutics.

3.1.2.4. Cell transport pathway

Endocytosis is the cell transport pathway by which the cell-derived nanovesicles are internalized by cells.[197] However, studies about the exact mechanism of internalization remain elusive. Due to the nature of these biomimetic systems, the hypothesis that it could occur by the direct fusion of plasma membranes is not to rule out. In fact, there are various examples of cell-derived nanocarriers which inherit the fusion capabilities, such as viruses or exosomes derived nanocarriers.[198,199]

To gain insights into CSMs behaviour when they are in contact with cells, the internalization mechanism was studied in different cell lines. Firstly, confocal microscopy was used to qualitatively investigate the intracellular fate of CSMs@HeLa. Cells were incubated for 3 h with DOPE-Atto488 labeled CSMs@HeLa and, finally, stained with CellMask Deep Red for the cellular membrane and with LysoTracker Blue for the lysosomes (Figure 3.1.16). The confocal images did not show any significant colocalization of the cell membrane staining (red channel) with that of the

CSMs@HeLa (green channel), excluding the possibility that CSMs fuse with the plasmatic membrane. On the other hand, a high degree of colocalization with the lysosomes (blue channel) is showed. This internalization profile suggested that the CSMs are incorporated by the cells following the endocytosis pathway, in agreement with the literature.[200] Moreover, the CSMs' signal appeared punctuated at the perinuclear region, which is a further evidence of endocytosis. It indicates that, after entering inside the cells and passing through early endosomes, the CSMs accumulate in the late endosomes and lysosomes, like other "hard" nanomaterials.

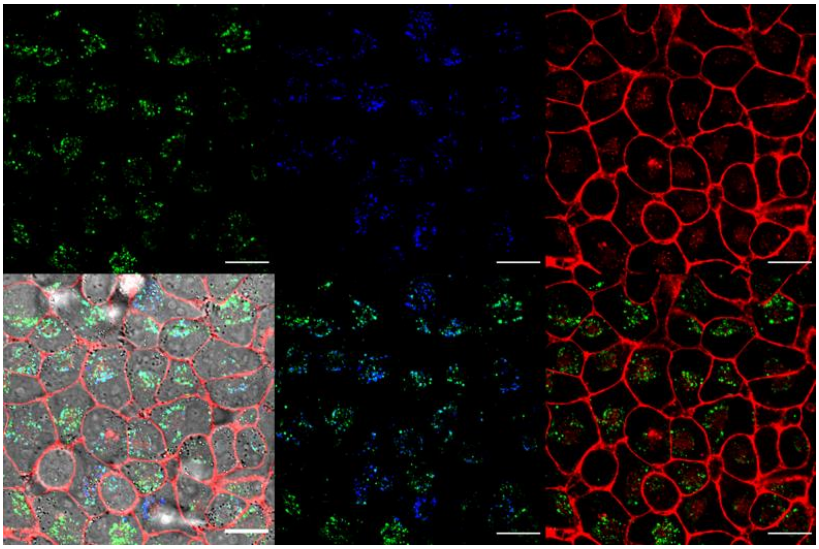

Figure 3.1.16. Confocal images of intracellular delivery of CSMs@DOPE-Atto488 (green labeled) after 3 h incubation with HeLa cells. CellMask Deep Red is used for cell membrane labeling and LysoTracker Blue for lysosomes. Scale bars: 25 μm.

Endocytosis is the process by which cells internalize and transport surface proteins, lipids and other macromolecules enveloped within small membrane vesicles formed by invagination of the plasma membrane into the cell interior. This process is key in the regulation of many essential cellular processes involved in homeostasis and communication, including internalization of transmembrane receptors, uptake of extracellular vesicles, plasma membrane remodeling and cell surface signaling.[201] Endocytosis takes place through several distinct pathways including clathrin-mediated endocytosis (CME), a selective mechanism whereby cell surface proteins containing specific sorting sequences are gathered into membrane

depressions by associating with adaptor proteins that recruit clathrin. CME endosomes pinch off from the cell surface by recruiting the dynamin GTPase to the bud neck. Another dynamin dependent pathway is the fast endophilin-mediated endocytosis (FEME) that is induced upon ligan binging to specific receptors and it is a clathrin independent mechanism. Clathrin-independent endocytosis (CIE) is involved in the internalization of glycolipid-binding toxins, glycosylphosphatidyl inositol-anchored proteins (GPI-AP), and many cell surface proteins (channels, transporters, proteins involved in cell-cell and cell-matrix interactions and in cellular immune function). CIE occurs independently from adaptor proteins and clathrin coats, and mostly does not require dynamin for vesicle scission. It has been shown that the small GTPase Arf6 is associated with the uptake and sorting of many plasma membrane proteins[202] while some lipid-raft associated pathways (called "CLIC/GEEC")[203] are involved in endocytosis of GPI-AP. Rho proteins have been implicated in yet another CIE pathway.[204] It is likely that the Arf6 and CLIC-GEEC pathways are closely related since they both are clathrin- and dynamin-independent, cholesterol-dependent and carry GPI-AP into the cell. Finally, macropinocytosis is a stimulated form of CIE where large pinosomes are brought into the cell interior as a consequence of cellular protrusions in an actin-dependent process (Figure 3.1.17).[205]

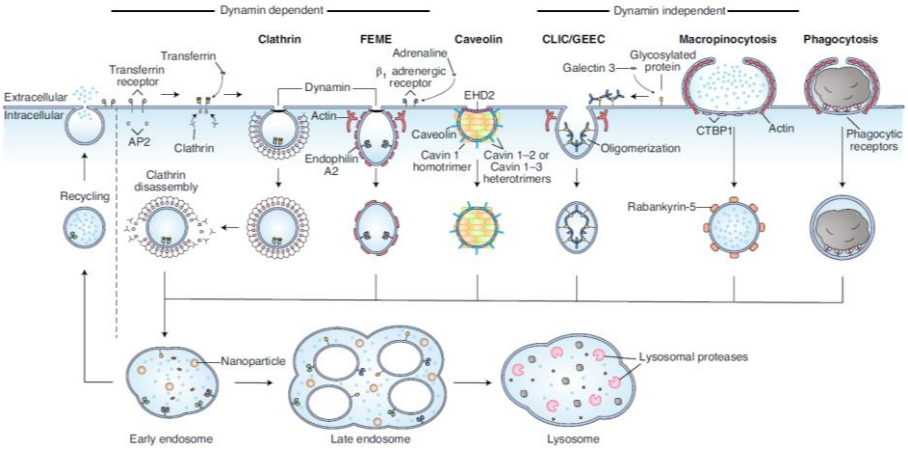

Figure 3.1.17. Overview of the primary endocytic pathway and mechanisms of cell uptake (adapted with permission from ref.[206]. Copyright 2021, Springer Nature Limited).

In this study, the endocytosis mechanism that involves the CSMs internalization was investigated using endocytosis inhibitors for the most

relevant internalizations pathways. In particular, clathrin-mediated endocytosis was evaluated using chlorpromazine (CP), chloroquine (CQ) and dynasor (DYN), while lipid raft-mediated endocytosis was investigated using methyl-β-cyclodextrin (MBC) and nystatin (NYS). CP is known to efficiently inhibit clathrin assembly and disassembly.[207] CQ is a lysosomotropic agent that prevents endosomal acidification and affects the function of clathrin coated- vesicles preventing the fusion of endosomes and lysosomes.[208] DYN is a GTPase inhibitor that rapidly and reversibly inhibits dynamin activity.[209] On the other hand, the MBC removes cholesterol from the plasma membrane inhibiting the lipid raft involved endocytosis.[210] Finally, NYS is a polyene antibiotic that induces a profound distortion of the structure and functions of the cholesterol-rich membrane domains, including aberrations in the caveolar shape,[211] dispersion of GPI-anchored proteins from these structures,[212] as well as the inhibition of lipid raft ligands internalization.[213]

Even though the efficacy of endocytosis inhibitors is clearly cell type dependent, we focused on HeLa and A549 cell lines, both tumorals. By FC analysis, all types of DOPE-Atto488-labeled CSMs (*i.e.*, CSMs@HeLa, CSMs@A549 and CSMs@HEK) showed similar internalization trend in HeLa and A549 cells with no significant difference among the cell line source used to prepare the CSMs (Figure 3.1.18). From these results, it is clear that the CSMs uptake does not follow a specific internalization pathway. All the inhibitor treatments led to a decrease of internalization compared with the CSMs´ uptake of untreated cells, proving that the CSMs uptake follows different endocytic pathways. However, in both cells (A549 and HeLa cells), CSMs internalization is inhibited more efficiently by CP and MBC (% uptake between 20-40 %), which prevent the clathrin-mediated and the lipid rafts-dependent endocytosis mechanisms, respectively. Our results agreed with similar studies about the entry mechanism of membrane coated NPs where it was shown that the CP has higher effectiveness on the cell uptake indicating that membrane coated NPs were internalized primarily by clathrin-dependent endocytosis.[197] Moreover, the inhibition by NYS, DYN and CQ partially reduced the CSMs uptake in HeLa cells (% uptake around 60-80 %) and, more significantly, in A549 cells where 50 % of uptake was shown. It has to be taken into account that NYS, acting on the mobility of the plasma membrane, could also affect the micropinocytosis pathway, which has been seen to be upregulated in A549.[214] This may explain the higher effect of NYS on the uptake inhibition in A549 cells compared to HeLa cells. In addition, in HeLa cells, the NYS, DYN and CQ

inhibition seems to be affected by the type of CSMs used. In these cases, the CSMs@HeLa and CSMs@A549 showed lower uptake % compared with CSMs@HEK indicating that the inhibitors were more effectiveness. On the other hand, this behavior is not observed in the A549 cells.

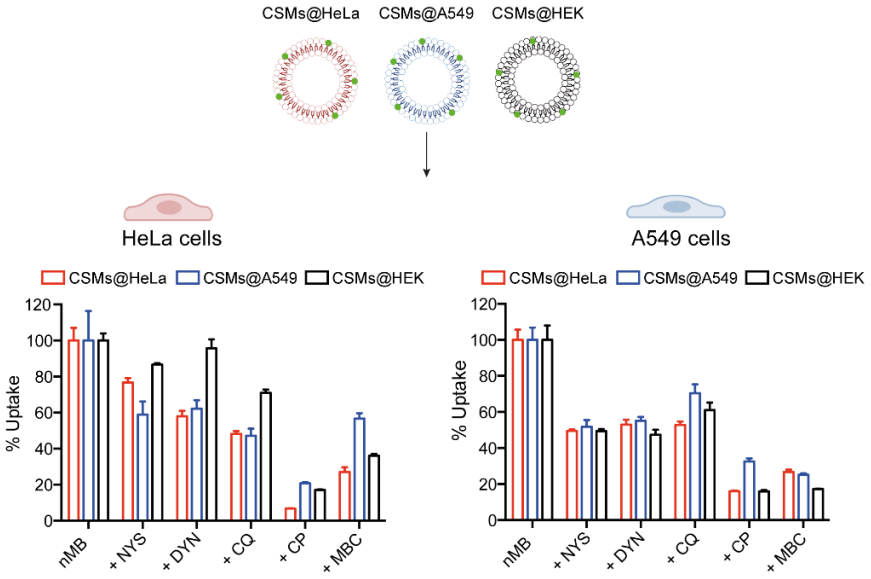

Figure 3.1.18. Effect of endocytosis inhibitors on the internalization of CSMs@HeLa, CSMs@A549 and CSMs@HEK after 3 h incubation in HeLa and A549 cellS. Green fluorescence intensity of DOPE-Atto488 functionalized CSMs internalized by cells was determined by FC end represented as relative uptake (%). Data expressed as mean ± s, n=3.

Further studies will be necessary in order to obtain more insights in the CSMs internalization process. With this purpose, a key point that has to be considered is that not all cells possess the same internalization machinery, and they can show different regulations of uptake pathways. Therefore, understanding the mechanisms of uptake can inform which cells will be likely to internalize NPs that are engineered to target specific pathways. Another important aspect that has to be taken into account is that commonly used inhibitors may have off-target effects on more than one internalization pathway. These aspects reflect the complexity to draw definitive conclusions about the endocytic pathways and it can lead to unexpected results when translating NPs from *in vitro* to *in vivo* studies.[206]

3.1.3. CSMs coating- solid NPs

Combining cell components and solid (organic or inorganic) NPs to create functional nano bio-inorganic assemblies with physical (*e.g.*, inorganic NPs) and biomimetic capabilities has proven outstanding for developing efficient delivery nanovesicles.[129,185,215] CSM coating allows translating the membrane features from specific cell lines to solid NPs. This cell-mimicking strategy helps increase the bloodstream circulating times of NPs, to evade the immune system (decreasing macrophage uptake and avoiding clearance by the organism) and improve the specific targeting of NPs.[136,216]

In order to study the possibility to develop biomimetic systems made of a core-shell structure, solid NPs, in particular rhodamine-labeled polystyrene NPs (rhodamine-labeled PSNP), were coated with CSMs membrane through a fusion process (see section 2.2.4). Using the membrane extrusion method, frequently used in the literature and previously here described,[112,133,135] 200 nm PSNPs were coated with DOPE-Atto488 labeled CSMs@HeLa. In order to maximize the fusion efficiency and the complete surface coverage, repeated passages through the extruder were performed to obtain CSMs@HeLa-coated PSNPs (CSMs@PSNPs).

CSMs@PSNPs were characterized in order to evaluate the biomimetic coating effects on the colloidal properties. NTA analysis showed an increase in size of CSMs@PSNPs (around 191 nm in size, Figure 3.1.19a, orange line) compared to individual solution of plain PSNPs (around 187 nm in size, Figure 3.1.19a, red line) and CSMs@HeLa (around 125 nm in size, Figure 3.1.19a, green line). The dispersion of CSMs@PSNPs was analyzed by FC (Figure 3.1.19b). The dotplot of CSMs@PSNPs dispersion showed no difference in the SSC and FSC distributions comparing with CSM's dispersion (Figure 3.1.19b (ii)). On the other hand, it was shown a population with dual-labeling of green fluorescence signal of DOPE-Atto488 labeled CSMs@HeLa and red fluorescence signal of rhodamine labeled PSNPs, indicating that the coating was achieved (Figure 3.1.19b (iv)).

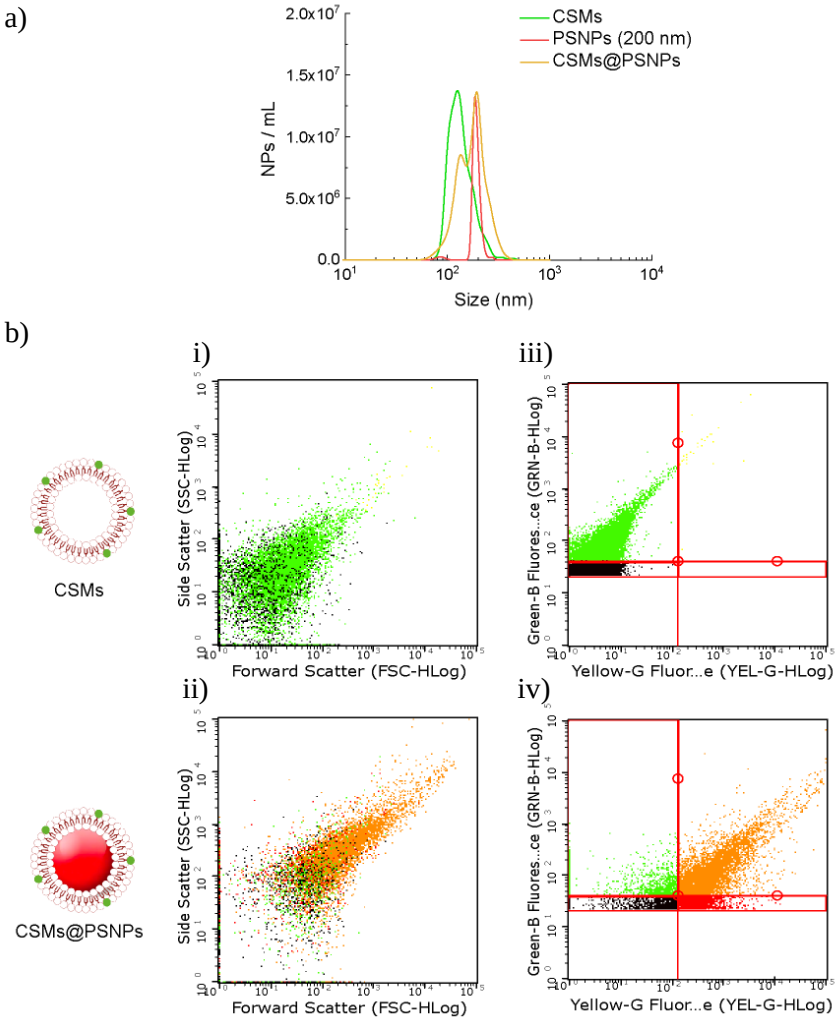

Figure 3.1.19. CSM coated PSNPs characterization. a) Independent NTA measurements of PSNPs (red line, mean 186.9 ± 1.5 nm) CSMs (green line, mean 124.6 ± 2.8 nm) and CSMs coated PSNPs (orange line, mean 191 ± 4.69 nm). b) FC analysis of CSMs and CSMs@PSNPs dispersions. Scatter density plots of SSC signal versus FSC signal for CSMs (i) and CSMs@PSNPs (ii). Scatter density plots of green fluorescence signal (Green-Blue channel, exc./em.: 488/525 nm) versus red fluorescence signal (Yellow-Green channel, exc./em.: 532/583 nm) for CSMs (iii) and CSMs@PSNPs (iv). Data expressed as mean ± s, n=3.

The biointerfacing behaviour of PSNPs and CSMs@PSNPs was investigated (Figure 3.1.20) in HeLa cells, the same cells from which the CSMs were originated, in A549 cells, different tumoral cells, and in RAW macrophage-like cells. Macrophages are major components of the immune system and play a critical role in clearing foreign objects from the circulation.[217,218] Therefore, RAW cells were selected as model to study the camouflaging ability of the CSMs coating to escape the recognition and the subsequential phagocytosis by cells of innate immune system. FC analyses were used to study the internalization trend of (i) CSMs by the mean fluorescence intensity collected in the green channel, as they are DOPE-Atto488 labeled, of (ii) PSNPs by the mean fluorescence intensity collected in the yellow channel, as they are rhodamine labeled, and of (iii) CSMs@PSNPs by the fluorescence of both. Following the uptake by the green fluorescence signal (Figure 3.1.20a), CSM-coated PSNPs showed the same internalization rate of empty CSMs. The results indicated similar rate of PSNPs internalization in both tumoral cells (MFI signal ~100 in HeLa and ~110 in A549 cells); this internalization was even higher in RAW cells (MFI signal ~ 120-130) (Figure 3.1.20b). On the other hand, when PSNPs were covered by HeLa derived CSMs coating, the internalization rate in A549 cells decreased to approximately to the half (up to 60 of MFI signal) while it remains high in the HeLa cells due to the homotypic affinity between the membrane coating and its cell source.

Furthermore, the RAW cells exhibited a strong decrease in internalization rate (13-fold decrease) of PSNPs when they were camouflaged by CSM coating. This confirm the fact that the CSM coating confers to solid NPs the ability to camouflage themselves and to be less recognized by macrophage cells, as it was observed previously for CSMs (Figure 3.1.13). According to similar studies in literature, the camouflaging ability of cell-derived nanovesicles is mainly due to the presence of CD47 integrin on their surface (also known as a *do not eat me* signal) that could suppress the uptake from macrophage cells.[136] The possibility to evade the immune system clearance provides remarkable features to avoids a rapid recognition by the RES and the activation of the immune response, therefore leading to an enhance of the therapeutic efficacy of synthetic NPs.

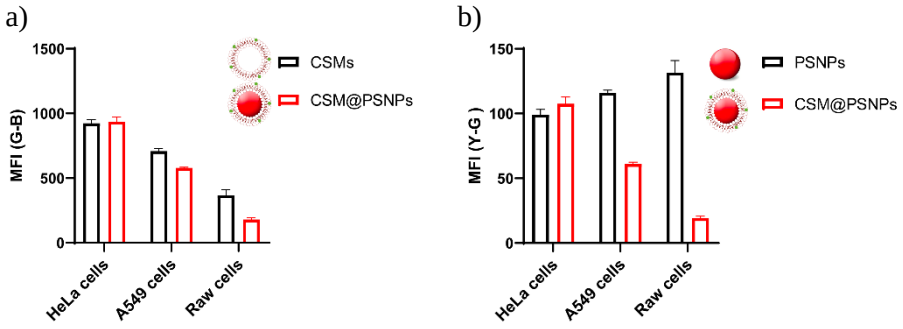

Figure 3.1.20. FC analysis of the internalization trend of CSMs@HeLa, bare PSNPs and CSM@PSNPs. a) MFI in Green-Blue channel (exc./em.: 488/525 nm) related to the fluorescence of CSMs coating previous labeled with DOPE-Atto488. b) MFI in Yellow-Green channel (exc./em.: 532/583 nm) related to the fluorescence of PSNPs (Rhodamine). Data expressed as mean ± s, n=3.

Following the methodology previously described, the cellular uptake mechanism of PSNPs and CSMs@PSNPs was investigated after 3 h incubation by using various endocytosis inhibitors: NYS, DYN, CQ, CP and MBC. As indicated by FC analysis (Figure 3.1.21a), all the inhibitor treatments led to a decrease of internalization of HeLa derived CSMs proving that does not follow a specific internalization pathway in all cell line type, as already seen above (Figure 3.1.18). On the other hand, the inhibition of PSNPs uptake is cell type depending. In fact, the tumoral cell lines, HeLa and A549, did not exhibit a significant inhibition effect with any of the treatments for the times and doses here studied. This result confirmed that the PSNPs might exploit different uptake mechanisms to enter different cell types.[219-221] Whereas macrophages RAW cells showed a decrease of internalization of bare PSNPs, specially upon the CQ and CP treatments indicating the clathrin-dependent endocytosis as preferential uptake pathway. In Figure 3.1.21b, the cellular uptake of CSMs@PSNPs is shown after 3 h incubation and upon the inhibitor treatments. The CSM-coating changed the internalization trend of the NPs comparing with bare PSNPs. In fact, the inhibitor effects on the internalization trend were analogous to the CSMs one, indicating that the coating influenced the interaction with the cells and the following internalization pathways.

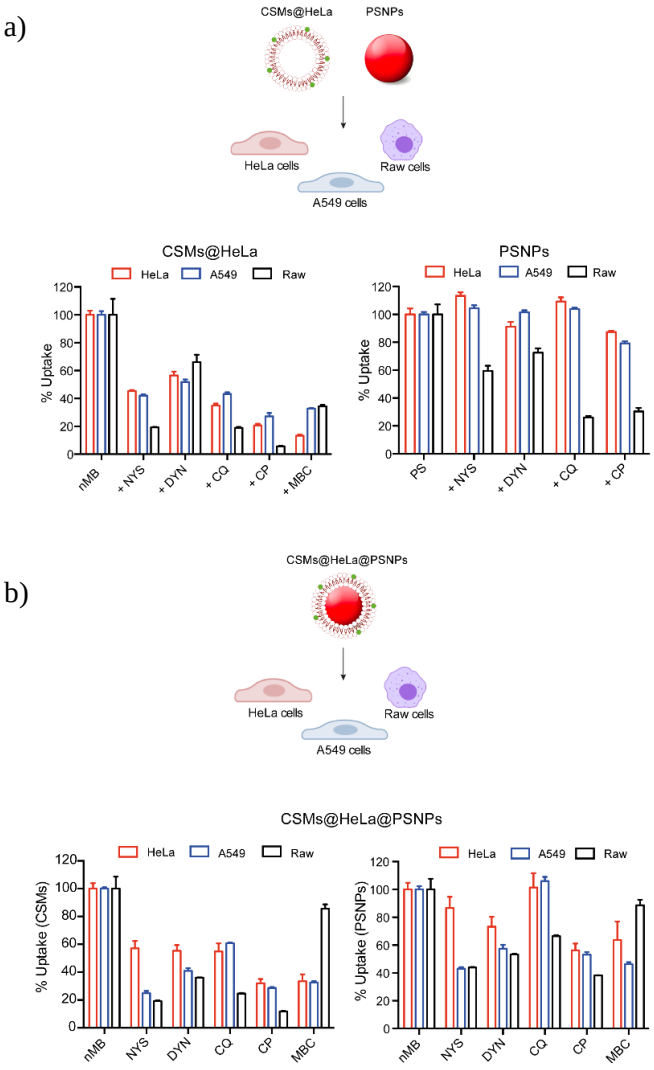

Figure 3.1.21. Effect of endocytosis inhibitors on the internalization of CSMs, PSNPs and CSMs@HeLa@PSNPs. a) Green fluorescence intensity of DOPE-Atto488 functionalized CSMs and red fluorescence intensity of PSNPs internalized by HeLa, A549 and RAW cells was determined by FC end represented as relative uptake (%). b) CSMs@HeLa@PSNPs internalization was represented as relative uptake (%) in both fluorescence channels (Green-Blue channel (exc./em.: 488/525 nm) on the left and Yellow-Green channel (exc./em.: 532/583 nm) on the right). All data are expressed as mean ± s, n=3.

3.1.4. Effects of biomimetic coating on the penetration into 3D cell culture

The current process for testing the effectiveness of nanosystems relies greatly on animal models. However, the animal models that are readily available such as the human tumor xenograft or genetically engineered mouse models are expensive, technically difficult, time-consuming to use and poorly representative of the clinical disease. Additionally, it is more difficult to achieve the resolution needed to see penetration at the cellular and tissue level, and so these models will be less useful for understanding and, inappropriate for mass screening of nanodelivery systems.[222] Beside technical and economic drawbacks, nowadays, the use of animals in research, teaching and testing is an important ethical and political issue, because many of these experiments cause pain to the animals involved or reduce their quality of life. 3D cell cultures could provide an attractive alternative to animal models.

3D cell cultures display a variety of features, which are absent in cell monolayers (2D), such as a complex network of cell-cell contacts and advanced extracellular matrix. They develop pH, oxygen, metabolic and proliferative gradients causing stratification in mature spheroids, which resemble vascular stages of solid tumors[223-226] and micrometastases,[227] mimicking the situation *in vivo*. The spheroid structure is driven by nutrient and signal gradients[223] resulting in an outer zone of proliferating cells, followed by an inner hypoxic area with quiescent cells,[228] which encloses a necrotic core.[229]

Here, 3D spheroids were developed as *in vitro* model to mimic the *in vivo* tumor microenvironment as far as possible. Following the protocol in the section 2.5.2, the 3D spheroids were made with tumoral HeLa cells. The cells were grown in agarose-pretreated plates in order to avoid the cell adhesion to the bottom plate surface. In this way, the cells grow agglomerating one on top of the other rather than forming the typical cell monolayer of the 2D culture.

Three days after cell seeding, confocal microscopy studies were performed to investigate the morphology of the HeLa spheroids. Under followed experimental conditions, the structure self-assembled with a spheroidal shape about 494.5 ± 20.7 µm in size. Cell membranes were stained with CellMask™ Green plasma Membrane stain and multiple images

were captured at different focal depths in order to get a Z stack imaging and a 3D reconstruction (Figure 3.1.22). The interior of the spheroid appears dark, as light scattering drastically reduces the fluorescence signal due to the opacity of the spheroids. This limitation implies that the signal is only detected from the outermost cells of the spheroid.

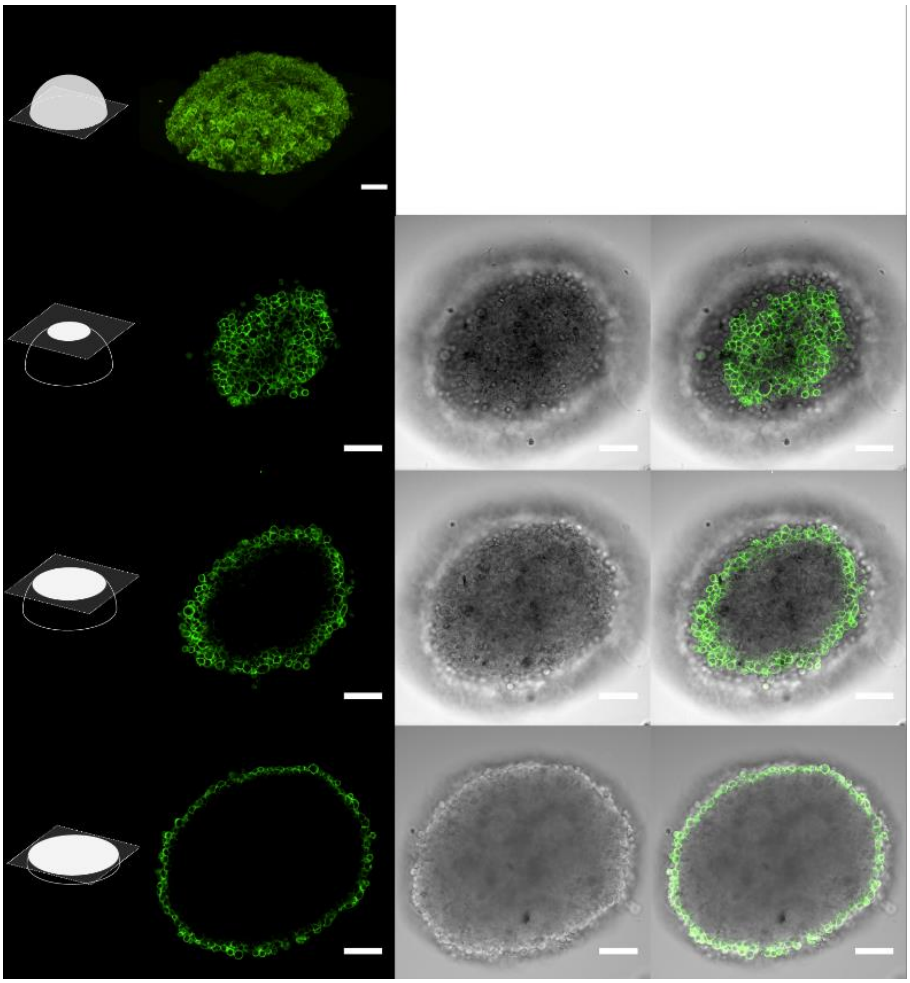

Figure 3.1.22. 3D projection of confocal Z scan of HeLa spheroid three day after cell seeding. The CellMask™ Green plasma membrane was used to label the membrane of the cells. Three individual scans at different depth are shown in green channel, bright field and both channels merged. Scale bars: 100 µm.

The number of seeded cells and the final time point determine the spheroid size achieved, and it controls the spheroid dimensions with low variability among several samples.~ 500 µm size is sufficient to establish physiological gradients for nutrients, oxygen, pH, and catabolites due to limitations in diffusion through the multicellular layers. The effect of these gradients is the establishment of heterogeneous cell populations with necrotic cells in the core and proliferating cells on the spheroid surface.

Cell viability assay was performed in order to evaluate the evolution of the tumor spheroid growth over time. Once the spheroids were made, they were disaggregated after a certain time: day 0 (time 0, 3 days after initial cell seeding), day 1 (24 h time) and day 2 (48 h time). Cell viability was studied by employing a dead/alive cell assay based on two fluorescence cell markers: calcein-AM, which is retained within live cells and produces a strong green fluorescence, and propidium iodide (PI), which binds to DNA of dead and/or necrotic cells, producing red fluorescence signal (see section 2.5.2). In Figure 3.1.23, FC graphs show the population distributions in the quadrant sectioning over the green (exc./em.: 488/525 nm) and red (exc./em.: 532/620 nm) fluorescence channels. Live cells (upper left quadrant) are traceable by a strong green signal but low red signal, while dead cells (lower right quadrant) by lower green signal and strong red signal. By these studies, it was observed that the live cell population % decreased over time from~73% to~60%, while the dead cell population increased from~11% to~13%, accordingly. It is possible that the dead cell % corresponded to the cell population that are located into the inner spheroid area, where they turn into necrotic cells caused to the hypoxic condition and to a less presence of nutrients. However, some studies showed that the cells in the inner part of 10-day-old spheroids are still able to migrate and repopulate after spheroid disaggregation, indicating that the core cells are still viable.[230]

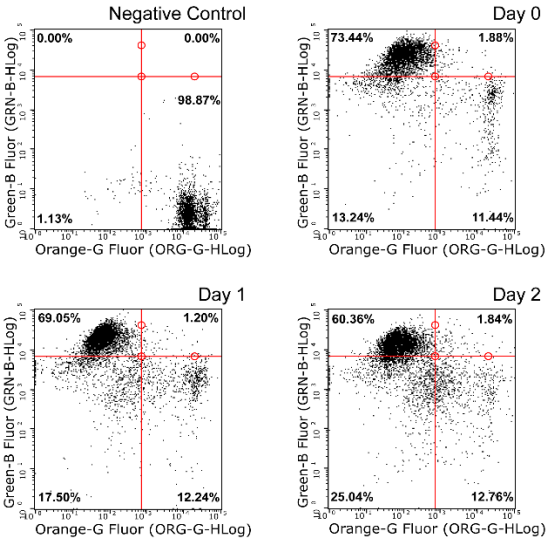

Figure 3.1.23. FC studies of spheroid cell viability by calcein-AM/PI staining. Data are represented by scatter density plots of green fluorescence signal (calcein-AM signal, viable cells, Green-Blue channel) versus red fluorescence (PI signal, non-viable cells, Orange-Green channel). Negative control was treated with triton 1.5 X to lysate the cells.

Then, the penetration and uptake of CSMs was studied in 3D spheroids models. Once the spheroids were made, DOPE-Atto647N labeled CSMs@HeLa were incubated for 30 min, 3 and 24 h. FC analysis showed that the CSMs internalization in 3D spheroids is time-dependent (Figure 3.1.24a), in agreement with the previously shown results in previous results with 2D cell cultures. After a short incubation time, the results showed low level of CSMs internalization indicating the poor spheroid penetration of CSMs probably due to that only the outermost cellular layers of the spheroid are truly exposed to the CSMs dispersion. After 24 hours, the CSMs rate increased, suggesting that longer incubation times allow an enhance interaction between the CSMs and the spheroid, leading to an increase of the CSMs´ their penetration into the inner part of the spheroid. Figure 3.1.24b shows the 3D reconstruction of confocal microscopy Z-scan of a HeLa spheroid incubated during 24 h with CSMs@HeLa. The fluorescence of CSMs (in violet) appeared partly colocalized with the cell membrane (stained in green by CellMask staining) of cells of the spheroid rim. However, the presence of isolated fluorescence signals of the CSMs indicated that, after 24 h incubation, CSMs penetrated the inner spheroid area.

a)

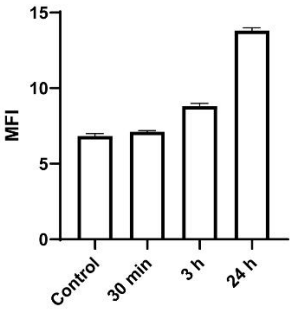

b)

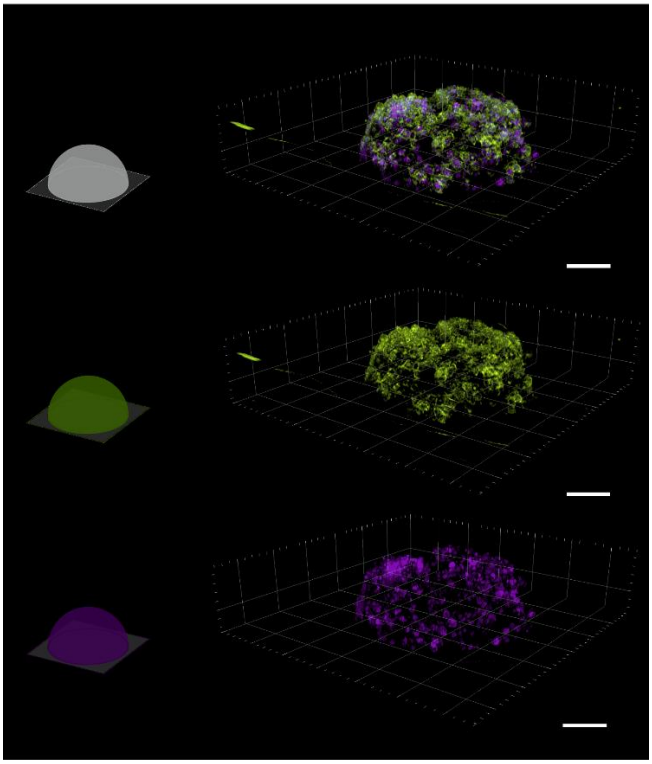

Figure 3.1.24. CSMs internalization in 3D spheroid models. a) FC dotplot of MFI values (red-green channel exc./em.: 532/695 nm) measuring uptake at different time points. The control represented the autofluorescence of no CSMs treated spheroid. All data are expressed as mean ± s, n=3. b) 3D reconstruction of confocal z-images of spheroid incubated with CSMs for 24 h. In green, the fluorescence of the cell membranes labeled by CellMask staining. In Violet, the DOPE-Atto647N labeled CSMs fluorescence. In last panel, both fluorescence merged. Scale bars: 100 µm.

Further investigations were carried out to study the effect of CSMs@HeLa coating on the penetration and uptake of PSNPs in 3D spheroid models. First, the viability of the spheroid cells was verified with calcein-AM, after PSNPs and CSMs 24 h incubations (Figure 3.1.25). FC analysis showed that the % of live cell population stained with calcein-AM was around 55% when the cells were incubated with CSMs, and around 69% when they ware incubated with PSNPs. These results indicated that the cell viability is not impaired neither upon the CSMs treatment nor upon the PSNPs treatment.

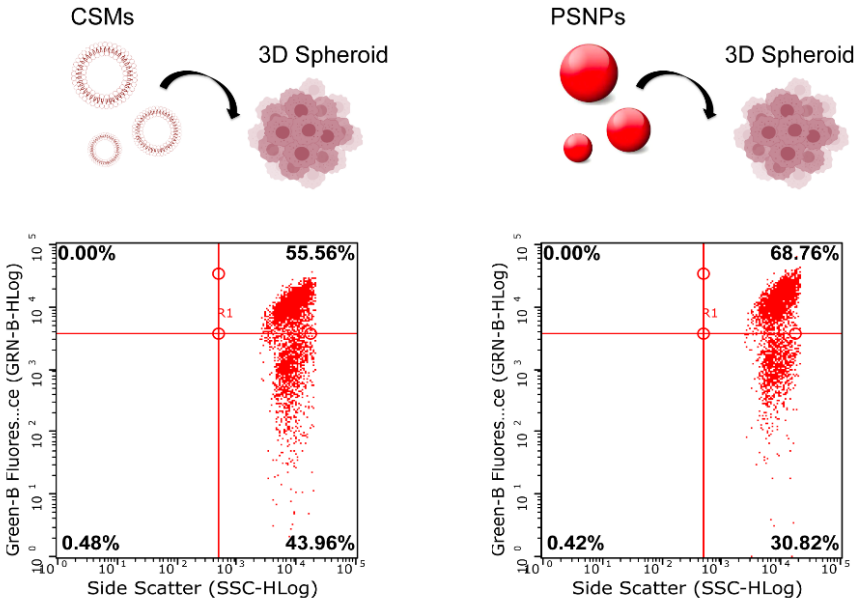

Figure 3.1.25. FC studies of spheroid cell viability by calcein-AM staining after 24 h incubation of CSMs and PSNPs. Data are represented by scatter density plots of green fluorescence signal (calcein-AM signal, viable cells, Green-Blue channel) versus side scatter.

By confocal microscopy, the fluorescence distributions of spheroids treated with CSMs (Figure 3.1.26a), CSMs@PSNPs (Figure 3.1.26b) and bare PSNPs (Figure 3.1.26c) were studied. 3D reconstruction of the spheroid treated with CSM-coated PSNPs showed that the green fluorescence of CSM coating and the red fluorescence of PSNPs is colocalized (observed as yellow in merged image) indicating that the NPs were efficiently coated by

the CSMs and internalized. Moreover, bare PSNPs showed less internalization comparing with the CSM@PSNPs, indicating that the coating significantly improved the interaction of PSNPs with 3D spheroid.

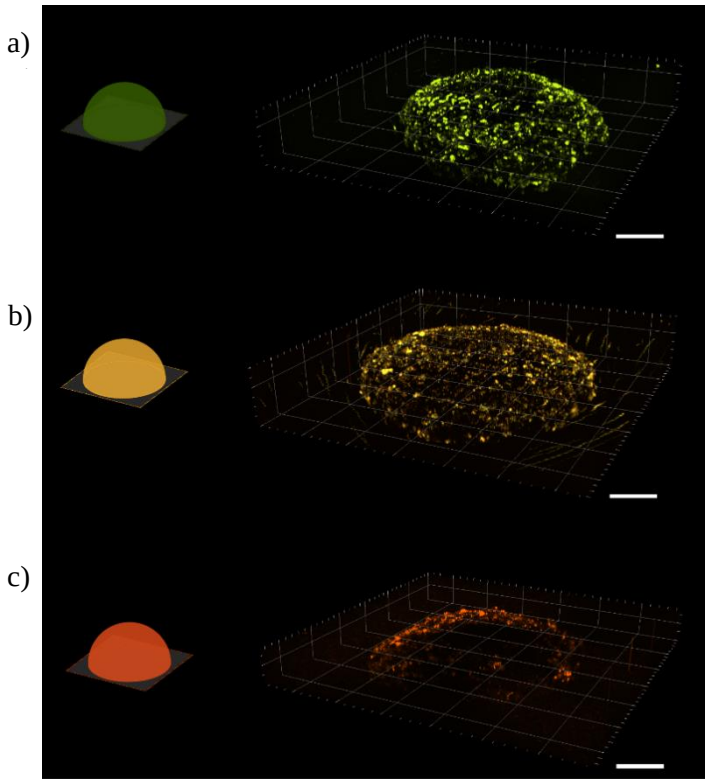

Figure 3.1.26. 3D reconstruction of confocal Z-images of spheroids incubated with a) CSMs, b) CSMs@PSNPs and c) bare PSNPs, for 24 h. In green, the fluorescence of the CSMs (DOPE-Atto488 labeling). In orange, the PSNPs fluorescence (Rhodamine labeling). In yellow, both merged signals derived from the colocalization of CSMs and PSNPs fluorescence of CSMs@PSNPs sample. Scale bars: 100 µm.

The effect of CSM coating on the PSNPs penetration was studied with more detail. With this purpose, confocal microscopy analysis was performed on 3D HeLa spheroids and they were incubated with bare PSNPs and CSM@HeLa@PSNPs, for 1 day (Figure 3.1.27) and 3 days (Figure 3.1.29). The figures report the 3D-recostraction of spheroids incubated with the two samples and three different planes in the z-axis. After 1 day incubation, the CSMs coating did not seem to have had a significant effect on the PSNPs

penetration, as the fluorescence signal appeared limited at the rim of the spheroids in both cases. It is confirmed by the fluorescent intensity plots obtained from the confocal image of one of the z-plane of the spheroids (Figure 3.1.28).

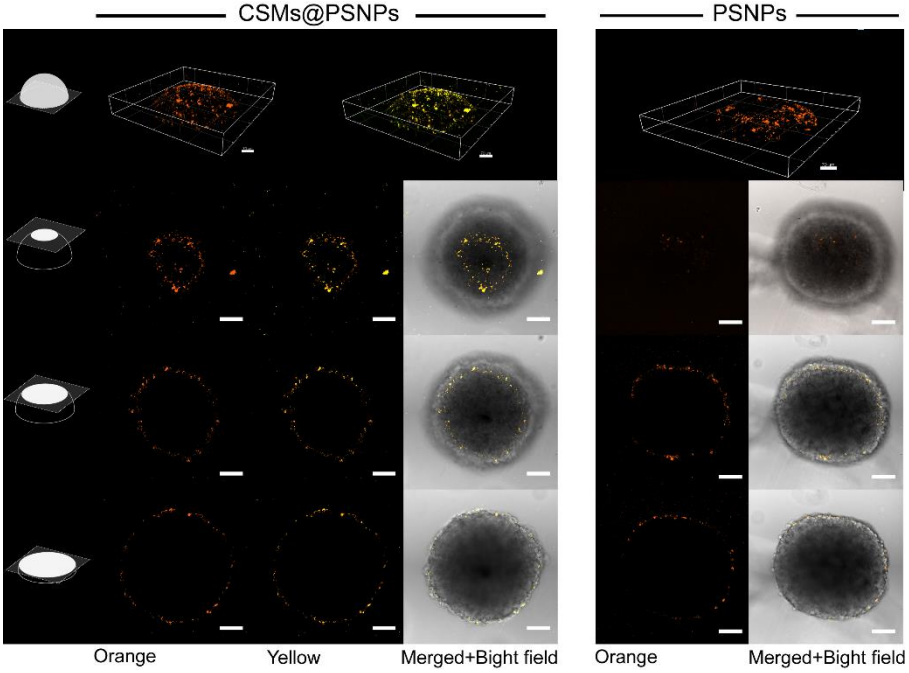

Figure 3.1.27. Set of pictures from a HeLa cell spheroid incubated for 24 h with PSNPs coated with CSMs@DOPE-Atto488, and bare PSNPs. Three individual scans at different depth in the Z-axis are shown. The depth of the plane increases from up to down. Orange: PSNP fluorescence. Yellow: merged PSNPs and CSMs fluorescences. Scale bars: 100 μm.

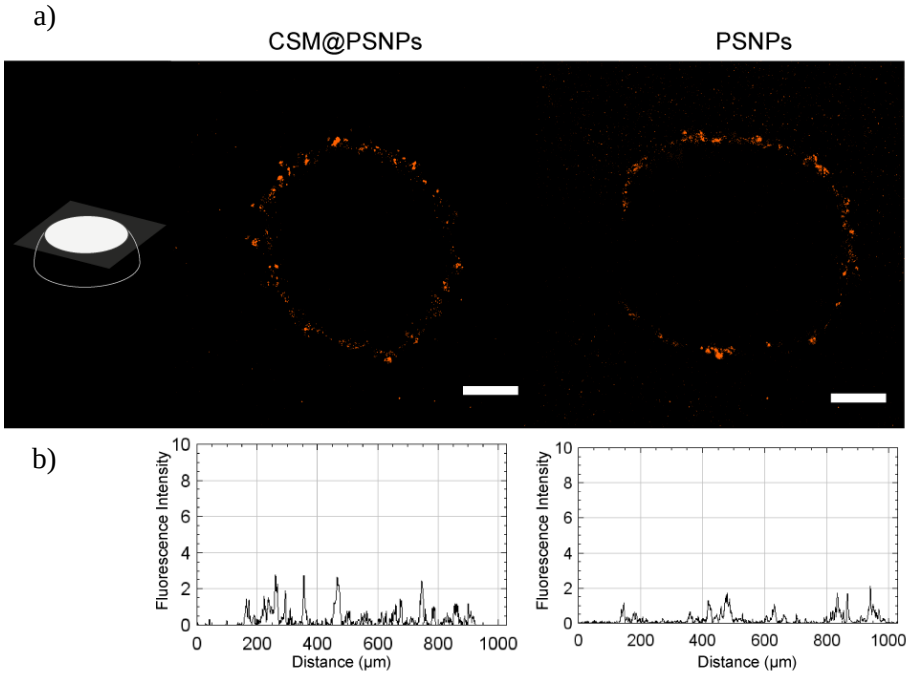

Figure 3.1.28. a) Individual scans of innermost sections of two spheroids incubated with CSMs@PSNPs and bare PSNPs for 24 h. b) The corresponding fluorescence intensity plot derived from the confocal images above. Scale bars: 100 μm.

After 3 days incubation, the fluorescence intensity of bare PSNPs increased in peripheral cells, without appreciable penetration in the central region of spheroid. On the other hand, the spheroid incubated with CSMs@PSNPs showed higher level of accumulation in the inner part of the spheroids, suggesting that the CSMs@PSNPs penetration into 3D models is time-depending. The fluorescence intensity profile of the selected z-sections (Figure 3.1.30b) showed higher intensity peaks of CSMs@PSNPs compared to the bare PSNPs, confirming that the coating improved the penetration into the spheroid core.

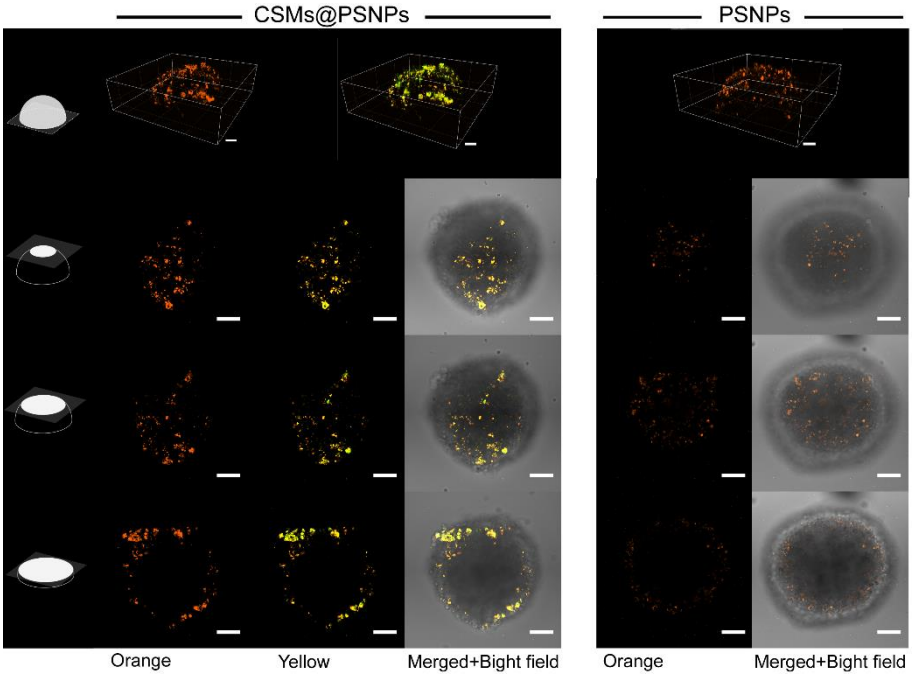

Figure 3.1.29. Set of pictures from a HeLa cell spheroid incubated for 72 h with PSNPs coated with CSMs@DOPE-Atto488, and bare PSNPs. Three individual scans at different depth in the Z-axis are shown. The depth of the plane increases from up to down. Orange: PSNP fluorescence. Yellow: merged PSNPs and CSMs fluorescence. Scale bars: 100 µm.

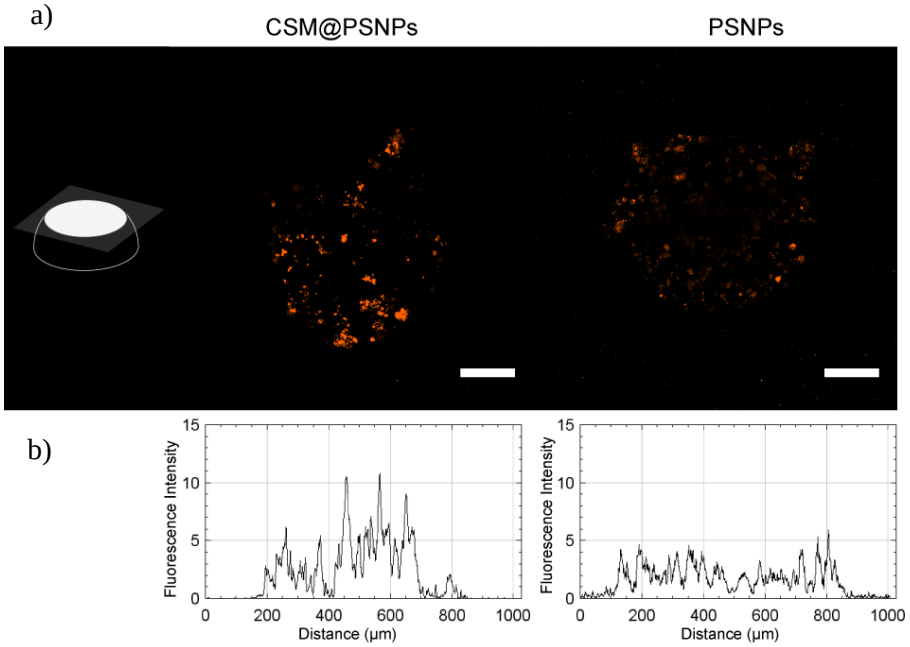

Figure 3.1.30. a) Individual scans of innermost sections of two spheroids incubated with CSMs@PSNPs and bare PSNPs for 72 h. b) The corresponding fluorescence intensity plot derived from the confocal images above. Scale bars: 100 μm.

The efficiency of the NPs to penetrate into target tissue as tumors can significantly reduce the tumor regrowth and augment the therapeutic benefit of the treatment.[231,232] Thus, improving NPs penetration is a powerful strategy for increasing the effectiveness of cancer therapy and CSM coating demonstrated to be a good strategy to enhance it in spheroids.

In conclusion, the 3D culture systems display a variety of feature as *in vitro* model to predict the success of nanoformulations in *in vivo* studies and to designing new formulations for effective drug delivery into tumors. However, one of the challenges of 3D cell culture microscopy is improving imaging in depth. Among some methods, the optical tissue clearing can be useful to overcome some technical limitations. It consists of rendering tissues transparent by reducing refraction index mismatches.[233]

3.2. Plasmonic CSMs for light-controlled cargo release inside living cells

*****The results from this chapter have already been published as Enrica Soprano[a], Aitor Alvarez[a], Beatriz Pelaz[a], Pablo Del Pino[a], Ester Polo[a]. Plasmonic Cell-Derived Nanocomposites for Light-Controlled Cargo Release inside Living Cells. *Advanced biosystems* **2020**, 4 (3), p. 1900260. https://doi.org/10.1002/adbi.201900260

[a] Centro Singular de Investigación en Química Biolóxica e Materiais Moleculares (CiQUS), Universidade de Santiago de Compostela, Santiago de Compostela, Spain.

CSMs are suitable candidates for drug delivery allowing the encapsulation of different molecules or drugs, and the solubilization of hydrophobic payloads. Small molecules such as drugs, fluorophores, carbohydrates, peptides, or large molecules such as antibodies, enzymes, polymers, *etc*. can be encapsulated inside the CSMs.

Based on the studies on their biomimetic properties and their exciting capability to interact with cells, the CSMs proved to be promising candidates for the development a biocompatible DDS. Moreover, implementing thermoplasmonic abilities by incorporation of plasmonic NPs, CSMs offers the opportunity to fabricate beyond state-of-art artificial biomimetic nanocomposites that upon illumination would induce the controlled delivery of cargo in complex, dynamic media such as the cytosol of cells.

With this aim, plasmonic CSMs were synthesized by integrating NIR active GNRs in its structure in order to trigger the controlled cargo release upon the external stimuli of a NIR laser (Figure 3.2.1).

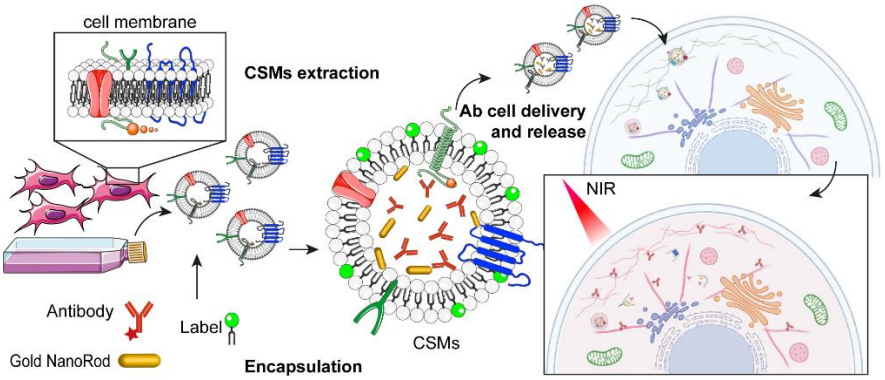

Figure 3.2.1. Schematic representation of GNRs functionalized CSMs and their potential application for NIR triggered intracellular delivery of macromolecules such as antibodies.

3.2.1. Synthesis of plasmonic CSMs

GNRs were selected as light-responsive nanoheating sources owing to their shape-dependent optical features, which leads to the photothermal effect upon NIR illumination. A NIR optical system with a laser source operating at 808 nm was used. To maximize photothermal conversion, low-scattering ultrathin GNRs were synthesized in aqueous solution at ~ 26 °C, in the presence of the cationic surfactant CTAB, using the method described by Sau *et al.*[188] SEM was used to study the GNRs morphology and size distribution (Figure 3.2.2). The aspect ratio (AR) of GNRs resulted about AR = 3.8 (length L_{GNR} = 41.7 ± 5.2 nm and width W_{GNR} = 11.1 ± 1.8 nm).

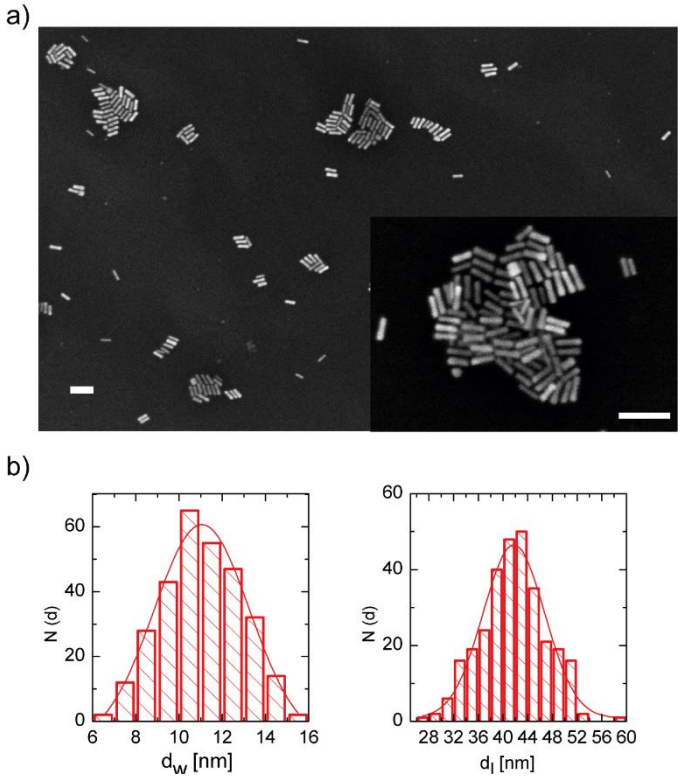

Figure 3.2.2. EM analysis of GNRs. a) Representative SEM micrographs or GNRs (scale bars: 100 nm). b) Representation of the corresponding size-frequency distributions (N = 300) of the GNR length (average d_l = 41.7 ± 5.2 nm) and GNR width (average d_w = 11.1 ± 1.8 nm) as determined from SEM images.

Then, in other to stabilize the GNRs in biological media and made them biocompatible, GNRs were functionalized with PEG linkers. These stealth ligands are commonly used to improve pharmacokinetic properties such as reduction on the non-specific protein adsorption and longer circulation lifetimes.[234] Furthermore, PEGylation can be exploited to modulate the size, the surface charge and hydrophobicity of NPs.[235] In this work, thiolated PEG polymers of 5 kDa weight (HS-PEG5K-NH_2) were used to obtain positively charged PEG grafted GNRs in order to increase the electrostatic interaction with the negatively charged glycocalyx of the cell membrane derived CSMs.

The GNR´s CTAB-coating was exchanged with PEG using a two-step ligand exchange process[235] and the physochemical properties of the resulting

GNRs were studied. The UV–vis absorption spectra showed virtually no differences in the position of the characteristic surface plasmon resonance (SPR) peak centered at 815 nm for the CTAB coated GNRs compared to the SPR peak at 793 nm for the positively charged PEGylated GNRs (Figure 3.2.3).

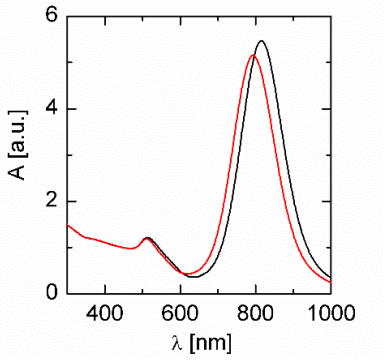

Figure 3.2.3. Optical characterization of the GNRs. UV-Vis absorption spectra of GNR (black) and positively PEGylated-GNR (GNR(+), red). Data were normalized using the absorption value at 450 nm wavelength.

GNR surface charge of CTAB coated GNRs and PEG coated GNRs was evaluated by the change in the ζ-potential value determined by laser Doppler anemometry (Figure 3.2.4). As expected, the HS-PEG-NH_2 grafting resulted in a positive value of the ζ-potential of PEGylated GNRs (26.8 ± 4.8 mV) after the CTAB exchange (40.6 ± 1.1 mV).

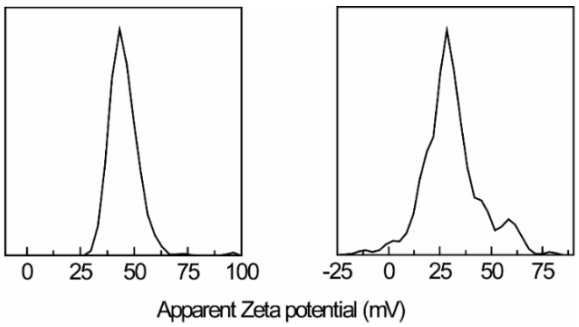

Figure 3.2.4. ζ potential distribution graphs of GNRs. ζ potential distribution graphs of the CTAB coated GNRs (left, value: 40.6 ± 1.1 mV) and PEG coated GNRs (right, value: 26.8 ± 4.8 mV). Data expressed as mean ± s, n=3.

CSMs were produced by the method described in the first chapter,[185,186] and the positively charged PEGylated GNRs and/or cargo (fluorescently labeled molecules, such as Alexa555 BT7R Ab or Alexa545-$PEG_{(4)}$) were introduced into the nanoconstructs by the fusion process. Briefly, HeLa cells were used for the cell membrane fragments extraction, as described in the Materials & Methods, section 2.2.6. The membrane fragments were self-assembled into CSMs by cycles of extrusion through 800 nm pore size polycarbonate membranes. The resulting CSMs were mixed with GNRs and/or the selected cargo and extruded again through the polycarbonate membrane leading to GNR-tagged CSMs (*i.e.*, CSMs@GNR) with or without cargo. After the purification steps (see section 2.3), the CSMs@GNRs@Alexa555 BT7R Ab were characterized with DLS, EM and NTA analyses. The DLS studies showed that, upon the GNRs fusion and the cargo loading, the hydrodynamic diameter (d_H) of the CSMs remained nearly constant at ~230 nm. As a result, cargo loading or GNR-tagging have no significant effect on the hydrodynamic size of the nanosystem (Figure 3.2.5 and Table 3.2.1).

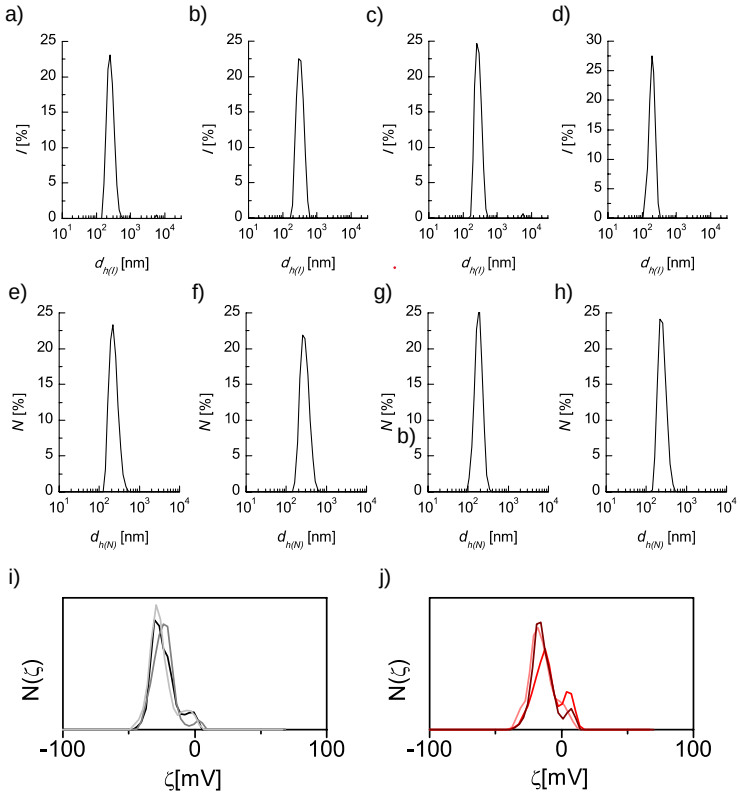

Figure 3.2.5. DLS measurements of CSMs. DLS distributions in number ($D_{H,N}$)), and intensity ($d_{H,I}$) of three independent measurements of different CSM samples: CSMs (a, e), CSMs@Cargo (b, f), CSMs@GNRs (c, g) and CSMs@GNRs@Cargo (d, h), where the cargo is Alexa555 BT7R Ab. ζ potential of the distribution graphs of CSMs (i) and CSMs@GNRs (j). Data expressed as mean ± s, n=3.

Table 3.2.1. Mean hydrodynamic diameter derived from the DLS distributions of CSMs, CSMS@GNRs and CSMs@GNRs@cargo where the cargo is Alexa555 BT7R Ab. [1] $d_{H,I}$ and d_H refer to the mean average hydrodynamic diameter from the intensity and number DLS distributions. PDI refers to polydispersity index. Standard deviation values were calculated from five measurements of the different CSMs samples.

Sample	Sample	$d_{H,I}$ (nm)[1]	$d_{H,N}$ (nm)[1]	PDI[1]	ζ-potential (mV)
CSMs	Without cargo	288 ± 33	234 ± 13	0.26	-24.1 ± 1.0
	Cargo	327 ± 7	295 ± 7	0.14	
CSMs@GNRs	Without cargo	279 ± 36	210 ± 9	0.16	-12.9 ± 2.5
	Cargo	287 ± 7	219 ± 10	0.25	

However, due to the inclusion of the positively charged PEGylated GNRs, the ζ-potential of the CSMs@GNRs system decreased (-15 vs. -25 mV) in comparison to the non-GNRs tagged CSMs (with or without Alexa555 BT7R Ab). NTA showed CSMs size distribution similar to the results obtained from DLS and allowed to define the CSMs concentration (Figure 3.2.6).

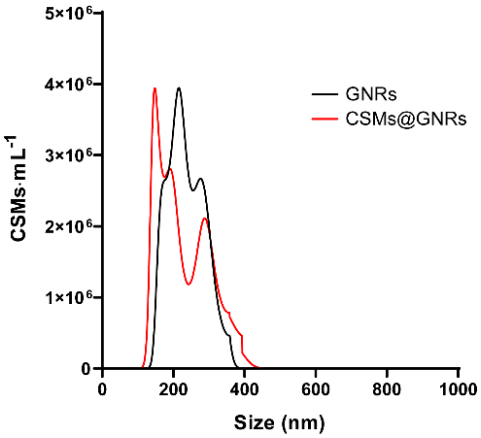

Figure 3.2.6. NTA measurements. Size distribution analysis of CSMs (red line, mean 267 ± 147 nm, $5.7 \cdot 10^8$ CSMs·mL^{-1}) and CSMs@GNRs (black line, mean 331 ± 125 nm, $2.4 \cdot 10^8$ CSMs·mL^{-1}) dispersed in PBS buffer pH 7.4.

EM was used to confirm the morphology of the CSMs and the functionalization with GNRs (Figure 3.2.7), which is also indicated by the plasmonic band centered at ~ 800 nm in the UV-Vis spectrum of the purified CSMs@GNRs structure (Figure 3.2.8).

a)

b)

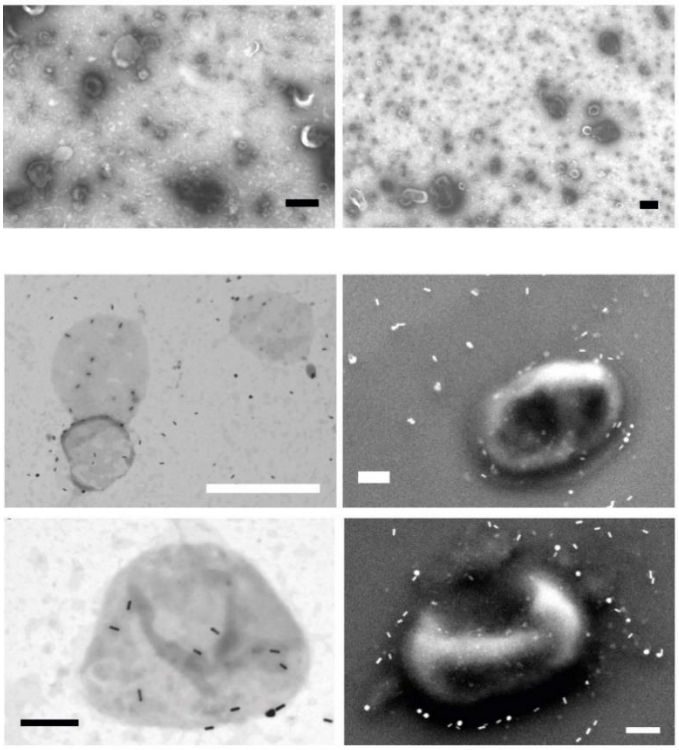

Figure 3.2.7. SEM images of CSMs. a) CSMs STEM images after Uranyl acetate negative staining. b) CSMs@GNRs STEM images. Scale bars: 200 nm.

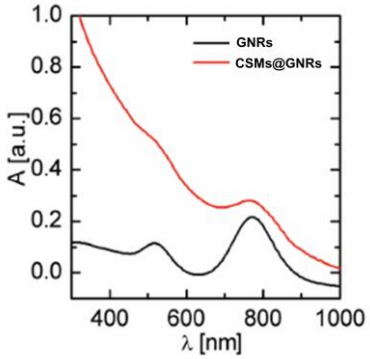

Figure 3.2.8. UV-Vis absorption spectra of CSMs@GNRs and GNRs.

In addition, ICP-MS measurements allowed us to confirm and quantify the amount of GNRs intercalated in the CSMs samples (Table 3.2.2).

Table 3.2.2. ICP-MS analysis of total GNRs added to the CSMs and purified CSMs@GNRs sample.

CSMs@GNRs	g Au·L^{-1}	Mol· L^{-1}	GNRs· L^{-1}	GNRs	CSMs	GNRs·CSM^{-1}
AV	0.0036	$1.48 \cdot 10^{10}$	$8.89 \cdot 10^{13}$	$8.89 \cdot 10^{10}$	$2.40 \cdot 10^{9}$	37.06
SD	0.0013	$5.28 \cdot 10^{11}$	$3.18 \cdot 10^{13}$	$3.18 \cdot 10^{10}$		13.25
GNRs	**g Au·L^{-1}**	**Mol· L^{-1}**	**GNRs· L^{-1}**	**GNRs**		
AV	0.0180	$7.32 \cdot 10^{-10}$	$4.41 \cdot 10^{14}$	$4.41 \cdot 10^{11}$		
SD	0.0040	$1.63 \cdot 10^{-10}$	$9.82 \cdot 10^{13}$	$9.82 \cdot 10^{10}$		

Then, the biological properties of the CSMs functionalized with GNRs were studied. FC was used to evaluate different surface parameters among the different CSM preparations, (Figure 3.2.9); [83] i) the CSM´s size distribution reported by of SSC signal versus FSC signal (Figure 3.2.9 column a, SSC), ii) cargo loading by the corresponding fluorescence signal (Figure 3.2.9 column b, Cargo) where the cargo is Alexa545-$PEG_{(4)}$, iii) the presence of lipids after CellMask staining (Figure 3.2.9 column c, cell membrane), and iv) the presence and correct orientation of some cell adhesion proteins (Figure 3.2.9 column d, protein membrane), using a fluorescence labeled Ab as a reporter for the cadherin-family proteins. The immunolabeling detection of the extracellular domain of the cadherins confirmed a right-side-out membrane orientation on the synthesized CSMs and the GNR-functionalized CSMs.

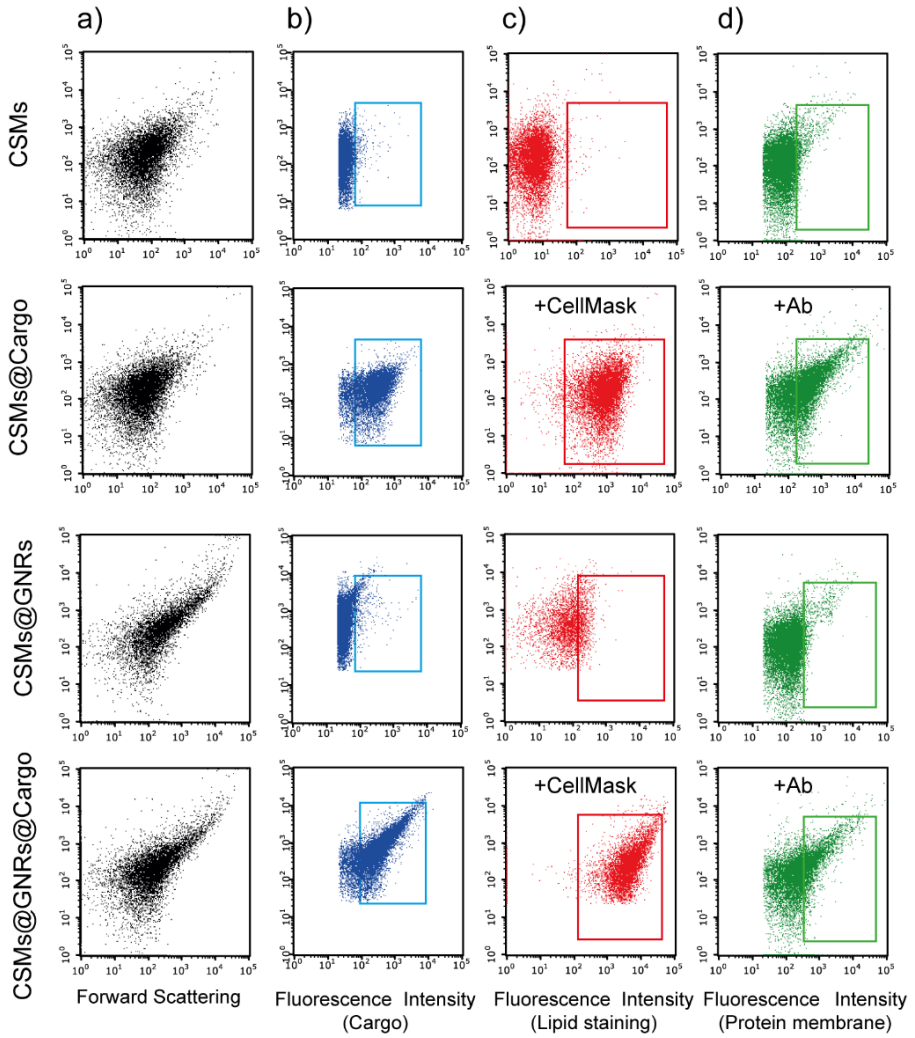

Figure 3.2.9. CSMs dispersion analysis by flow cytometry. The variation of the flow cytometry side scattering signal and the fluorescence signal as a function of the fluorescently labeled CSMs are shown. a) Scatter density plots of SSC signal versus FSC signal for different CSMs (with or without cargo and with or without GNRs), where the cargo is Alexa545-$PEG_{(4)}$. b-d) Scatter density plots of SSC signal versus fluorescence signal (from each corresponding channel: 525/30 nm, 583/26 nm and 695/50 nm) for the CSMs with encapsulated cargo (b, 583/26 nm channel) and with different labels: CellMask Deep Red lipid staining (c, 695/50 nm channel) and Alexa-488-anti-cadherine antibody (d, 525/30 nm)).

Furthermore, the protein content of the purified CSM samples was determined by a colorimetric assay, which showed a similar protein content in all final CSM samples produced from the same number of HeLa cells (Figure 3.2.10), independently of the GNRs incorporation to the CSMs.

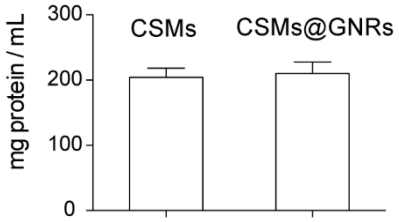

Figure 3.2.10. Protein determination on CSMs and CSMs@GNRs samples by Bradford assay. All data expressed as mean ± s.d., n=3.

The efficiency and robustness of the encapsulation method was studied in detail at pH 7.4, using a fluorescent Alexa545-$PEG_{(4)}$ molecule as a model cargo. The final concentration of the encapsulated cargo was obtained using a calibration curve of the fluorescently labeled cargo (see section 2.4) (Table 3.2.3. The concentration of encapsulated cargo (Alexa545-$PEG_{(4)}$ or Alexa555 BT7R Ab) was calculated by measuring the fluorescence intensity of the CSMs@Cargo samples (calibration curves of Figure 2.4.1 were used for the quantification).Table 3.2.3). The stability of the cargo encapsulated in the CSMs and its release were studied by monitoring the fluorescence signal over time (t_{max} = 72 h) (Figure 3.2.11) using dialysis purification process. The results showed a fast release during the initial hours due to the unspecific adsorption of the cargo onto the CSM surface. After 24 h of dialysis no more free cargo was found in the solution.

Table 3.2.3. The concentration of encapsulated cargo (Alexa545-$PEG_{(4)}$ or Alexa555 BT7R Ab) was calculated by measuring the fluorescence intensity of the CSMs@Cargo samples (calibration curves of Figure 2.4.1 were used for the quantification).

Cargo	Conc. cargo ($g \cdot mL^{-1}$)	Conc. CSMs ($CSM \cdot mL^{-1}$)	Cargo·CSM^{-1}
Alexa545-$PEG_{(4)}$	0.28 ± 0.1	$7 \cdot 10^9$	24353 ± 8777
Alexa555 BT7R	0.15 ± 0.03	$10 \cdot 10^9$	60 ± 22

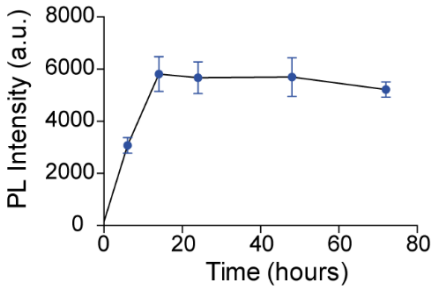

Figure 3.2.11. Stability study over time of the cargo encapsulated on the CSMs at pH 7.4; the leaking of the cargo over time was measured by the fluorescence signal in the buffer solution. All data expressed as mean ± s.d., n=3.

3.2.2. Biomimetic properties

The biomimetic potential of CSMs derived from different type of cell sources such as neutrophils, leukocytes, erythrocytes, *etc*., along with their ability of targeting activated endothelia, resolving inflammation and repairing tissue damage, have been reported before in the literature.[127,135,236,237] Herein, CSMs@HeLa were synthesized, with or without GNRs, which were incubated with two tumoral cell lines, the HeLa (same origin as the CSMs) and the A549 cells, and with HEK cells for 1, 3 or 6 h. The two different types of CSMs (CSMs and CSMs@GNRs) were equivalently labeled with DOPE-Atto488. The uptake of different nanosystems was studied by FC (Figure 3.2.12). The CSMs excess that was not internalized by the cells was removed by three washing steps with PBS. MFI values were normalized by the autofluorescence signal of each cell line, leading to dimensionless fold increase MFI values, which we used to compare cell uptake among the different CSMs and cells. Additionally, as control experiment, we incubated cells with a dose of free DOPE-Atto488 equivalent to the amount labeling the CSMs (equivalent among CSMs and CSMs@GNRs) which, as expected, was more efficiently incorporated by the tumoral cell lines than by the HEK cells, due to the alteration of cancer cell metabolism in comparison to non-tumoral cells.[196]

We should notice that the uptake of free DOPE-Atto488 is higher in A549 than in HeLa cells, at any incubation time (1, 3 or 6 h). The GNRs incorporation has no significant effect on cell uptake of CSMs, at any incubation time or cell type (for derivatization of the CSMs or as internalization target). In contrast, we found that HeLa-derived CSMs, with

or without GNR functionalization, were more efficiently internalized by HeLa cells than in the other cell lines (2-fold and 10-fold MFI than in A549 and HEK cells, respectively), at all the incubation times tested.

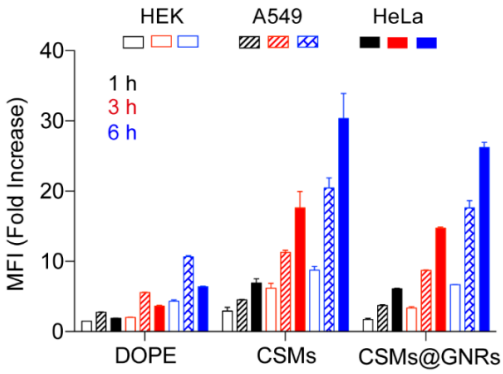

Figure 3.2.12. Quantification of the MFI of the cellular uptake of CSMs@DOPE-Atto488, CSMs@DOPE@GNRs and free DOPE in HEK, A549 and HeLa cells after 1 h, 3 h and 6 h incubations. Green fluorescence intensity of DOPE-Atto488 functionalized CSMs internalized by HeLa cells was determined by FC. Data expressed as mean ± s, n=3.

These results demonstrate that HeLa derived CSMs show a higher affinity to the cell lines from which they are derived (homotypic targeting), which significantly improves the uptake by the homotypic cells.

These results were consistent with those reported in the literature in which homotypic cancer cell membranes have been used to achieve highly specific self-recognition to the source cell line, corroborating that strong cellular internalization levels of cell-derived membrane can be obtained for the same cell line *in vitro*[135] and self-tumor targeting *in vivo*.[185,238] The fact that residual biomolecules from the cancer cell membrane remain at the surface of the CSMs leads to preserve their primary targeting capabilities.[239] Tumor cells readily agglomerate with strong adhesion to constitute solid tumors, which could be caused by adhesive interactions of specific proteins (focal adhesion proteins, integrins, *etc*.) of the cell surface. These specific strong adhesions among homotypic tumor cells may be applied for tumor self-targeting strategy by biomimetic coatings enable of self-recognition.[185,238]

3.2.3. Thermoplasmonic properties

After the preparation and bio-characterization of CSMs, the thermoplasmonic properties of the CSMs@GNRs system, as well as the corresponding quantification of cargo (Alexa545-$PEG_{(4)}$) release induced by NIR photostimulation, were studied with a NIR optical system (see Materials and Methods). For this purpose, solutions of CSMs@GNRs nanostructures in PBS (10^8 CSMs·mL^{-1} concentrated) were irradiated with an 808 nm collimated NIR beam (illumination area ~ 0.33 cm^2, 30 W·cm^2) during different times (0.5 – 4 min). The heating profile is shown in Figure 3.2.13, the temperature of the CSM@GNR solution raised rapidly reaching the maximum at 2 min under laser irradiation (ΔT ~ 50 ºC).

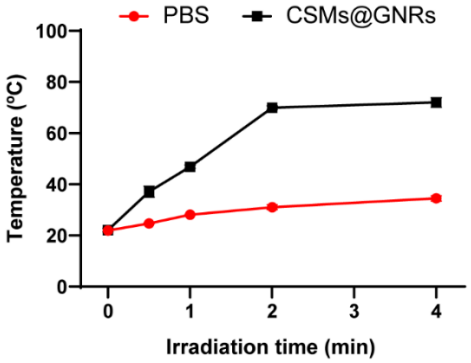

Figure 3.2.13. Temperature curve of PBS and CSMs@GNRs dispersions under NIR laser irradiation of 808 nm at 30 W·cm^{-2}. Data expressed as mean ± s, n=3.

As expected, the temperature of the solution increased above room temperature (~ 23 ºC) with longer irradiation times, which also resulted in an increase of the cargo release. As shown in Figure 3.2.13, the temperature of the CSMs@GNRs solution raised rapidly reaching the maximum between 2 and 4 min under laser irradiation (ΔT ~ 15 – 50 ºC). Indeed, using low (0.5 min) and high (4 min) NIR treatments allows delivering 40% - 75% of the encapsulated cargo, respectively (Figure 3.2.14).

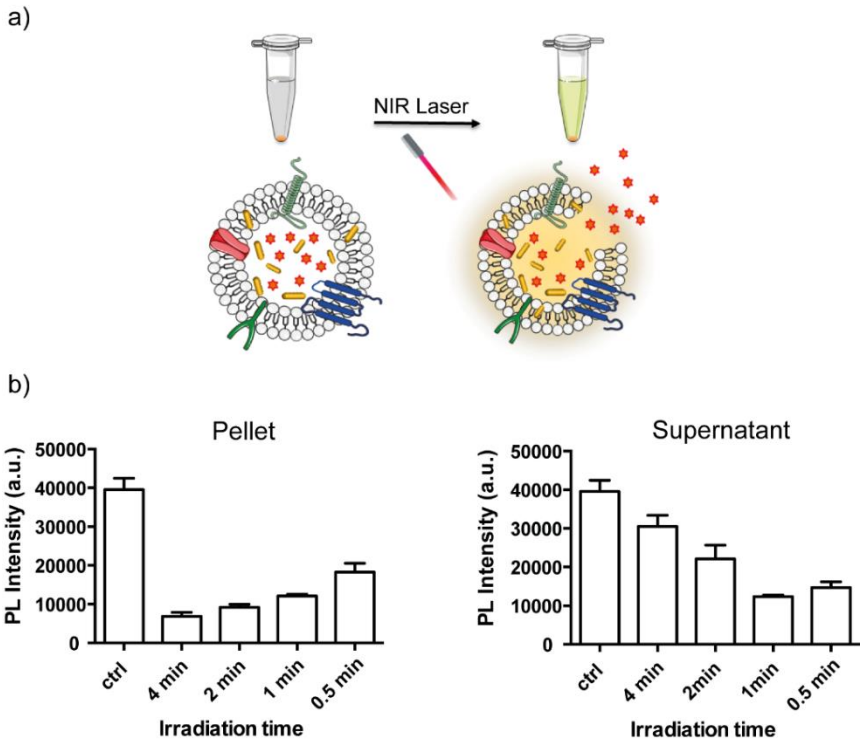

Figure 3.2.14. In tube irradiation of CSMs@GNRs@Alexa545-PEG$_{(4)}$. a) Scheme Upon of NIR laser irradiation, the cargo is released from the CSMs and is measured by the supernatant fluorescence. b) In tube test of release of cargo from CSMs@GNRs after NIR irradiation at 30 W·cm^{-2}; control sample (ctrl) corresponds to the quantification of the cargo encapsulated with no NIR irradiation treatment. Data expressed as mean ± s, n=3.

After the study of the thermoplasmonic properties of the CSMs, the effect of the irradiation treatments on the cell viability was investigated by the resazurin assay (see section 2.6.2). The cell culture was previously supplemented with $8 \cdot 10^2$ CSMs/cell (with and without GNRs) and subsequently irradiated with different power of the NIR laser during different time intervals. As showed in Figure 3.2.15, cell viability was only compromised after 4 min under laser irradiation at power density of 30 W·cm^{-2}. At these specific conditions, the temperature of CSMs@GNRs solution could rapidly go up to 70 ºC; however, cell toxicity assay shows around 50% of cell death.

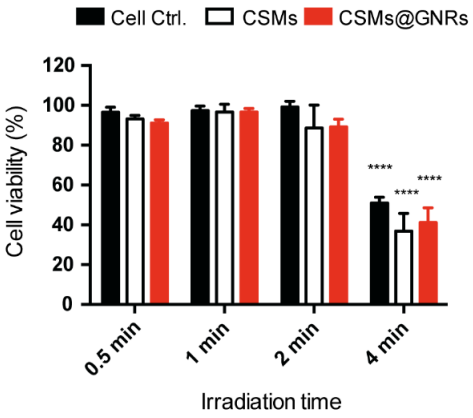

Figure 3.2.15. Viability assay of HeLa cells supplemented with CSMs or CSMs@GNRs after irradiation with a NIR laser at 30 W·cm^{-2}. Data expressed as mean ± s.d., n=3.

This result emphasized the importance of modulating the CSMs@GNRs dose and the NIR photostimulation in order to find a compromise between cargo release and cell viability, which can be achieved by adjusting the irradiation time and the power intensity of the NIR laser.[240] In fact, according to the results obtained, the controlled photothermal effect of CSMs@GNRs under NIR irradiation could be used to release ~ 60% of the encapsulated cargo (under the irradiation at 30 W·cm^{-2} during a maximum of 2 min), while the integrity of the cells is maintained.

3.2.4. Photoinduced cargo release inside cytosol

Once the thermoplasmonic properties of the nanocomposites were assessed, next step was to exploit them to achieve the cargo release inside the living cells. To this aim, a NIR laser pointer with a diameter of ~ 5 μm was used to excite DOPE-Atto488-labeled CSMs@GNRs inside living cells to induce cargo release on a single cell level (Figure 3.2.16). This micrometric irradiation set-up was achieved by coupling a NIR laser through the optical path of confocal microscope as in optical tweezers (see Materials and Methods, section 2.6), which is equivalent to other NIR setups used for analogous experiments.[76-78] Although the highly focused NIR spots have an extremely high power densities (~ 10^4 W·cm^{-2}) they are harmless to single cells, and have been previously used to deliver macromolecules encapsulated in micrometric layer-by-layer capsules into living cells[78] and more complex organisms such as *Hydra vulgaris*, a fresh-water polyp.[76]

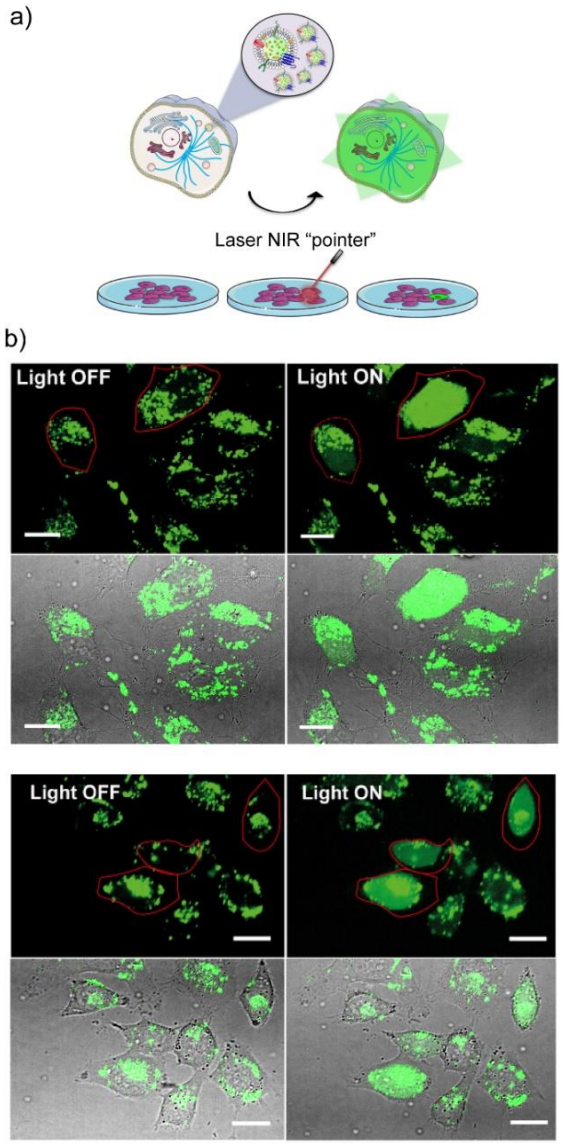

Figure 3.2.16. a) Schematic representation of *in vitro* photo-triggered release of DOPE-Atto488 functionalized CSMs@GNRs mediated by NIR laser "pointer" with diameter ~ 5 μm. b) Confocal images of single cells before (Light OFF) and after (Light ON) irradiation. Irradiated cell shape is outlined by a red solid line. Scale bars: 25 μm.

Highlighted cells were selected for the irradiation during ~5 s (see red outlines in Figure 3.2.16, light OFF), inducing to the staining of the whole cell (Figure 3.2.16, light ON), while the non-irradiated cells remained unaltered. These experiments showed that upon the focused NIR irradiation, the presence of GNRs in the CSMs promote the photothermal effect and, due to the thermal disruption, the DOPE-Atto488 used for labeling the nanocomposites could be rapidly distributed throughout the cell, thereby allowing for endosomal escape.

The next challenge was to achieve the cargo release upon the irradiation of a higher area of cell culture (0.33 cm^2 corresponding to ~10^4 cells), that is the simultaneous irradiation of thousands of cells. Following the single cell experiments, we performed similar experiments dealing with DOPE-Atto488 uncaging using a low power density NIR setup (1 - 30 $W \cdot cm^{-2}$). Different irradiation doses were tested, ranging from 30 s to 2 min irradiation to study and select the correct irradiation time, sufficient to achieve release without inducing cell death. The images showed that in all treatment times tested (1 min and 2 min at 32 $W \cdot cm^{-2}$, and 5 min at 16 $W \cdot cm^{-2}$), DOPE-Atto488 release was achieved (Figure 3.2.17).

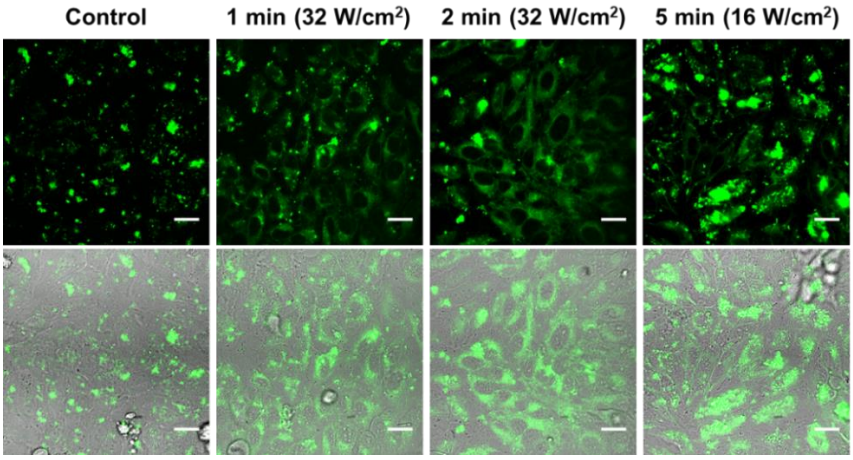

Figure 3.2.17. Confocal images of HeLa cells incubated with CSMs@GNRs@DOPE-Atto488 after NIR laser irradiation at different experimental conditions (irradiation time and power). Scale bars: 25 μm.

Taking in account the previous cell viability studies (Figure 3.2.15) after 2 min irradiation, cell viability was slightly compromised (~80 - 90%), the

irradiation experiment set-up conditions were fixed at 30 W·cm^2 for 1 min. Thus, CSMs@GNRs@DOPE-Atto488 preloaded cells were irradiated with collimated NIR beam. The treatment was able to promote the DOPE-Atto488 uncaging into the cytosol as demonstrated by confocal images in Figure 3.2.18.

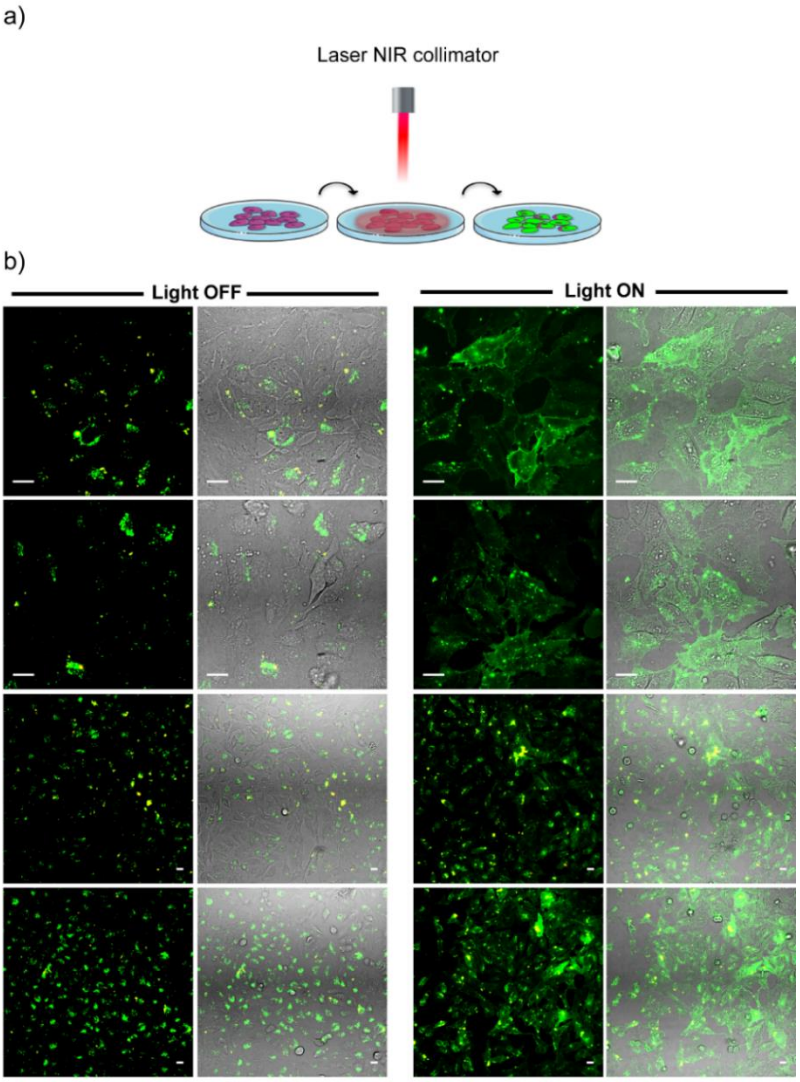

Figure 3.2.18. *In vitro* photo-triggered release of CSMs@GNRs@DOPE-Atto488 in large areas of cell culture by using a NIR collimated beam of 0.33 cm^2. Scale bars: 25 μm.

Analogous experiments were performed as control samples using DOPE-Atto488 functionalized CSMs without GNRs. No DOPE-Atto488 release was observed neither immediately after the NIR irradiation nor 5 h later (Figure 3.2.19), confirming the specific NIR triggered cargo release form the CSMs@GNRs after internalization by HeLa cells.

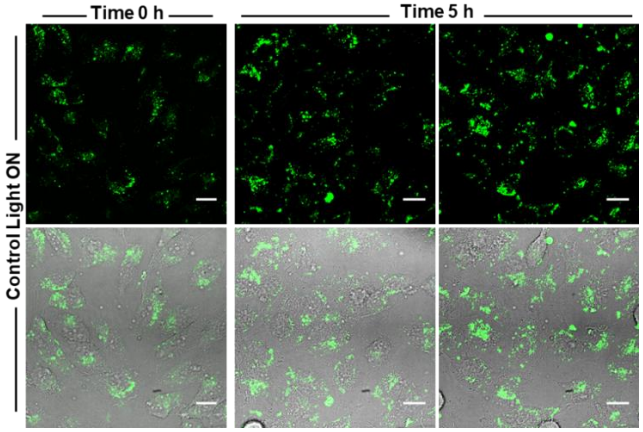

Figure 3.2.19. *In vitro* experiments of photo-triggered release of CSMs@DOPE-Atto488 without GNRs with NIR collimated beam of 0.33 cm^2. Confocal images of HeLa cells were analyzed after laser irradiation and 5 h after the laser irradiation. Scale bars: 25 μm.

Although the detailed molecular mechanisms of the cargo delivery from the biomimetic CSMs inside the cells are not fully addressed here, these results confirm that the photothermal effect caused by GNRs under NIR laser irradiation can compromise the CSMs structure integrity. As it has been previously reported[78,80,144,238] the local heat generated can also affect the membranes of the surrounding compartments and release the cargo to the cytosol of the cell.

3.2.5. Photoinduced antibody release inside cytosol

As a proof of concept, the plasmonic CSMs were tested to deliver non-cell-permeant molecules inside the cytosol of living cells. Monoclonal Ab based-therapies have shown a great potential due to their low immunogenicity and target specificity. However, low circulating times and limited intracellular delivery are still some of the main drawbacks that drive the research to developing new Ab intracellular delivery strategies (such as cell penetrating peptides, virus-like carriers, lipid-based particles, and organic or inorganic

NPs).[241,242] CSMs may provide a suitable alternative for efficient Ab cytosolic delivery.[243] Homotypic targeting of specific cells, effective internalization, and cytosolic delivery of the cargo can lead to successful applications of Abs involving targeting of intracellular proteins. In this thesis work, the Alexa555 BT7R Ab was selected to be encapsulated inside the CSMs@GNR system (Table 3.2.3). Alexa555 BT7R Ab is typically used to stain the cytoskeletal protein, tubulin, allowing to visualize microtubules in permeabilized and fixed cells but it is not able to cross the cellular membrane and reach the intracellular compartment. As shown in Figure 3.2.20, cells incubated with free Alexa555 BT7R Ab (a) did not internalize the molecule. For this reason, the immunostaining requires the cell membrane permeabilization to allow the delivery of the Ab to the cell cytosol.

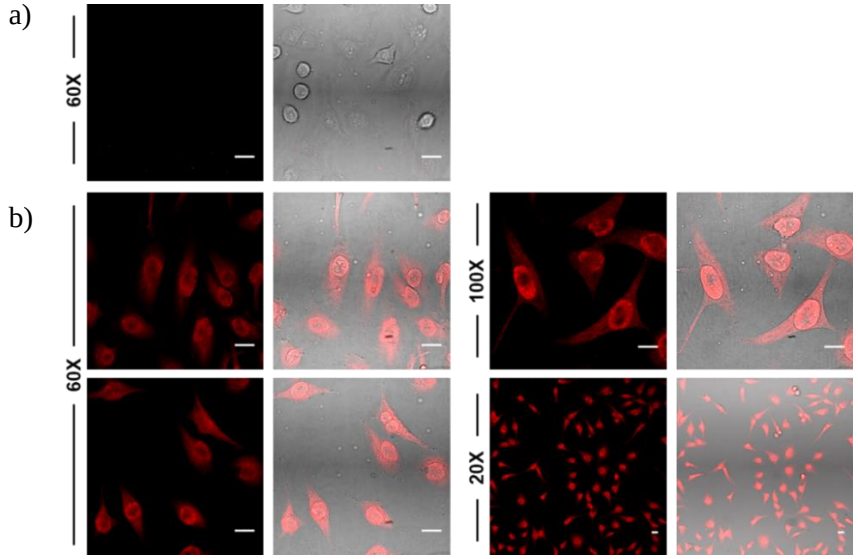

Figure 3.2.20. Control experiments for Alexa555 BT7R Ab release in HeLa cells. a) Negative control: HeLa cells incubated with Ab without cell permeabilization. b) Positive controls: Ab internalization in HeLa cells after cell permeabilization and fixation. Scale bars: 25 μm.

Using the plasmonic CSMs, the permeabilization step is not required because the CSMs vehicle system is exploited to deliver the Ab inside the intracellular compartment. As shown by confocal images in Figure 3.2.22 and Figure 3.2.22 (Light OFF), after 3 h incubation the CSMs@GNRs@Ab were efficiently internalized in HeLa cells and the colocalization between

the DOPE-Atto488 functionalized CSMs and the encapsulated Ab was seen (yellow spots in panels OFF). After 1 min NIR excitation at 30 $W \cdot cm^{-2}$ (panels ON), the Ab fluorescence signal is spread across the irradiated cells due to the release into the cytosol (endolysosomal escape), promoting the microtubule staining.

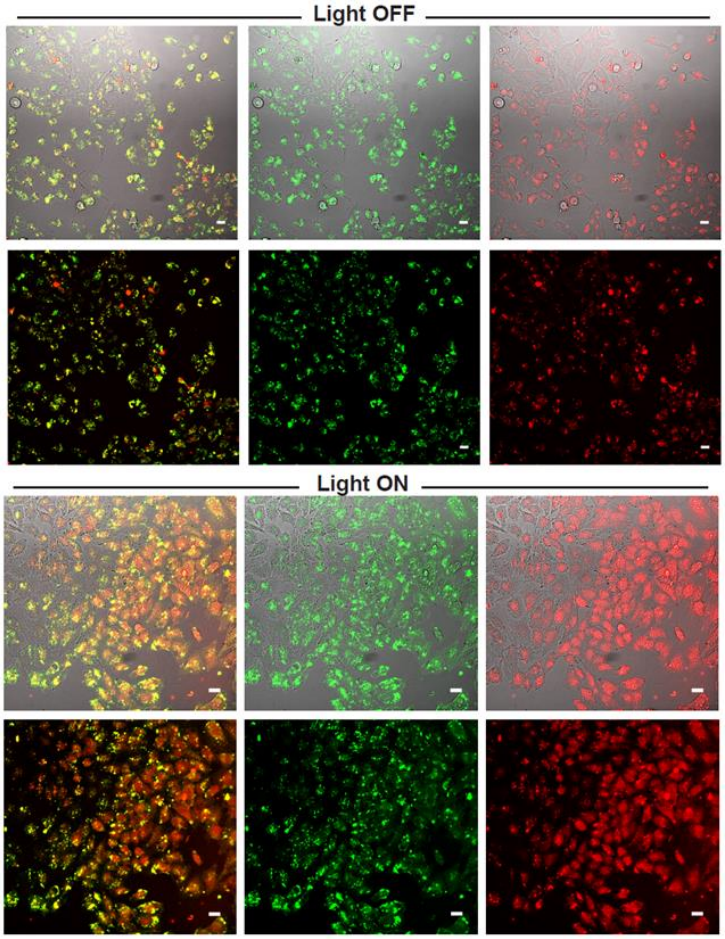

Figure 3.2.21. Confocal microscopy images of *in vitro* Ab delivery inside cytosol of HeLa cells by NIR laser triggered released from CSMs@GNRs (20X objective). The green color indicates the fluorescence signal from the DOPE-Atto488 functionalized CSMs and the red color indicates the fluorescence signal from the Alexa555 BT7R Ab encapsulated inside the CSMs. Fluorescence images of HeLa cells after 3 h incubation with CSMs@GNRs@Ab shows the CSMs internalization inside the cells (light OFF). After 1 min of NIR laser illumination at 30 $W \cdot cm^{-2}$, the red fluorescence signal is observed in the cytosol of the cell (light ON). Scale bars: 25 μm.

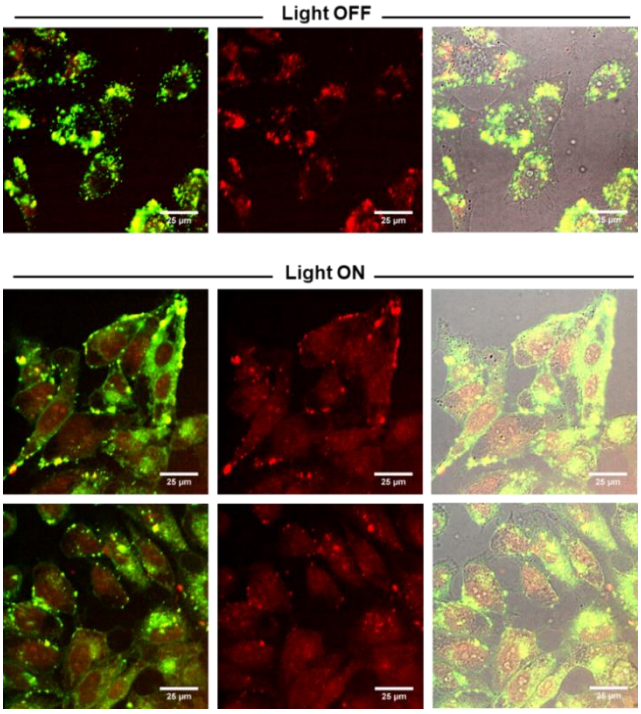

Figure 3.2.22. Confocal microscopy images of *in vitro* Ab delivery inside cytosol of HeLa cells by NIR laser triggered released from CSMs@GNRs (60X objective). The green color indicates the fluorescence signal from the DOPE-Atto488 functionalized CSMs and the red color indicates the fluorescence signal from the Alexa555 BT7R Ab encapsulated inside the CSMs. Fluorescence images of HeLa cells after 3 h incubation with CSMs@GNRs@Ab shows the CSMs internalization inside the cells (light OFF). After 1 min of NIR laser illumination at 30 $W \cdot cm^{-2}$, the red fluorescence signal is observed in the cytosol of the cell (light ON). Scale bars: 25 μm.

Hence the use of plasmonic CSMs is proven to allow the efficient and safe intracellular delivery of functional Abs, preserving its active conformation without requiring the membrane-disruption based procedures, nor the use of viral vectors or lipid transfection agents.[244] This work introduces a promising photodelivery technology, which combines the properties of stimuli-sensitive biomimetic nanocarrier with the advantages of Ab selectivity, enabling spatiotemporal dynamics control. Moreover, the versatility of the system makes it translatable to any target inside cells by delivering the corresponding macromolecule, such as active inhibitory Abs (or minibodies or nanobodies) as well as other stimulatory transcription factors, siRNA, miRNA, and so forth, to the cytosol of cells.

3.3. Fusogenic CSMs for cytosolic delivery of active cargo inside living cells

Direct drug delivery into the cell cytoplasm is a very promising perspective because it reduces the impact of endocytosis thereby protecting the drug load from the acidic environment as well as the cargo sequestration by lysosomes. Among several endosomal escape strategies, the direct fusion of the nanocarrier with the plasma membrane of the cells is a way out to achieve the intracellular delivery of the carried cargos.[245] Upon contact, two discrete lipid bilayer motifs fuse, bridging phospholipid domains and mixing internal components. Research on viruses has shown that fusion may be induced by membrane proteins.[246] Conversely, simple alterations in lipid profiles have been shown to impart fusogenic properties, allowing lipid-based NPs to subvert endocytosis pathways in the absence of fusogenic proteins.[176] Specifically, novel liposome systems based on a lipid combinations have been developed which are directly related with fusogenic efficiency (Csiszár *et al.*[176,187]).

Taking inspiration from those fusogenic liposomes and the role played by their lipidic mixtures, new class of CSMs (fusogenic CSMs, FCSMs) were developed. The CSMs structure was implemented with cationic and neutral lipids that enhance the fusion with the cell membrane and allow to achieve efficient cytosolic delivery of encapsulated active molecules inside living cells.

In this part of the thesis, different lipid combinations were tested to obtain FCSMs, with effective fusogenic ability. Moreover, the self-tumor target ability inherited by the tumoral cell membrane was investigated in different cell lines. The nanocarriers were loaded, as a proof of concept, with manifold types of cargoes and their cytosolic delivery was investigated by confocal microscopy studies (Figure 3.3.1).

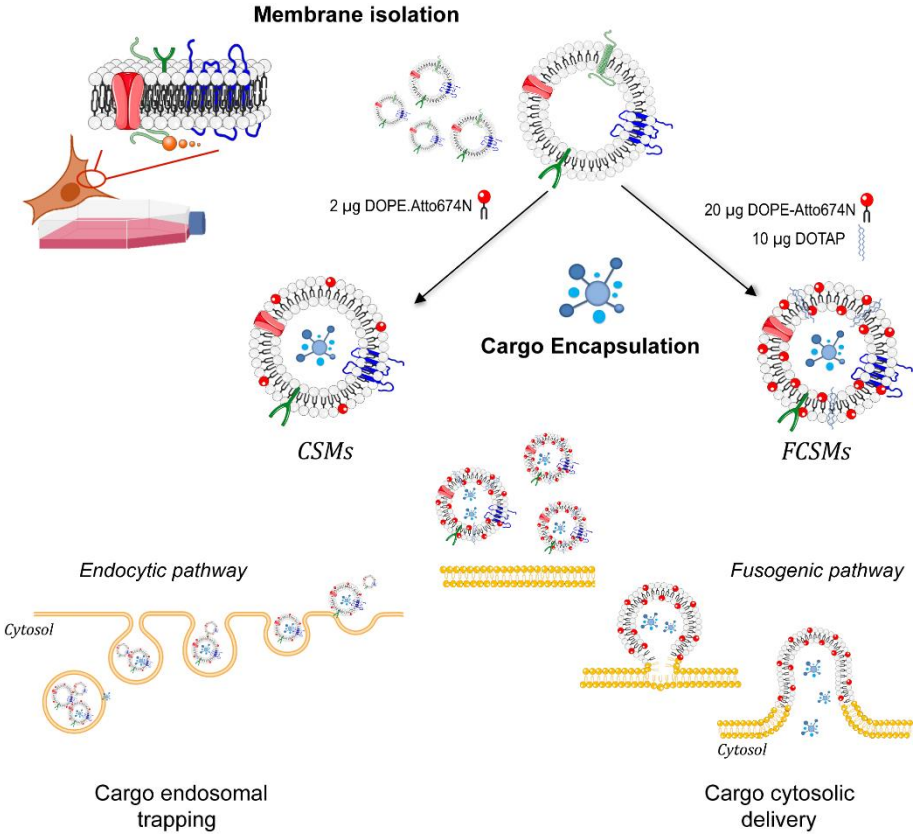

Figure 3.3.1. Schematic illustration of the synthesis of CSMs and FCSMs from cell membranes. FCSMs were functionalized with cationic and neutral fluorescently labeled lipids. The implementation of lipidic mixture changes the fate of the encapsulate cargo in cells. In the case of CSMs, the nanostructure is taken up by cell by endocytic pathway and the carried cargo is entrapped in endosomal/lysosomal vesicles. When the phospholipidic membrane of the CSMs is enriched with higher concentration of DOPE-Atto647N and an equimolar quantity of DOTAP, FCSMs are generated. These FCSMs fuse their phospholipidic membrane with the cell plasma membrane and, subsequentially, the cargo in released into the cytosol where it is free to reach the intracellular target.

3.3.1. Synthesis and characterization of FCSMs

Based on previously described results with CSMs (see sections 3.1 and 3.2), the synthesis of CSMs was modified to add a step for their implementation with a lipidic mixture (Figure 3.3.1). Briefly, A549 cells were used for the cell membrane fragments extraction, as described in the Materials & Methods, section 2.1.1. The membrane fragments were self-assembled into CSMs@A549 by cycles of extrusion through 800 nm pore size polycarbonate membranes. The resulting CSMs were mixed with lipidic components and extruded again through the polycarbonate membrane leading to their intercalation into the phospholipidic bilayer of the nanostructure.

The selection of a lipidic mixture for enhanced fusion was inspired by Csiszár *et al.*'s studies, where a synergistic combination of three lipidic compounds were used: a neutral lipid (DOPE, Figure 3.3.2a), positively charged lipid (DOTAP, Figure 3.3.2b), and lipids with an aromatic group (*i.e.,* BODIPY-FL-DHPE, Figure 3.3.2e). The positive charge of DOTAP allows to increase the electrostatic interaction between the liposomes and the negatively charged glycocalyx of the cell membrane, thus promoting the fusion.[177,178] The presence of a neutral lipid with cone-like structure such as DOPE assists in membrane destabilization due to the low hydration of its small head group causing it to adopt a hexagonal conformation involved in the fusion process.[178,179] The addition of a third lipidic component containing large delocalized π electron systems coupled to either the hydrophobic or the hydrophilic lipid parts seems to intervene in cellular uptake processes thanks to the tendency to induce local instabilities in the lipidic membrane.[178,179] The mechanism of fusion has not been deeply elucidated yet, but this combination resulted in an effective fusogenic mixture which allowed the lipid-based structure to fuse with the cell membranes and deliver its cargo into the cell cytoplasm.[176]

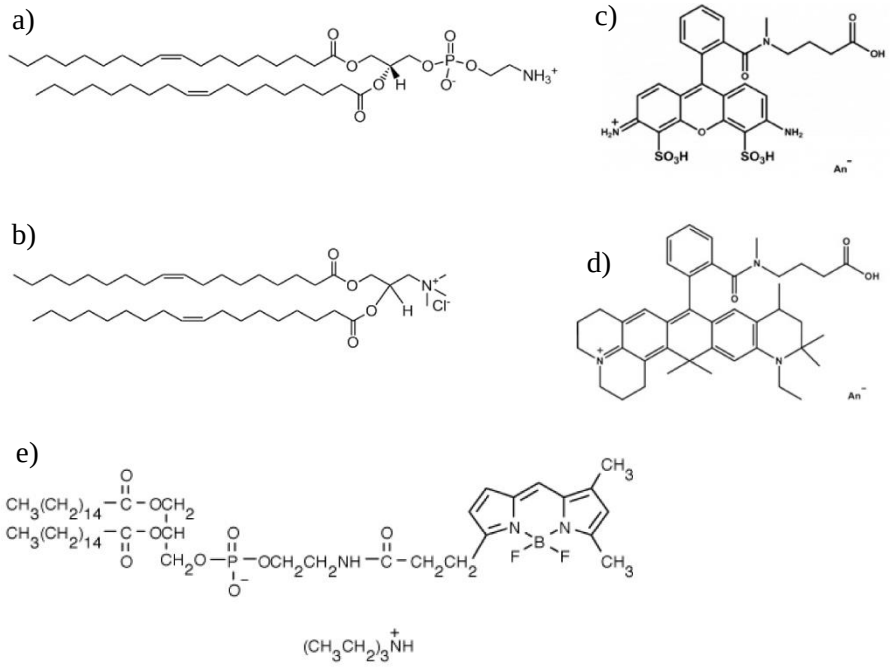

Figure 3.3.2. Chemical structures of DOPE (a) and DOTAP (b) lipids, Atto488 (c) and Atto647N (d) fluorescent dyes, and BODIPY-FL-DHPE (e).

Here, the performance of different FCSMs samples was tested changing the lipidic mixture composition of DOPE, DOTAP and BODIPY-FL-DHPE and the fusogenic effectiveness was evaluated by epifluorescence and/or confocal microscopy. Upon incubation with FCSMs, cell shape became visible due to homogenously stained plasma membranes caused by FCSMs membrane fusion. Results of tests made with different mixtures and concentrations are shown in Table 3.3.1. Firstly, in the lipidic mixture 20 µg of DOPE labeled with Atto488 (Figure 3.3.2c) (DOPE-Atto488) or Atto647N (Figure 3.3.2d) (DOPE-Atto647N) were used instead of the non-fluorescent DOPE used by Csiszár *et al.*[176,183] along with the other two lipids (Samples 1 and 2 in Table 3.3.1), corresponding to the ratio 1/1/0.1 (mol/mol/mol) of DOPE/DOTAP/BODIPY-FL-DHPE. The cell membranes resulted stained in green in the case of DOPE-Atto488 and in violet in the case of DOPE-Atto647N with similar efficiency. Fluorescence of the cell

membranes was evident in the 3 h experiment and even in the 10 min ones, showing that the fusion process is rapid and does not require longer incubation time. However, fluorescently labeled DOPE alone, without DOTAP and BODIPY-FL-DHPE lipids, was not able to induce the fusion, as FCSM fluorescence signal appeared as dots inside the cells rather than in the cell membrane (Sample 3 in Table 3.3.1). Subsequently, a lipidic mixture of 20 µg of DOPE-Atto674N and 10 µg of DOTAP (1/1 molar ratio) was tested (Sample 4 in Table 3.3.1). In this case, FCSMs incubated with cells resulted in completely stained plasma membranes, demonstrating a highly efficient membrane fusion between FCSMs and cellular membranes. These results suggested that the presence of BODIPY-FL-DHPE is not necessary to induce the fusion. The role of this compound BODIPY-FL-DHPE in the fusion is linked to the presence of the aromatic chromophore (BODIPY),[187] causing instabilities that probably initiate the formation of fusion intermediate phases, *e.g.*, inverted-hexagonal or cubic phases.[178,179] Apparently, in the FCSM formulation, the fluorophore Atto674N (or Atto488) anchored on the DOPE molecule is sufficient to induce high local instabilities in the phospholipid membrane, with no need of a third fluorescent lipid.

Based on the results obtained, fluorescent DOPE (Atto488 o Atto647N) and DOTAP were finally used at 1/1 (mol/mol) ratio to prepare the final FCSM nanostructure (Sample 4, Table 3.3.1). As control sample, CSMs not implemented with the lipidic mixture were used. The cellular uptake processes of CSMs, already investigated in section 3.1.2, showed a strong prevalence of endocytosis pathways. The control CSMs were labeled with 2 µg of DOPE-Atto647N following the general protocol used to prepare fluorescently labeled CSMs (see section 2.2.1) in order to track them inside the cells in the *in vitro* experiments. As seen above (Sample 3, Table 3.3.1), the addition of only fluorescent DOPE to the CSMs does not to induce fusogenic behavior not even at high concentrations, therefore the fluorescently labeled CSMs were used as control.

Table 3.3.1. Results of tests made with different FCSMs samples (from 1 to 4) changing the lipid composition. For each sample, microscopy images are shown in fluorescence channel (violet channel for DOPE-Atto647N and green channel for DOPE-Atto488). A549 cells were incubated with samples for 1 h and/or 10 min. Scale bars: 20 μm.

Sample	Composition	μg	Incubation Time	Microscopy Images
1 (FCSMs)	CSMs	20 μg	*10 min*	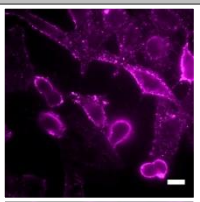
	DOPE-Atto647N	20 μg		
	DOTAP	10 μg	*3 h*	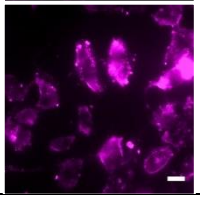
	BODIPY-FL-DHPE	1 μg		
2 (FCSMs)	CSMs	20 μg	*10 min*	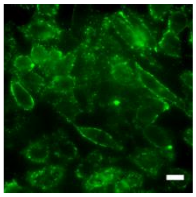
	DOPE-Atto488	20 μg		
	DOTAP	10 μg	*3h*	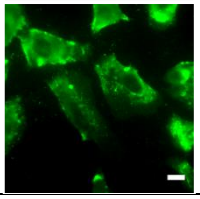
	BODIPY-FL-DHPE	1 μg		
3 (CSMs)	CSMs	20 μg	*10 min*	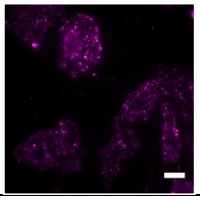
	DOPE-Atto647N	20 μg		
	DOTAP	-		
	BODIPY-FL-DHPE	-		
4 (FCSMs)	CSMs	20 μg	*10 min*	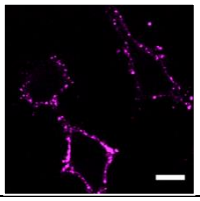
	DOPE-Atto647N	20 μg		
	DOTAP	10 μg		
	BODIPY-FL-DHPE	-		

The DLS analysis showed that, upon the functionalization with the lipidic mixture, the hydrodynamic diameter (d_h) of the FCSMs remained nearly constant at ~300 nm. Hence the presence of lipids does not have any significant effect on the hydrodynamic size of these nanosystems (Table 3.3.2 and Figure 3.3.3). The inclusion of the positively charged DOTAP caused a slight decrease of the ζ-potential values of the FCSMs (-19.3 vs. -24.1 mV) in comparison to CSMs.

Table 3.3.2. Mean hydrodynamic diameter derived from the DLS distributions and ζ potential values of CSMs and FCSMs samples. [1] $d_{H,I}$, $d_{H,N}$ and $d_{h,v}$ refer to the mean average hydrodynamic diameter from the intensity, number and volume DLS distributions. PDI refers to polydispersity index. Standard deviation values were calculated from three measurements of CSMs/FCSMs samples.

	PDI	$d_{H,I}$ (nm)[1]	$d_{H,N}$ (nm)[1]	ζ-potential (mV)
CSMs	0.188 ± 0.034	327± 44.5	217.3 ± 6.5	-24.1 ± 1.0
FCSMs	0.17± 0.015	254.6± 8.1	194.4± 25.9	-19.3 ± 0.9

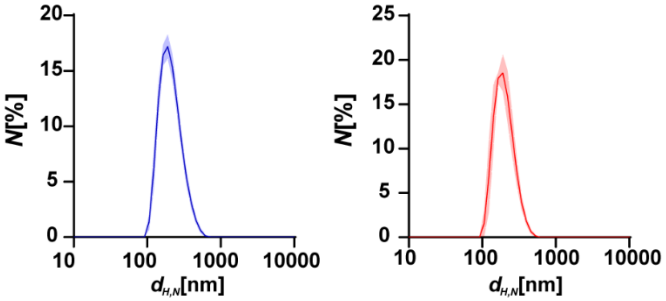

Figure 3.3.3. DLS size distributions in number ($d_{H,N}$) based on three independent measurements of CSM (blue line) and FCSM (red line) samples.

NTA measurements showed a FCSMs size distribution similar to that obtained from DLS and allowed to define the CSM concentration (Table 3.3.3 and Figure 3.3.4).

Once proved that the size distribution was not influenced by adding the lipids to the nanostructure formulation, A549 cells were incubated with CSMs and FCSMs for 10 and 60 min. Upon incubation with FCSMs, confocal microscopy showed efficient membrane fusion at both incubation times (Figure 3.3.5).

Table 3.3.3. Mean diameter of the CSMs and FCSMs obtained from the NTA distributions. Standard deviation values were calculated from three measurements.

	Conc (F)CSMs·mL^{-1}·10^{11}	Size (nm)
CSMs	3.22 ± 0.47	157.9 ± 19
FCSMs	2.65 ± 0.15	155 ± 7.1

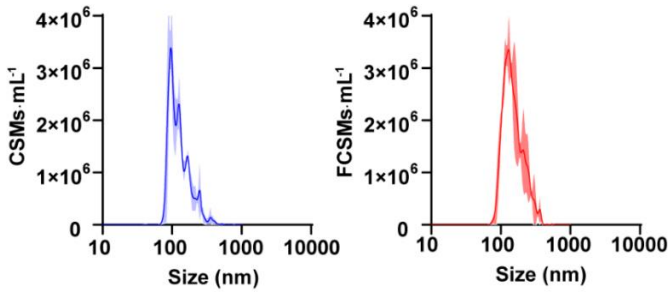

Figure 3.3.4. Size distribution analysis (NTA) based on three independent measurements of CSMs (blue line) and FCSMs (red line) dispersed in HEPES buffer pH 7.4.

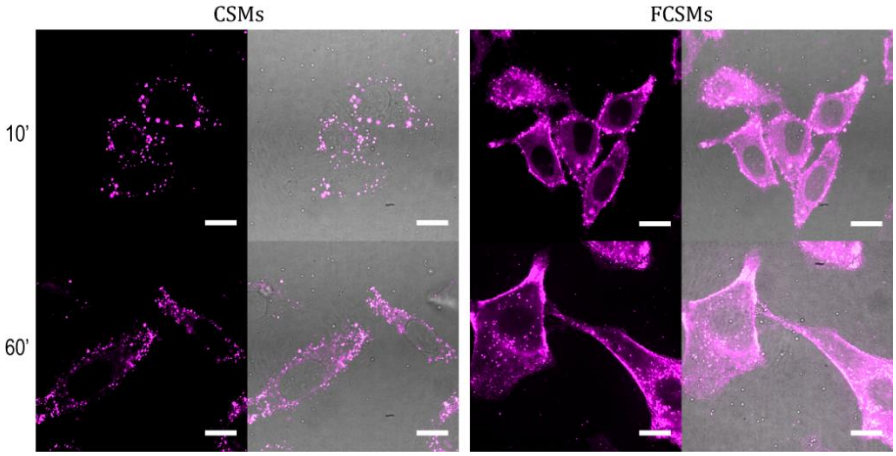

Figure 3.3.5. Confocal images of A549 cells incubated with CSMs and FCSMs for 10 and 60 min. Fluorescence signal (left) and bright field merged with fluorescence (right) are shown. Scale bars: 20 µm.

Most of the fluorescence signal appeared homogeneously distributed in the cell cytoplasm and in the plasmatic membrane, revealing the cell shapes. On the other hand, as previously discussed, cells incubated with CSMs

presented fluorescent dots punctual distributed in the cytosol. This distribution corresponds with the typical endocytic internalization profile.

In conclusion, a new protocol was stablished to produce a new class of CSMs in which the addition of a lipid component confers them effective fusogenic capabilities while keeping their size.

3.3.2. Homotypic targeting of FCSMs *in vitro*

Tumoral cell-derived membrane coating is well known for its tumor targeting properties, and the homotypic ability of CSMs to preferentially interact with their cell sources was already studied in section 3.1.2 of this thesis work. Here, the *in vitro* targeting efficacy of FCSMs was also investigated by FC in order to confirm that the homotypic properties were maintained in the new lipid modified formulation.

The uptake of FCSMs@A549 and CSMs@A549 was analyzed in A549 cells, HeLa cells and MRC5 fibroblasts MRC5 by FC analysis. The results showed that the FCSMs@A549 were more efficiently internalized by A549 cells than in the other cell lines after either 10 or 60 min incubation time (Figure 3.3.6). Likewise, this preferential recognition was also found in the case of CSMs@A549, confirming that FCSMs present homotypic affinity for their cell source, as was previously shown for CSMs.

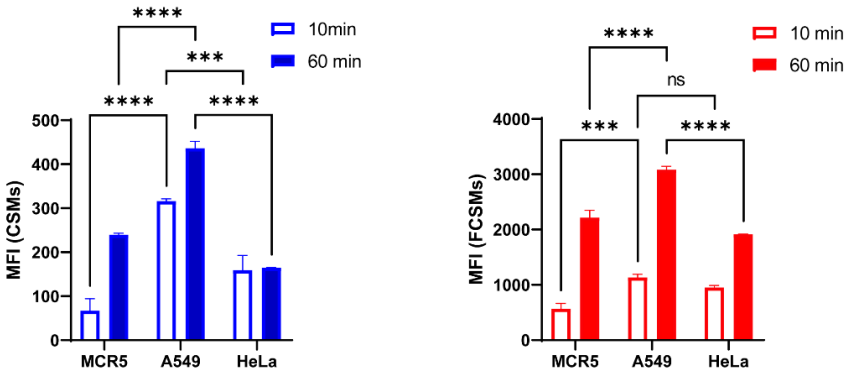

Figure 3.3.6. FC quantification of the cellular uptake of CSMs and FCSMs derived from A549 cells after 10 and 60 min incubations. MF values (Red fluorescence intensity) of DOPE-Atto647N functionalized (F)CSMs internalized by cells expressed as mean ± s, n=3. In all data, statistical analysis was assessed by the two-way ANOVA. ***P=0.0003; ****P<0.0001.

3.3.3. Cytosolic delivery of active cargo inside living cells

To investigate the intracellular delivery of the cargo by fusion membrane, different kinds of molecules were selected to be encapsulated into the (F)CSMs. The efficiency and robustness of the encapsulation method was already studied in detail in section 3.2.1. In this study, four different bioactive cargo/reporters were selected to load into the (F)CSMs: i) Hoechst H 33258 (HOE), a small hydrophobic molecule; ii) Dextran-SNARF (DS), a hydrophilic polysaccharide of 70 kDa conjugated with fluorescent SNARF dye; iii) FITC labeled Phalloidin (PHA), a cyclic peptide which interacts with actin of the cells, and iv) Polystyrene beads (PSNPs), solid NPs of 100 nm diameter. To incorporate the cargo into the (F)CSM carrier, the cargo solution was added to the CSMs and extruded through the polycarbonate membrane with or without lipidic mixture obtaining FCSMs@cargo and CSMs@cargo, respectively (see section 2.2.2). The excess of non-encapsulated cargo molecules was purified with the adequate methodology (see section 2.3) and the loading efficiency was calculated by fluorescence using the corresponding calibration curve for each cargo (Table 3.3.4).

Table 3.3.4. The concentration of encapsulated cargo calculated by measuring the fluorescence intensity of the (F)CSMs@Cargo.

Cargo		Conc. cargo	Conc. CSM·mL^{-1}	Cargo/CSM
DS	CSMs	36.75 μg·ml^{-1} / 0.53 μM	2.28 · 10^{12}	1387
	FCSMs	44.0 μg·ml^{-1} / 0.6 μM	2.16 · 10^{12}	1753
HOE	CSMs	19.5 μg·ml^{-1} /31.25 μM	8.2 · 10^{12}	2332
	FCSMs	23.1 μg·ml^{-1} / 37.02 μM	8.4 · 10^{12}	2685
PHA	CSMs	1.59 μg·ml^{-1} / 1.27 μM	2.29 · 10^{12}	333
	FCSMs	2.32 μg·ml^{-1} / 1.85 μM	2.49 · 10^{12}	447
PSNP	CSMs	0.7 · 10^{11} NPs·mL^{-1}	/	1
	FCSMs	0.1 · 10^{11} NPs·mL^{-1}	/	1

The resulted CSMs@cargo and FCSMs@cargo were characterized with DLS and NTA analyses. The DLS studies showed that, upon the the cargo loading, the hydrodynamic diameter (d_h) of the (F)CSMs remained nearly constant around 200-300 nm. Hence, the encapsulation had no significant effect on the hydrodynamic size of the (F)CSMs (Figure 3.3.7 and Table 3.3.5).

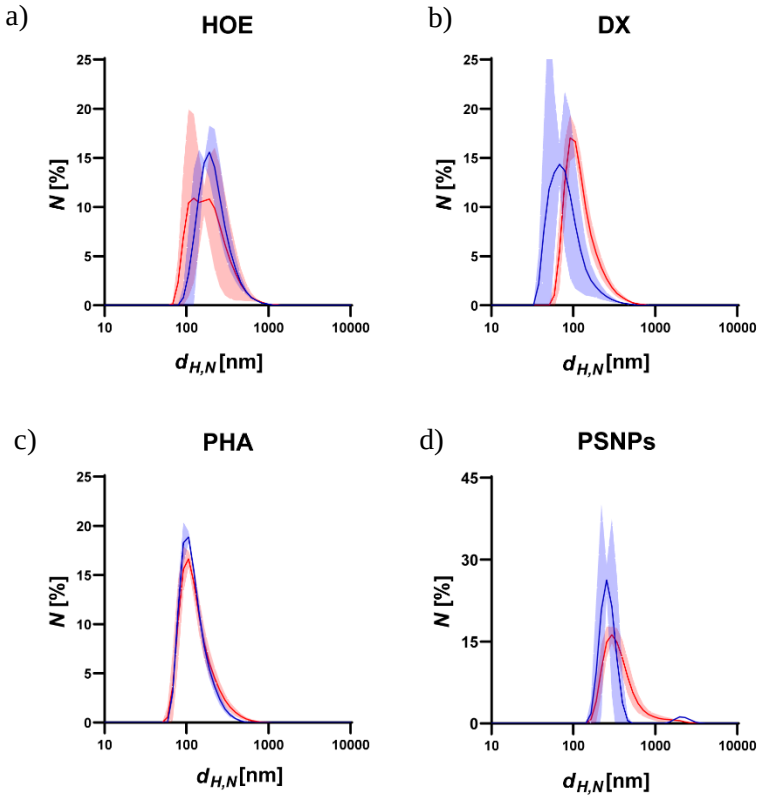

Figure 3.3.7. DLS measurements of CSMs@Cargo (Blue) and FCSMs@Cargo (Red). DLS distributions in number (dh(N)) of three independent measurements of a) (F)CSMs@HOE, b) (F)CSMs@DS, c) (F)CSMs@PHA and d) (F)CSMs@PSNPs.

Table 3.3.5. Mean hydrodynamic diameter derived from the DLS distributions of (F)CSMs loaded with different kinds of cargo. [1] $d_{H,I}$, $d_{H,N}$ and $d_{h,v}$ refer to the mean average hydrodynamic diameter from the intensity, number and volume DLS distributions. PDI refers to polydispersity index. Standard deviation values were calculated from three measurements of loaded CSMs/FCSMs samples.

Cargo		PDI	$d_{H,I}$ (nm)[1]	$d_{H,N}$ (nm)[1]
/	CSMs	0.188 ± 0.034	327± 44.5	217.3 ± 6.5
	FCSMs	0.17± 0.015	254.6± 8.1	194.4± 25.9
PHA	CSMs	0.167± 0.016	233.4± 27.3	108.5± 40.9
	FCSMs	0.236± 0.012	344.3± 39.4	136.9± 11.9
DS	CSMs	0.215± 0.009	269.9± 29.1	72.53± 31.2
	FCSMs	0.209± 0.006	280.9± 12.1	127.7± 4.5
HOE	CSMs	0.259± 0.024	397.8± 1.8	141.8± 98
	FCSMs	0.207± 0.016	406.9± 21	249.3± 39.37
PSNP	CSMs	0.65± 0.045	273.4± 48.93	265.8± 48.1
	FCSMs	0.383± 0.042	399.95± 49.29	381.4± 29.42

NTA measurements showed a (F)CSM size distribution similar to that obtained from DLS and allowed to define the (F)CSM concentration (Figure 3.3.8 and Table 3.3.6).

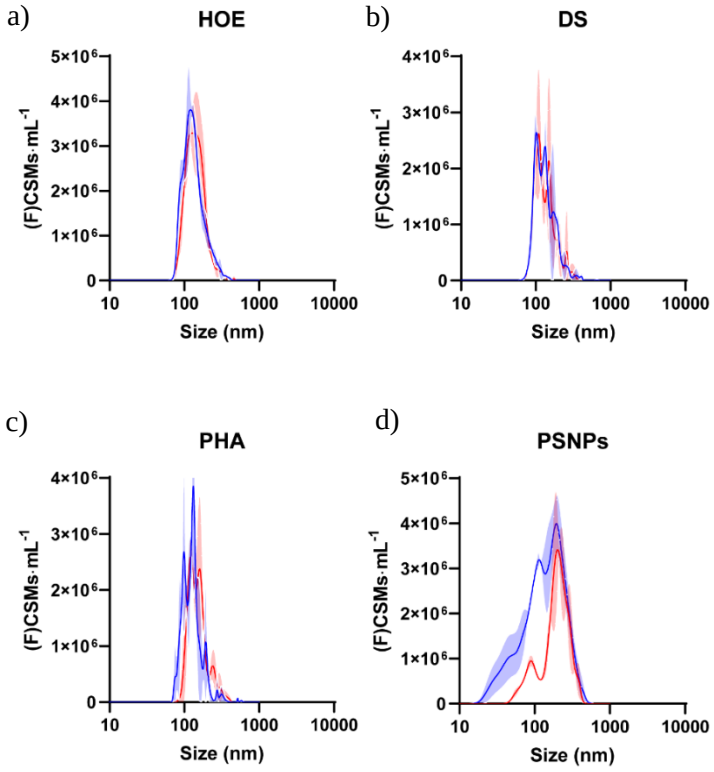

Figure 3.3.8. NTA measurements of CSMs@Cargo (Blue) and FCSMs@Cargo (Red) dispersed in PBS buffer pH 7.4. Size distributions of three independent measurements of a) (F)CSMs@HOE, b) (F)CSMs@DS, c) (F)CSMs@PHA and d) (F)CSMs@PSNPs.

Table 3.3.6. Mean diameter (size) and sample concentration (Conc. CSMs·mL^{-1} ·10^{11}) derived from the NTA distributions. Standard deviation values were calculated from three measurements of (F)CSMs samples

Cargo		Conc CSMs·mL^{-1} ·10^{11}	Size (nm)
/	CSMs	3.22 ± 0.47	157.9 ± 19
	FCSMs	2.65 ± 0.15	155 ± 7.1
PHA	CSMs	2.29 ± 0.56	128 ± 7
	FCSMs	2.49 ± 0.34	137.1 ± 20.4
DS	CSMs	2.28 ± 0.57	117.1 ± 24.8
	FCSMs	2.16 ± 0.15	155 ± 7.1
HOE	CSMs	8.2 ± 0.1	128.47 ± 7.7
	FCSMs	8.4 ± 0.5	165.7 ± 4
PSNP	CSMs	0.65 ± 0.02	247.33 ± 19.4
	FCSMs	0.22 ± 0.02	219.47 ± 10.1

Next, the intracellular delivery process of HOE carried by FCSMs was studied by confocal microscopy. HOE is a small hydrophobic bisbenzimide compound that bind the DNA minor groove at A–T-rich region. As a cell-permanent blue-fluorescent dye, it is typically used in molecular biology to stain the nuclei of live and fixed cells.[247] A549 cells were incubated for 10 min with FCSMs@HOE, CSMs@HOE or free HOE at the concentration of 3.3 µM of HOE for all three samples. In the first case (Figure 3.3.9, Figure 3.3.11a), the nuclei are efficiently fluorescence-stained in blue. It can be assumed that the FCSMs@HOE, upon their interaction and fusion with the cell membrane, released their cargo inside the cytosol where the HOE is able to achieve the nuclei and stain the DNA. A homogeneous cell membrane staining was also observed by the fluorescence signal from the DOPE-Atto647N which is used to label the phospholipidic structure of FCSMs. As expected, A549 cell nuclei remained unstained upon the incubation with CSMs@HOE (Figure 3.3.10a, Figure 3.3.11b), although fluorescence signals from DOPE-Atto647N indicated that the CSMs@HOE were successfully internalized. Since the fluorescence appeared as dots inside the cells, it is

assumed that the CSMs@HOE were internalized by endosomal/lysosomal vesicles in which they accumulated. In this case, the cargo was not free to achieve its intracellular target (DNA). Thus, encapsulated HOE kept its DNA-unbound state for which the fluorescence was low. Indeed, it is known that the HOE fluorescence increases ~30-fold upon DNA binding.[248] After 3 h incubation, the nuclei of CSMs@HOE treated cells began to be stained probably because of HOE leaking from the CSMs (Figure 3.3.12). For all the experimental conditions, control cells were incubated with free HOE at 3.3 µM concentration. (Figure 3.3.10b, Figure 3.3.11c and Figure 3.3.12c). The free HOE treatments showed residual staining compared to when delivered by FCSMs, after 10 min (Figure 3.3.10b and Figure 3.3.11c) as well as 3 h (Figure 3.3.12c) incubations.

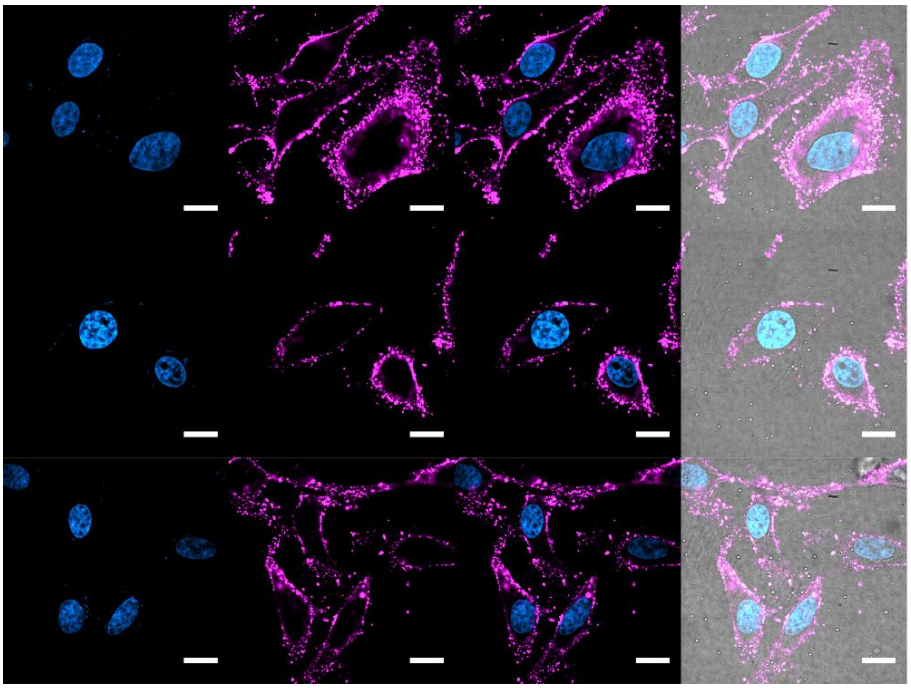

Figure 3.3.9. Confocal images of *in vitro* HOE delivery inside cytosol of A549 cells by fusion of FCSMs@HOE after 10 min incubation. For each panel row, the images from left to right show cell the fluorescence signal by HOE (blue), the fluorescence signal from the DOPE-Atto 647N functionalized FCSMs (violet), overlays of the two images and both merged with brightfield. Scale bars: 20 µm.

a)

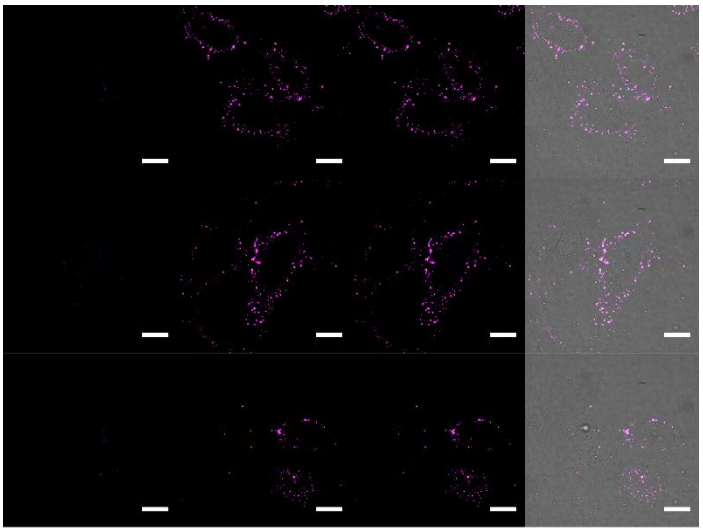

b)

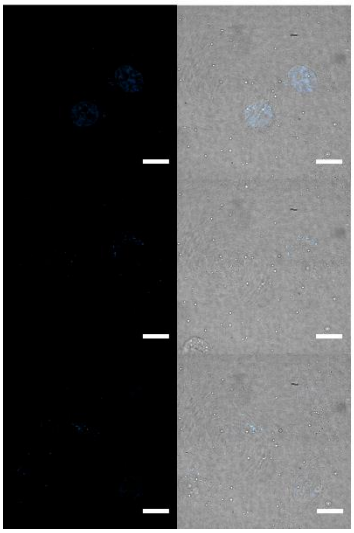

Figure 3.3.10. Confocal images of A549 cells incubated with CSMs@HOE (a) and free HOE (b) for 10 min. For each panel, the images from left to right show cell the fluorescence signal by HOE (blue), the fluorescence signal from the DOPE-Atto 647N functionalized CSMs (violet), overlays of the two images and both merged with brightfield. Scale bars: 20 μm.

a)

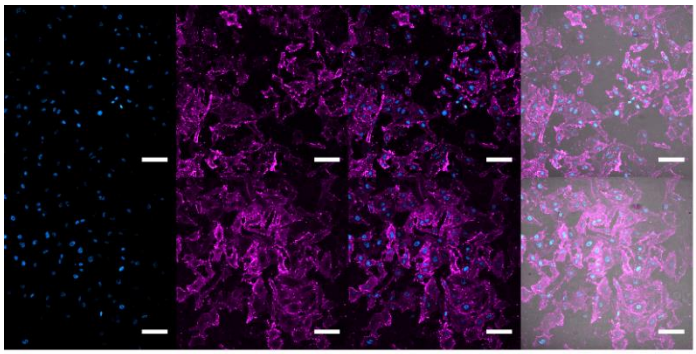

b)

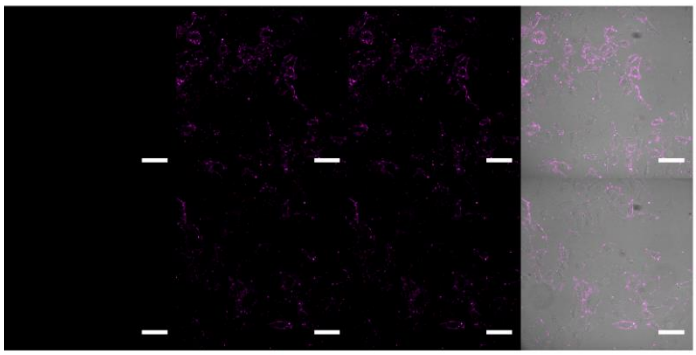

c)

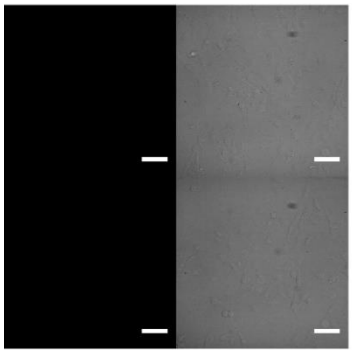

Figure 3.3.11. Confocal images of A549 cells incubated with FCSMs@HOE (a), CSMs@HOE (b) and free HOE (c) for 10 min. For each panel, the images from left to right show cell the fluorescence signal by HOE (blue), the fluorescence signal from the DOPE-Atto 647N functionalized (F)CSMs (violet), overlays of the two images and both merged with brightfield. Scale bars: 100 μm.

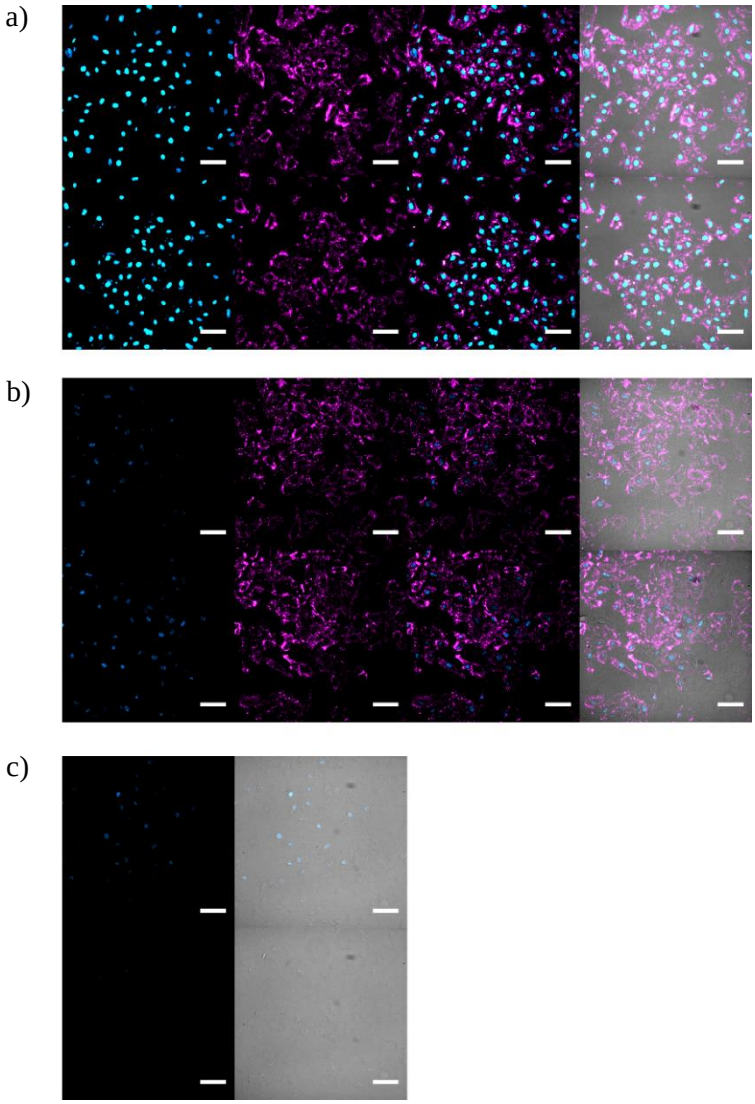

Figure 3.3.12. Confocal images of A549 cells incubated with FCSMs@HOE (a), CSMs@HOE (b) and free HOE (c) for 3 h. For each panel, the images from left to right show cell the fluorescence signal by HOE (blue), the fluorescence signal from the DOPE-Atto 647N functionalized (F)CSMs (violet), overlays of the two images and both merged with brightfield. Scale bars: 100 μm.

The fluorescence intensity of a single whole cell was analyzed by Image J software and the corrected total cell fluorescence (CTCF) was calculated for each experimental condition (cells treated with CSMs@HOE, FCSMs@HOE and free HOE, for 10 min and 3 h). The analysis confirmed that the fluorescence intensity of the nuclei stained by HOE was higher when it was encapsulated into the FCSMs than the CSMs that shown similar values of fluorescence to the free HOE (Figure 3.3.13). This result indicates that an effective intracellular HOE delivery was obtained when the cargo was loaded into the FCSMs, as a result of membrane fusion that allowed the reporter to reach the nuclei and bind the DNA.

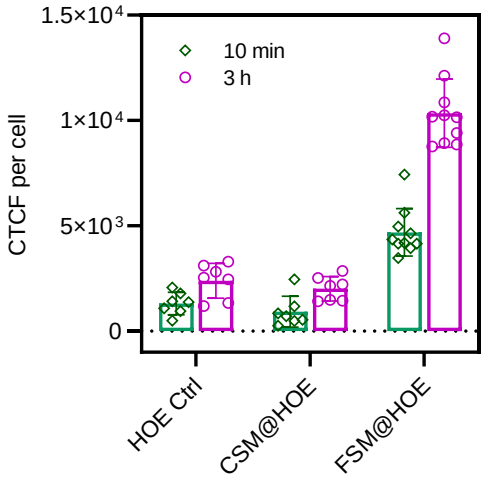

Figure 3.3.13. Corrected total cell fluorescence (CTCF) of A549 cells incubated with free HOE, CSMs@HOE and FCSMs@HOE for 10 min and 3 h.

As proof of concept, a larger macromolecule was used as cargo to confirm the efficiency of the intracellular delivery also in case of FCSMs loaded with higher molecular weight cargo. The 70 kDa DS is a hydrophilic polysaccharide commonly used in microscopy studies and introduced into the cells via microinjection. A549 cells were incubated with CSMs@DS, FCSMs@DS and free DS at the concentration of 70 nM of DS for all three samples. Confocal images of cells after 10 (Figure 3.3.14) and 60 min (Figure 3.3.15) of incubations showed the DS fluorescence when delivered by FCSMs as homogeneously distributed inside the cells, staining the whole cytosol whereas, in case of CSMs@DS, it appeared distributed inside cells as dots, which can be interpreted as a consequence of endocytic

internalization of the CSMs (Figure 3.3.16a and Figure 3.3.17a). It can be also observed the colocalization between the DS fluorescence signal and the DOPE-Atto647N with which the CSMs were stained. It suggested that DS was not released and kept into the CSMs. Control cells were incubated with free DS. As expected, they did not show a significant uptake, (Figure 3.3.16b and Figure 3.3.17b) due to the DS low cell permeability.[249] CTCF calculated for each experimental condition confirmed the strong increase of the DS fluorescence signal inside the cell when it was delivered by the FCSMs (Figure 3.3.18). Taken together, the confocal image analyses confirmed the versatility of FCSMs as fusogenic carrier that can be efficiently exploited to encapsulate large non-cell permeable macromolecules and mediate their intracellular delivery.

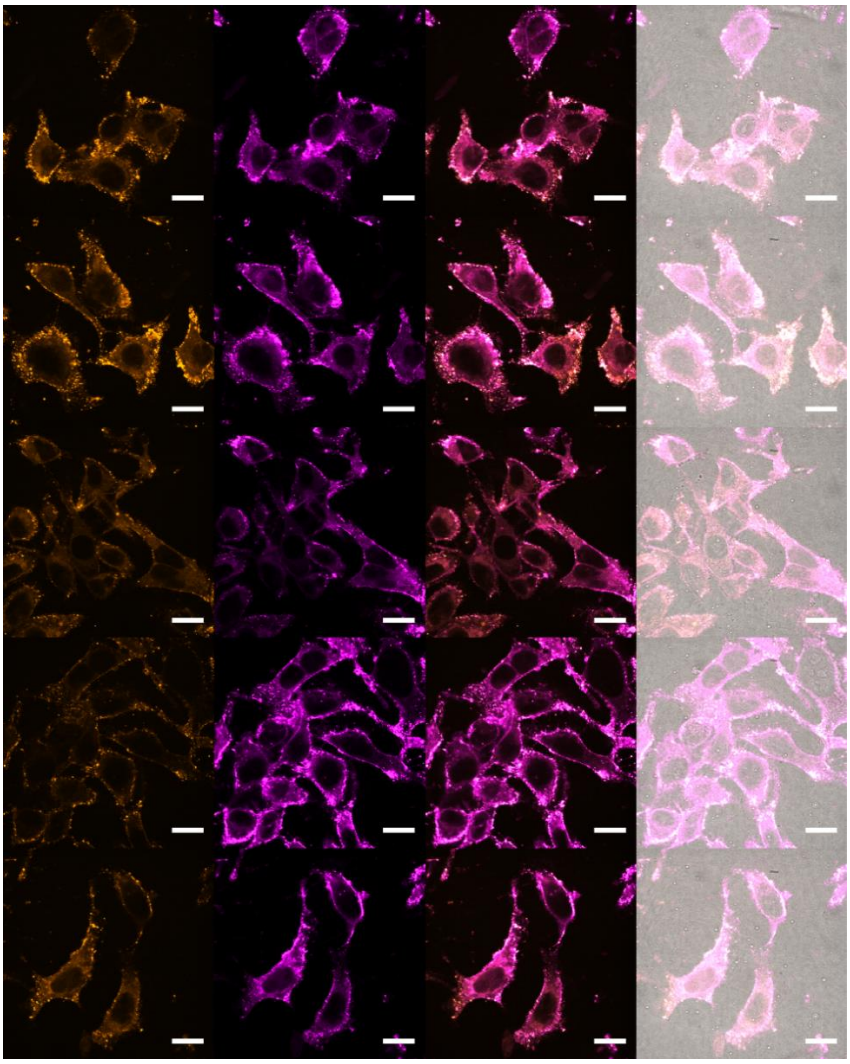

Figure 3.3.14. Confocal images of *in vitro* DS delivery inside cytosol of A549 cells by fusion of FCSMs@DS after 10 min incubation. For each panel, the images from left to right show cell the fluorescence signal by DS (orange), the fluorescence signal from the DOPE-Atto647N functionalized FCSMs (violet), overlays of the two images and both merged with brightfield ones. Scale bars: 20 μm.

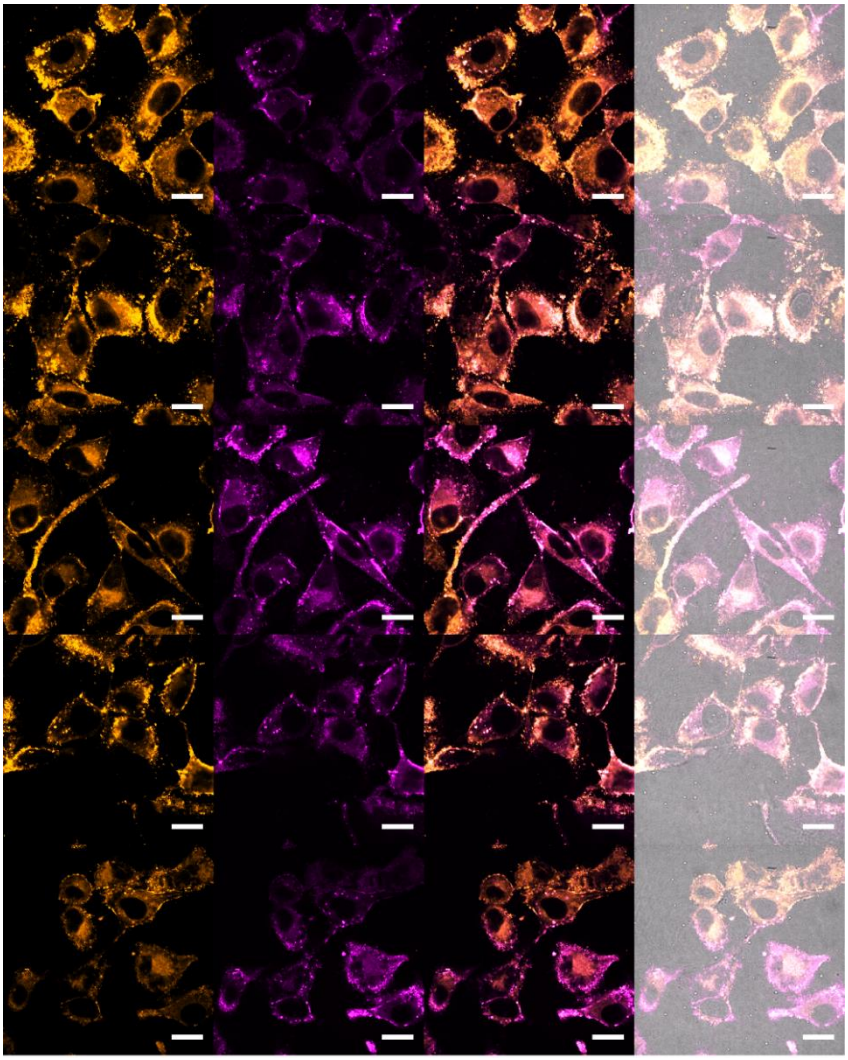

Figure 3.3.15. Confocal images of *in vitro* DS delivery inside cytosol of A549 cells by fusion of FCSMs@DS after 60 min incubation. For each panel, the images from left to right show cell the fluorescence signal by DS (orange), the fluorescence signal from the DOPE-Atto647N functionalized FCSMs (violet), overlays of the two images and both merged with brightfield ones. Scale bars: 20 μm.

a)

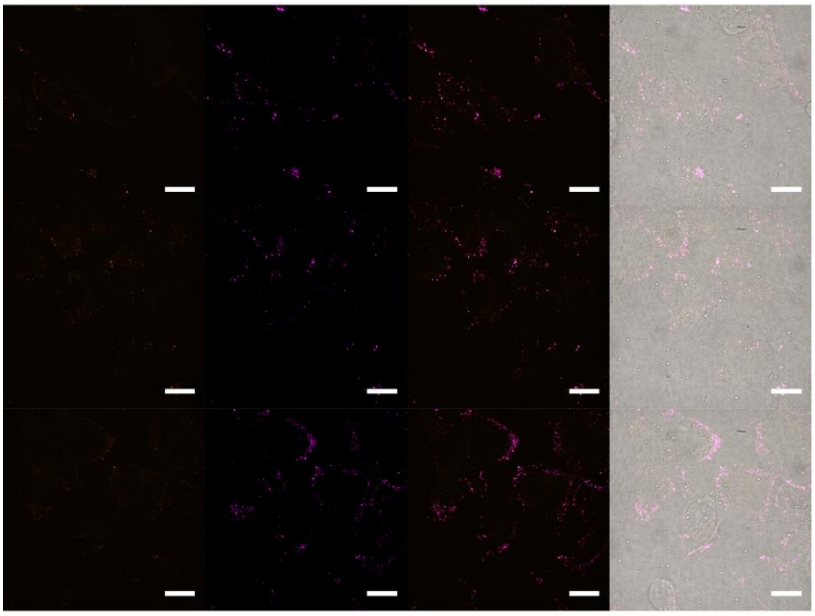

b)

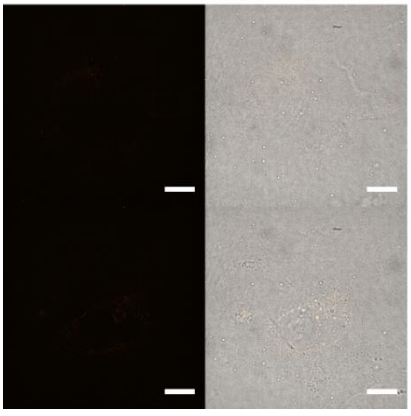

Figure 3.3.16. Confocal images of A549 cells incubated with CSMs@DS (a) and free DS (b) for 10 min. For each panel, the images from left to right show cell the fluorescence signal by DS (orange), the fluorescence signal from the DOPE-Atto647N functionalized CSMs (violet), overlays of the two images and both merged with brightfield ones. Scale bars: 20 μm.

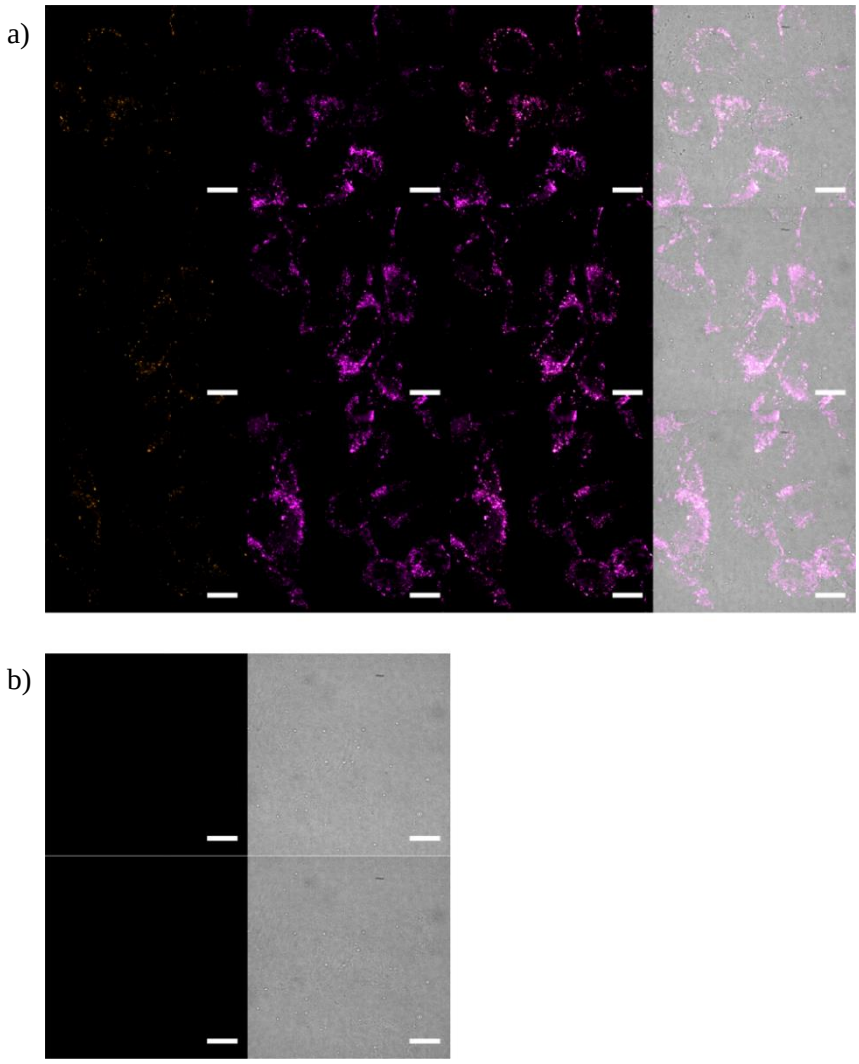

Figure 3.3.17. Confocal images of A549 cells incubated with CSMs@DS (a) and free DS (b) for 60 min. For each panel, the images from left to right show cell the fluorescence signal by DS (orange), the fluorescence signal from the DOPE-Atto647N functionalized CSMs (violet), overlays of the two images and both merged with brightfield ones. Scale bars: 20 μm.

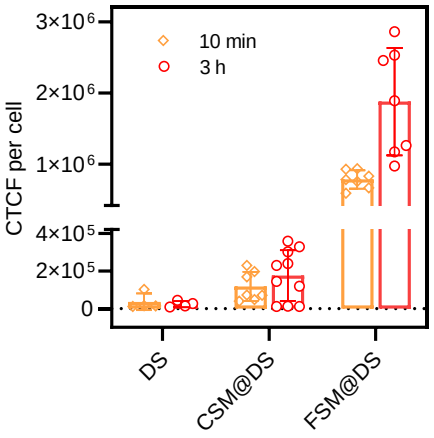

Figure 3.3.18. Corrected total cell fluorescence (CTCF) of A549 cells incubated with free DS, CSM@DS and FCSM@DS for 10 min and 3 h.

Next, FITC labeled bicyclic heptapeptide phalloidin (PHA) was used to further testify the effective cytosolic delivery of cargo substances by using the FCSMs. PHA is a phallotoxin produced by death cap mushroom *Amanita phalloides* which interacts with the polymeric actin of eukaryotic cells. Conjugated to fluorescent dyes, PHA is commonly used in imaging applications to selectively label F-actin in fixed cells, permeabilized cells, and cell-free experiments. In fact, free PHA is not able to cross the cellular membrane reaching the intracellular compartment unless the cell membrane is permeabilized. FCSMs and CSMs were loaded with PHA and A549 cells were incubated for 30 min with PHA-loaded CSMs, PHA-loaded FCSMs and PHA alone at the concentration of 0.2 µM of PHA for all three treatment conditions. Confocal images showed that the F-actin were successfully labeled when PHA was delivered by the FCSMs (Figure 3.3.19a). This result suggests that, thanks to ability of FCSMs to fuse their phospholipidic bilayer with the plasmatic membrane, the carried FITC was directly released inside the cytosol, where it was able to bind and label the F-actin of living cells, without requiring the membrane permeabilization or other disruption methods. In case of CSM@PHA, no cells with stained actin were found despite the evidence of CSMs fluorescence (violet) inside the cells (Figure 3.3.19b). Although the carrier-cargo complex was efficiently internalized, it remained trapped inside endosomes and could not reach its cytosolic target, the F-actin.

a)

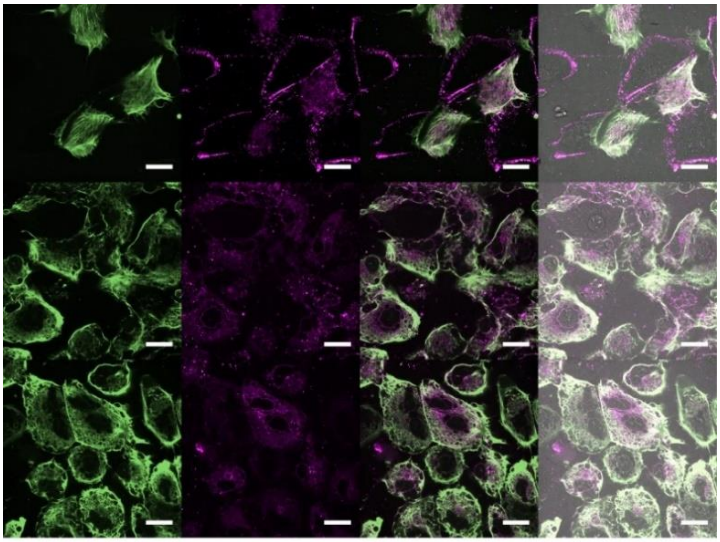

b)

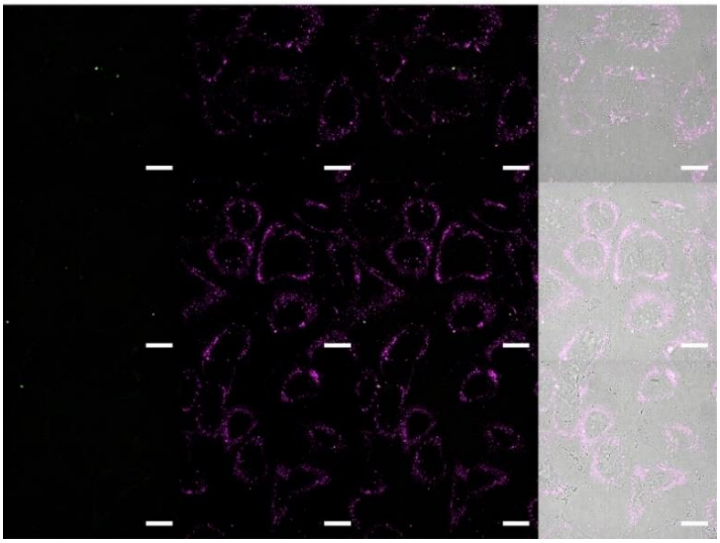

Figure 3.3.19. Confocal images of *in vitro* PHA delivery inside the cytosol of A549 cells by fusion of FCSMs@PHA (a) and CSMs@PHA (b) after 30 min incubation. For each panel, the images from left to right show cell the fluorescence signal by PHA (green), the fluorescence signal from the DOPE-Atto647N functionalized (F)CSMs (violet), overlays of the two images and both merged with brightfield ones. Scale bars: 20 μm.

Finally, a solid inorganic NP was used as cargo. PSNPs coated with a cell membrane derived phospholipid layer of CSMs and FCSMs. PS NPs are widely used as model for the study of the interactions between cells and NPs.[250] The pathway of PS NPs internalization has been shown to depend on cell type, size, shape, surface chemistry. PS NPs with 100 nm diameter follow the endosomal-lysosomal pathway inside cells.[251] FCSM and CSM coated PSNPs were prepared as reported in Materials and Methods (see section 2.2.4 and incubated with A549 cells at the concentration of 12,000 NPs/cell. In addition, cells were incubated with bare PSNPs at the same concentration as control. In the case of FCSM coated PSNPs (FCSM@PSNPs), fluorescence signal from PSNPs (shown in red in Figure 3.3.20a) appeared homogeneously diffused in the cytosol with some dots of higher intensity. This result suggests that solid particles such as PSNPs, by fusogenic coating, were directly released into the cytosol and partly internalized via endocytosis too. When PSNPs were coated by CSMs, the red fluorescence resulted clearly localized in distinguishable dots, indicating that their inclusion in the cell followed the endocytosis pathway and remained trapped inside the endosome/lysosomes as for the free PSNPs. Nevertheless, the CSM coating visibly increased the uptake rate compared to bare PSNPs (Figure 3.3.20) at this specific incubation time (30 min).

In conclusion, this study has shown the intrinsic ability of the Atto labeled DOPE-DOTAP functionalized CSMs for efficient intracellular cytoplasmic delivery. This new lipidic design of fusogenic CSMs allows to combine the features of cell membrane derived nanovesicles (homotypic targeting, biocompatibility, cargo encapsulation flexibility, easy manufacturing, *etc*.) with the ability to induce fusion events between the carrier phospholipidic structure and the cell membrane, avoiding the endocytosis pathway and lysosomal entrapping of the cargo.

Fusogenic cell membrane derived nanovesicles showed a great potential as a cytoplasmic delivery tool especially for *in vitro* experiments. Cargo release is fast and independent of the cargo molecular nature. They could be a powerful tool for fast cytoplasmic delivery of susceptible drugs, especially proteins and nucleic acids, enable of designing a new generation of carriers for nanovaccines.

Although the exact fusion mechanisms are yet to be elucidated, such bioinspired systems may represent a new generation of nanovehicles in biomimetic nanomedicine.

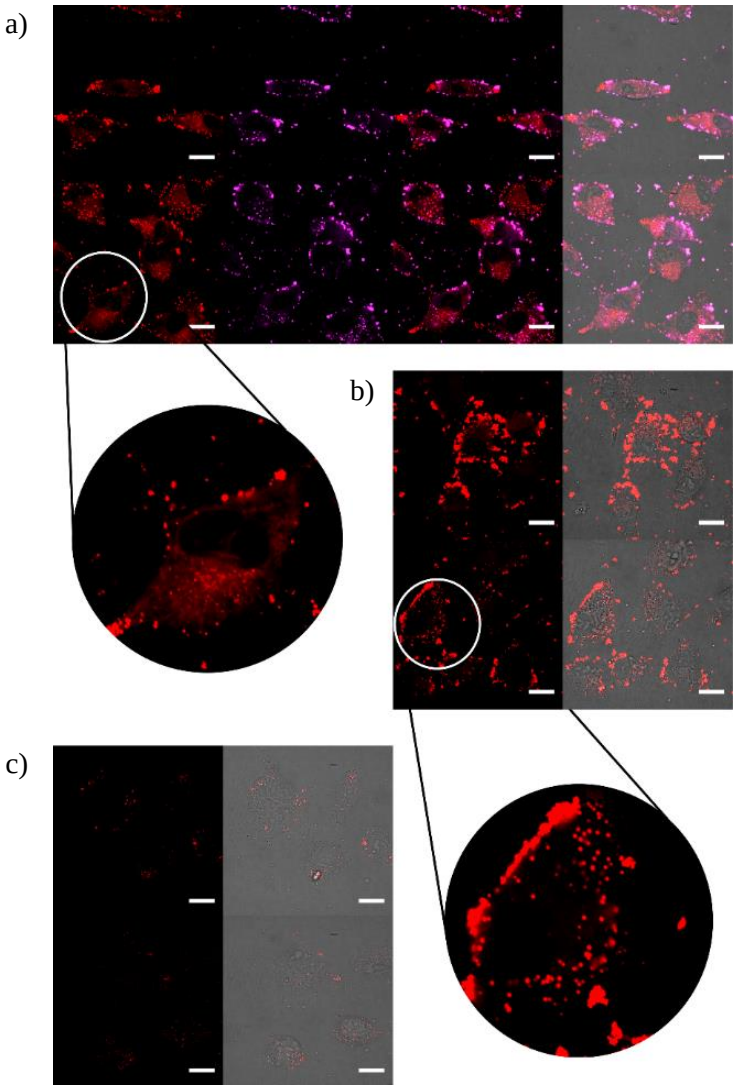

Figure 3.3.20. Confocal images of *in vitro* PSNPs delivery inside cytosol of A549 cells by fusion of FCSMs@PSNPs (a) and CSMs@PSNPs (b) and bare PSNPs (c) after 30 min incubation. For each panel, the images from left to right show cell the fluorescence signal by PSNPs (red), the fluorescence signal from the DOPE-Atto647N functionalized FCSMs (violet), overlays of the two images and both merged with brightfield ones. Scale bars: 20 μm.

.

Conclusions

4. Conclusions

The results of the research conducted in this thesis underline the importance of the biomimetic cell-derived coating technology, which offers a versatile tool for developing improved drug delivery nanovectors by easily recreating natural scenarios at the bionano-interface. These biomimetic interfaces have emerged to overcome some of the main drawbacks inherent to synthetic nanomaterials by translating specific complex functionalities of the cell surfaces that otherwise would not be simple to replicate synthetically.

Here a diversity of cell types (several tumoral cell lines) selected as membrane source allowed to develop innovative biomimetic nanosystems (cellsomes, CSMs), having the following main properties: (i) self-recognition (homotypic targeting), (ii) evading early recognition by immune cells, and (iii) circumventing common drawbacks of nanoparticles interacting with cells. The development and optimization of protocols for synthesizing and characterizing nano-scale biomimetic nanocarriers were described in Section 3.1. The self-recognition capability between the CSMs and their source cell line was demonstrated for several tumoral cell lines. Moreover, hybrid CSMs composed of tumoral and non-tumoral cell membranes fragments proved the possibility of translating the targeting capabilities of the tumoral derived CSMs into other CSMs, thereby expanding their versatility and potential applications. Cell membrane coating of solid NPs (*i.e.*, polystyrene NPs selected as model) was also capable of transferring key functionalities of the origin cells to the nanoconstructs, modifying the NP-cell interactions, in 2D and 3D cell culture models.

The results obtained from these studies lead to a better understanding to control nanocarriers for a more efficient targeting and to mimic the cell membrane signaling complexity in order to interact with other cells. Based on the results, which highlight their biomimetic properties and their exciting capability to interact with cells, the CSM-based carrier proved to be a promising candidate for the development of biocompatible DDS. Specifically, the developed nanosystems proved to be effective in the intracellular delivery of different cargos that otherwise would not overcome the cell membrane barrier or would be trapped in endo/lysosome compartments.

Two kinds of smart CSMs-based nanocarriers were set up in this study. One type, reported in section 3.2, is based on the stimuli-responsive drug

delivery hybrid nanostructure combining cell membrane derived nanovesicles and plasmonic NPs (GNRs). This photo-responsive biomimetic nanocarriers present several advantages: (i) targeting of specific cell populations (homotypic targeting); (ii) preventing cargo´s degradation; and (iii) spatio-temporal controlled cargo release into the cytosol of living cells, triggered by NIR stimulation. Through this procedure, photo-controlled intracellular delivery of non-cell permeant antibodies (Abs) was achieved without compromising cell viability and the biomolecule targeting capabilities; an anti-tubulin Ab was used, thereby enabling cytoskeleton immunolabeling. Moreover, NIR-triggered Ab release have proven by using two NIR laser illumination systems, namely a highly focused NIR laser for single cell experiments and unfocused NIR laser for illumination of thousands of cells. The versatility of this nanobuilding technology promises a straightforward access to other related immunocarriers (for instance, by integrating other Abs and/or using other cell membrane sources), which could operate as photoresponsive nanovaccines or highly selective nanomedicines for application in different immunotherapies.

A second alternative strategy to achieve the intracellular cargo delivery has successfully been developed in Section 3.3 by surface-engineering of the cell-derived nanocarrier to obtain fusogenic CSMs (FCSMs). This study has shown the ability of direct fusion between the phospholipidic structure of FCSMs and the plasmatic cell membrane. This new lipidic design of FCSMs (dye-labeled DOPE-DOTAP functionalized CSMs) allows to combine the features of cell membrane derived nanovesicles (homotypic targeting, biocompatibility, cargo encapsulation flexibility, easy manufacturing, *etc*.) with the ability to induce fusion events between the carrier´s phospholipidic structure and the cell membrane, avoiding the endocytosis pathway and lysosomal entrapping of the cargo. Fusogenic cell membrane derived nanovesicles showed a great potential as a cytoplasmic delivery tool, especially, for *in vitro* experiments. Manifold cargoes (from small molecules to large macromolecules) were efficiently encapsulated and rapidly delivered to the cytosol. This technology could represent a powerful tool for fast cytoplasmatic delivery of sensitive drugs, especially proteins and nucleic acids, enabling of designing a new generation of carriers for nanovaccines.

Overall, the scientific results obtained, as well as the know-how acquired in this thesis, will contribute to a wide range of potential innovations in the nanomedicine field, for the design of smart drug delivery carriers. Their potential application for the treatment of different diseases may be achieved

by selecting the specific cargo and a biomimetic coating capable of translating and implementing specific cell functions and improving pharmacokinetics and targeting specific tissues. The efficient intracellular delivery of exogenous compounds and macromolecular cargo will facilitate progress in multiple applications, including cell-based therapies, gene editing, cell reprograming, nanovaccines and intracellular biomarker detection, among others.

5. Bibliography

1. Porter, A. L.; Youtie, J.; Shapira, P.; Schoeneck, D. J., Refining search terms for nanotechnology. *Journal of Nanoparticle Research* **2008,** *10* (5), 715-728.

2. Drexler, K. E., Nanotechnology: From Feynman to Funding. *Bulletin of Science, Technology and Society* **2004,** *24* (1), 21-27.

3. Kovvuru, S. K.; Mahita, V. N.; Manjunatha, B. S.; Babu, B. S., *Nanotechnology: The Emerging Science in Dentistry*. Jaypee Brothers Medical Publishers: 2012; Vol. 2, p 33-36.

4. Murray, C. B. K. C. R.; Bawendi, M. G., Synthesis and Characterization of Monodisperse Nanocrystals and Close-Packed Nanocrystal Assemblies. *Annual Review of Materials Science* **2000,** *30*, 545-610.

5. Rogers-Hayden, T.; Pidgeon, N., Moving engagement "upstream"? Nanotechnologies and the Royal Society and Royal Academy of Engineering's inquiry. *Public Understanding of Science* **2007,** *16* (3), 345-364.

6. Goesmann, H.; Feldmann, C., Nanoparticulate Functional Materials. *Angewandte Chemie International Edition* **2010,** *49* (8), 1362-1395.

7. Brunk, C.; Warren, O.; Chan, C. W.; Walker, N. J. *Small is Different: A Science Perspective on the Regulatory Channenges of the Nanoscale*; 2008.

8. Albanese, A.; Tang, P. S.; Chan, W. C., The effect of nanoparticle size, shape, and surface chemistry on biological systems. *Annu Rev Biomed Eng* **2012,** *14*, 1-16.

9. Sanchez, C.; Belleville, P.; Popall, M.; Nicole, L., Applications of advanced hybrid organic–inorganic nanomaterials: from laboratory to market. *Chemical Society Reviews* **2011,** *40* (2), 696-753.

10. Moon, J. J.; Huang, B.; Irvine, D. J., Engineering Nano- and Microparticles to Tune Immunity. *Advanced Materials* **2012,** *24* (28), 3724-3746.

11. Sun, T.; Zhang, Y. S.; Pang, B.; Hyun, D. C.; Yang, M.; Xia, Y., Engineered nanoparticles for drug delivery in cancer therapy. *Angew Chem Int Ed Engl* **2014,** *53* (46), 12320-64.

12. Irvine, D. J.; Hanson, M. C.; Rakhra, K.; Tokatlian, T., Synthetic Nanoparticles for Vaccines and Immunotherapy. *Chemical Reviews* **2015,** *115* (19), 11109-11146.

13. Pelaz, B.; Alexiou, C.; Alvarez-Puebla, R. A.; Alves, F.; Andrews, A. M.; Ashraf, S.; Balogh, L. P.; Ballerini, L.; Bestetti, A.; Brendel, C.; Bosi, S.; Carril, M.; Chan, W. C. W.; Chen, C.; Chen, X.; Chen, X.; Cheng, Z.; Cui, D.; Du, J.; Dullin, C.; Escudero, A.; Feliu, N.; Gao, M.; George, M.; Gogotsi, Y.; Grünweller, A.; Gu, Z.; Halas, N. J.; Hampp, N.; Hartmann, R. K.; Hersam, M. C.; Hunziker, P.; Jian, J.; Jiang, X.; Jungebluth, P.; Kadhiresan, P.; Kataoka, K.; Khademhosseini, A.; Kopeček, J.; Kotov, N. A.; Krug, H. F.; Lee, D. S.; Lehr, C.-M.; Leong, K. W.; Liang, X.-J.; Ling Lim, M.; Liz-Marzán, L. M.; Ma, X.; Macchiarini, P.; Meng, H.; Möhwald, H.; Mulvaney, P.; Nel, A. E.; Nie, S.; Nordlander, P.; Okano, T.; Oliveira, J.; Park, T. H.; Penner, R. M.; Prato, M.; Puntes, V.; Rotello, V. M.; Samarakoon, A.; Schaak, R. E.; Shen, Y.; Sjöqvist, S.; Skirtach, A. G.; Soliman, M. G.; Stevens, M. M.; Sung, H.-W.; Tang, B. Z.; Tietze, R.; Udugama, B. N.; VanEpps, J. S.; Weil, T.; Weiss, P. S.; Willner, I.; Wu, Y.; Yang, L.; Yue, Z.; Zhang, Q.; Zhang, Q.; Zhang, X.-E.; Zhao, Y.; Zhou, X.; Parak, W. J., Diverse Applications of Nanomedicine. *ACS Nano* **2017,** *11* (3), 2313-2381.

14. Polo, E.; Navarro Poupard, M. F.; Guerrini, L.; Taboada, P.; Pelaz, B.; Alvarez-Puebla, R. A.; del Pino, P., Colloidal bioplasmonics. *Nano Today* **2018,** *20*, 58-73.

15. Parak, W. J.; Gerion, D.; Pellegrino, T.; Zanchet, D.; Micheel, C.; Williams, S. C.; Boudreau, R.; Gros, M. A. L.; Larabell, C. A.; Alivisatos, A. P., Biological applications of colloidal nanocrystals. *Nanotechnology* **2003,** *14* (7), R15-R27.

16. Colombo, M.; Carregal-Romero, S.; Casula, M. F.; Gutiérrez, L.; Morales, M. P.; Böhm, I. B.; Heverhagen, J. T.; Prosperi, D.; Parak, W. J., Biological applications of magnetic nanoparticles. *Chemical Society Reviews* **2012,** *41* (11), 4306-4334.

17. Ghosh Chaudhuri, R.; Paria, S., Core/Shell Nanoparticles: Classes, Properties, Synthesis Mechanisms, Characterization, and Applications. *Chemical Reviews* **2012,** *112* (4), 2373-2433.

18. Malam, Y.; Loizidou, M.; Seifalian, A. M., Liposomes and nanoparticles: nanosized vehicles for drug delivery in cancer. *Trends in Pharmacological Sciences* **2009,** *30* (11), 592-599.

19. Tenchov, R.; Bird, R.; Curtze, A. E.; Zhou, Q., Lipid Nanoparticles─From Liposomes to mRNA Vaccine Delivery, a Landscape of Research Diversity and Advancement. *ACS Nano* **2021,** *15* (11), 16982-17015.

20. Mustafa, D. E.; Yang, T.; Xuan, Z.; Chen, S.; Tu, H.; Zhang, A., Surface Plasmon Coupling Effect of Gold Nanoparticles with Different Shape and Size on Conventional Surface Plasmon Resonance Signal. *Plasmonics* **2010,** *5* (3), 221-231.

21. Sperling, R. A.; Parak, W. J., Surface modification, functionalization and bioconjugation of colloidal inorganic nanoparticles. *Philosophical Transactions of the Royal Society A: Mathematical, Physical and Engineering Sciences* **2010,** *368* (1915), 1333-1383.

22. Katz, E.; Willner, I., Integrated Nanoparticle-Biomolecule Hybrid Systems: Synthesis, Properties, and Applications. *Angewandte Chemie International Edition* **2004,** *43* (45), 6042-6108.

23. Willner, I.; Baron, R.; Willner, B., Integrated nanoparticle–biomolecule systems for biosensing and bioelectronics. *Biosensors and Bioelectronics* **2007,** *22* (9-10), 1841-1852.

24. Peng, E.; Wang, F.; Xue, J. M., Nanostructured magnetic nanocomposites as MRI contrast agents. *Journal of Materials Chemistry B* **2015,** *3* (11), 2241-2276.

25. Sabu, C.; Rejo, C.; Kotta, S.; Pramod, K., Bioinspired and biomimetic systems for advanced drug and gene delivery. *Journal of Controlled Release* **2018,** *287* (June), 142-155.

26. Fortina, P.; Kricka, L. J.; Surrey, S.; Grodzinski, P., Nanobiotechnology: the promise and reality of new approaches to molecular recognition. *Trends in Biotechnology* **2005,** *23* (4), 168-173.

27. Jain, K. K., Applications of Nanobiotechnology in Clinical Diagnostics. *Clinical Chemistry* **2007,** *53* (11), 2002-2009.

28. Na, H. B.; Song, I. C.; Hyeon, T., Inorganic Nanoparticles for MRI Contrast Agents. *Advanced Materials* **2009,** *21* (21), 2133-2148.

29. Huang, J.; Xie, J.; Chen, K.; Bu, L.; Lee, S.; Cheng, Z.; Li, X.; Chen, X., HSA coated MnO nanoparticles with prominent MRI contrast for tumor imaging. *Chemical Communications* **2010,** *46* (36), 6684-6684.

30. Xu, C.; Akakuru, O. U.; Ma, X.; Zheng, J.; Zheng, J.; Wu, A., Nanoparticle-Based Wound Dressing: Recent Progress in the Detection and Therapy of Bacterial Infections. *Bioconjugate Chemistry* **2020,** *31* (7), 1708-1723.

31. Wang, X.; Qian, X.; Beitler, J. J.; Chen, Z. G.; Khuri, F. R.; Lewis, M. M.; Shin, H. J. C.; Nie, S.; Shin, D. M., Detection of Circulating Tumor Cells in Human Peripheral Blood Using Surface-Enhanced Raman Scattering Nanoparticles. *Cancer Research* **2011,** *71* (5), 1526-1532.

32. Maggiorella, L.; Barouch, G.; Devaux, C.; Pottier, A.; Deutsch, E.; Bourhis, J.; Borghi, E.; Levy, L., Nanoscale radiotherapy with hafnium oxide nanoparticles. *Future Oncology* **2012,** *8* (9), 1167-1181.

33. Deng, H.; Zhong, Y.; Du, M.; Liu, Q.; Fan, Z.; Dai, F.; Zhang, X., Theranostic Self-Assembly Structure of Gold Nanoparticles for NIR Photothermal Therapy and X-Ray Computed Tomography Imaging. *Theranostics* **2014,** *4* (9), 904-918.

34. Soppimath, K. S.; Aminabhavi, T. M.; Kulkarni, A. R.; Rudzinski, W. E., Biodegradable polymeric nanoparticles as drug delivery devices. *Journal of Controlled Release* **2001,** *70* (1-2), 1-20.

35. Wilczewska, A. Z.; Niemirowicz, K.; Markiewicz, K. H.; Car, H., Nanoparticles as drug delivery systems. *Pharmacological Reports* **2012,** *64* (5), 1020-1037.

36. Shenoy, D. B.; Amiji, M. M., Poly(ethylene oxide)-modified poly(ε-caprolactone) nanoparticles for targeted delivery of tamoxifen in breast cancer. *International Journal of Pharmaceutics* **2005,** *293* (1-2), 261-270.

37. Riley, R. S.; June, C. H.; Langer, R.; Mitchell, M. J., Delivery technologies for cancer immunotherapy. *Nature Reviews Drug Discovery* **2019,** *18* (3), 175-196.

38. McDonald, D. M.; Baluk, P., Significance of Blood Vessel Leakiness in Cancer. *Cancer Research* **2002,** *62* (3), 867-874.

39. Bates, D. O.; Hillman, N. J.; Williams, B.; Neal, C. R.; Pocock, T. M., Regulation of microvascular permeability by vascular endothelial growth factors. *Journal of Anatomy* **2002,** *200* (6), 581-597.

40. Nagamitsu, A.; Greish, K.; Maeda, H., Elevating Blood Pressure as a Strategy to Increase Tumor-targeted Delivery of Macromolecular Drug

SMANCS: Cases of Advanced Solid Tumors. *Japanese Journal of Clinical Oncology* **2009,** *39* (11), 756-766.

41. Kiessling, F.; Hennink, W. E.; Storm, G., Drug targeting to tumors: Principles, pitfalls and (pre-) clinical progress. *Journal of Controlled Release* **2012,** *161* (2), 175-187.

42. Upreti, M.; Jyoti, A.; Sethi, P., Tumor microenvironment and nanotherapeutics. *Translational Cancer Research* **2013,** *2* (4), 309-319.

43. Mitchell, M. J.; Jain, R. K.; Langer, R., Engineering and physical sciences in oncology: Challenges and opportunities. In *Nature Reviews Cancer*, Nature Publishing Group: 2017; Vol. 17, pp 659-675.

44. Shi, Y.; van der Meel, R.; Chen, X.; Lammers, T., The EPR effect and beyond: Strategies to improve tumor targeting and cancer nanomedicine treatment efficacy. In *Theranostics*, Ivyspring International Publisher: 2020; Vol. 10, pp 7921-7924.

45. Bertrand, N.; Wu, J.; Xu, X.; Kamaly, N.; Farokhzad, O. C., Cancer nanotechnology: The impact of passive and active targeting in the era of modern cancer biology. *Advanced Drug Delivery Reviews* **2014,** *66*, 2-25.

46. Lammers, T.; Hennink, W. E.; Storm, G., Tumour-targeted nanomedicines: principles and practice. *British Journal of Cancer* **2008,** *99* (3), 392-397.

47. Misra, R.; Acharya, S.; Sahoo, S. K., Cancer nanotechnology: application of nanotechnology in cancer therapy. *Drug Discovery Today* **2010,** *15* (19-20), 842-850.

48. Acharya, S.; Dilnawaz, F.; Sahoo, S. K., Targeted epidermal growth factor receptor nanoparticle bioconjugates for breast cancer therapy. *Biomaterials* **2009,** *30* (29), 5737-5750.

49. Guo, J.; Gao, X.; Su, L.; Xia, H.; Gu, G.; Pang, Z.; Jiang, X.; Yao, L.; Chen, J.; Chen, H., Aptamer-functionalized PEG-PLGA nanoparticles for enhanced anti-glioma drug delivery. *Biomaterials* **2011,** *32* (31), 8010-8020.

50. Hong, M.; Zhu, S.; Jiang, Y.; Tang, G.; Sun, C.; Fang, C.; Shi, B.; Pei, Y., Novel anti-tumor strategy: PEG-hydroxycamptothecin conjugate loaded transferrin-PEG-nanoparticles. *Journal of Controlled Release* **2010,** *141* (1), 22-29.

51. Master, A. M.; Sen Gupta, A., EGF receptor-targeted nanocarriers for enhanced cancer treatment. In *Nanomedicine*, Future Medicine Ltd London, UK: 2012; Vol. 7, pp 1895-1906.

52. Nukolova, N. V.; Oberoi, H. S.; Cohen, S. M.; Kabanov, A. V.; Bronich, T. K., Folate-decorated nanogels for targeted therapy of ovarian cancer. *Biomaterials* **2011,** *32* (23), 5417-5426.

53. Xiong, H.; Du, S.; Ni, J.; Zhou, J.; Yao, J., Mitochondria and nuclei dual-targeted heterogeneous hydroxyapatite nanoparticles for enhancing therapeutic efficacy of doxorubicin. *Biomaterials* **2016,** *94*, 70-83.

54. Xu, C.; Xie, J.; Kohler, N.; Walsh, E. G.; Chin, Y. E.; Sun, S., Monodisperse magnetite nanoparticles coupled with nuclear localization signal peptide for cell-nucleus targeting. *Chemistry - An Asian Journal* **2008,** *3* (3), 548-552.

55. Koshkaryev, A.; Piroyan, A.; Torchilin, V. P., Increased apoptosis in cancer cells in vitro and in vivo by ceramides in transferrin-modified liposomes. *Cancer Biology and Therapy* **2012,** *13* (1), 50-60.

56. Gao, W.; Chan, J. M.; Farokhzad, O. C., PH-responsive nanoparticles for drug delivery. In *Molecular Pharmaceutics*, American Chemical Society: 2010; Vol. 7, pp 1913-1920.

57. Li, Z.; Clemens, D. L.; Lee, B. Y.; Dillon, B. J.; Horwitz, M. A.; Zink, J. I., Mesoporous Silica Nanoparticles with pH-Sensitive Nanovalves for Delivery of Moxifloxacin Provide Improved Treatment of Lethal Pneumonic Tularemia. *ACS Nano* **2015,** *9* (11), 10778-10789.

58. Remant, R. B.; Chandrashekaran, V.; Cheng, B.; Chen, H.; Peña, M. M. O.; Zhang, J.; Montgomery, J.; Xu, P., Redox potential ultrasensitive nanoparticle for the targeted delivery of camptothecin to HER2-positive cancer cells. *Molecular Pharmaceutics* **2014,** *11* (6), 1897-1905.

59. Renoux, B.; Raes, F.; Legigan, T.; Péraudeau, E.; Eddhif, B.; Poinot, P.; Tranoy-Opalinski, I.; Alsarraf, J.; Koniev, O.; Kolodych, S.; Lerondel, S.; Le Pape, A.; Clarhaut, J.; Papot, S., Targeting the tumour microenvironment with an enzyme-responsive drug delivery system for the efficient therapy of breast and pancreatic cancers. *Chemical Science* **2017,** *8* (5), 3427-3433.

60. Mo, R.; Jiang, T.; Disanto, R.; Tai, W.; Gu, Z., ATP-triggered anticancer drug delivery. *Nature Communications* **2014,** *5* (1), 1-10.

61. Ruehle, B.; Clemens, D. L.; Lee, B. Y.; Horwitz, M. A.; Zink, J. I., A Pathogen-Specific Cargo Delivery Platform Based on Mesoporous Silica Nanoparticles. *Journal of the American Chemical Society* **2017,** *139* (19), 6663-6668.

62. Sun, W.; Jiang, T.; Lu, Y.; Reiff, M.; Mo, R.; Gu, Z., Cocoon-like self-degradable DNA nanoclew for anticancer drug delivery. *Journal of the American Chemical Society* **2014,** *136* (42), 14722-14725.

63. De Smet, M.; Heijman, E.; Langereis, S.; Hijnen, N. M.; Grüll, H., Magnetic resonance imaging of high intensity focused ultrasound mediated drug delivery from temperature-sensitive liposomes: An in vivo proof-of-concept study. *Journal of Controlled Release* **2011,** *150* (1), 102-110.

64. Paris, J. L.; Cabanas, M. V.; Manzano, M.; Vallet-Regí, M., Polymer-Grafted Mesoporous Silica Nanoparticles as Ultrasound-Responsive Drug Carriers. *ACS Nano* **2015,** *9* (11), 11023-11033.

65. Li, H.; Tan, L. L.; Jia, P.; Li, Q. L.; Sun, Y. L.; Zhang, J.; Ning, Y. Q.; Yu, J.; Yang, Y. W., Near-infrared light-responsive supramolecular nanovalve based on mesoporous silica-coated gold nanorods. *Chemical Science* **2014,** *5* (7), 2804-2808.

66. Qiu, M.; Wang, D.; Liang, W.; Liu, L.; Zhang, Y.; Chen, X.; Sang, D. K.; Xing, C.; Li, Z.; Dong, B.; Xing, F.; Fan, D.; Bao, S.; Zhang, H.; Cao, Y., Novel concept of the smart NIR-light-controlled drug release of black phosphorus nanostructure for cancer therapy. *Proceedings of the National Academy of Sciences of the United States of America* **2018,** *115* (3), 501-506.

67. Guisasola, E.; Asín, L.; Beola, L.; De La Fuente, J. M.; Baeza, A.; Vallet-Regí, M., Beyond Traditional Hyperthermia: In Vivo Cancer Treatment with Magnetic-Responsive Mesoporous Silica Nanocarriers. *ACS Applied Materials and Interfaces* **2018,** *10* (15), 12518-12525.

68. Saint-Cricq, P.; Deshayes, S.; Zink, J. I.; Kasko, A. M., Magnetic field activated drug delivery using thermodegradable azo-functionalised PEG-coated core-shell mesoporous silica nanoparticles. *Nanoscale* **2015,** *7* (31), 13168-13172.

69. Kong, S. D.; Zhang, W.; Lee, J. H.; Brammer, K.; Lal, R.; Karin, M.; Jin, S., Magnetically vectored nanocapsules for tumor penetration and remotely switchable on-demand drug release. *Nano Letters* **2010,** *10* (12), 5088-5092.

70. Min, H. S.; Son, S.; You, D. G.; Lee, T. W.; Lee, J.; Lee, S.; Yhee, J. Y.; Lee, J.; Han, M. H.; Park, J. H.; Kim, S. H.; Choi, K.; Park, K.; Kim, K.; Kwon, I. C., Chemical gas-generating nanoparticles for tumor-targeted ultrasound imaging and ultrasound-triggered drug delivery. *Biomaterials* **2016,** *108*, 57-70.

71. Correa-Paz, C.; Navarro Poupard, M. F.; Polo, E.; Rodríguez-Pérez, M.; Taboada, P.; Iglesias-Rey, R.; Hervella, P.; Sobrino, T.; Vivien, D.; Castillo, J.; del Pino, P.; Campos, F.; Pelaz, B., In vivo ultrasound-activated delivery of recombinant tissue plasminogen activator from the cavity of sub-micrometric capsules. *Journal of Controlled Release* **2019,** *308*, 162-171.

72. Weissleder, R., A clearer vision for in vivo imaging. *Nature Biotechnology* **2001,** *19* (4), 316-317.

73. Agarwal, A.; MacKey, M. A.; El-Sayed, M. A.; Bellamkonda, R. V., Remote triggered release of doxorubicin in tumors by synergistic application of thermosensitive liposomes and gold nanorods. *ACS Nano* **2011,** *5* (6), 4919-4926.

74. Dickerson, E. B.; Dreaden, E. C.; Huang, X.; El-Sayed, I. H.; Chu, H.; Pushpanketh, S.; McDonald, J. F.; El-Sayed, M. A., Gold nanorod assisted near-infrared plasmonic photothermal therapy (PPTT) of squamous cell carcinoma in mice. *Cancer Letters* **2008,** *269* (1), 57-66.

75. Bardhan, R.; Lal, S.; Joshi, A.; Halas, N. J., Theranostic nanoshells: From probe design to imaging and treatment of cancer. *Accounts of Chemical Research* **2011,** *44* (10), 936-946.

76. Ambrosone, A.; Marchesano, V.; Carregal-Romero, S.; Intartaglia, D.; Parak, W. J.; Tortiglione, C., Control of Wnt/β-Catenin Signaling Pathway in Vivo via Light Responsive Capsules. *ACS Nano* **2016,** *10* (4), 4828-4834.

77. Carregal-Romero, S.; Ochs, M.; Rivera-Gil, P.; Ganas, C.; Pavlov, A. M.; Sukhorukov, G. B.; Parak, W. J., NIR-light triggered delivery of macromolecules into the cytosol. *Journal of Controlled Release* **2012,** *159* (1), 120-127.

78. Javiern, A. M.; Del Pino, P.; Bedard, M. F.; Ho, D.; Skirtach, A. G.; Sukhorukov, G. B.; Plank, C.; Parak, W. J., Photoactivated release of cargo from the cavity of polyelectrolyte capsules to the cytosol of cells. *Langmuir* **2008,** *24* (21), 12517-12520.

79. Ochs, M.; Carregal-Romero, S.; Rejman, J.; Braeckmans, K.; De Smedt, S. C.; Parak, W. J., Light-addressable capsules as caged compound matrix for controlled triggering of cytosolic reactions. *Angewandte Chemie - International Edition* **2013,** *52* (2), 695-699.

80. Kantner, K.; Rejman, J.; Kraft, K. V. L.; Soliman, M. G.; Zyuzin, M. V.; Escudero, A.; del Pino, P.; Parak, W. J., Laterally and Temporally Controlled Intracellular Staining by Light-Triggered Release of Encapsulated Fluorescent Markers. *Chemistry - A European Journal* **2018,** *24* (9), 2098-2102.

81. Bobo, D.; Robinson, K. J.; Islam, J.; Thurecht, K. J.; Corrie, S. R., Nanoparticle-Based Medicines: A Review of FDA-Approved Materials and Clinical Trials to Date. In *Pharmaceutical Research*, Springer New York LLC: 2016; Vol. 33, pp 2373-2387.

82. Zhang, Y. N.; Poon, W.; Tavares, A. J.; McGilvray, I. D.; Chan, W. C. W., Nanoparticle–liver interactions: Cellular uptake and hepatobiliary elimination. *Journal of Controlled Release* **2016,** *240*, 332-348.

83. Lo Giudice, M. C.; Herda, L. M.; Polo, E.; Dawson, K. A., In situ characterization of nanoparticle biomolecular interactions in complex biological media by flow cytometry. *Nature Communications* **2016,** *7* (1), 1-10.

84. Moghimi, S. M.; Hunter, A. C.; Andresen, T. L., Factors controlling nanoparticle pharmacokinetics: An integrated analysis and perspective. *Annual Review of Pharmacology and Toxicology* **2012,** *52*, 481-503.

85. Polo, E.; Collado, M.; Pelaz, B.; Del Pino, P., Advances toward More Efficient Targeted Delivery of Nanoparticles in Vivo: Understanding Interactions between Nanoparticles and Cells. *ACS Nano* **2017,** *11* (3), 2397-2402.

86. Lundqvist, M.; Augustsson, C.; Lilja, M.; Lundkvist, K.; Dahlbäck, B.; Linse, S.; Cedervall, T., The nanoparticle protein corona formed in human blood or human blood fractions. *PLoS ONE* **2017,** *12* (4), e0175871-e0175871.

87. Yang, Q.; Lai, S. K., Anti-PEG immunity: emergence, characteristics, and unaddressed questions. *Wiley Interdisciplinary Reviews: Nanomedicine and Nanobiotechnology* **2015,** *7* (5), 655-677.

88. Knop, K.; Hoogenboom, R.; Fischer, D.; Schubert, U. S., Poly(ethylene glycol) in drug delivery: Pros and cons as well as potential

alternatives. In *Angewandte Chemie - International Edition*, John Wiley & Sons, Ltd: 2010; Vol. 49, pp 6288-6308.

89. Al-jamal, T.; Kostarelos, K., Liposomes: From a Clinically Established Drug Delivery System to a Nanoparticle Platform for Theranostic Nanomedicine. **2011,** *44* (10), 48-48.

90. Muthu, M. S.; Feng, S. S., Theranostic liposomes for cancer diagnosis and treatment: Current development and pre-clinical success. In *Expert Opinion on Drug Delivery*, Taylor & Francis: 2013; Vol. 10, pp 151-155.

91. Beltrán-Gracia, E.; López-Camacho, A.; Higuera-Ciapara, I.; Velázquez-Fernández, J. B.; Vallejo-Cardona, A. A., Nanomedicine review: clinical developments in liposomal applications. *Cancer Nanotechnology* **2019,** *10* (1), 11.

92. Immordino, M. L.; Dosio, F.; Cattel, L., Stealth liposomes: Review of the basic science, rationale, and clinical applications, existing and potential. In *International Journal of Nanomedicine*, Dove Press: 2006; Vol. 1, pp 297-315.

93. Torchilin, V. P., Recent advances with liposomes as pharmaceutical carriers. In *Nature Reviews Drug Discovery*, Nature Publishing Group: 2005; Vol. 4, pp 145-160.

94. Fang, R. H.; Kroll, A. V.; Gao, W.; Zhang, L., Cell Membrane Coating Nanotechnology. *Advanced Materials* **2018,** *30* (23), 1-34.

95. Chai, Z.; Hu, X.; Wei, X.; Zhan, C.; Lu, L.; Jiang, K.; Su, B.; Ruan, H.; Ran, D.; Fang, R. H.; Zhang, L.; Lu, W., A facile approach to functionalizing cell membrane-coated nanoparticles with neurotoxin-derived peptide for brain-targeted drug delivery. *Journal of Controlled Release* **2017,** *264*, 102-111.

96. Luk, B. T.; Fang, R. H.; Hu, C. M. J.; Copp, J. A.; Thamphiwatana, S.; Dehaini, D.; Gao, W.; Zhang, K.; Li, S.; Zhang, L., Safe and immunocompatible nanocarriers cloaked in RBC membranes for drug delivery to treat solid tumors. *Theranostics* **2016,** *6* (7), 1004-1011.

97. Qiao, Z.; Wang, Z.; Zhang, C.; Yuan, S.; Zhu, Y.; Wang, J., Engineering red-blood-cell-membrane–coated nanoparticles for broad biomedical applications. *AIChE Journal* **2012,** *59* (4), 215-228.

98. Lang, T.; Yin, Q.; Li, Y., Progress of Cell-Derived Biomimetic Drug Delivery Systems for Cancer Therapy. *Advanced Therapeutics* **2018,** *1* (7), 1800053-1800053.

99. Wu, Z.; Esteban-Fernández De Ávila, B.; Martín, A.; Christianson, C.; Gao, W.; Thamphiwatana, S. K.; Escarpa, A.; He, Q.; Zhang, L.; Wang, J., RBC micromotors carrying multiple cargos towards potential theranostic applications. *Nanoscale* **2015,** *7* (32), 13680-13686.

100. Shi, Q.; Montgomery, R. R., Platelets as delivery systems for disease treatments. In *Advanced Drug Delivery Reviews*, Elsevier: 2010; Vol. 62, pp 1196-1203.

101. Levy, O.; Brennen, W. N.; Han, E.; Rosen, D. M.; Musabeyezu, J.; Safaee, H.; Ranganath, S.; Ngai, J.; Heinelt, M.; Milton, Y.; Wang, H.; Bhagchandani, S. H.; Joshi, N.; Bhowmick, N.; Denmeade, S. R.; Isaacs, J. T.; Karp, J. M., A prodrug-doped cellular Trojan Horse for the potential treatment of prostate cancer. *Biomaterials* **2016,** *91*, 140-150.

102. Fu, J.; Wang, D.; Mei, D.; Zhang, H.; Wang, Z.; He, B.; Dai, W.; Zhang, H.; Wang, X.; Zhang, Q., Macrophage mediated biomimetic delivery system for the treatment of lung metastasis of breast cancer. *Journal of Controlled Release* **2015,** *204*, 11-19.

103. Rosenthal, J. A.; Chen, L.; Baker, J. L.; Putnam, D.; DeLisa, M. P., Pathogen-like particles: Biomimetic vaccine carriers engineered at the nanoscale. In *Current Opinion in Biotechnology*, Elsevier Ltd: 2014; Vol. 28, pp 51-58.

104. Paulitschke, M.; Nash, G. B.; Anstee, D. J.; Tanner, M. J. A.; Gratzer, W. B., Perturbation of red blood cell membrane rigidity by extracellular ligands. *Blood* **1995,** *86* (1), 342-348.

105. Naldini, L., Ex vivo gene transfer and correction for cell-based therapies. *Nature Reviews Genetics* **2011,** *12* (5), 301-315.

106. Van Niel, G.; D'Angelo, G.; Raposo, G., Shedding light on the cell biology of extracellular vesicles. In *Nature Reviews Molecular Cell Biology*, Nature Publishing Group: 2018; Vol. 19, pp 213-228.

107. Lamichhane, T. N.; Jeyaram, A.; Patel, D. B.; Parajuli, B.; Livingston, N. K.; Arumugasaamy, N.; Schardt, J. S.; Jay, S. M., Oncogene Knockdown via Active Loading of Small RNAs into Extracellular Vesicles by Sonication. *Cellular and Molecular Bioengineering* **2016,** *9* (3), 315-324.

108. Ohno, S. I.; Takanashi, M.; Sudo, K.; Ueda, S.; Ishikawa, A.; Matsuyama, N.; Fujita, K.; Mizutani, T.; Ohgi, T.; Ochiya, T.; Gotoh, N.; Kuroda, M., Systemically injected exosomes targeted to EGFR deliver antitumor microrna to breast cancer cells. *Molecular Therapy* **2013,** *21* (1), 185-191.

109. Tian, Y.; Li, S.; Song, J.; Ji, T.; Zhu, M.; Anderson, G. J.; Wei, J.; Nie, G., A doxorubicin delivery platform using engineered natural membrane vesicle exosomes for targeted tumor therapy. *Biomaterials* **2014,** *35* (7), 2383-2390.

110. Rachakatla, R. S.; Balivada, S.; Seo, G. M.; Myers, C. B.; Wang, H.; Samarakoon, T. N.; Dani, R.; Pyle, M.; Kroh, F. O.; Walker, B.; Leaym, X.; Koper, O. B.; Chikan, V.; Bossmann, S. H.; Tamura, M.; Troyer, D. L., Attenuation of Mouse Melanoma by A/C magnetic field after delivery of Bi-magnetic nanoparticles by neural progenitor cells. *ACS Nano* **2010,** *4* (12), 7093-7104.

111. Kooijmans, S. A. A.; Vader, P.; van Dommelen, S. M.; van Solinge, W. W.; Schiffelers, R. M., Exosome mimetics: A novel class of drug delivery systems. In *International Journal of Nanomedicine*, Dove Press: 2012; Vol. 7, pp 1525-1541.

112. Hu, C. M. J.; Zhang, L.; Aryal, S.; Cheung, C.; Fang, R. H.; Zhang, L., Erythrocyte membrane-camouflaged polymeric nanoparticles as a biomimetic delivery platform. *Proceedings of the National Academy of Sciences of the United States of America* **2011,** *108* (27), 10980-10985.

113. Hu, C. M. J.; Fang, R. H.; Luk, B. T.; Chen, K. N. H.; Carpenter, C.; Gao, W.; Zhang, K.; Zhang, L., 'Marker-of-self' functionalization of nanoscale particles through a top-down cellular membrane coating approach. *Nanoscale* **2013,** *5* (7), 2664-2668.

114. Luk, B. T.; Jack Hu, C. M.; Fang, R. H.; Dehaini, D.; Carpenter, C.; Gao, W.; Zhang, L., Interfacial interactions between natural RBC membranes and synthetic polymeric nanoparticles. *Nanoscale* **2014,** *6* (5), 2730-2737.

115. Zhai, Y.; Su, J.; Ran, W.; Zhang, P.; Yin, Q.; Zhang, Z.; Yu, H.; Li, Y., Preparation and application of cell membrane-camouflaged nanoparticles for cancer therapy. In *Theranostics*, Ivyspring International Publisher: 2017; Vol. 7, pp 2575-2592.

116. Reuven, E. M.; Leviatan Ben-Arye, S.; Yu, H.; Duchi, R.; Perota, A.; Conchon, S.; Bachar Abramovitch, S.; Soulillou, J. P.; Galli, C.; Chen, X.; Padler-Karavani, V., Biomimetic Glyconanoparticle Vaccine for Cancer Immunotherapy. *ACS Nano* **2019,** *13* (3), 2936-2947.

117. Liang, X.; Ye, X.; Wang, C.; Xing, C.; Miao, Q.; Xie, Z.; Chen, X.; Zhang, X.; Zhang, H.; Mei, L., Photothermal cancer immunotherapy by erythrocyte membrane-coated black phosphorus formulation. *Journal of Controlled Release* **2019,** *296*, 150-161.

118. Gentry, P. A., The mammalian blood platelet: Its role in haemostasis, inflammation and tissue repair. In *Journal of Comparative Pathology*, J Comp Pathol: 1992; Vol. 107, pp 243-270.

119. Ojha, A.; Nandi, D.; Batra, H.; Singhal, R.; Annarapu, G. K.; Bhattacharyya, S.; Seth, T.; Dar, L.; Medigeshi, G. R.; Vrati, S.; Vikram, N. K.; Guchhait, P., Platelet activation determines the severity of thrombocytopenia in dengue infection. *Scientific Reports* **2017,** *7*.

120. Schumacher, D.; Strilic, B.; Sivaraj, K. K.; Wettschureck, N.; Offermanns, S., Platelet-Derived Nucleotides Promote Tumor-Cell Transendothelial Migration and Metastasis via P2Y2 Receptor. *Cancer Cell* **2013,** *24* (1), 130-137.

121. Gay, L. J.; Felding-Habermann, B., Contribution of platelets to tumour metastasis. In *Nature Reviews Cancer*, Nature Publishing Group: 2011; Vol. 11, pp 123-134.

122. Chaffer, C. L.; Weinberg, R. A., A perspective on cancer cell metastasis. In *Science*, American Association for the Advancement of Science: 2011; Vol. 331, pp 1559-1564.

123. Hu, Q.; Sun, W.; Qian, C.; Wang, C.; Bomba, H. N.; Gu, Z., Anticancer Platelet-Mimicking Nanovehicles. *Advanced Materials* **2015,** *27* (44), 7043-7050.

124. Hu, Q.; Sun, W.; Qian, C.; Bomba, H. N.; Xin, H.; Gu, Z., Relay Drug Delivery for Amplifying Targeting Signal and Enhancing Anticancer Efficacy. *Advanced Materials* **2017,** *29* (13), 1605803-1605803.

125. Parodi, A.; Quattrocchi, N.; Van De Ven, A. L.; Chiappini, C.; Evangelopoulos, M.; Martinez, J. O.; Brown, B. S.; Khaled, S. Z.; Yazdi, I. K.; Enzo, M. V.; Isenhart, L.; Ferrari, M.; Tasciotti, E., Synthetic nanoparticles functionalized with biomimetic leukocyte membranes possess cell-like functions. *Nature Nanotechnology* **2013,** *8* (1), 61-68.

126. Corbo, C.; Parodi, A.; Evangelopoulos, M.; A. Engler, D.; K. Matsunami, R.; C. Engler, A.; Molinaro, R.; Scaria, S.; Salvatore, F.; Tasciotti, E., Proteomic Profiling of a Biomimetic Drug Delivery Platform.

127. Molinaro, R.; Corbo, C.; Martinez, J. O.; Taraballi, F.; Evangelopoulos, M.; Minardi, S.; Yazdi, I. K.; Zhao, P.; De Rosa, E.; Sherman, M. B.; De Vita, A.; Toledano Furman, N. E.; Wang, X.; Parodi, A.; Tasciotti, E., Biomimetic proteolipid vesicles for targeting inflamed tissues. *Nature Materials* **2016,** *15* (9), 1037-1046.

128. Martinez, J. O.; Molinaro, R.; Hartman, K. A.; Boada, C.; Sukhovershin, R.; De Rosa, E.; Kirui, D.; Zhang, S.; Evangelopoulos, M.; Carter, A. M.; Bibb, J. A.; Cooke, J. P.; Tasciotti, E., Biomimetic nanoparticles with enhanced affinity towards activated endothelium as versatile tools for theranostic drug delivery. *Theranostics* **2018,** *8* (4), 1131-1145.

129. Xuan, M.; Shao, J.; Dai, L.; Li, J.; He, Q., Macrophage Cell Membrane Camouflaged Au Nanoshells for in Vivo Prolonged Circulation Life and Enhanced Cancer Photothermal Therapy. *ACS Applied Materials and Interfaces* **2016,** *8* (15), 9610-9618.

130. Näkki, S.; Martinez, J. O.; Evangelopoulos, M.; Xu, W.; Lehto, V. P.; Tasciotti, E., Chlorin e6 Functionalized Theranostic Multistage Nanovectors Transported by Stem Cells for Effective Photodynamic Therapy. *ACS Applied Materials and Interfaces* **2017,** *9* (28), 23441-23449.

131. Corradetti, B.; Taraballi, F.; Martinez, J. O.; Minardi, S.; Basu, N.; Bauza, G.; Evangelopoulos, M.; Powell, S.; Corbo, C.; Tasciotti, E., Hyaluronic acid coatings as a simple and efficient approach to improve MSC homing toward the site of inflammation. *Scientific Reports* **2017,** *7* (1), 1-12.

132. Toledano Furman, N. E.; Lupu-Haber, Y.; Bronshtein, T.; Kaneti, L.; Letko, N.; Weinstein, E.; Baruch, L.; Machluf, M., Reconstructed stem cell nanoghosts: A natural tumor targeting platform. *Nano Letters* **2013,** *13* (7), 3248-3255.

133. Changyong, G.; Jurado-Sánchez, B., Stem Cell Membrane-Coated Nanogels for Highly Efficient In Vivo Tumor Targeted Drug Delivery microrobot View project Applications of Multiscaled Simulations on Biomembrane and Biomolecules View project. **2016**.

134. Siegel, R. L.; Miller, K. D.; Fedewa, S. A.; Ahnen, D. J.; Meester, R. G. S.; Barzi, A.; Jemal, A., Colorectal cancer statistics, 2017. *CA: A Cancer Journal for Clinicians* **2017,** *67* (3), 177-193.

135. Fang, R. H.; Hu, C. M. J.; Luk, B. T.; Gao, W.; Copp, J. A.; Tai, Y.; O'Connor, D. E.; Zhang, L., Cancer cell membrane-coated nanoparticles for anticancer vaccination and drug delivery. *Nano Letters* **2014,** *14* (4), 2181-2188.

136. Sun, H.; Su, J.; Meng, Q.; Yin, Q.; Chen, L.; Gu, W.; Zhang, P.; Zhang, Z.; Yu, H.; Wang, S.; Li, Y., Cancer-Cell-Biomimetic Nanoparticles for Targeted Therapy of Homotypic Tumors. *Advanced Materials* **2016,** *28* (43), 9581-9588.

137. Heimburg, J.; Yan, J.; Morey, S.; Glinskii, O. V.; Huxley, V. H.; Wild, L.; Klick, R.; Roy, R.; Glinsky, V. V.; Rittenhouse-Olson, K., Inhibition of spontaneous breast cancer metastasis by anti-Thomsen-Friedenreich antigen monoclonal antibody JAA-F11. *Neoplasia* **2006,** *8* (11), 939-948.

138. Zhao, Q.; Barclay, M.; Hilkens, J.; Guo, X.; Barrow, H.; Rhodes, J. M.; Yu, L. G., Interaction between circulating galectin-3 and cancer-associated MUC1 enhances tumour cell homotypic aggregation and prevents anoikis. *Molecular Cancer* **2010,** *9* (1), 1-12.

139. Fidler, I. J., The pathogenesis of cancer metastasis: The 'seed and soil' hypothesis revisited. In *Nature Reviews Cancer*, Nature Publishing Group: 2003; Vol. 3, pp 453-458.

140. Glinsky, V. V.; Glinsky, G. V.; Glinskii, O. V.; Huxley, V. H.; Turk, J. R.; Mossine, V. V.; Deutscher, S. L.; Pienta, K. J.; Quinn, T. P., Intravascular metastatic cancer cell homotypic aggregation at the sites of primary attachment to the endothelium. *Cancer research* **2003,** *63* (13), 3805-3811.

141. Naor, D.; Sionov, R. V.; Ish-Shalom, D., CD44: Structure, function, and association with the malignant process. In *Advances in Cancer Research*, Academic Press Inc.: 1997; Vol. 71, pp 241-319.

142. Ito, K.; Ralph, S. J., Inhibiting galectin-1 reduces murine lung metastasis with increased CD4+ and CD8+ T cells and reduced cancer cell adherence. *Clinical and Experimental Metastasis* **2012,** *29* (6), 561-572.

143. Wang, D.; Dong, H.; Li, M.; Cao, Y.; Yang, F.; Zhang, K.; Dai, W.; Wang, C.; Zhang, X., Erythrocyte–Cancer Hybrid Membrane

Camouflaged Hollow Copper Sulfide Nanoparticles for Prolonged Circulation Life and Homotypic-Targeting Photothermal/Chemotherapy of Melanoma. *ACS Nano* **2018,** *12* (6), 5241-5252.

144. Sun, H.; Su, J.; Meng, Q.; Yin, Q.; Chen, L.; Gu, W.; Zhang, Z.; Yu, H.; Zhang, P.; Wang, S.; Li, Y., Cancer Cell Membrane-Coated Gold Nanocages with Hyperthermia-Triggered Drug Release and Homotypic Target Inhibit Growth and Metastasis of Breast Cancer. *Advanced Functional Materials* **2017,** *27* (3).

145. Rao, L.; Bu, L. L.; Cai, B.; Xu, J. H.; Li, A.; Zhang, W. F.; Sun, Z. J.; Guo, S. S.; Liu, W.; Wang, T. H.; Zhao, X. Z., Cancer Cell Membrane-Coated Upconversion Nanoprobes for Highly Specific Tumor Imaging. *Adv Mater* **2016,** *28* (18), 3460-6.

146. Kroll, A. V.; Fang, R. H.; Jiang, Y.; Zhou, J.; Wei, X.; Yu, C. L.; Gao, J.; Luk, B. T.; Dehaini, D.; Gao, W.; Zhang, L., Nanoparticulate Delivery of Cancer Cell Membrane Elicits Multiantigenic Antitumor Immunity. *Advanced Materials* **2017,** *29* (47), 1703969-1703969.

147. Fontana, F.; Shahbazi, M. A.; Liu, D.; Zhang, H.; Mäkilä, E.; Salonen, J.; Hirvonen, J. T.; Santos, H. A., Multistaged Nanovaccines Based on Porous Silicon@Acetalated Dextran@Cancer Cell Membrane for Cancer Immunotherapy. *Advanced Materials* **2017,** *29* (7), 1603239-1603239.

148. Lollini, P.-L.; Cavallo, F.; Nanni, P.; Forni, G., Vaccines for tumour prevention. *Nature Reviews Cancer* **2006,** *6* (3), 204-216.

149. Lokhov, P. G.; Balashova, E. E., Cellular cancer vaccines: an update on the development of vaccines generated from cell surface antigens. *J Cancer* **2010,** *1*, 230-41.

150. Yameen, B.; Choi, W. I.; Vilos, C.; Swami, A.; Shi, J.; Farokhzad, O. C., Insight into nanoparticle cellular uptake and intracellular targeting. *Journal of Controlled Release* **2014,** *190*, 485-499.

151. Kim, K.; Ryu, S. M.; Kim, S. T.; Baek, G.; Kim, D.; Lim, K.; Chung, E.; Kim, S.; Kim, J. S., Highly efficient RNA-guided base editing in mouse embryos. *Nature Biotechnology* **2017,** *35* (5), 435-437.

152. Clift, D.; McEwan, W. A.; Labzin, L. I.; Konieczny, V.; Mogessie, B.; James, L. C.; Schuh, M., A Method for the Acute and Rapid Degradation of Endogenous Proteins. *Cell* **2017,** *171* (7), 1692-1706.e18.

153. König, I.; Zarrine-Afsar, A.; Aznauryan, M.; Soranno, A.; Wunderlich, B.; Dingfelder, F.; Stüber, J. C.; Plückthun, A.; Nettels, D.; Schuler, B., Single-molecule spectroscopy of protein conformational dynamics in live eukaryotic cells. *Nature Methods* **2015,** *12* (8), 773-779.

154. Lin, C.; Engbersen, J. F. J., Effect of chemical functionalities in poly(amido amine)s for non-viral gene transfection. *Journal of Controlled Release* **2008,** *132* (3), 267-272.

155. Erazo-Oliveras, A.; Najjar, K.; Dayani, L.; Wang, T. Y.; Johnson, G. A.; Pellois, J. P., Protein delivery into live cells by incubation with an endosomolytic agent. *Nature Methods* **2014,** *11* (8), 861-867.

156. Akishiba, M.; Takeuchi, T.; Kawaguchi, Y.; Sakamoto, K.; Yu, H. H.; Nakase, I.; Takatani-Nakase, T.; Madani, F.; Gräslund, A.; Futaki, S., Cytosolic antibody delivery by lipid-sensitive endosomolytic peptide. *Nature Chemistry* **2017,** *9* (8), 751-761.

157. Reissmann, S.; Filatova, M. P., New generation of cell-penetrating peptides: Functionality and potential clinical application. In *Journal of Peptide Science*, John Wiley and Sons Ltd: 2021; Vol. 27, pp e3300-e3300.

158. Futaki, S.; Nakase, I., Cell-Surface Interactions on Arginine-Rich Cell-Penetrating Peptides Allow for Multiplex Modes of Internalization. *Accounts of Chemical Research* **2017,** *50* (10), 2449-2456.

159. Peraro, L.; Kritzer, J. A., Emerging Methods and Design Principles for Cell-Penetrant Peptides. In *Angewandte Chemie - International Edition*, Wiley-VCH Verlag: 2018; Vol. 57, pp 11868-11881.

160. Heldwein, E. E.; Krummenacher, C., Entry of herpesviruses into mammalian cells. In *Cellular and Molecular Life Sciences*, Springer: 2008; Vol. 65, pp 1653-1668.

161. Spear, P. G., Herpes simplex virus: Receptors and ligands for cell entry. In *Cellular Microbiology*, John Wiley & Sons, Ltd: 2004; Vol. 6, pp 401-410.

162. Maurer, U. E.; Sodeik, B.; Grünewald, K., Native 3D intermediates of membrane fusion in herpes simplex virus 1 entry. *Proceedings of the National Academy of Sciences of the United States of America* **2008,** *105* (30), 10559-10564.

163. Brian Dyer, R.; Eller, M. W., Dynamics of hemagglutinin-mediated membrane fusion. In *Proceedings of the National Academy of Sciences of*

the United States of America, National Academy of Sciences: 2018; Vol. 115, pp 8655-8657.

164. Everts, M.; Saini, V.; Leddon, J. L.; Kok, R. J.; Stoff-Khalili, M.; Preuss, M. A.; Millican, C. L.; Perkins, G.; Brown, J. M.; Bagaria, H.; Nikles, D. E.; Johnson, D. T.; Zharov, V. P.; Curiel, D. T., Covalently Linked Au Nanoparticles to a Viral Vector: Potential for Combined Photothermal and Gene Cancer Therapy. *Nano Letters* **2006,** *6* (4), 587-591.

165. Günther, C.; Schmidt, U.; Rudolph, R.; Böhm, G., Protein and peptide delivery via engineered polyomavirus-like particles. *The FASEB Journal* **2001,** *15* (9), 1646-1648.

166. de Jonge, J.; Holtrop, M.; Wilschut, J.; Huckriede, A., Reconstituted influenza virus envelopes as an efficient carrier system for cellular delivery of small-interfering RNAs. *Gene Therapy* **2006,** *13* (5), 400-411.

167. Ghosh, S.; Brown, A. M.; Jenkins, C.; Campbell, K., Viral Vector Systems for Gene Therapy: A Comprehensive Literature Review of Progress and Biosafety Challenges. In *Applied Biosafety*, SAGE Publications Inc.: 2020; Vol. 25, pp 7-18.

168. Daemen, T.; De Mare, A.; Bungener, L.; De Jonge, J.; Huckriede, A.; Wilschut, J., Virosomes for antigen and DNA delivery. In *Advanced Drug Delivery Reviews*, Elsevier B.V.: 2005; Vol. 57, pp 451-463.

169. Zhao, Q.; Chen, W.; Chen, Y.; Zhang, L.; Zhang, J.; Zhang, Z., Self-assembled virus-like particles from rotavirus structural protein VP6 for targeted drug delivery. *Bioconjugate Chemistry* **2011,** *22* (3), 346-352.

170. Dashti, N. H.; Abidin, R. S.; Sainsbury, F., Programmable in Vitro Coencapsidation of Guest Proteins for Intracellular Delivery by Virus-like Particles. *ACS Nano* **2018,** *12* (5), 4615-4623.

171. Abbing, A.; Blaschke, U. K.; Grein, S.; Kretschmar, M.; Stark, C. M. B.; Thies, M. J. W.; Walter, J.; Weigand, M.; Woith, D. C.; Hess, J.; Reiser, C. O. A., Efficient intracellular delivery of a protein and a low molecular weight substance via recombinant polyomavirus-like particles. *Journal of Biological Chemistry* **2004,** *279* (26), 27410-27421.

172. Ashley, C. E.; Carnes, E. C.; Phillips, G. K.; Durfee, P. N.; Buley, M. D.; Lino, C. A.; Padilla, D. P.; Phillips, B.; Carter, M. B.; Willman, C. L.; Brinker, C. J.; Caldeira, J. D. C.; Chackerian, B.; Wharton, W.; Peabody, D. S. In *Cell-specific delivery of diverse cargos by bacteriophage*

MS2 virus-like particles, ACS Nano, 2011/7//; American Chemical Society: 2011; pp 5729-5745.

173. Wen, A. M.; Shukla, S.; Saxena, P.; Aljabali, A. A. A.; Yildiz, I.; Dey, S.; Mealy, J. E.; Yang, A. C.; Evans, D. J.; Lomonossoff, G. P.; Steinmetz, N. F., Interior engineering of a viral nanoparticle and its tumor homing properties. *Biomacromolecules* **2012,** *13* (12), 3990-4001.

174. Kaczmarczyk, S. J.; Sitaraman, K.; Young, H. A.; Hughes, S. H.; Chatterjee, D. K., Protein delivery using engineered virus-like particles. *Proceedings of the National Academy of Sciences of the United States of America* **2011,** *108* (41), 16998-17003.

175. Abraham, A.; Natraj, U.; Karande, A. A.; Gulati, A.; Murthy, M. R. N.; Murugesan, S.; Mukunda, P.; Savithri, H. S., Intracellular delivery of antibodies by chimeric Sesbania mosaic virus (SeMV) virus like particles. *Scientific Reports* **2016,** *6* (1), 1-12.

176. Csisza, A.; Hersch, N.; Dieluweit, S.; Biehl, R.; Merkel, R.; Hoffmann, B., Novel Fusogenic Liposomes for Fluorescent Cell Labeling and Membrane Modification. *Biomedical Engineering - Technical Applications in Medicine* **2010**, 537-543.

177. Pedroso De Lima, M. C.; Faneca, H.; Mano, M.; Penacho, N.; Düzgüneş, N.; Simões, S., Biophysical characterization of cationic liposome-DNA complexes and their interaction with cells. *Methods in Enzymology* **2003,** *373*, 298-312.

178. Chernomordik, L. V.; Kozlov, M. M., Mechanics of membrane fusion. In *Nature Structural and Molecular Biology*, Nature Publishing Group: 2008; Vol. 15, pp 675-683.

179. Siegel, D. P.; Epand, R. M., The mechanism of lamellar-to-inverted hexagonal phase transitions in phosphatidylethanolamine: Implications for membrane fusion mechanisms. *Biophysical Journal* **1997,** *73* (6), 3089-3111.

180. Kube, S.; Hersch, N.; Naumovska, E.; Gensch, T.; Hendriks, J.; Franzen, A.; Landvogt, L.; Siebrasse, J. P.; Kubitscheck, U.; Hoffmann, B.; Merkel, R.; Csiszár, A., Fusogenic liposomes as nanocarriers for the delivery of intracellular proteins. *Langmuir* **2017,** *33* (4), 1051-1059.

181. Yang, J.; Tu, J.; Lamers, G. E. M.; Olsthoorn, R. C. L.; Kros, A., Membrane Fusion Mediated Intracellular Delivery of Lipid Bilayer Coated

Mesoporous Silica Nanoparticles. *Advanced Healthcare Materials* **2017,** *6* (20), 1700759-1700759.

182. O'Brien, P. J.; Elahipanah, S.; Rogozhnikov, D.; Yousaf, M. N., Bio-Orthogonal Mediated Nucleic Acid Transfection of Cells via Cell Surface Engineering. *ACS Central Science* **2017,** *3* (5), 489-500.

183. Csiszár, A.; Csiszar, A.; Pinto, J. T.; Gautam, T.; Kleusch, C.; Hoffmann, B.; Tucsek, Z.; Toth, P.; Sonntag, W. E.; Ungvari, Z., Resveratrol encapsulated in novel fusogenic liposomes activates Nrf2 and attenuates oxidative stress in cerebromicrovascular endothelial cells from aged rats. *Journals of Gerontology - Series A Biological Sciences and Medical Sciences* **2015,** *70* (3), 303-313.

184. Farid, M.; Faber, T.; Dietrich, D.; Lamprecht, A., Cell membrane fusing liposomes for cytoplasmic delivery in brain endothelial cells. *Colloids and Surfaces B: Biointerfaces* **2020,** *194*, 111193-111193.

185. Zhu, J. Y.; Zheng, D. W.; Zhang, M. K.; Yu, W. Y.; Qiu, W. X.; Hu, J. J.; Feng, J.; Zhang, X. Z., Preferential Cancer Cell Self-Recognition and Tumor Self-Targeting by Coating Nanoparticles with Homotypic Cancer Cell Membranes. *Nano Letters* **2016,** *16* (9), 5895-5901.

186. Soprano, E.; Alvarez, A.; Pelaz, B.; del Pino, P.; Polo, E., Plasmonic Cell-Derived Nanocomposites for Light-Controlled Cargo Release inside Living Cells. *Advanced Biosystems* **2020,** *4* (3), 1900260.

187. Kolašinac, R.; Kleusch, C.; Braun, T.; Merkel, R.; Csiszár, A., Deciphering the functional composition of fusogenic liposomes. *International Journal of Molecular Sciences* **2018,** *19* (2).

188. Sau, T. K.; Murphy, C. J., Seeded high yield synthesis of short Au nanorods in aqueous solution. *Langmuir* **2004,** *20* (15), 6414-6420.

189. Hühn, J.; Carrillo-Carrion, C.; Soliman, M. G.; Pfeiffer, C.; Valdeperez, D.; Masood, A.; Chakraborty, I.; Zhu, L.; Gallego, M.; Yue, Z.; Carril, M.; Feliu, N.; Escudero, A.; Alkilany, A. M.; Pelaz, B.; Pino, P. D.; Parak, W. J., Selected standard protocols for the synthesis, phase transfer, and characterization of inorganic colloidal nanoparticles. *Chemistry of Materials* **2017,** *29* (1), 399-461.

190. Simons, K.; Vaz, W. L. C., Model Systems, Lipid Rafts, and Cell Membranes. *Annual Review of Biophysics and Biomolecular Structure* **2004,** *33* (1), 269-295.

191. Hu, C. M. J.; Fang, R. H.; Wang, K. C.; Luk, B. T.; Thamphiwatana, S.; Dehaini, D.; Nguyen, P.; Angsantikul, P.; Wen, C. H.; Kroll, A. V.; Carpenter, C.; Ramesh, M.; Qu, V.; Patel, S. H.; Zhu, J.; Shi, W.; Hofman, F. M.; Chen, T. C.; Gao, W.; Zhang, K.; Chien, S.; Zhang, L., Nanoparticle biointerfacing by platelet membrane cloaking. *Nature* **2015,** *526* (7571), 118-121.

192. Abdelmonem, A. M.; Pelaz, B.; Kantner, K.; Bigall, N. C.; del Pino, P.; Parak, W. J., Charge and agglomeration dependent in vitro uptake and cytotoxicity of zinc oxide nanoparticles. *Journal of Inorganic Biochemistry* **2015,** *153*, 334-338.

193. Hadjidemetriou, M.; Al-Ahmady, Z.; Mazza, M.; Collins, R. F.; Dawson, K.; Kostarelos, K., In Vivo Biomolecule Corona around Blood-Circulating, Clinically Used and Antibody-Targeted Lipid Bilayer Nanoscale Vesicles. *ACS Nano* **2015,** *9* (8), 8142-8156.

194. Monopoli, M. P.; Walczyk, D.; Campbell, A.; Elia, G.; Lynch, I.; Baldelli Bombelli, F.; Dawson, K. A., Physical−Chemical Aspects of Protein Corona: Relevance to in Vitro and in Vivo Biological Impacts of Nanoparticles. *Journal of the American Chemical Society* **2011,** *133* (8), 2525-2534.

195. Maziveyi, M.; Alahari, S. K., Cell matrix adhesions in cancer: The proteins that form the glue. In *Oncotarget*, Impact Journals LLC: 2017; Vol. 8, pp 48471-48487.

196. Cairns, R. A.; Harris, I. S.; Mak, T. W., Regulation of cancer cell metabolism. In *Nature Reviews Cancer*, Nature Publishing Group: 2011; Vol. 11, pp 85-95.

197. Liu, L.; Bai, X.; Martikainen, M.-V.; Kårlund, A.; Roponen, M.; Xu, W.; Hu, G.; Tasciotti, E.; Lehto, V.-P., Cell membrane coating integrity affects the internalization mechanism of biomimetic nanoparticles. *Nature Communications* **2021,** *12* (1), 5726.

198. Gao, X.; Li, S.; Ding, F.; Fan, H.; Shi, L.; Zhu, L.; Li, J.; Feng, J.; Zhu, X.; Zhang, C., Rapid Detection of Exosomal MicroRNAs Using Virus-Mimicking Fusogenic Vesicles. *Angewandte Chemie International Edition* **2019,** *58* (26), 8719-8723.

199. El Andaloussi, S.; Mäger, I.; Breakefield, X. O.; Wood, M. J. A., Extracellular vesicles: biology and emerging therapeutic opportunities. *Nature Reviews Drug Discovery* **2013,** *12* (5), 347-357.

200. Gilleron, J.; Querbes, W.; Zeigerer, A.; Borodovsky, A.; Marsico, G.; Schubert, U.; Manygoats, K.; Seifert, S.; Andree, C.; Stöter, M.; Epstein-Barash, H.; Zhang, L.; Koteliansky, V.; Fitzgerald, K.; Fava, E.; Bickle, M.; Kalaidzidis, Y.; Akinc, A.; Maier, M.; Zerial, M., Image-based analysis of lipid nanoparticle-mediated siRNA delivery, intracellular trafficking and endosomal escape. *Nature Biotechnology* **2013,** *31* (7), 638-646.

201. Mettlen, M.; Chen, P.-H.; Srinivasan, S.; Danuser, G.; Schmid, S. L., Regulation of Clathrin-Mediated Endocytosis. *Annual Review of Biochemistry* **2018,** *87* (1), 871-896.

202. Naslavsky, N.; Weigert, R.; Donaldson, J. G., Convergence of non-clathrin- and clathrin-derived endosomes involves Arf6 inactivation and changes in phosphoinositides. *Molecular Biology of the Cell* **2003,** *14* (2), 417-431.

203. Sabharanjak, S.; Sharma, P.; Parton, R. G.; Mayor, S., GPI-anchored proteins are delivered to recycling endosomes via a distinct cdc42-regulated clathrin-independent pinocytic pathway. *Developmental Cell* **2002,** *2* (4), 411-423.

204. Grassart, A.; Dujeancourt, A.; Lazarow, P. B.; Dautry-Varsat, A.; Sauvonnet, N., Clathrin-independent endocytosis used by the IL-2 receptor is regulated by Rac1, Pak1 and Pak2. *EMBO reports* **2008,** *9* (4), 356-362.

205. Swanson, J. A., Shaping cups into phagosomes and macropinosomes. In *Nature Reviews Molecular Cell Biology*, Nature Publishing Group: 2008; Vol. 9, pp 639-649.

206. Rennick, J. J.; Johnston, A. P. R.; Parton, R. G., Key principles and methods for studying the endocytosis of biological and nanoparticle therapeutics. *Nature Nanotechnology* **2021,** *16* (3), 266-276.

207. Stuart, A. D.; Brown, T. D. K., Entry of Feline Calicivirus Is Dependent on Clathrin-Mediated Endocytosis and Acidification in Endosomes. *Journal of Virology* **2006,** *80* (15), 7500-7509.

208. Wang, L. H.; Rothberg, K. G.; Anderson, R. G. W., Mis-assembly of clathrin lattices on endosomes reveals a regulatory switch for coated pit formation. *Journal of Cell Biology* **1993,** *123* (5), 1107-1117.

209. Macia, E.; Ehrlich, M.; Massol, R.; Boucrot, E.; Brunner, C.; Kirchhausen, T., Dynasore, a Cell-Permeable Inhibitor of Dynamin. *Developmental Cell* **2006,** *10* (6), 839-850.

210. Kilsdonk, E. P. C.; Yancey, P. G.; Stoudt, G. W.; Bangerter, F. W.; Johnson, W. J.; Phillips, M. C.; Rothblat, G. H., Cellular cholesterol efflux mediated by cyclodextrins. *Journal of Biological Chemistry* **1995,** *270* (29), 17250-17256.

211. Ros-Baró, A.; López-Iglesias, C.; Peiró, S.; Bellido, D.; Palacín, M.; Zorzano, A.; Camps, M., Lipid rafts are required for GLUT4 internalization in adipose cells. *Proceedings of the National Academy of Sciences of the United States of America* **2001,** *98* (21), 12050-12055.

212. Rothberg, K. G.; Ying, Y. S.; Kamen, B. A.; Anderson, R. G. W., Cholesterol controls the clustering of the glycophospholipid-anchored membrane receptor for 5-methyltetrahydrofolate. *Journal of Cell Biology* **1990,** *111* (6 II), 2931-2938.

213. Monis, G. F.; Schultz, C.; Ren, R.; Eberhard, J.; Costello, C.; Connors, L.; Skinner, M.; Trinkaus-Randall, V., Role of endocytic inhibitory drugs on internalization of amyloidogenic light chains by cardiac fibroblasts. *American Journal of Pathology* **2006,** *169* (6), 1939-1952.

214. Yoon, Y.-K.; Kim, H.-P.; Han, S.-W.; Oh, D. Y.; Im, S.-A.; Bang, Y.-J.; Kim, T.-Y., KRAS mutant lung cancer cells are differentially responsive to MEK inhibitor due to AKT or STAT3 activation: Implication for combinatorial approach. *Molecular Carcinogenesis* **2010,** *49* (4), 353-362.

215. Rao, L.; Meng, Q.-F.; Bu, L.-L.; Cai, B.; Huang, Q.; Sun, Z.-J.; Zhang, W.-F.; Li, A.; Guo, S.-S.; Liu, W.; Wang, T.-H.; Zhao, X.-Z., Erythrocyte Membrane-Coated Upconversion Nanoparticles with Minimal Protein Adsorption for Enhanced Tumor Imaging. *ACS Applied Materials & Interfaces* **2017,** *9* (3), 2159-2168.

216. Wang, C.; Wu, B.; Wu, Y.; Song, X.; Zhang, S.; Liu, Z., Camouflaging Nanoparticles with Brain Metastatic Tumor Cell Membranes: A New Strategy to Traverse Blood–Brain Barrier for Imaging and Therapy of Brain Tumors. *Advanced Functional Materials* **2020,** *30* (14), 1909369.

217. Gustafson, H. H.; Holt-Casper, D.; Grainger, D. W.; Ghandehari, H., Nanoparticle uptake: The phagocyte problem. *Nano Today* **2015,** *10* (4), 487-510.

218. Nishanth, R. P.; Jyotsna, R. G.; Schlager, J. J.; Hussain, S. M.; Reddanna, P., Inflammatory responses of RAW 264.7 macrophages upon

exposure to nanoparticles: Role of ROS-NFκB signaling pathway. *Nanotoxicology* **2011,** *5* (4), 502-516.

219. dos Santos, T.; Varela, J.; Lynch, I.; Salvati, A.; Dawson, K. A., Effects of Transport Inhibitors on the Cellular Uptake of Carboxylated Polystyrene Nanoparticles in Different Cell Lines. *PLOS ONE* **2011,** *6* (9), e24438.

220. Zhang, S.; Gao, H.; Bao, G., Physical Principles of Nanoparticle Cellular Endocytosis. *ACS Nano* **2015,** *9* (9), 8655-8671.

221. Behzadi, S.; Serpooshan, V.; Tao, W.; Hamaly, M. A.; Alkawareek, M. Y.; Dreaden, E. C.; Brown, D.; Alkilany, A. M.; Farokhzad, O. C.; Mahmoudi, M., Cellular uptake of nanoparticles: journey inside the cell. *Chemical Society Reviews* **2017,** *46* (14), 4218-4244.

222. Tchoryk, A.; Taresco, V.; Argent, R. H.; Ashford, M.; Gellert, P. R.; Stolnik, S.; Grabowska, A.; Garnett, M. C., Penetration and uptake of nanoparticles in 3D tumor spheroids. *Bioconjugate Chemistry* **2019,** *30* (5), 1371-1384.

223. Kelm, J. M.; Timmins, N. E.; Brown, C. J.; Fussenegger, M.; Nielsen, L. K., Method for generation of homogeneous multicellular tumor spheroids applicable to a wide variety of cell types. *Biotechnology and Bioengineering* **2003,** *83* (2), 173-180.

224. Froehlich, K.; Haeger, J. D.; Heger, J.; Pastuschek, J.; Photini, S. M.; Yan, Y.; Lupp, A.; Pfarrer, C.; Mrowka, R.; Schleußner, E.; Markert, U. R.; Schmidt, A., Generation of Multicellular Breast Cancer Tumor Spheroids: Comparison of Different Protocols. *J Mammary Gland Biol Neoplasia* **2016,** *21* (3-4), 89-98.

225. Nederman, T.; Norling, B.; Glimelius, B.; Carlsson, J.; Brunk, U., Demonstration of an Extracellular Matrix in Multicellular Tumor Spheroids. *Cancer Research* **1984,** *44* (7).

226. Rotin, D.; Robinson, B.; Tannock, I. F., Influence of Hypoxia and an Acidic Environment on the Metabolism and Viability of Cultured Cells: Potential Implications for Cell Death in Tumors. *Cancer Research* **1986,** *46* (6).

227. Carver, K.; Ming, X.; Juliano, R. L., Multicellular tumor spheroids as a model for assessing delivery of oligonucleotides in three dimensions. *Molecular Therapy - Nucleic Acids* **2014,** *3*, e153-e153.

228. Mellor, H. R.; Ferguson, D. J. P.; Callaghan, R., A model of quiescent tumour microregions for evaluating multicellular resistance to chemotherapeutic drugs. *British Journal of Cancer* **2005,** *93* (3), 302-309.

229. Desoize, B.; Jardillier, J. C., Multicellular resistance: A paradigm for clinical resistance? In *Critical Reviews in Oncology/Hematology*, Elsevier: 2000; Vol. 36, pp 193-207.

230. Gong, X.; Lin, C.; Cheng, J.; Su, J.; Zhao, H.; Liu, T.; Wen, X.; Zhao, P., Generation of Multicellular Tumor Spheroids with Microwell-Based Agarose Scaffolds for Drug Testing. *PLOS ONE* **2015,** *10* (6), e0130348.

231. Minchinton, A. I.; Tannock, I. F., Drug penetration in solid tumours. *Nature Reviews Cancer* **2006,** *6* (8), 583-592.

232. Tannock, I. F.; Lee, C. M.; Tunggal, J. K.; Cowan, D. S. M.; Egorin, M. J., Limited Penetration of Anticancer Drugs through Tumor Tissue. *Clinical Cancer Research* **2002,** *8* (3), 878.

233. Costa, E. C.; Silva, D. N.; Moreira, A. F.; Correia, I. J., Optical clearing methods: An overview of the techniques used for the imaging of 3D spheroids. In *Biotechnology and Bioengineering*, John Wiley and Sons Inc.: 2019; Vol. 116, pp 2742-2763.

234. Pelaz, B.; Del Pino, P.; Maffre, P.; Hartmann, R.; Gallego, M.; Rivera-Fernández, S.; De La Fuente, J. M.; Nienhaus, G. U.; Parak, W. J., Surface Functionalization of Nanoparticles with Polyethylene Glycol: Effects on Protein Adsorption and Cellular Uptake. *ACS Nano* **2015,** *9* (7), 6996-7008.

235. Polo, E.; Araban, V.; Pelaz, B.; Alvarez, A.; Taboada, P.; Mahmoudi, M.; del Pino, P., Photothermal effects on protein adsorption dynamics of PEGylated gold nanorods. *Applied Materials Today* **2019,** *15*, 599-604.

236. Zhang, Q.; Dehaini, D.; Zhang, Y.; Zhou, J.; Chen, X.; Zhang, L.; Fang, R. H.; Gao, W.; Zhang, L., Neutrophil membrane-coated nanoparticles inhibit synovial inflammation and alleviate joint damage in inflammatory arthritis. *Nature Nanotechnology* **2018,** *13* (12), 1182-1190.

237. Dehaini, D.; Wei, X.; Fang, R. H.; Masson, S.; Angsantikul, P.; Luk, B. T.; Zhang, Y.; Ying, M.; Jiang, Y.; Kroll, A. V.; Gao, W.; Zhang, L., Erythrocyte–Platelet Hybrid Membrane Coating for Enhanced

Nanoparticle Functionalization. *Advanced Materials* **2017,** *29* (16), 1606209-1606209.

238. Zhang, N.; Li, M.; Sun, X.; Jia, H.; Liu, W., NIR-responsive cancer cytomembrane-cloaked carrier-free nanosystems for highly efficient and self-targeted tumor drug delivery. *Biomaterials* **2018,** *159*, 25-36.

239. Pasto, A.; Giordano, F.; Evangelopoulos, M.; Amadori, A.; Tasciotti, E., Cell membrane protein functionalization of nanoparticles as a new tumor-targeting strategy. *Clinical and Translational Medicine* **2019,** *8* (1).

240. Pérez-Hernández, M.; Del Pino, P.; Mitchell, S. G.; Moros, M.; Stepien, G.; Pelaz, B.; Parak, W. J.; Gálvez, E. M.; Pardo, J.; De La Fuente, J. M., Dissecting the molecular mechanism of apoptosis during photothermal therapy using gold nanoprisms. *ACS Nano* **2015,** *9* (1), 52-61.

241. Singh, K.; Ejaz, W.; Dutta, K.; Thayumanavan, S., Antibody Delivery for Intracellular Targets: Emergent Therapeutic Potential. *Bioconjugate Chemistry* **2019,** *30* (4), 1028-1041.

242. Slastnikova, T. A.; Ulasov, A. V.; Rosenkranz, A. A.; Sobolev, A. S., Targeted Intracellular Delivery of Antibodies: The State of the Art. *Frontiers in Pharmacology* **2018,** *9* (1208).

243. Gao, L.; Han, L.; Ding, X.; Xu, J.; Wang, J.; Zhu, J.; Lu, W.; Sun, J.; Yu, L.; Yan, Z.; Wang, Y., An effective intracellular delivery system of monoclonal antibody for treatment of tumors: Erythrocyte membrane-coated self-associated antibody nanoparticles. *Nanotechnology* **2017,** *28* (33), 335101-335101.

244. Stewart, M. P.; Sharei, A.; Ding, X.; Sahay, G.; Langer, R.; Jensen, K. F., In vitro and ex vivo strategies for intracellular delivery. In *Nature*, Nature Publishing Group: 2016; Vol. 538, pp 183-192.

245. Stewart, M. P.; Sharei, A.; Ding, X.; Sahay, G.; Langer, R.; Jensen, K. F., In vitro and ex vivo strategies for intracellular delivery. *Nature* **2016,** *538* (7624), 183-192.

246. Blijleven, J. S.; Boonstra, S.; Onck, P. R.; van der Giessen, E.; van Oijen, A. M., Mechanisms of influenza viral membrane fusion. *Seminars in Cell & Developmental Biology* **2016,** *60*, 78-88.

247. Bucevičius, J.; Lukinavičius, G.; Gerasimaitė, R., The Use of Hoechst Dyes for DNA Staining and Beyond. *Chemosensors* **2018,** *6* (2), 18.

248. Han, F.; Taulier, N.; Chalikian, T. V., Association of the minor groove binding drug Hoechst 33258 with d(CGCGAATTCGCG)2: volumetric, calorimetric, and spectroscopic characterizations. *Biochemistry* **2005,** *44* (28), 9785-94.

249. Moumaris, M.; Rajoelya, B.; Abuafa, N., Fluorescein isothiocyanate-dextran can track apoptosis and necrosis induced by heat shock of peripheral blood mononuclear cells and HeLa cells. *Open Biological Sciences Journal* **2015,** *1* (1).

250. Loos, C.; Syrovets, T.; Musyanovych, A.; Mailänder, V.; Landfester, K.; Nienhaus, G. U.; Simmet, T., Functionalized polystyrene nanoparticles as a platform for studying bio-nano interactions. *Beilstein J Nanotechnol* **2014,** *5*, 2403-12.

251. Varela, J. A.; Bexiga, M. G.; Åberg, C.; Simpson, J. C.; Dawson, K. A., Quantifying size-dependent interactions between fluorescently labeled polystyrene nanoparticles and mammalian cells. *Journal of Nanobiotechnology* **2012,** *10* (1), 39.

6. List of Publications

1. **Enrica Soprano**, Miriam Lopez, Beatriz Pelaz, Ester Polo, Pablo del Pino. Fusogenic Cell-derived Nanocarriers for Cytosolic Delivery of Active Cargo Inside living cells. *In prep*.
2. **Enrica Soprano**, Martina Migliavacca, Beatriz Pelaz, Pablo Del Pino, Ester Polo. Protocols for engineering Cell-derived Nanocarriers for Bioapplications. *In prep.*
3. **Enrica Soprano**, Aitor Alvarez, Beatriz Pelaz, Pablo Del Pino, Ester Polo. *Plasmonic Cell-Derived Nanocomposites for Light-Controlled Cargo Release inside Living Cells*. Advanced biosystems, 4 (3): p. 1900260 (2020).

   Author contribution: the author, Enrica Soprano, performed the sample preparation and nanomaterial characterization, all in vitro cell experiments, and data analysis.

   Quality Indexes: the journal where the manuscript corresponding to the work presented in Chapter 3.2 was published, has an impact score of 3.59 and an h-Index of 18. The best quartile for the journal is Q1 in Biochemistry, Genetics and Molecular Biology; Biomaterials; Biomedical Engineering. According to SCImago Journal Rank (SJR 2020), this journal is ranked 1.15.

   Autorization: Advanced Biosystems, property of the publisher Wiley, where Chapter 3.2 was published, allows reuse of the author's article as part of her thesis.

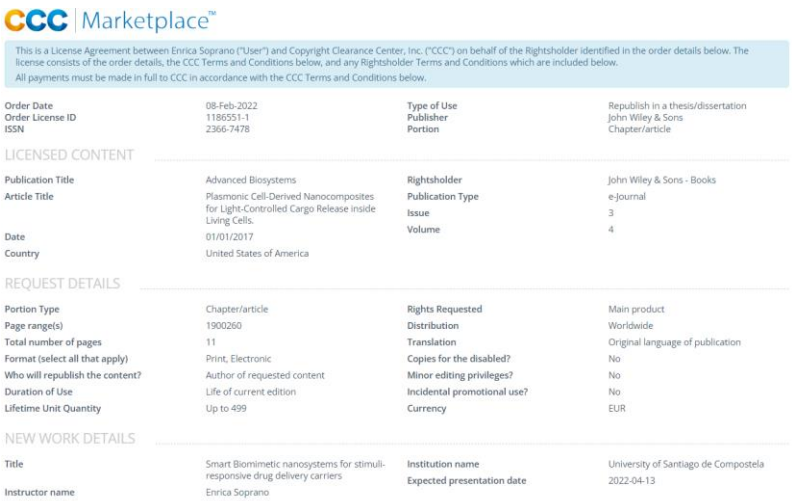

CCC Marketplace™

This is a License Agreement between Enrica Soprano ("User") and Copyright Clearance Center, Inc. ("CCC") on behalf of the Rightsholder identified in the order details below. The license consists of the order details, the CCC Terms and Conditions below, and any Rightsholder Terms and Conditions which are included below.

All payments must be made in full to CCC in accordance with the CCC Terms and Conditions below.

Order Date	08-Feb-2022	Type of Use	Republish in a thesis/dissertation
Order License ID	1186551-1	Publisher	John Wiley & Sons
ISSN	2366-7478	Portion	Chapter/article

LICENSED CONTENT

Publication Title	Advanced Biosystems	Rightsholder	John Wiley & Sons - Books
Article Title	Plasmonic Cell-Derived Nanocomposites for Light-Controlled Cargo Release inside Living Cells.	Publication Type	e-Journal
		Issue	3
		Volume	4
Date	01/01/2017		
Country	United States of America		

REQUEST DETAILS

Portion Type	Chapter/article	Rights Requested	Main product
Page range(s)	1900260	Distribution	Worldwide
Total number of pages	11	Translation	Original language of publication
Format (select all that apply)	Print, Electronic	Copies for the disabled?	No
Who will republish the content?	Author of requested content	Minor editing privileges?	No
Duration of Use	Life of current edition	Incidental promotional use?	No
Lifetime Unit Quantity	Up to 499	Currency	EUR

NEW WORK DETAILS

Title	Smart Biomimetic nanosystems for stimuli-responsive drug delivery carriers	Institution name	University of Santiago de Compostela
		Expected presentation date	2022-04-13
Instructor name	Enrica Soprano		

4. Raquel Martínez, María F Navarro Poupard, Aitor Álvarez, **Enrica Soprano**, Martina Migliavacca, Carolina Carrillo-Carrión, Ester Polo, Beatriz Pelaz, Pablo del Pino. *Nanoparticles behavior and stability in biological environments (Chapter 2)*. Nanoparticles for Biomedical Applications (Micro and Nano Technologies, Elsevier), ISBN 9780128166628: p. 5-18 (2020).
5. Francisco Triana-Martínez, Pilar Picallos-Rabina, Sabela Da Silva-Álvarez, Federico Pietrocola, Susana Llanos, Verónica Rodilla, **Enrica Soprano**, Pablo Pedrosa, Alba Ferreirós, Marta Barradas, Fernanda Hernández-González, Marta Lalinde, Neus Prats, Cristina Bernadó, Patricia González, María Gómez, Maria P Ikonomopoulou, Pablo J Fernández-Marcos, Tomás García-Caballero, Pablo Del Pino, Joaquín Arribas, Anxo Vidal, Miguel González-Barcia, Manuel Serrano, María I Loza, Eduardo Domínguez, Manuel Collado. *Identification and characterization of Cardiac Glycosides as senolytic compounds*. Nature Communications, 10 (1): p. 1-12 (2019).

7. List of Figures

8. List of Tables

9. Appendix-Figures Rights & Permissions

Chapter	Rights & Permissions
3.2	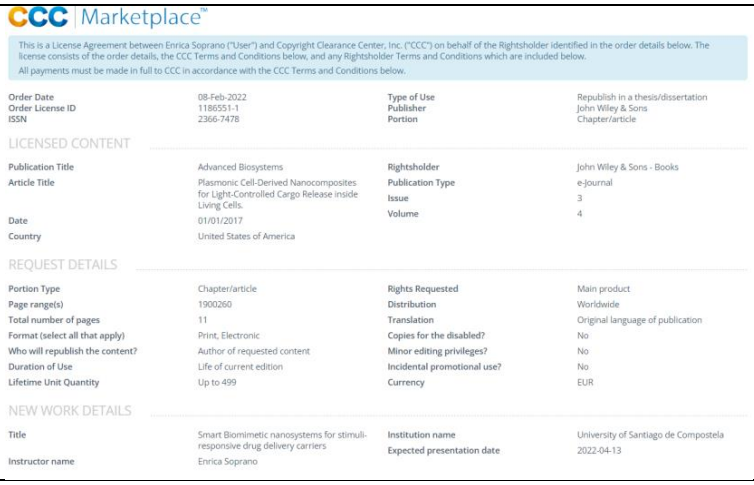

Figure	Rights & Permissions
1.1.4	

1.2.1

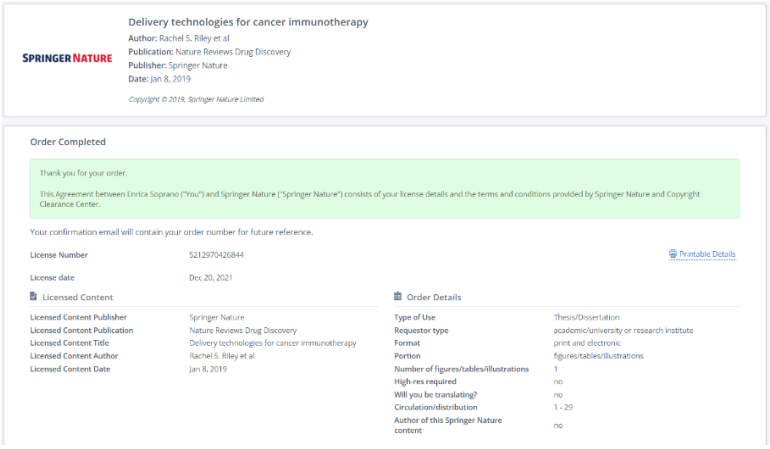

SPRINGER NATURE

Delivery technologies for cancer immunotherapy

Author: Rachel S. Riley et al
Publication: Nature Reviews Drug Discovery
Publisher: Springer Nature
Date: Jan 8, 2019

Copyright © 2019, Springer Nature Limited

Order Completed

Thank you for your order.

This Agreement between Enrica Soprano ("You") and Springer Nature ("Springer Nature") consists of your license details and the terms and conditions provided by Springer Nature and Copyright Clearance Center.

Your confirmation email will contain your order number for future reference.

License Number	5212970426844
License date	Dec 20, 2021

Printable Details

Licensed Content

Licensed Content Publisher	Springer Nature
Licensed Content Publication	Nature Reviews Drug Discovery
Licensed Content Title	Delivery technologies for cancer immunotherapy
Licensed Content Author	Rachel S. Riley et al
Licensed Content Date	Jan 8, 2019

Order Details

Type of Use	Thesis/Dissertation
Requestor type	academic/university or research institute
Format	print and electronic
Portion	figures/tables/illustrations
Number of figures/tables/illustrations	1
High-res required	no
Will you be translating?	no
Circulation/distribution	1 - 29
Author of this Springer Nature content	no

1.2.2

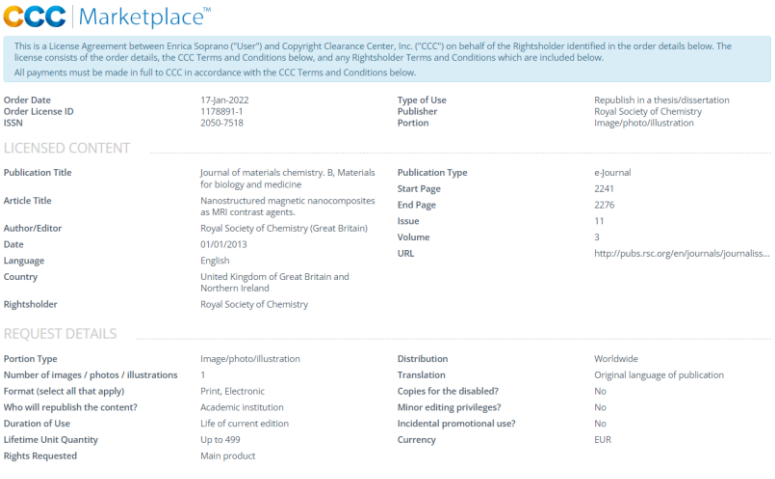

CCC Marketplace™

This is a License Agreement between Enrica Soprano ("User") and Copyright Clearance Center, Inc. ("CCC") on behalf of the Rightsholder identified in the order details below. The license consists of the order details, the CCC Terms and Conditions below, and any Rightsholder Terms and Conditions which are included below.

All payments must be made in full to CCC in accordance with the CCC Terms and Conditions below.

Order Date	17-Jan-2022	Type of Use	Republish in a thesis/dissertation
Order License ID	1178891-1	Publisher	Royal Society of Chemistry
ISSN	2050-7518	Portion	Image/photo/illustration

LICENSED CONTENT

Publication Title	Journal of materials chemistry. B, Materials for biology and medicine	Publication Type	e-Journal
Article Title	Nanostructured magnetic nanocomposites as MRI contrast agents.	Start Page	2241
Author/Editor	Royal Society of Chemistry (Great Britain)	End Page	2276
Date	01/01/2013	Issue	11
Language	English	Volume	3
Country	United Kingdom of Great Britain and Northern Ireland	URL	http://pubs.rsc.org/en/journals/journaliss...
Rightsholder	Royal Society of Chemistry		

REQUEST DETAILS

Portion Type	Image/photo/illustration	Distribution	Worldwide
Number of images / photos / illustrations	1	Translation	Original language of publication
Format (select all that apply)	Print, Electronic	Copies for the disabled?	No
Who will republish the content?	Academic institution	Minor editing privileges?	No
Duration of Use	Life of current edition	Incidental promotional use?	No
Lifetime Unit Quantity	Up to 499	Currency	EUR
Rights Requested	Main product		

1.3.1

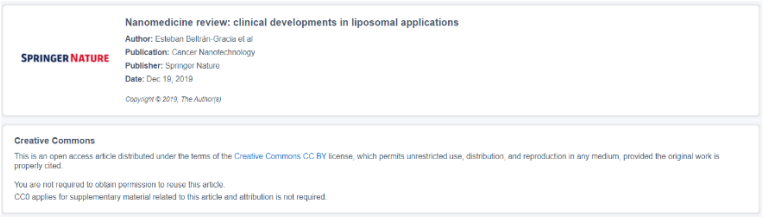

SPRINGER NATURE

Nanomedicine review: clinical developments in liposomal applications

Author: Esteban Beltrán-Gracia et al
Publication: Cancer Nanotechnology
Publisher: Springer Nature
Date: Dec 19, 2019

Copyright © 2019, The Author(s)

Creative Commons

This is an open access article distributed under the terms of the Creative Commons CC BY license, which permits unrestricted use, distribution, and reproduction in any medium, provided the original work is properly cited.

You are not required to obtain permission to reuse this article.
CC0 applies for supplementary material related to this article and attribution is not required.

1.4.1

Progress of Cell-Derived Biomimetic Drug Delivery Systems for Cancer Therapy

Author: Yaping Li, Qi Yin, Tianqun Lang
Publication: ADVANCED THERAPEUTICS
Publisher: John Wiley and Sons
Date: Aug 23, 2018

Order Completed

Thank you for your order.

This Agreement between Enrica Soprano ("You") and John Wiley and Sons ("John Wiley and Sons") consists of your license details and the terms and conditions provided by John Wiley and Sons and Copyright Clearance Center.

Your confirmation email will contain your order number for future reference.

Printable Details

License Number	5212631420843
License date	Dec 19, 2021

Licensed Content

Licensed Content Publisher	John Wiley and Sons
Licensed Content Publication	ADVANCED THERAPEUTICS
Licensed Content Title	Progress of Cell-Derived Biomimetic Drug Delivery Systems for Cancer Therapy
Licensed Content Author	Yaping Li, Qi Yin, Tianqun Lang
Licensed Content Date	Aug 23, 2018
Licensed Content Volume	1
Licensed Content Issue	7

Order Details

Type of use	Dissertation/Thesis
Requestor type	University/Academic
Format	Print and electronic
Portion	Figure/table
Number of figures/tables	1
Will you be translating?	No

1.4.3

Photothermal cancer immunotherapy by erythrocyte membrane-coated black phosphorus formulation

Author: Xin Liang,Xinyu Ye,Chao Wang,Chenyang Xing,Qianwei Miao,Zhongjian Xie,Xiuli Chen,Xudong Zhang,Han Zhang,Lin Mei
Publication: Journal of Controlled Release
Publisher: Elsevier
Date: 28 February 2019

Order Completed

Thank you for your order.

This Agreement between Enrica Soprano ("You") and Elsevier ("Elsevier") consists of your license details and the terms and conditions provided by Elsevier and Copyright Clearance Center.

Your confirmation email will contain your order number for future reference.

Printable Details

License Number	5210150761208
License date	Dec 15, 2021

Licensed Content

Licensed Content Publisher	Elsevier
Licensed Content Publication	Journal of Controlled Release
Licensed Content Title	Photothermal cancer immunotherapy by erythrocyte membrane-coated black phosphorus formulation
Licensed Content Author	Xin Liang,Xinyu Ye,Chao Wang,Chenyang Xing,Qianwei Miao,Zhongjian Xie,Xiuli Chen,Xudong Zhang,Han Zhang,Lin Mei
Licensed Content Date	Feb 28, 2019
Licensed Content Volume	296
Licensed Content Issue	n/a
Licensed Content Pages	12

Order Details

Type of Use	reuse in a thesis/dissertation
Portion	figures/tables/illustrations
Number of figures/tables/illustrations	2
Format	both print and electronic
Are you the author of this Elsevier article?	No
Will you be translating?	No

1.4.4

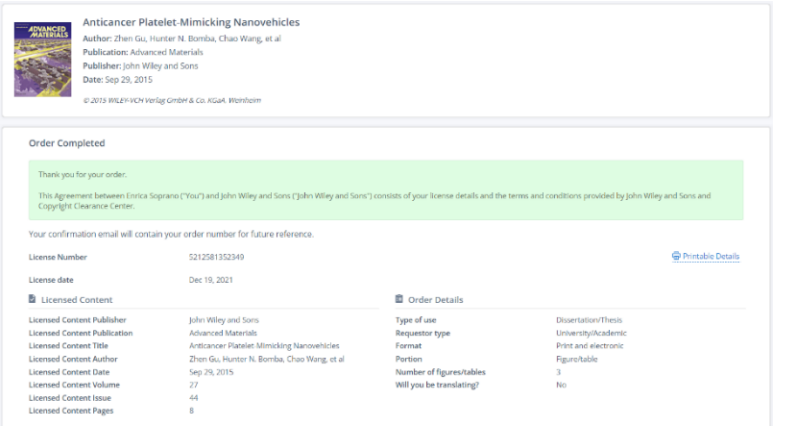

Anticancer Platelet-Mimicking Nanovehicles

Author: Zhen Gu, Hunter N. Bomba, Chao Wang, et al
Publication: Advanced Materials
Publisher: John Wiley and Sons
Date: Sep 29, 2015

© 2015 WILEY-VCH Verlag GmbH & Co. KGaA, Weinheim

Order Completed

Thank you for your order.

This Agreement between Enrica Soprano ("You") and John Wiley and Sons ("John Wiley and Sons") consists of your license details and the terms and conditions provided by John Wiley and Sons and Copyright Clearance Center.

Your confirmation email will contain your order number for future reference.

Printable Details

License Number	5212581352349
License date	Dec 19, 2021

Licensed Content

Licensed Content Publisher	John Wiley and Sons
Licensed Content Publication	Advanced Materials
Licensed Content Title	Anticancer Platelet-Mimicking Nanovehicles
Licensed Content Author	Zhen Gu, Hunter N. Bomba, Chao Wang, et al
Licensed Content Date	Sep 29, 2015
Licensed Content Volume	27
Licensed Content Issue	44
Licensed Content Pages	8

Order Details

Type of use	Dissertation/Thesis
Requestor type	University/Academic
Format	Print and electronic
Portion	Figure/table
Number of figures/tables	3
Will you be translating?	No

1.4.5

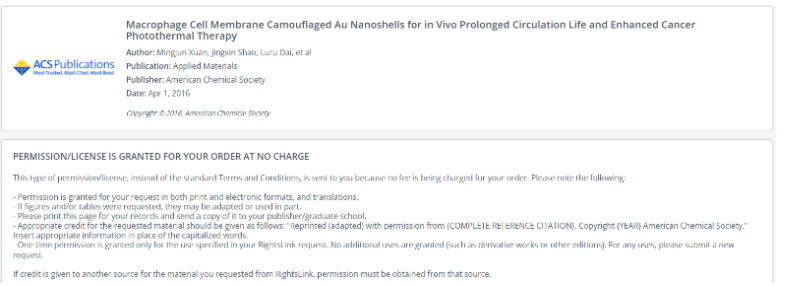

Macrophage Cell Membrane Camouflaged Au Nanoshells for in Vivo Prolonged Circulation Life and Enhanced Cancer Photothermal Therapy

Author: Mingjun Xuan, Jingxin Shao, Luru Dai, et al
Publication: Applied Materials
Publisher: American Chemical Society
Date: Apr 1, 2016

Copyright © 2016, American Chemical Society

PERMISSION/LICENSE IS GRANTED FOR YOUR ORDER AT NO CHARGE

This type of permission/license, instead of the standard Terms and Conditions, is sent to you because no fee is being charged for your order. Please note the following:

- Permission is granted for your request in both print and electronic formats, and translations.
- If figures and/or tables were requested, they may be adapted or used in part.
- Please print this page for your records and send a copy of it to your publisher/graduate school.
- Appropriate credit for the requested material should be given as follows: "Reprinted (adapted) with permission from (COMPLETE REFERENCE CITATION). Copyright (YEAR) American Chemical Society." Insert appropriate information in place of the capitalized words.
- One-time permission is granted only for the use specified in your RightsLink request. No additional uses are granted (such as derivative works or other editions). For any uses, please submit a new request.

If credit is given to another source for the material you requested from RightsLink, permission must be obtained from that source.

1.4.6

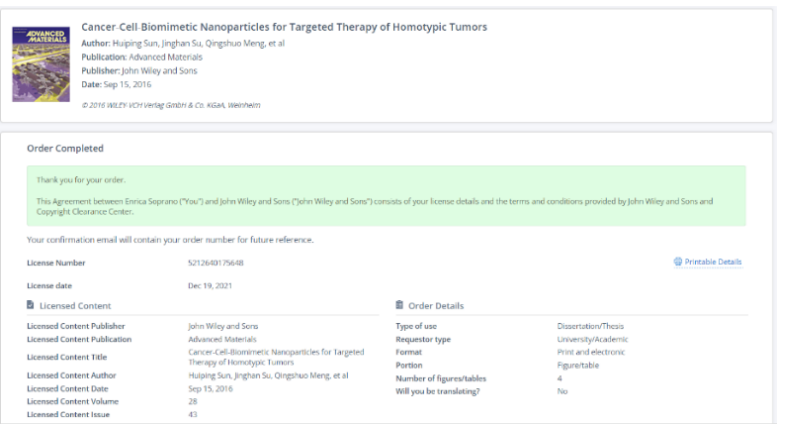

Cancer-Cell-Biomimetic Nanoparticles for Targeted Therapy of Homotypic Tumors

Author: Huiping Sun, Jinghan Su, Qingshuo Meng, et al
Publication: Advanced Materials
Publisher: John Wiley and Sons
Date: Sep 15, 2016

© 2016 WILEY-VCH Verlag GmbH & Co. KGaA, Weinheim

Order Completed

Thank you for your order.

This Agreement between Enrica Soprano ("You") and John Wiley and Sons ("John Wiley and Sons") consists of your license details and the terms and conditions provided by John Wiley and Sons and Copyright Clearance Center.

Your confirmation email will contain your order number for future reference.

Printable Details

License Number	5212640175648
License date	Dec 19, 2021

Licensed Content

Licensed Content Publisher	John Wiley and Sons
Licensed Content Publication	Advanced Materials
Licensed Content Title	Cancer-Cell-Biomimetic Nanoparticles for Targeted Therapy of Homotypic Tumors
Licensed Content Author	Huiping Sun, Jinghan Su, Qingshuo Meng, et al
Licensed Content Date	Sep 15, 2016
Licensed Content Volume	28
Licensed Content Issue	43

Order Details

Type of use	Dissertation/Thesis
Requestor type	University/Academic
Format	Print and electronic
Portion	Figure/table
Number of figures/tables	4
Will you be translating?	No

1.4.7	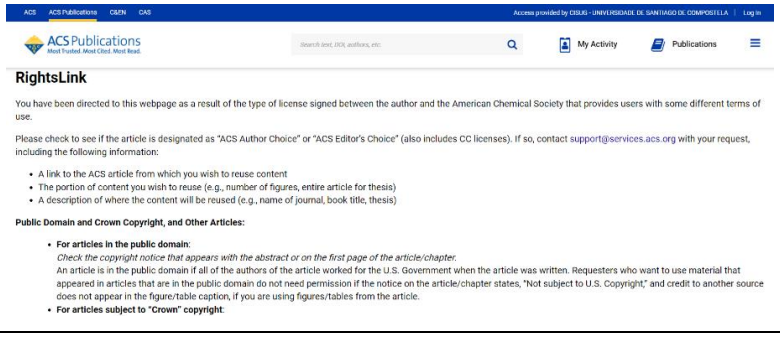
1.5.3a	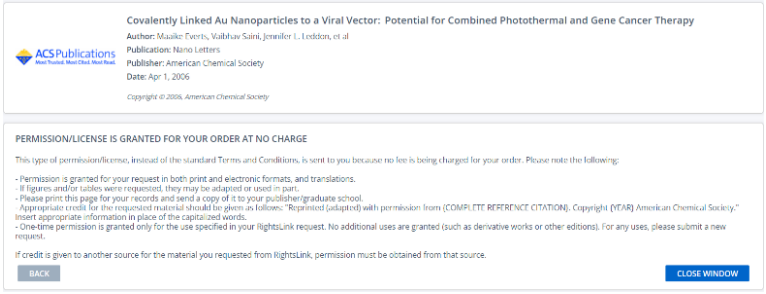
1.5.3b	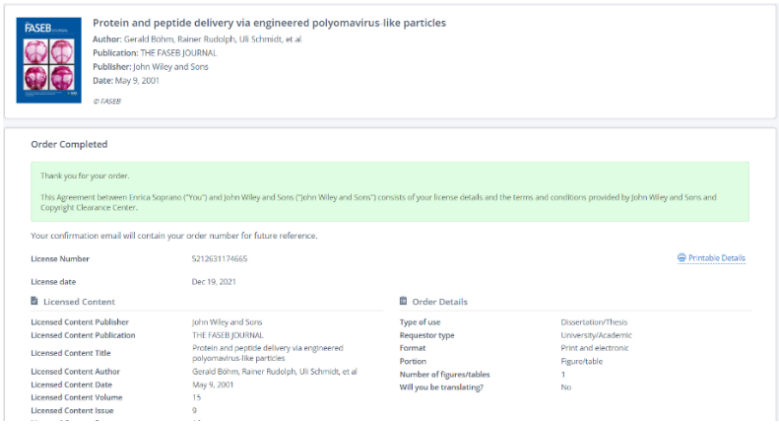

1.5.3c

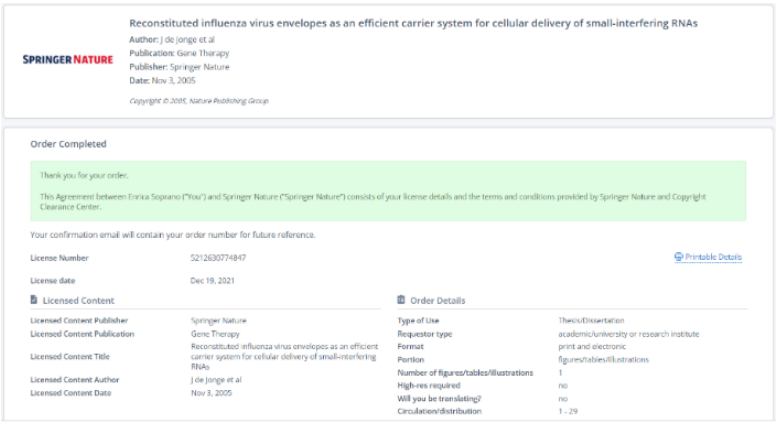

Reconstituted influenza virus envelopes as an efficient carrier system for cellular delivery of small-interfering RNAs

Author: J de Jonge et al
Publication: Gene Therapy
Publisher: Springer Nature
Date: Nov 3, 2005

Copyright © 2005, Nature Publishing Group

Order Completed

Thank you for your order.

This Agreement between Enrica Soprano ("You") and Springer Nature ("Springer Nature") consists of your license details and the terms and conditions provided by Springer Nature and Copyright Clearance Center.

Your confirmation email will contain your order number for future reference.

License Number	5212630774847
License date	Dec 19, 2021

Printable Details

Licensed Content

Licensed Content Publisher	Springer Nature
Licensed Content Publication	Gene Therapy
Licensed Content Title	Reconstituted influenza virus envelopes as an efficient carrier system for cellular delivery of small-interfering RNAs
Licensed Content Author	J de Jonge et al
Licensed Content Date	Nov 3, 2005

Order Details

Type of Use	Thesis/Dissertation
Requestor type	academic/university or research institute
Format	print and electronic
Portion	figures/tables/illustrations
Number of figures/tables/illustrations	1
High-res required	no
Will you be translating?	no
Circulation/distribution	1 - 29

1.5.5a

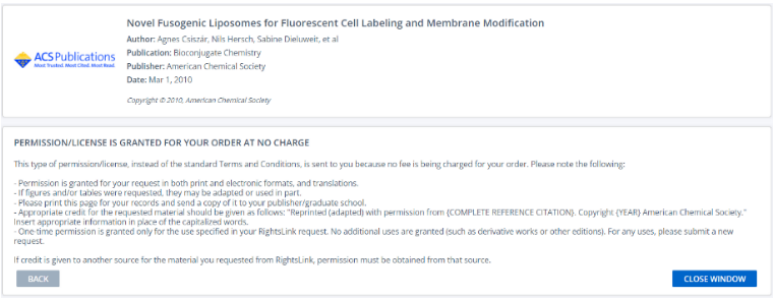

Novel Fusogenic Liposomes for Fluorescent Cell Labeling and Membrane Modification

Author: Agnes Csiszár, Nils Hersch, Sabine Dieluweit, et al
Publication: Bioconjugate Chemistry
Publisher: American Chemical Society
Date: Mar 1, 2010

Copyright © 2010, American Chemical Society

PERMISSION/LICENSE IS GRANTED FOR YOUR ORDER AT NO CHARGE

This type of permission/license, instead of the standard Terms and Conditions, is sent to you because no fee is being charged for your order. Please note the following:

- Permission is granted for your request in both print and electronic formats, and translations.
- If figures and/or tables were requested, they may be adapted or used in part.
- Please print this page for your records and send a copy of it to your publisher/graduate school.
- Appropriate credit for the requested material should be given as follows: "Reprinted (adapted) with permission from (COMPLETE REFERENCE CITATION). Copyright (YEAR) American Chemical Society." Insert appropriate information in place of the capitalized words.
- One-time permission is granted only for the use specified in your RightsLink request. No additional uses are granted (such as derivative works or other editions). For any uses, please submit a new request.

If credit is given to another source for the material you requested from RightsLink, permission must be obtained from that source.

BACK CLOSE WINDOW

1.5.5b

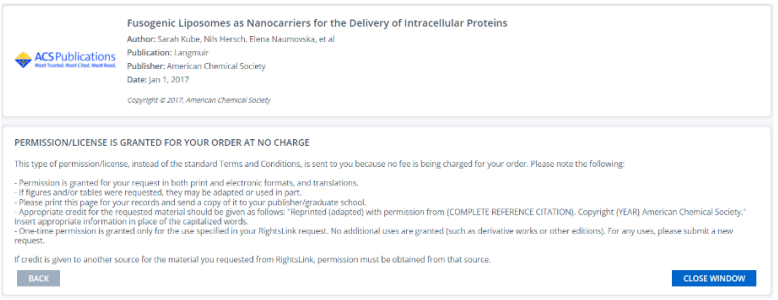

Fusogenic Liposomes as Nanocarriers for the Delivery of Intracellular Proteins

Author: Sarah Kube, Nils Hersch, Elena Naumovska, et al
Publication: Langmuir
Publisher: American Chemical Society
Date: Jan 1, 2017

Copyright © 2017, American Chemical Society

PERMISSION/LICENSE IS GRANTED FOR YOUR ORDER AT NO CHARGE

This type of permission/license, instead of the standard Terms and Conditions, is sent to you because no fee is being charged for your order. Please note the following:

- Permission is granted for your request in both print and electronic formats, and translations.
- If figures and/or tables were requested, they may be adapted or used in part.
- Please print this page for your records and send a copy of it to your publisher/graduate school.
- Appropriate credit for the requested material should be given as follows: "Reprinted (adapted) with permission from (COMPLETE REFERENCE CITATION). Copyright (YEAR) American Chemical Society." Insert appropriate information in place of the capitalized words.
- One-time permission is granted only for the use specified in your RightsLink request. No additional uses are granted (such as derivative works or other editions). For any uses, please submit a new request.

If credit is given to another source for the material you requested from RightsLink, permission must be obtained from that source.

BACK CLOSE WINDOW

3.1.17	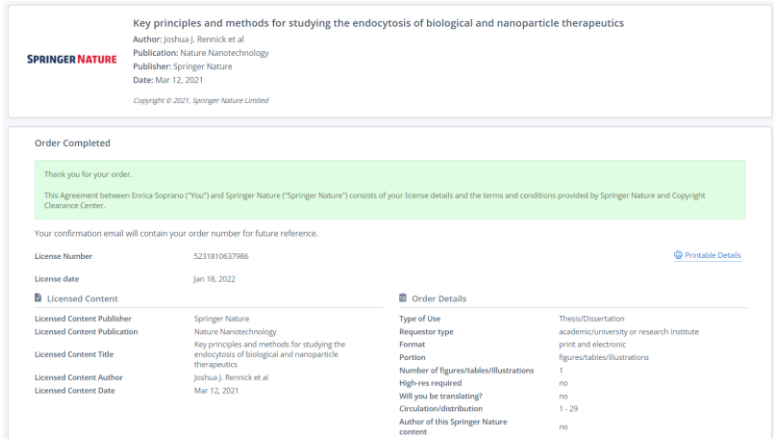

The research conducted in this thesis finds its purpose in the development of cell-based nanosystems that further broaden nanomedicine towards advanced therapeutics in the drug delivery field. Cancer cells were used to obtain biomimetic membrane-based nanoparticles, with the aim of exploiting natural cell membrane features to enhance biocompatibility, obtain high specific targeting efficacy and improve immune evading capability. Two kinds of smart nanocarriers were set up, focusing on the development of innovative strategies to achieve the intracellular cargo delivery.